LiDAR and InSAR analysis of deformation in the Krafla rift zone, NE Iceland

Emma Kristy Bramham

Submitted in accordance with the requirements for the degree of
Doctor of Philosophy

The University of Leeds
School of Earth and Environment
Institute of Geophysics and Tectonics
January 2014

Declaration

The candidate confirms that the work submitted is her own and that appropriate credit has been given where reference has been made to the work of others.

Acknowledgements

Firstly, I would like to thank my supervisors, Tim Wright and Douglas Paton, who gave me the opportunity to set out along this path and continued throughout to provide me with the support, guidance and understanding that I needed along the way. Their enthusiasm and motivation for the field was infectious and their constant encouragement let me explore my work freely and inquisitively. Also helping me throughout my PhD as part of my Research Support Group was Carolina Pagli and I must thank her most wholeheartedly for her assistance with all things InSAR and for her untiring patience with explaining the ins and outs of InSAR processing.

My time spent in Iceland was an essential and most memorable part of my PhD. For this I thank Freysteinn Sigmundsson for both his guidance and for putting me in touch with Ásta Rut Hjartardottir to help me with my fieldwork. Ásta Rut's warm welcome to Iceland, her knowledge of the field and her willingness to let me drive off-road were all most appreciated. I'd also like to thank Páll Einarsson for coming out to the field and letting me tag along and benefit from his vast knowledge of the region. Páll's willingness to answer constant questions from my children will never be forgotten.

All of this would have not been possible without the support of the Centre for the Observation and Modelling of Earthquakes, Volcanoes and Tectonics (COMET+). COMET+ was part of the UK Natural Environment Research Council's National Centre for Earth Observation (NCEO) and funded my studentship, for which I am very grateful.

Many thanks to all the excellent people that I have had the good fortune to spend my last four years with. The advice, support and good humour from so many made my time at Leeds all the better.

My firmest supporters, my sisters Jo and Becca, and, in no particular order, my friends Sinead, Cindy, Claire and Jackie, with their often quite misguided, but much apprepciated belief that I am capable of achieving everything I set out to do. You are each and every one of you superstars in my book.

Just when they thought they could stop worrying about their children my mum and dad had to start all over again. Their very freely given and unwavering love and support made me feel that I could keep going against all the odds, it always has. I can never express how much I've always appreciated this.

To my Peggy and Taffy, for listening without judgement and always being there when I needed to procrastinate with a long and hearty walk.

Thank you to Sam, Joe and Tom. It wasn't always easy for you having a student

mum and you certainly learnt how to go without, but it didn't stop your unwavering support for me and your endless supply of hugs, without which I would've given up at the first post.

And finally to Dale, for encouraging me to go for the original interview with Tim and Douglas. For helping me through all the trials, tribulations and emotional rollercoasters that was the starting, working on and completing my PhD. For changing your life right alongside mine just to support me through it. I can never thank you enough.

Abstract

Current models of fault growth examine the relationship of fault length (L) to vertical displacement (D) where the faults exhibit the classic fault shape of gradually increasing vertical displacement from zero at the fault tips to a maximum displacement (D_{max}) at the middle of the fault. These models cannot adequately explain displacement-length observations at the Krafla fissure swarm, in Iceland's northern volcanic zone, where I observe that many of the faults with significant vertical displacements still retain fissure-like features, with no vertical displacement, along portions of their lengths. I have created a high resolution digital elevation model (DEM) of the Krafla region using airborne LiDAR and measured the displacement/length profiles of 775 faults, with lengths ranging from 10s to 1000s of metres. I have categorised the faults based on the proportion of the profile that was still fissure-like. Fully-developed faults (no fissure-like regions) were further grouped into those with profiles that had a flattened appearance (large regions of constant vertical displacment), those with a classical fault shape and those that show regions of fault linkage. I measured the D_{max}/L ratio of each identifiable original fault within the linked fault profiles, evidencing that the majority of the original faults had reached the maximum D/L prior to linkage. I suggest that a fault can most easily accommodate stress by displacing regions that are still fissure-like, and that a fault would be more likely to accommodate stress by linkage once it has reached the maximum displacement for its fault length. My results demonstrate that there is a pattern of growth from fissure to fault in the D_{max}/L ratio of the categorised faults and propose a model for this growth. I suggest it is possible to better understand how faults grow in their earliest stages of development and that the proposed model can be incorporated as an early stage of fault growth for current models which only model behaviour of a fault once it has acquired the classical D/L profile.

The range in the distribution of the published D_{max}/L data is mainly attributed to tectonic setting, rock type and resolution limiting the choice of sample rate and fault length range. Using the LiDAR data I have examined the effect that data resolution has on the interpretation of the D/L relationship. I have resampled the LiDAR point data to produce two additional DEMs of 10 m and 30 m resolution, from which I have measured 90 and 40 fault profiles respectively. I have compared (D_{max})/L for all of these fault profiles with those of the published data. I have shown that by varying resolution the interpretation of the (D_{max})/L relationship gives trends for each resolution that together account for the spread in results of the combined published data for the length of faults

measured. I have proposed that it may be possible to identify whether a measured fault is a single structure or if it is actually a segmented structure, when measured at a higher resolution, based on its location in the D_{max}/L published distribution.

The currently available surface displacement data in post-rifting Krafla and inter-rifting Askja are limited either to single point time series of displacement or regional displacement maps that are averaged over time and do not provide details of changes in rate through time. I have created a 24-epoch InSAR time series from ERS-1 and ERS-2 satellite SAR images over the 16-year period between 1992-2008. Using this I have extracted time series at 39 locations, both along- and across-axis at Krafla and Askja, and have identified trends in displacement rates over time. I have produced cumulative displacement profiles, based on the trends in displacement rate, both along- and across-axis and identifed key periods of displacement behaviour in the NVZ. I suggest that Krafla has three possible major sources of surface displacement: the shallow magma chamber under the Krafla caldera provides a decaying surface deflation between 1992 and 1999 and two possible deeper sources further north, the first between the Krafla and Fremrinamar fissure swarms creating uplift between 1992 and 1999 and the second beneath the Theistareykir volcanic centre between 2004 and 2008. In Askja I observe that the displacement rate in the caldera, previously thought to be a slowly decaying inflation, incurred a signifcant increase in rate to ∼30 mm/yr in 1996-2004 followed by a decrease in rate to ∼10 mm/yr.

Contents

List of Figures

List of Tables

Chapter 1

Introduction

The majority of oceanic tectonic rifting takes place in the submerged and difficult to monitor environment at the bottom of the ocean. The rifting behaviour would be better understood by observing regions in a subaerial environment. Active subaerial rift zones such as Krafla, Iceland and Afar, Ethiopia provide good examples of currently active regions that can not only be monitored and measured using land-based methods (e.g. GPS, tilt-meters, seismic) but due to the low levels of vegetation at both locations, can also provide ideal locations for remote sensing using InSAR. Iceland forms part of the Mid-Atlantic Ridge and the Krafla volcanic zone in the north east of Iceland was subject to one of the first major subaerial rifting episodes in which both surface deformation and sub-surface seismic data were recorded throughout. As the Krafla region has good SAR satellite coverage from 1992 onwards, this region of Iceland presents an ideal area for studies of present-day surface displacement behaviour using satellite based InSAR. A region in the north of Krafla covered by a heavily faulted 10,000 year-old lava flow presents an ideal region to study fault behaviour with the age of the surface constraining any deformation to within the age of the lava flow. This provides the opportunity to measure such things as total vertical deformation and horizontal opening that has occurred within a restricted time period and can be used to determine a geologic rate of extension and vertical deformation during the last 10,000 years.

1.1 Aims and objectives of thesis

The main goals of this thesis are:

1 To measure the length and displacement of faults in the Krafla fissure swarm and identify any patterns of fault growth

2 To examine the effect of data resolution on the analysis of fault growth

3 To examine the surface displacement in the post-rifting Krafla and inter-rifting Askja volcanic systems, and identify changes in rates of displacement and displacement behaviour.

4 To measure the horizontal surface opening across the fissure swarm to calculate rates of extension and compare these with the total extension needed for plate spreading in Iceland, and current rates of deformation.

I will acheive these aims by analysis of data captured via two main methods: LiDAR (Light Detection and Radar) elevation mapping which is used to create a high resolution digital elevation model (DEM) and remote sensing using InSAR (Interferometric Synthetic Aperture Radar) to map surface deformation over specific time periods. In addition, fieldwork in Krafla involved GPS surveying to assess the validity of the LiDAR model and which also provides the opportunity to better understand the topographical features of the rift area.

1.2 Layout of thesis

In Chapter 2, I give an introduction to Iceland, the Northern Volcanic Zone (NVZ) and the fissure swarm and caldera of the Krafla volcanic system. I also include an overview of the rifting cycle and discuss the three key phases, co-rifting, post-rifting and inter-rifting.

In Chapter 3, I discuss the acquisition and processing of the two LiDAR surveys I used in this thesis. I present the two key methods used to produce the DEMs used in this thesis and discuss the rationale for needing to produce different DEMs. I discuss coverage and appropriate resolution for processing of the LiDAR data, comparing results with previously available DEM resolutions. I present the GPS data acquired during fieldwork I performed in the Krafla fissure swarm to provide ground-truthing for the LiDAR survey. I compare the GPS data with the LiDAR DEMs at the same locations and examine any variance between the GPS and LiDAR data.

In Chapter 4, I give an overview of the current literature pertaining to fault growth, presenting some of the current fault growth models and providing a more detailed review of the literature available on faulting in the Krafla region. I discuss the methodology

I used for examining the faults in Krafla going over difficulties with identification and measurement of faults and complexities of the Krafla fissure swarm. I discuss the rationale in choosing the regions I used for high resolution fault analysis and present maps of the faults picked. Using the maximum displacement (D_{max}) and length, L, of the measured faults, I present the results of the fault analysis and identify and discuss categorisation of the Krafla faults based on the development of the structure between fissures with surface opening, but no vertical displacement, through to fully displaced faults. I present further categorisation of fully-formed faults. I discuss the spatial distribution of the categories within the published data and present a model of fissure to fault growth that acts a precursor to the fault growth models presented inthe introduction.

In Chapter 5, I give an overview and discuss the variability across the published (D_{max})/L data based on factors such as survey type and tectonic setting. I discuss the re-sampling of the LiDAR data to produce DEMs of differing resolution and present the faults picked at three different resolutions in order to examine the relationship between resolution and the fault length/displacement relationship. I also present three 'fault systems'- sets of faults that appear to be long, single faults at 30 m resolution but are actually a series of individual segmented faults at 0.5 m resolution.

In Chapter 6, I examine the present-day deformation over the northern volcanic zone, specifically over the post-rifting Krafla and inter-rifting Askja volcanic zones. I start the chapter with a review of the published deformation data over the two main current zones of deformation in the NVZ: post-event deformation in Krafla and inter-event deformation in Askja. I then discuss the methodology used for InSAR processing, detailing the steps used to produce a final time series from the original SAR images. I select a series of profiles across Krafla and Askja and extract the time series at select locations along each of the profiles. Using trends in displacement rate identified in the time series I produce cumulative plots across epochs to examine changes in displacement behaviour through time along entire profiles.

In Chapter 7, I look at using both the InSAR time series and the LiDAR to better understand some of the long-term and short-term displacement in the Krafla fissure swarm. I discuss the methodology used to extract real values of vertical displacement from the InSAR time series by removing the horizontal values of displacement calculated from published GPS data and correcting for the angle of the satellite. I use the vertical

displacement to examine a small region of deflation identified in the displacement rate maps in chapter 6, ∼10 km north of the Krafla caldera. Comparing the region of vertical displacement with the high resolution LiDAR DEM, I present possible causes for the subsidence. Using the LiDAR DEM I have taken a selection of profiles perpendicular to the main rift axis and have extracted the total throw across the Krafla fissure swarm. Using dip angles to convert total throw into horizontal opening and combining with the total opening measured across fissures along the same profile, I present a value of total opening across the fissure swarm and discuss the implications with regards to the expected opening needed to accommodate plate spreading in Iceland and the present-day distribution of strain.

In the final chapter I discuss the key findings within the thesis, provide my final conclusions and discuss future recommended work.

Chapter 2

Iceland, Krafla and the Rifting Cycle

2.1 Iceland

Iceland lies along the northern Mid Atlantic Ridge (MAR) which currently marks the diverging plate boundary that first opened around 60 million years ago between the North American and Eurasian plates (see figure 2.1).

Iceland itself marks a topographical anomaly along the current plate boundary attributed to a hotspot (e.g. Morgan, 1971, Tryggvason et al., 1983, Wolfe et al., 1997). This hotspot covers an area of around 1000 km in radius, showing a gradual decrease in ocean depth from its outer edges towards its centre above the ocean's surface at Iceland. This anomaly is thought to be associated with a large upwelling of hot material from lower in the mantle and has been characterised by a number of studies (e.g. Allen et al., 2002, Tryggvason et al., 1983, Wolfe et al., 1997, Maclennan et al., 2001). These studies resulted in a favoured model for the plume which shows a vertical plume conduit, with a radius of ∼100 km, extending up toward the surface from the maximum depth of resolution at 400 km to around 200 km depth where it spreads out beneath the lithosphere forming a horizontal plume head. It is generally considered to extend from a much greater depth than 400 km (e.g. Shen et al., 1996, 1998) but these depths are hard to resolve with current technology.

The pole of relative rotation between the two major plates is located in NE-Siberia at 62.4° N and 135.8° E, and according to the Nuvel-1A model of plate motions (DeMets et al., 1994),the relative rotation speed is 0.21° per million years. Holding the North America Plate fixed, this gives a plate velocity vector of 18.2 mm/year in a direction

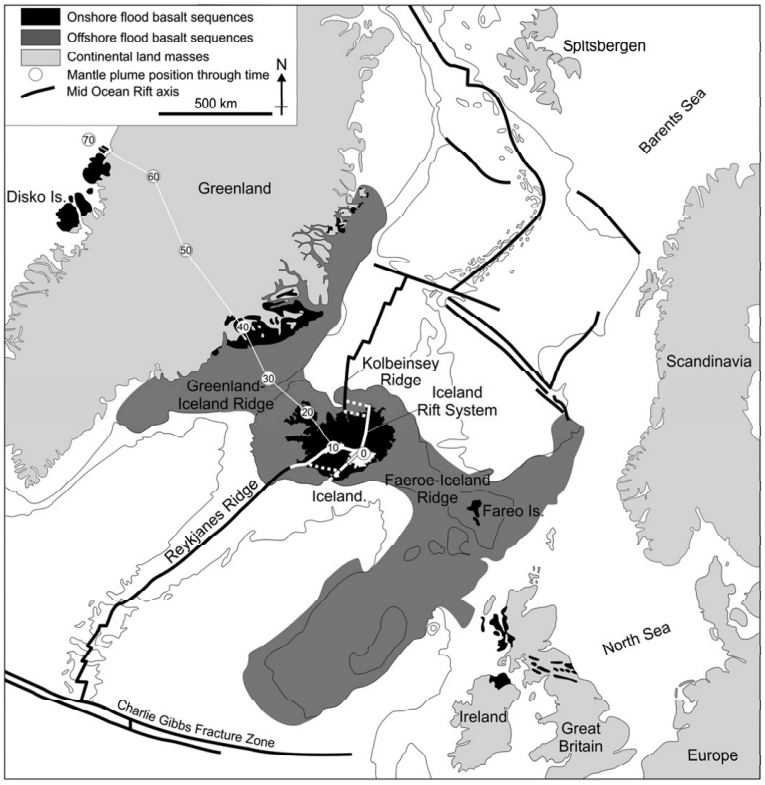

Figure 2.1: Iceland lies on the Mid Atlantic Ridge at the junction between the Rekjanes and Kolbeinsey ridge segments (from Thordarson and Larsen (2007) as a modification from Saunders et al. (1997)). Reprinted from Journal of Geodynamics, Vol. 43, Issue 1, Thordarson and Larsen (2007),Volcanism in Iceland in historical time: Volcano types, eruption styles and eruptive history, pages 118-152, ©2007, with permission from Elsevier

of 105° for Central Iceland, slightly faster and more easterly for South Iceland, slightly slower and more southerly for North Iceland. This velocity is valid for the last few millions of years, the time scale of the magnetic and structural data used to constrain the Nuvel-1A model (Einarsson, 2008).

The geologic setting of Iceland can be divided into four distinct parts (Opheim and Gudmundsson, 1989): the Holocene lava formation; the Upper Pleistocene rocks belonging to the Bruhnes magnetic epoch, age 0.01-0.7 Myr; the Lower Pleistocene rocks, age 0.7-3.1 Myr, and the Tertiary lava pile, age 3.1-16 Myr (see figure 2.2 for geological map of Iceland).

In addition, Iceland is divided into volcanic zones and seismic zones that cover around a quarter of the island's surface area, shown in figure 2.3. These zones are

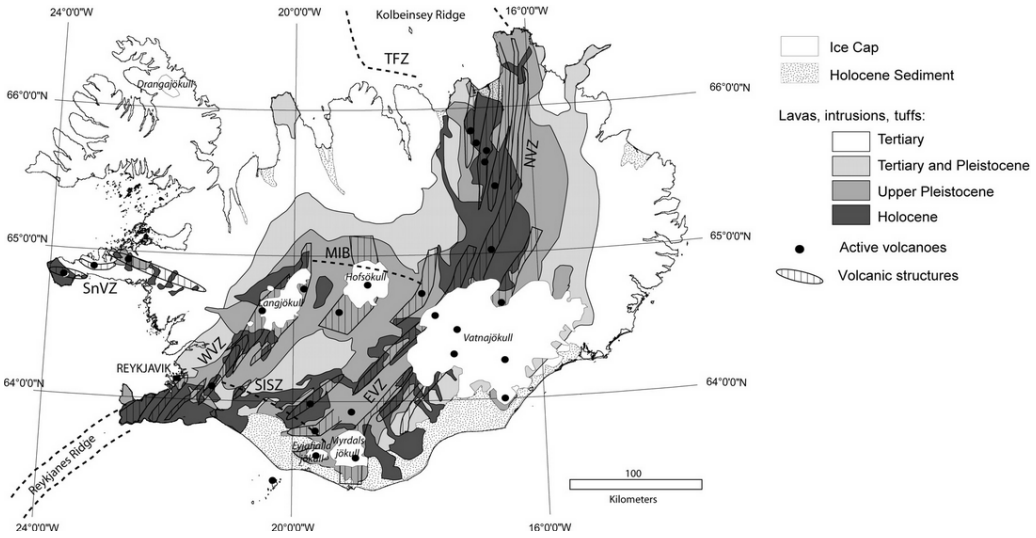

Figure 2.2: Geological map of Iceland from Le Breton et al. (2010) (based on map produced by Jóhannesson and Sæmundsson (1998)).

characterised by high levels of seismic activity and volcanic rocks that are dated younger than 0.7 Myr (Saemundsson, 1978).

There are two distinct types of neovolcanic zones in Iceland, defined by the amounts of crustal spreading in the region. The first type is the volcanic flank zone where little or no crustal spreading occurs. There are three of these zones in Iceland: the Snæfellsnes Volcanic Zone (SnVZ), the South Iceland Volcanic Flank Zone (SIFZ) and the Ọræfajọkull-Snæfell Flank Zone. The second type is the volcanic rift zone which is associated with extensive amounts of crustal spreading and forms the spreading plate boundary across Iceland. The four main volcanic rift zones in Iceland are as follows (and shown in figure 2.3):

- Reykjanes Peninsula Volcanic Zone, RP
- Western Volcanic Zone, WVZ
- Eastern Volcanic Zone, EVZ
- Northern Volcanic Zone, NVZ.

The RP and WVZ form two arms of a triple junction in the plate boundaries, with the pivot of the junction in the Hengill volcanic area just NE of Reykjavik and the

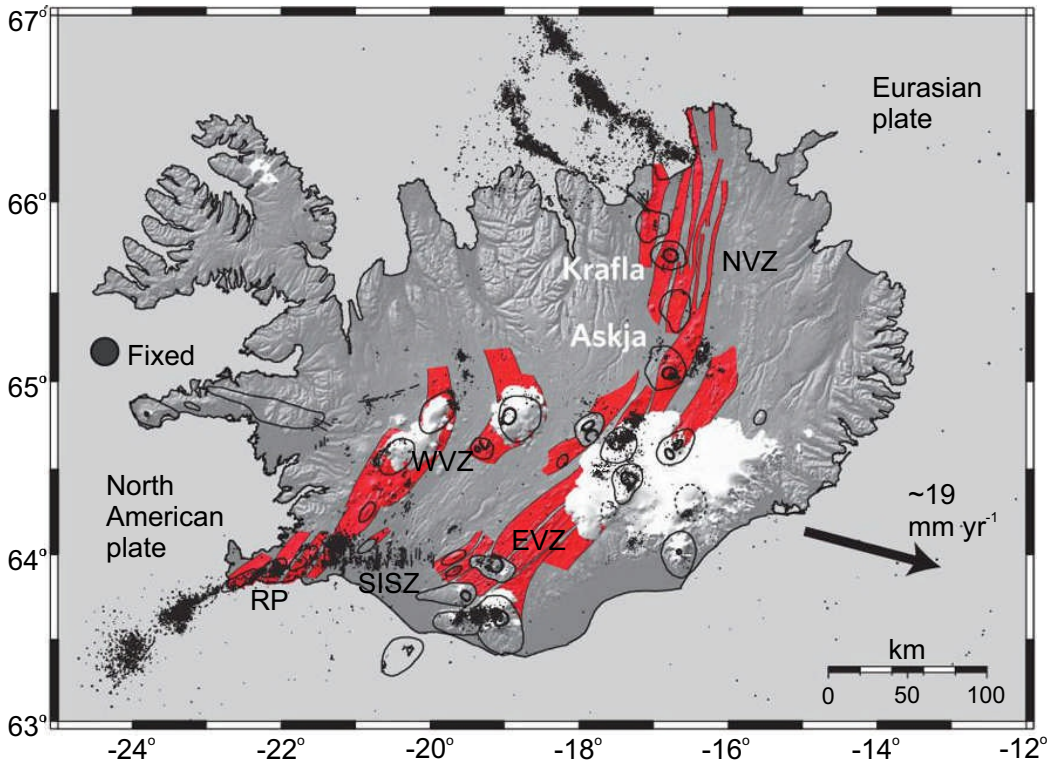

Figure 2.3: Tectonic map of Iceland modified from Wright et al. (2012). Fissure swarms are shown in red, earthquakes (black dots) are from 1995-2010 as listed by the Icelandic Meteorological Office. Calderas and volcanic centres are marked with black ringed regions (thick and thin lines respectively. NVZ - Northern Volcanic Zone, EVZ - Eastern Volcanic Zone, WVZ - Western Volcanic Zone and SISZ - South Iceland Seismic Zone. Reprinted by permission from Macmillan Publishers Ltd: Nature Geoscience, Wright et al. (2012), ©2012

third arm across the South Iceland Seismic Zone (SISZ). The activity in this region has been fairly continuous for the last 6-7 million years (Saemundsson, 1979), with dramatic variability in behaviour between the three zones due to the differences in the plate motion and proximity to the plume. To the east of Iceland there are two distinct volcanic zones, EVZ and NVZ, separated by the Vatnajökull Icecap with the EVZ to its south and the NVZ to its north (Einarsson, 1991a). The zones vary in both age and character with the NVZ being active for 6-7 Myr whereas the EVZ for only around 2-3 Myr.

The two main seismic zones in Iceland are the aforementioned SISZ which extends out eastwards from the Hengill triple junction to the EVZ and the Tjörnes Fracture Zone (TFZ in figure 2.2) in the north. Both these zones are of complex nature and are areas of crustal shear transforming plate motion from one rift zone to another - the SISZ encounters shear between the RP and EVZ and the TFZ between the NVZ and

the submarine Kolbeinsey Ridge.

2.2 Northern Volcanic Zone

The Northern Volcanic Zone (NVZ) lies on an area of constructive plate boundary extending from the glacier Vatnajökull in central Iceland all the way up to the north coast where it meets the Tjörnes Fracture Zone (see figure 2.4).

The NVZ consists of 5 main volcanic systems whose fissure swarms make a left-stepping, en echelon pattern striking north-northeast following the orientation of the plate boundary (Einarsson, 2008). The fissure swarms vary in size across the five volcanic systems with widths ranging from 5 to 20 km and lengths from 60 to 100 km (Pálmason, 1973, Saemundsson, 1979). The five main volcanic systems are:

- Kverkfjöll
- Askja
- Fremrinámar
- Krafla
- Theistareykir

The behaviour and characteristics of these five zones differ widely from each other (Einarsson, 2008). For example Askja has a very long fissure swarm but due to the high amount of activity in the central volcano, fissuring is almost completely absent in the central caldera region (Hjartardóttir, 2008). Meanwhile the central region of Fremrinámar is covered by two large lava shields with no visible caldera, the Krafla caldera is cut by an extensive fissure swarm and the Theistareykir zone has a well developed fissure swarm and a large volcanic centre but no central caldera.

The activity in the NVZ appears to be episodic (Einarsson, 2008) with a single rifting episode of related magmatic and tectonic events that can last as long as a decade followed by long dormant periods that can last hundreds and sometimes thousands of years before the onset of the next rifting episode. In historical times the only recorded activity in the NVZ has been in the Askja and Krafla volcanic zones, with a possible indication of non-eruptive rifting activity in the Theistareykir zone.

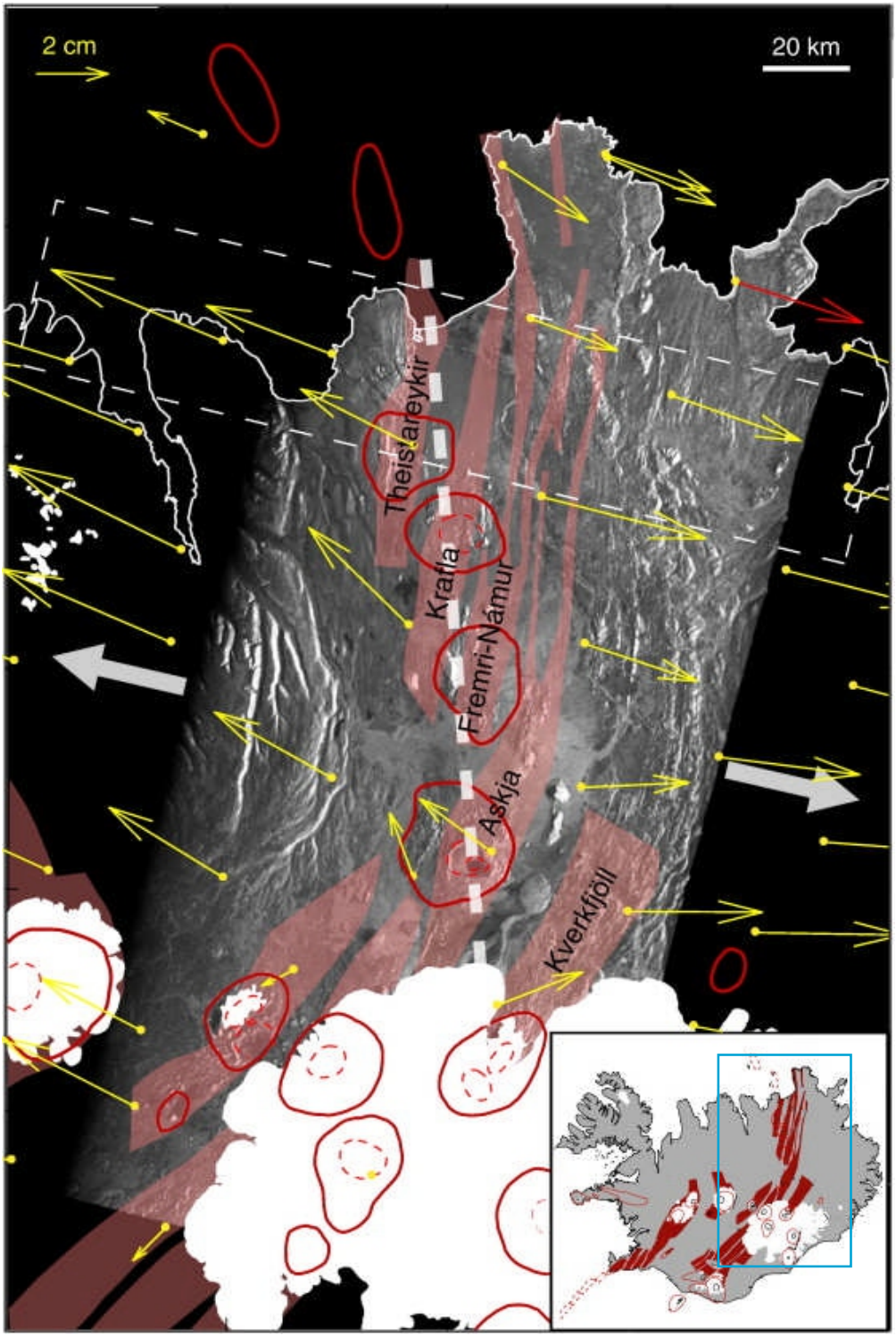

Figure 2.4: Map of the Northern Volcanic Zone (NVZ) from (Pedersen et al., 2009) with GPS vectors (shown in yellow) form Árnadóttir et al. (2009) showing 5 years of plate spreading deformation. Volcanic centres and calderas are shown by red ellipses (solid and dotted lines respectively), fissure swarms are red shaded areas and the white areas are glaciers. The thick white dotted line represents the regional trend of the spreading ridge. Region shown in main figure is denoted by the blue box in the inset map. Reprinted from Earth and Planetary Science Letters, vol. 281, Pedersen et al. (2009), Rheologic controls on inter-rifting deformation of the Northern Volcanic Zone, Iceland, pages 14-26, ©2009 with permission from Elsevier.

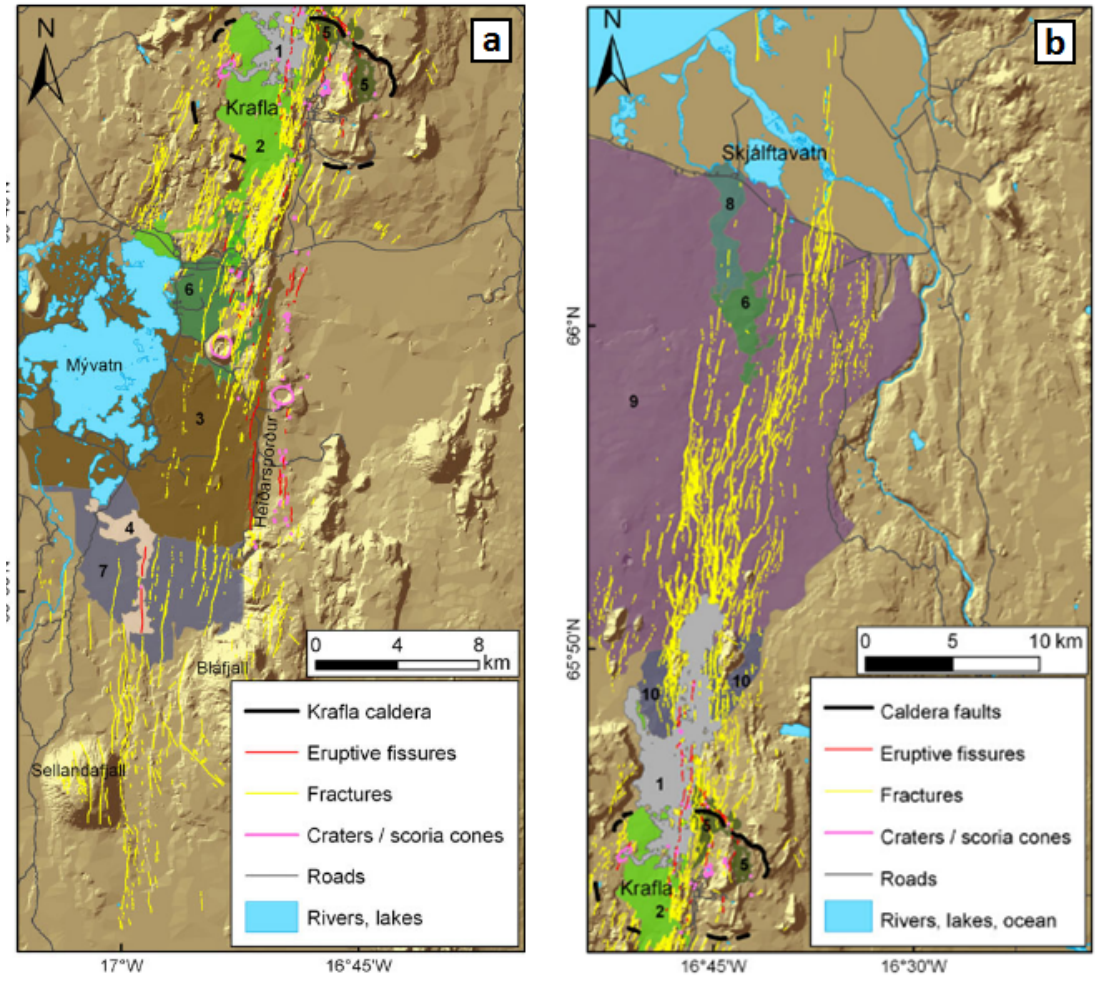

Figure 2.5: Map of the fractures and lava flows in the Krafla fissure swarm taken from Hjartardóttir et al. (2012).The numbers denote lava flow fields as shown in table 2.1. Reprinted from Bulletin of Volcanology, vol. 74, Hjartardóttir et al. (2012), The Krafla fissure swarm, Iceland, and its formation by rifting events, pages 2139-2153, ©2012, with kind permission from Springer Science and Business Media

2.3 Krafla Volcanic System

The Krafla fissure swarm consists of the Krafla Central Volcano (KCV) and the fissure swarm that transects it. The Krafla fissure swarm is a 100 km long swarm that follows a SSW to NNE path across the central caldera, with a width between 5-10 km. The KCV is a shield volcano that has built up over repeated eruptions with the oldest measureable formations dated at around 200,000 years old (Saemundsson, 1991) and a caldera dated as forming during the interglacial period ∼100,000 years ago. A shallow magma chamber lies beneath the caldera at a depth of ∼3 km (Einarsson and Brandsdottir, 1978, Tryggvason, 1980, Brandsdóttir et al., 1997). The zone extends from the south of Lake Mývatn between the mountains Sellandafjall and Bláfjall all the way up to the north coast at Öxarfjördur. Around 35 Holocene eruptions have occurred in the Krafla fissure swarm, with the majority of these occurring either in the central caldera region or to the west/southwest at the mountain Namafjall (Björnsson and Saemundsson, 1977).

There have been 10 major lava flows in the Krafla Volcanic System in the last 10,000 years (Thorarinsson, 1979, Saemundsson, 1991, Höskuldsson et al., 2010). These are detailed in table 2.1 and are shown in figure 2.5.

Table 2.1: Lava flows in the Krafla Volcanic System (table from Hjartardóttir et al. (2012) based on results from Thorarinsson (1979), Saemundsson (1991), Höskuldsson et al. (2010)).

Lava flow(s)	Number	Age (years BP)
Krafla rifting episode	1	∼30
Mývatn rifting episode	2	∼280
Younger Laxa lava flow	3	∼2,200
Graenavatnsbruni lava flow	4	∼2,200
Holseldar lava flow	5	∼2,350
Hverfjallseldar lava flow	6	∼2,800
Older Laxa lava flow	7	∼3,800
Hraungardar lava flow	8	∼8,000-10,000
Storaviti lava flow	9	∼10,000
Gjastykkisbunga lava flow	10	∼10,000

The northern area of the Krafla fissure swarm is dominated by a large lava flow (the Storaviti lava flow, shown as lava flow 9 in figure 2.5b), formed during the eruption of the Theistareykir volcano around 10,000 years ago. As can be seen in figure 2.5b, this region is riddled with large fissures and faults (marked in yellow on the map) and is a key area used in this thesis. In the far north of the fissure swarm, close to the coast, is

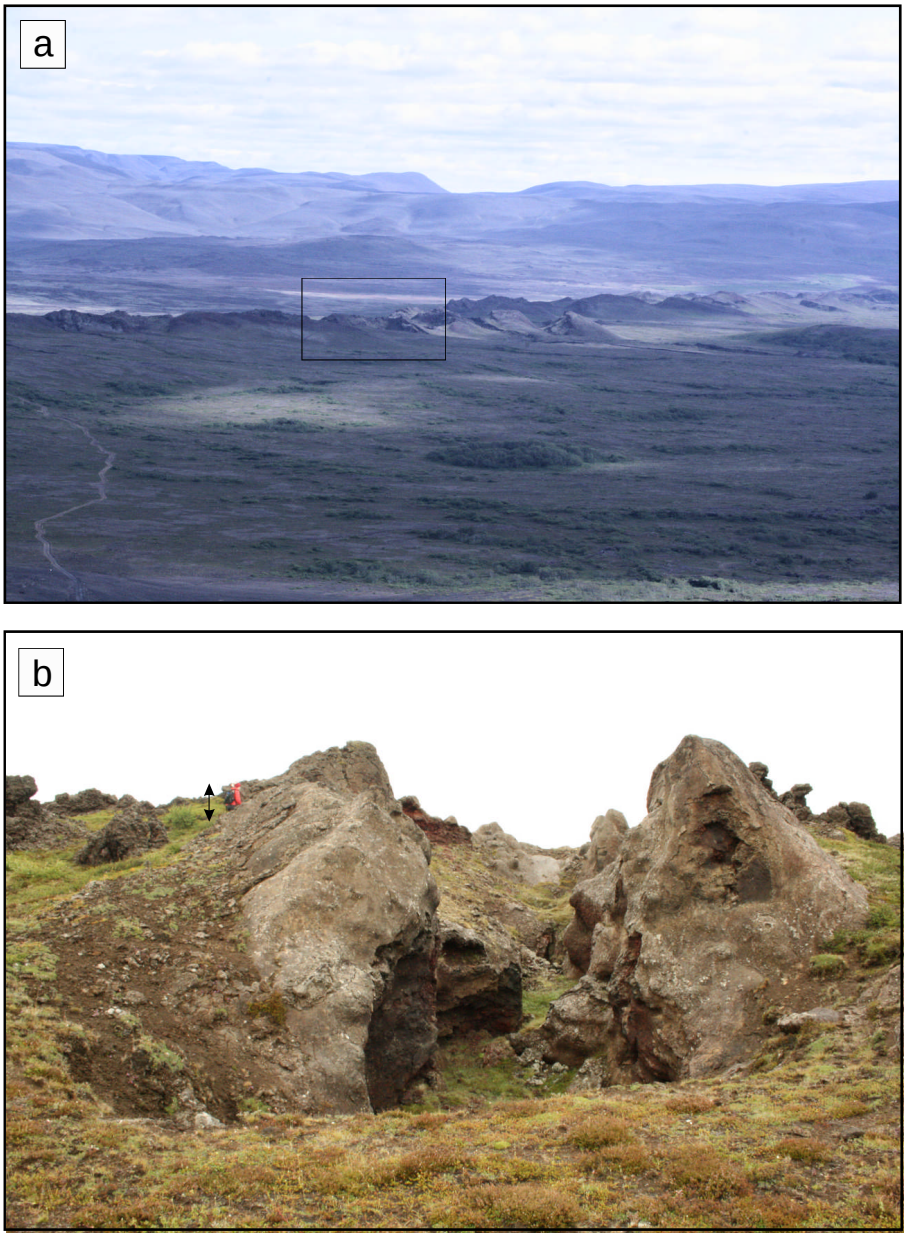

Figure 2.6: Image a) shows the fissure row of Ludentarborgir and Threnslabogir in the south of the Krafla fissure swarm. b) Shows a view along one of the fissures in the fissure row (in the region in the black boxed area in a). The black arrow gives human size for perspective.

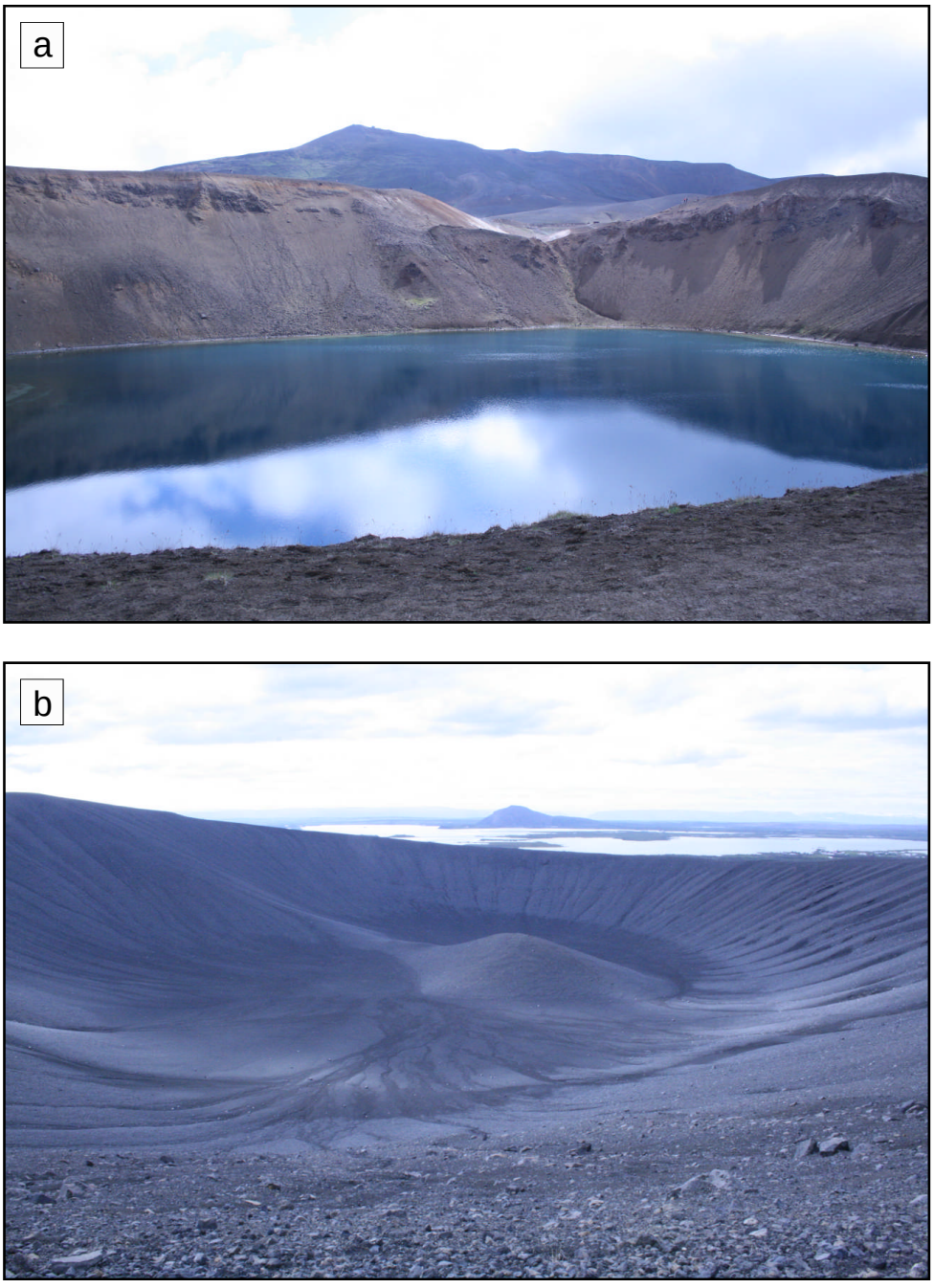

Figure 2.7: Image a) shows the Viti crater formed inside the main caldera during the Mývatn Fires. b) Shows of the inside of the 1 km diameter Hverfjall phreatomagmatic tuff ring, with Lake Mỳvatn in the background.

an area of basaltic fissure eruption dated around 1500-2000 years ago.

South of the central caldera there was a major fissure eruption around 2,200 years ago (the Yonger Laxa lava flow (3) in table 2.1 and figure 2.5) resulting in the 15-km-long fissure row of Ludentarborgir and Threnslaborgir (see figure 2.6 and shown by red lines on the eastern side of lava flow 3 in figure 2.5a). This eruption was responsible for the lava shield that flows across to the west from the fissure rows, across Mývatn Lake with the resulting pseudocraters (or rootless cones) that feature across the lake and then continuing down the Laxadalur river valley all the way to the coast.

Dominating the landscape in the southern fissure swarm is the Hverfjall tuff ring (see figure 2.7b and shown as pink ring at the southern end of lava flow 6 in figure 2.5a), the result of a phreatomagmatic eruption ~2,800 years ago. The crater lies at the southern end of a 20 km long fissure that extends northwards through the main caldera. Originally Lake Mývatn extended to cover the southern extent of the fissure and when the fissure erupted the magma mixed with the water to form an effusive eruption that created the 150 m high, 1 km diameter tuff ring and miles of tephra fallout (e.g. Thorarinsson, 1952, Saemundsson, 1991). A second phase of eruption created the Hverfjallseldar lava flow (shown as lava flow 6 in figure 2.5).

There are two historically-documented episodes of rifting in the Krafla fissure swarm: the Mývatn Fires from 1724-1729 and the Krafla Fires from 1975-1984. Together, the two episodes activated the majority of the Krafla fissure swarm. The Mývatn Fires episode mainly activated the fissure swarm from the central caldera going south (the extent of the lava extrusion is shown as lava flow 2 in figure 2.5) whilst the Krafla Fires episode mainly activated the fissure swarm from the central caldera going north (lava flow 1 in figure 2.5). Both the Mývatn Fires and Krafla Fires rifting episodes initiated in the centre of the Krafla caldera at a location known as Leirhnjukur (see figure 2.8).

2.3.1 Mývatn Fires

The 1724 eruption at Viti (see figure 2.7a and figure 2.5a, denoted by the water-filled (blue) pink ring located in the main caldera between lava flows 2 and 5) marked the start of the Mývatn Fires rifting episode (Saemundsson, 1991). From written descriptions of events found in historical records the Mývatn Fires were thought to start with a series of rifting events followed by four lava eruptions that lasted from weeks to a final eruption that lasted for several months, coming to an end in 1729. The majority of the lava flows

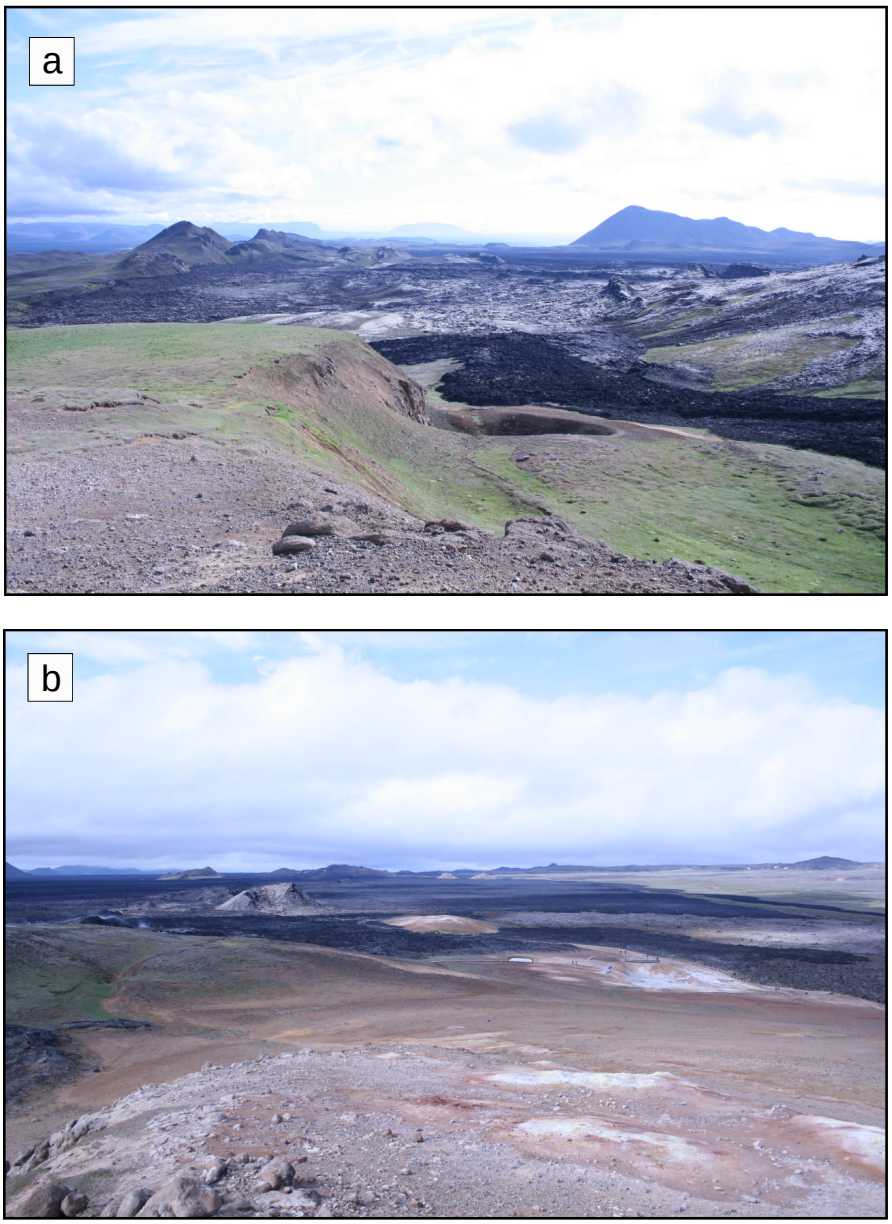

Figure 2.8: Images of the Mývatn and Krafla Fires lava flows taken from the top of Leirhnjukur in the central caldera. a) Looking south towards Lake Mývatn, the black lava flows from the Krafla Fires can be seen flowing over the light grey lava flows of the Mývatn Fires (the whitish colour is from vegetation).This was one of the only lava flows to travel south during the Krafla Fires. b) Shows the view to the north, again the dark Krafla Fires cover the lighter, older Mývatn Fires lava flows.

went south and have been mapped by Saemundsson (1991), shown in figure 2.9.

2.3.2 Krafla Fires

The Krafla Fires rifting episode lasted from 1975-1984 and was one of the first major opportunities to accurately study the behaviour of a sub-aerial volcanic system during a rifting event (e.g. Björnsson and Saemundsson, 1977, Einarsson and Brandsdottir, 1978, Björnsson et al., 1979, Brandsdottir and Einarsson, 1979, Tryggvason, 1980, 1984, 1986, Einarsson, 1991a, Buck et al., 2006, Hollingsworth et al., 2012). The rifting episode consisted of a sequence of dyke-induced fissuring and lava extrusion events (see figure 2.10a) each affecting only one region of the fissure swarm.

The initial event was the largest, starting with a small eruption at the centre of inflation within the caldera, followed by a rapid deflation and rifting in the fissure swarm both to the south (∼10 km) and to the north (∼60 km). Seismic data obtained during later events (1977 onwards, see figure 2.11) identified lateral dyke intrusions associated with both deflation of the magma chamber and with subsequent rifting at the surface. The dyke intrusions propagated into the fissure swarm at an average rate of 1 to 2 m/s from the central magma chamber (Brandsdottir and Einarsson, 1979) with seismicity showing activity as deep as 10 km below the surface.. The initial dyke intrusion produced a large amount of slip and only a small amount of magma extrusion. In the 9 years following on from the initial large event many smaller events were measured that resulted in surface rupture (through fissuring and surface opening, slip on surface faults and lava extrusion). All the observed events were associated with a re-inflation of the central magma chamber just prior to and a deflation during the time of the event (see figure 2.10c).

The early surface ruptures, up to ∼1980, were mostly surface opening and slip events with very little lava extrusion producing as much as 2 m of slip on normal faults in the fissure swarm (Björnsson and Saemundsson, 1977, Tryggvason, 1984). Post-1980 most events involved fissure eruptions confined to a 9 km section extending to the north from the centre of the caldera, culminating in the final event in 1984 (see figure 2.13). The extent of lava flow through the Krafla Fires and locations of eruptive fissures are shown in figure 2.12. Tryggvason (1984) estimated an average surface opening along the fissure swarm of ∼5 m with a maximum of 8 m of surface opening during the Krafla Fires (this values does not include opening in the final 1985 event, estimated to be an additional

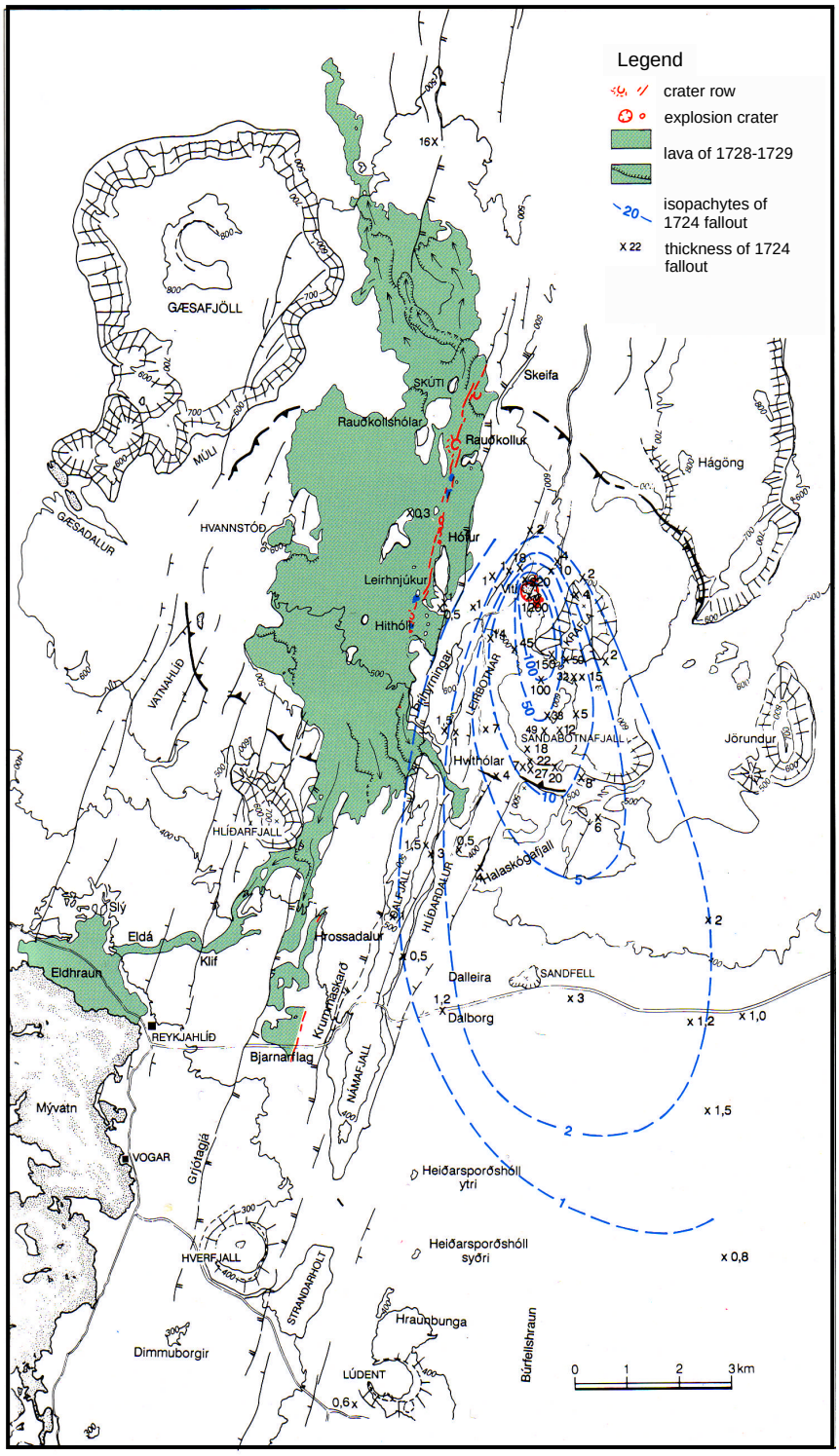

Figure 2.9: Map of the Mývatn Fires rifting episode, 1724-1729 as produced by Saemundsson (1991).

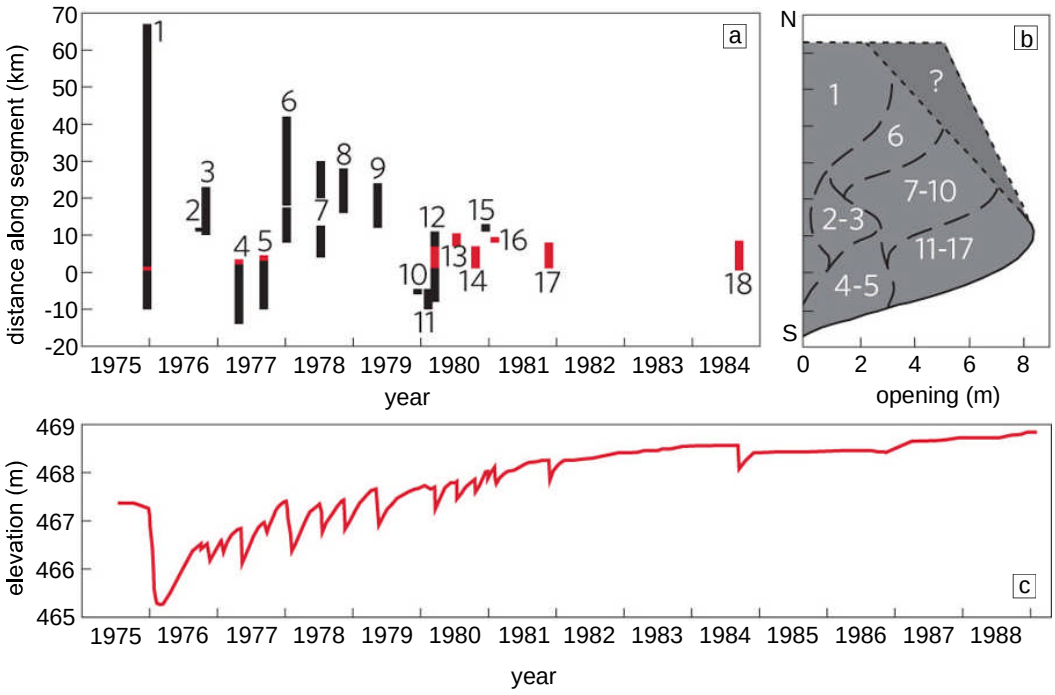

Figure 2.10: a) Shows the distance of surface fissuring (black) and lava extrusion (red) from the central point of inflation in the caldera (above the shallow magma chamber) through time. b) The estimated opening of the fissure swarm against distance from the central inflation and c) plots the surface elevation in the caldera, a measure of the inflation and deflation of the central magma chamber. Image from Wright et al. (2012) reproduced from Einarsson (1991a), Tryggvason (1984). Reprinted by permission from Macmillan Publishers Ltd: Nature Geoscience, Wright et al. (2012), ©2012

1 m of opening). A plot of the estimated surface opening with distance along the fissure swarm during the Krafla Fires is shown in figure 2.10b. The total volume of lava erupted during the rifting episode was ∼250 million m^3 (Tryggvason, 1994). The final eruptive event in 1984 resulted in an estimated ∼100 million m^3 of lava being extruded at the surface, covering an area of ∼24 km^2 with an average thickness estimated to be ∼5 m (Tryggvason, 1994).

Overall, there is a pattern in the rifting events during Krafla Fires, initiating with a very large rifting event and followed by a series of much smaller events that jump back and forth in location along the fissure swarm and ending with series of lava eruptions all focused in one region of the fissure swarm. A similar pattern of rifting events was observed in the 2005-2010 rifting episode in Afar, Ethiopia (Hamling et al., 2009). Commencing with the largest rifting event of the episode, a ∼60 km-long dyke intrusion,

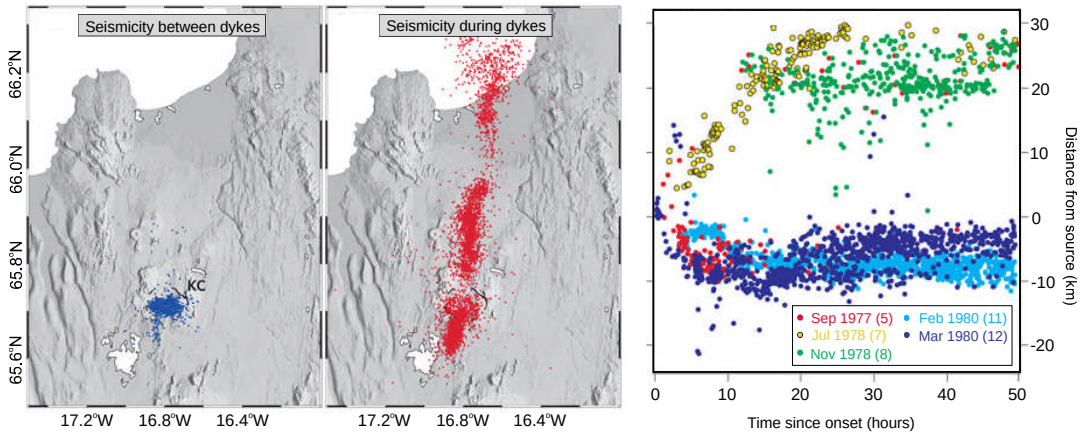

Figure 2.11: Seismicity recorded between 1977-1980 during the Krafla Fires rifting episodes. Image from Wright et al. (2012) reproduced from Brandsdottir and Einarsson (1979), Einarsson and Brandsdottir (1978). Reprinted by permission from Macmillan Publishers Ltd: Nature Geoscience, Wright et al. (2012), ©2012

followed by a series of events that jump back and forth in location along the fissure swarm. Hamling et al. (2010) proposes that the dyke intrusion events in Afar were linked by a transfer of stress, identifying the regions of increased tensile strength due to changes in the stress field caused by each new dyke opening. Hamling et al. (2010) identified these regions of increased tensile stress with the location of the next dyke intrusion.

2.4 The rifting cycle

The rifting cycle is composed of three main phases:

- inter-rifting
- co-rifting
- post-rifting

In order to accommodate stress along the entire plate boundary, different parts of a plate boundary can be at different phases of the rifting cycle at any point in time. For example, in the NVZ Krafla is currently in the post-rifting phase of the cycle following

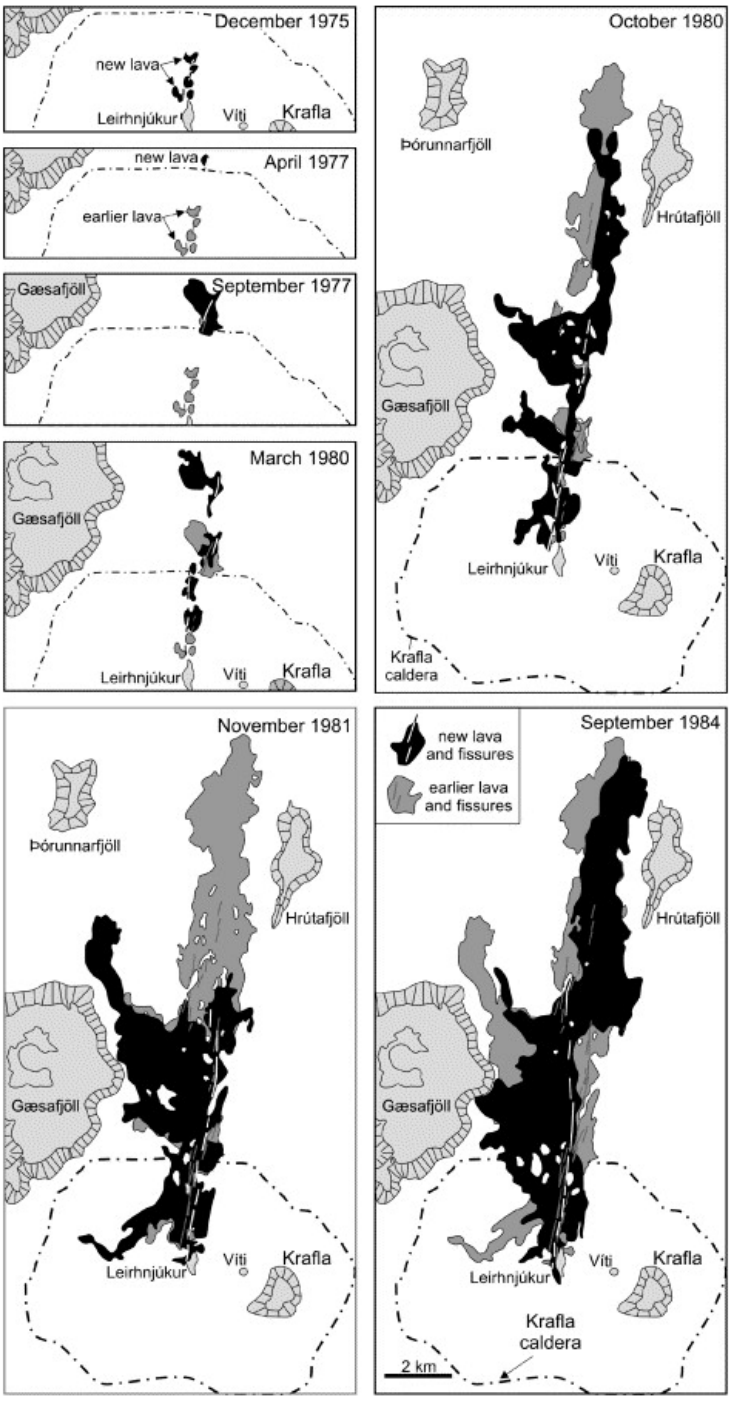

Figure 2.12: Sequential maps of the vent and lava flows during the Krafla Fires, figure from Thordarson and Larsen (2007) (modified from Saemundsson (1991).Reprinted from Journal of Geodynamics, Vol. 43, Issue 1, Thordarson and Larsen (2007),Volcanism in Iceland in historical time: Volcano types, eruption styles and eruptive history, pages 118-152, ©2007, with permission from Elsevier

Figure 2.13: Images of the 1984 Krafla Fires lava flow, taken at the northernmost tip of the lava flow looking back towards the caldera.

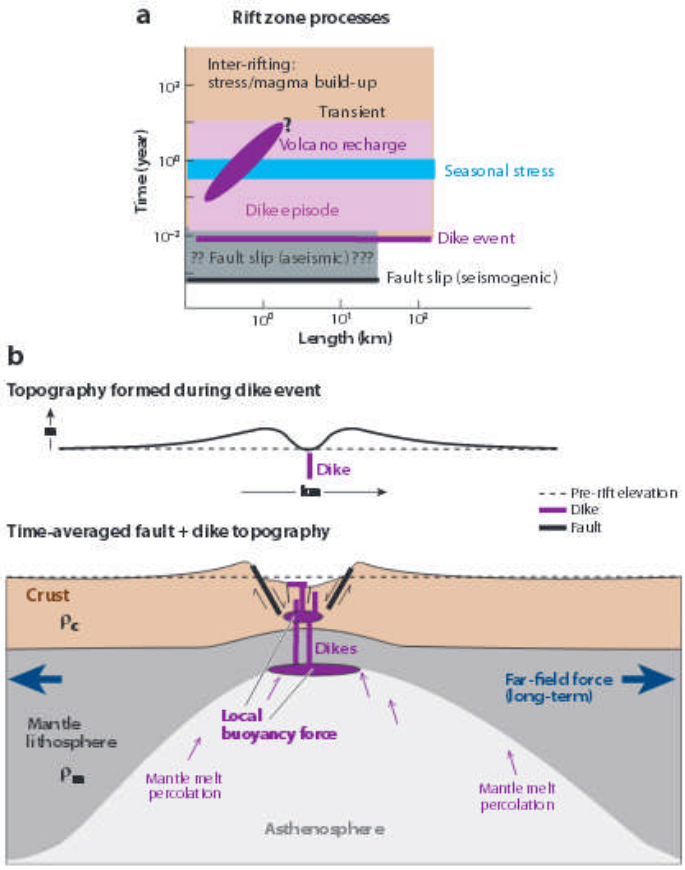

Figure 2.14: Schematic from Ebinger et al. (2010) showing a) the length and timescales involved in extensional strain processes and b) the magmatic and faulting processes in plate boundary deformation. The schematic is based on studies of the Afar rifting episode (Wright et al., 2006, Pagli et al., 2009).

on from the co-rifting phase 30 years ago, whereas Askja is currently considered to be in the inter-rifting phase of the cycle (e.g. Pedersen et al., 2009).

Ebinger et al. (2010) outlines how plate boundary deformation and spreading is achieved through rifting in figure 2.14. The far-field extensional forces causing crustal thinning contrast to the vertical buoyancy force of the upwelling magma and increased pressurisation in magma chambers resulting in an increased tensile stress and eventual failure through dyking and faulting.

2.4.1 Inter-rifting

The inter-rifting phase of the cycle is characterised by the background rate of displacement caused by stretching due to plate spreading. Any fluctuations in displacement that might further characterise behaviour during the Inter-rifting phase are difficult to

constrain as displacements are usually very small compared to those during the co- and post-rifting phases.

The displacement behaviour of the inter-rifting plate can be modelled assuming that the stretched upper crust is behaving as an incompressible elastic plate Sigmundsson (2006a). In this situation the plate stretching will be balanced by a thinning of the plate with strain accumulation, and consequent build-up of tectonic stress, at the plate boundary. Failure at the plate boundary occurs once strain accumulation has reached a critical limit and tectonic stresses exceeds the tensile strength of the surrounding crust, at this point rifting occurs and the plate boundary moves into the co-rifting phase of the cycle.

2.4.2 Co-rifting

Co-rifting is the active rifting phase of the rifting cycle, relieving stresses that have built up during the inter-rifting phase. Due to the extent of deformation during co-rifting it is the most readily measurable phase of the cycle. Deformation in the co-rifting phase is through dyking causing opening at the surface as fissures or slip on pre-existing fault surfaces. A multiple dyking event may cause up to several metres of cumulative opening over many kilometres of a fissure swarm (e.g. Sigmundsson, 2006a).

Rifting episodes both in Krafla and more recently in the Asal-Ghoubbet rift, Djibouti in 1978 (e.g. Doubre et al., 2007) and Afar, Ethiopia from 2005-2010 (e.g. Wright et al., 2006, Grandin et al., 2009) have provided opportunities to monitor sub-surface behaviour by monitoring seismic events (as in figure 2.11) and measuring geochemical signatures of erupted basalts. These have been combined with measurements of surface rupture and deformation to build models of sub-surface behaviour before, during and after rifting events.

Two key models of sub-surface volcanic system that drive tectonic rifting have been proposed based on studies in Iceland (e.g. Brandsdottir and Einarsson, 1979, Björnsson, 1985, Einarsson, 1991a, Gudmundsson, 1995, 2000). These can be seen as a schematic in figure 2.15b. The first model involves magma replenishment from a deep magma source to a shallow crustal magma chamber. As the shallow magma chamber fills and inflates, the pressure in the chamber increases. Once the pressure exceeds the tensile strength of the surrounding crust, magma is injected as lateral dykes into the fissure swarm. The second model involves the replenishment of deep magma chambers at the

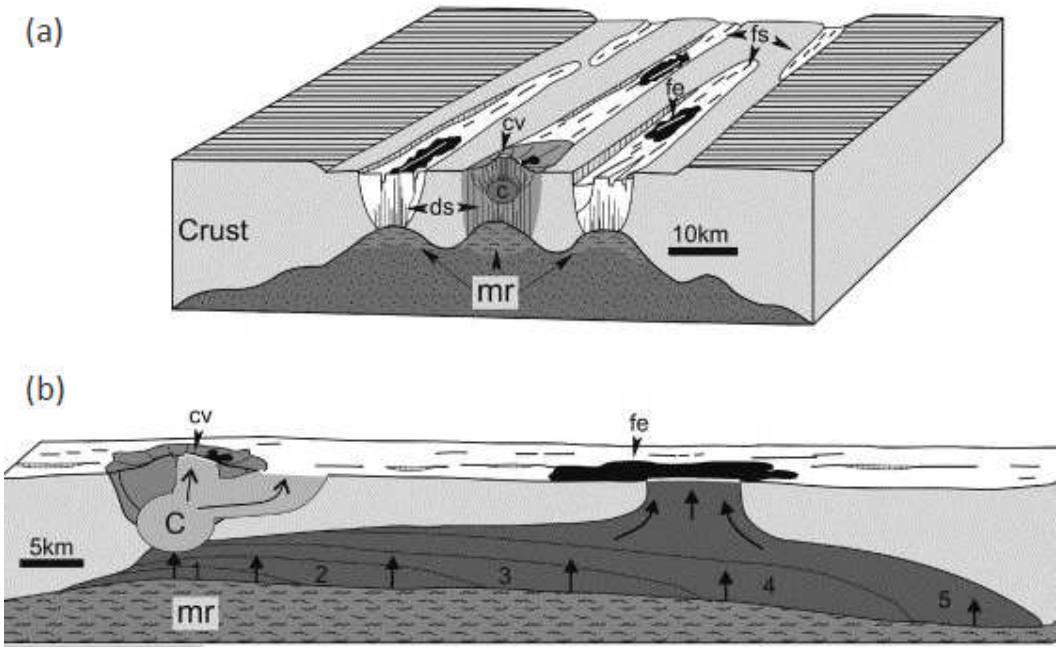

Figure 2.15: Schematic of the key structures in a volcanic system as presented by Thordarson and Larsen (2007). a) Shows the main structural elements of a volcanic system with the magma reservoir (mr), crustal magma chamber (c), dyke swarm (ds), central volcano (cv), fissure swarm (fs) and fissure eruption (fe). b) Shows two possible modes of dyke injection as predicted by the models in Thordarson and Larsen (2007), with the numbers 1-5 giving the sequence of growth of the vertical dyke. Reprinted from Journal of Geodynamics, Vol. 43, Issue 1, Thordarson and Larsen (2007),Volcanism in Iceland in historical time: Volcano types, eruption styles and eruptive history, pages 118-152, ©2007, with permission from Elsevier.

base of the crust injecting vertical dykes in to the upper crust once pressurisation of the deep chamber exceeds the tensile strength of the surrounding crust. It is possible that rifting actually involves a combination of the two. Rifting in Krafla showed the most similarity with the first model. However, the magma extruded inside the caldera differed chemically from the magma extruded outside the caldera, the composition of which suggested a deeper source than that supplying magma inside the caldera (e.g. Tryggvason, 1986, Árnadóttir et al., 1998). Behaviour in the Asel-Ghoubbet rift and the Afar rift provide similar models of behaviour, with Asel-Ghoubbet following behaviour from the first model with dykes fed from a shallow magma chamber near the centre of the rift (as with Krafla). The Afar rift presented a possible mix between the two models. Studies by Wright et al. (2006) and Grandin et al. (2009) indicate a deep

source and geochemical signatures that indicate a possible combination of shallow and deep sources (Ferguson et al., 2010). A schematic from Sigmundsson (2006b) shows a simplified cross-section of the rifting in Afar in 2005.

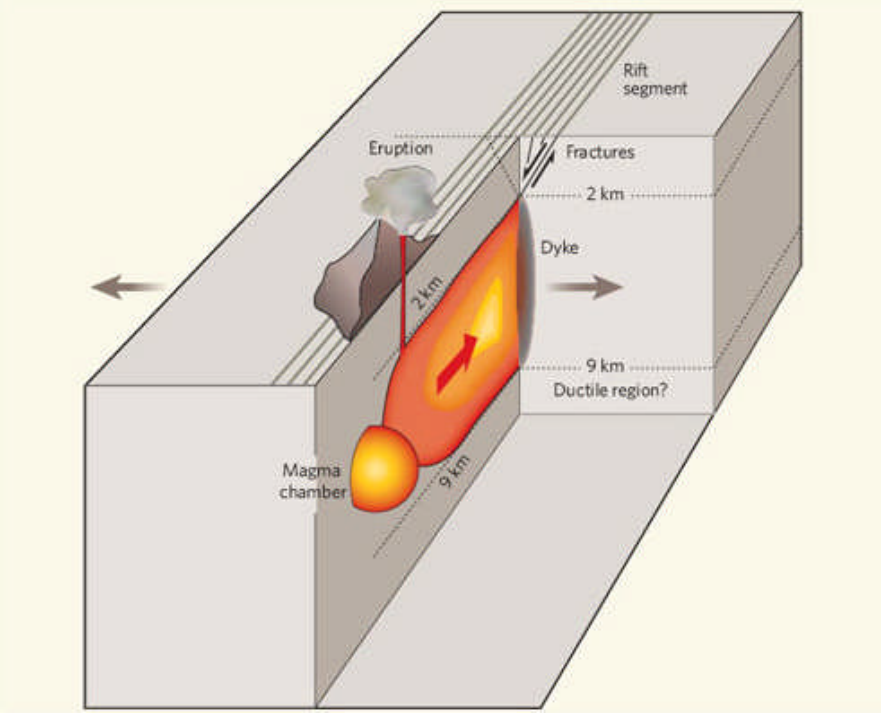

Figure 2.16: Schematic by Sigmundsson (2006b) of the magmatic processes involved in the 2005 rifting event in Afar, Ethiopia. Slip of up to 7 metres (Wright et al., 2006) on the fractures was mostly limited to the uppermost 2 km. Below this a dyke formed that caused lateral displacement to the plates of ∼2-4 m in either direction. The dyke is shown to be supplied laterally by magma chambers below the Gabho and Dabbahu volcanoes.Figure reprinted by permission from Macmillan Publishers Ltd:Nature,Sigmundsson (2006b),©2006.

2.4.3 Post-rifting

Post-rifting deformation occurs in the period immediately following the rifting episode, with a decay in the rate of surface displacement over time, from days and months to tens of years later. During the post-rifting period the surface displaces at a faster rate than observed during the inter-rifting plate spreading rate.

Modelling of the interaction between a ductile lower crust and an elastic brittle upper crust showed that the observed post-rifting displacement following on from the Krafla Fires was a response to transient stress relaxation built up in the ductile layer during rifting (Sigmundsson, 2006a). Cooling and/or deflation of shallow magma chambers and

in some cases, re-inflation due to feeding of magma from deeper chambers to a shallow magma chamber, are all additional sources of displacement during the post-rifting phase.

There are currently two volcanic systems in the NVZ undergoing measurable displacement as a result of the rifting cycle: Krafla is currently in the post-rifting phase following on from the Krafla Fires rifting episode and Askja is in the inter-rifting phase with its most recent major rifting episode having occurred between 1874-1875 (Sigurdsson and Sparks, 1978). Chapter 6 will focus on the measurement of the displacements occuring across the surface of both Krafla and Askja volcanic systems, examining any changes in displacement rate through time.

Chapter 3

LiDAR Survey of the Krafla Fissure Swarm

In this chapter I will use a series of airborne Light Detection and Ranging (LiDAR) surveys made over the Krafla fissure swarm by ARSF (NERC's Airborne Research and Survey Facility) to produce a high resolution digital elevation model (DEM) with a resolution of ∼0.5 m. I will use the DEM in later chapters to make accurate measurements of the faulting and deformation in the fissure swarm. In order to ground-truth the LiDAR survey I have completed a number of GPS surveys in the Krafla caldera and fissure swarm, measuring regions covered by the LiDAR survey. I will make a comparison of the acquired values of elevation between LiDAR and GPS and look to understand any horizontal and vertical variance.

3.1 LiDAR - How it works

Airborne LiDAR is a method of measuring distances by sending out laser pulses from an aircraft that in turn reflect off the Earth's surface. The return pulses are then picked up by the equipment's sensor, see fig 3.1. The time it takes for the light pulses to return is evaluated to give an accurate measurement of the distance between ground and aircraft, using the below equation:

$$D = \frac{rt}{2} \tag{3.1}$$

where D is the distance from the sensor to the target, r is the speed of the light pulse and t is the time it takes for the pulse to complete its journey. LiDAR sends out thousands of laser pulses: 33,000 pulses per second in the case of the equipment used in this survey.

The pulses are directed by an oscillating mirror which allows for a very dense set of data points to be collected in a wide swath following along the flight path of the plane.

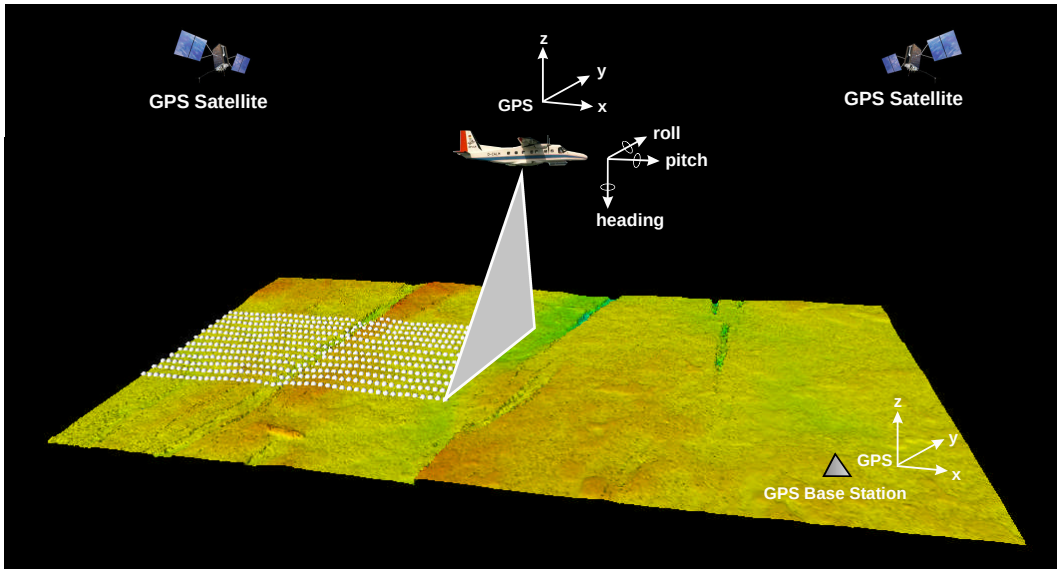

Figure 3.1: Schematic of an airborne LiDAR survey.

Four major components are needed to complete an airborne LiDAR survey:

- LiDAR system
- Aircraft
- Global Positioning System (GPS)
- Inertial Navigation System (INS)

3.1.1 LiDAR system

The LiDAR system consists of a number of parts; the laser source and detector, the scanning mechanism, and the computational apparatus for timing the pulses travel times and for processing and recording the data in real time. The light emitted by the laser source is monochromatic with a wavelength usually within the near-infrared range. The source is also directional, with the light concentrated into a very strong, tightly

focused pulse forming a 'cone' of light that has a Gaussian distribution of power across the beam. Due to the conical nature of the beam it is highly likely that a beam will strike more than one feature within a given pulse, producing multiple returns to the detector. The detector, mounted alongside the laser source, is typically able to record the multiple returns, with the ALTM 3033 LiDAR used for the survey taken over Krafla able to record up to four returns. The diameter of the pulse's footprint at the surface, L_f, and hence the horizontal accuracy of the survey, can be calculated as follows:

$$L_f = H\gamma \tag{3.2}$$

where H is the altitude of the laser above ground level and γ is the beam divergence in radians. For the ALTM 3033, the operational altitude range is 150-4000 m with a dual beam divergence of 0.25 mrad and 0.8 mrad. Thus for a flying altitude of 1500 m, a maximum footprint, L_f, of 1.2 m would be attained. The range accuracy of the ALTM 3033 is given by the manufacturer as between 5-35 cm dependent on flying height. At a flying height of ∼1200 m the accuracy is ∼15 cm.

3.1.2 Aircraft

LiDAR can be acquired using either helicopter or airplane mounted equipment, the choice of which will depend on the needs of the survey and the survey area. The survey in this research made use of a NERC airborne research aircraft, ARSF-Dornier 228-101, an unpressurised twin-turboprop airplane, with the LiDAR system precision mounted on the bottom of the plane.

3.1.3 GPS

The survey plane carries its own GPS unit with a known antenna position relative to the LiDAR instrumentation. In addition, fixed ground-based GPS stations are used to provide accurate positioning of the acquired elevation data providing co-initialisation of the on-board GPS unit prior to the start of the survey. Optimally, the plane should be within ∼100 km range of the base-station throughout the survey to ensure that the aircraft records measurements from the same satellites as the base-station. On-board GPS measurements are taken every 0.5 seconds recording the x, y and z positions of the GPS antenna for the duration of the survey. Post-processing, performed by the Unit for Landscape Modelling (ULM), Cambridge, combines the data from the onboard GPS

and the base-station to provide x, y and z positioning of the LiDAR instrumentation and hence the ground position of the elevation data.

3.1.4 Inertial Navigation System (INS)

Measuring the motion of the aircraft itself, the Inertial Navigation System plays a crucial part in ensuring the accuracy of the final processed data. With the onboard GPS keeping track of the aircraft's position in space, the INS records the movement of the plane calculating the pitch, roll and yaw of the plane using accelerometers to track the relative changes in movement of the plane through time. These corrections are then applied to the data in post-processing.

3.2 The 2007/2008 LiDAR Surveys of Krafla

The LiDAR data used in this research were acquired during two surveys by NERC's ARSF Dornier aircraft. The first survey was flown on the 7th August 2007, and the second flown on the 5th September 2008. The Dornier carried Optech's ALTM 3033 (Airborne Laser Terrain Mapper 3033). This was mounted over an opening in the aircraft floor, scanning during flight from beneath the aircraft to produce a wide swath over which the distance to the ground was measured and recorded. The angle of the scanning laser, which rotated about a scan width range of 0 - 50°, was also recorded for each point to allow for correction in the final elevation calculation. A GPS receiver in the aircraft recorded the aircraft's position and the INS recorded the aircraft's pitch, roll and yaw at fixed intervals of 0.5 seconds. Improved position estimation using ground-based GPS to provide differential correction was supplied by the primary GPS base station MYVA during the 2007 survey and the GPS station AKUR in the 2008 survey (see figure 3.3 for locations).The ALTM 3033 collected 33,000 laser observations per second and for the purposes of this survey was set in standard operating mode collecting first pulse, last pulse and intensity data only. In post-flight processing, the laser range, scan angle, GPS data and INS data were combined to determine the accurate position of each measured point on the earth's surface.

The initial stage of post-processing to x,y and z coordinates was completed at the ULM, Cambridge. The GPS data were processed using Applanix PosPac 4.2 software with the best estimate positional accuracy for the survey calculated to be 0.068 m for Eastings, 0.055 m for Northings and 0.119 m for the Z-range. The LiDAR data were

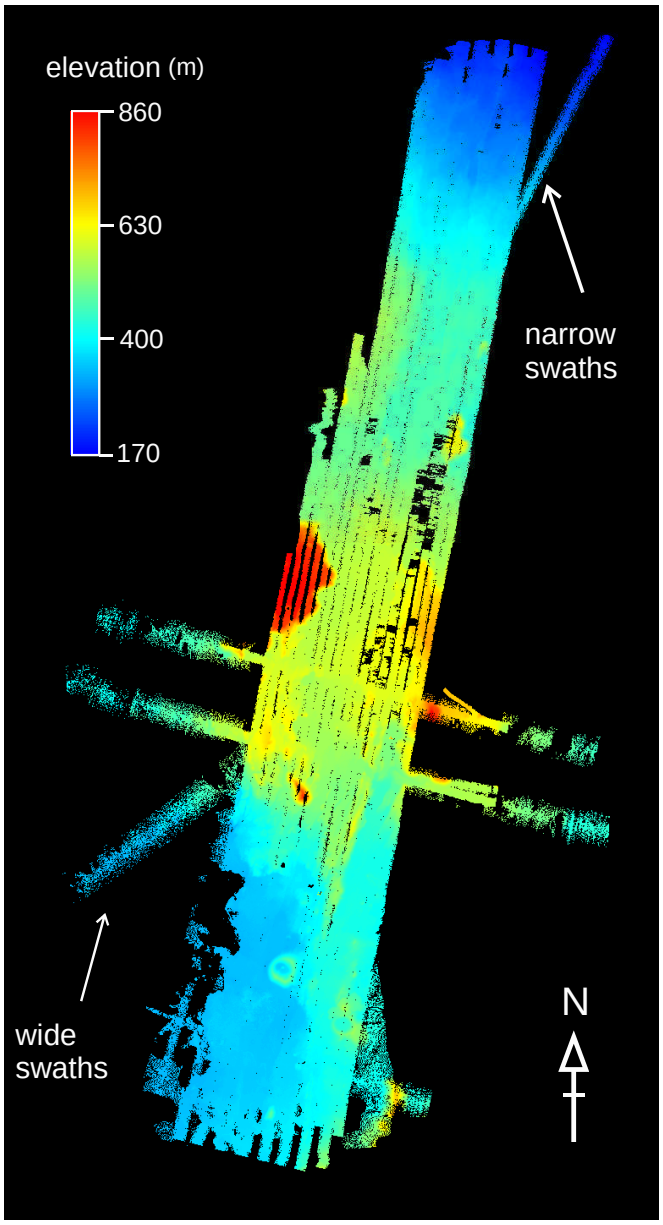

Figure 3.2: The LiDAR survey coverage over the Krafla region made using a scatter plot of the point cloud. The wider swaths taken by the first survey over the area, with the narrower swaths showing the coverage from the second survey.

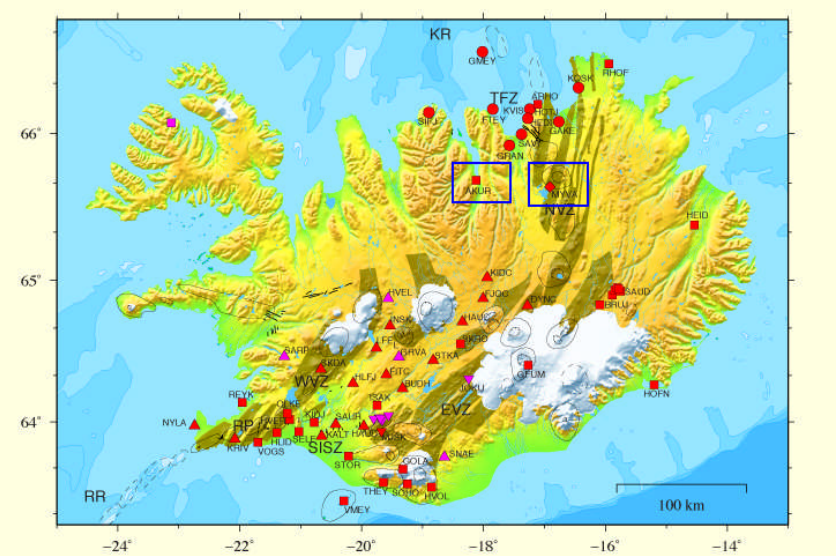

Figure 3.3: Map of continuous GPS stations in Iceland, image from Nordic Volcanological Center website (http://www.norvol.hi.is/). The location of CGPS stations MYVA and AKUR, used in the LiDAR survey, are shown by the blue rectangles.

processed using Optech REALM v3.5 software and I was provided with a processed dataset consisting of a value for Easting, Northing, height and intensity for points in the final point cloud.

Acquired at an average height above the surface of 2,575 m, producing ∼1.6 km wide swaths of data, the August 2007 survey encountered a large amount of atmospheric interference resulting in a patchy dataset. Due to cloud cover, the 2008 survey was flown at the lower average height of 1,180 m, producing narrower swaths of around 0.4 km width. The 2007 and 2008 datasets were combined, producing a total of over 400 million points over the 1300 km^2 and obtaining a mean data resolution of 0.97 points/m^2.

The complete LiDAR survey coverage can be seen in figure 3.2. The wider swaths, most observable going from east-west across the survey, are those acquired during the 2007 survey over the region, with the narrower swaths showing the coverage from the 2008 survey. A number of holes can be seen in the coverage, due mainly to gaps between flight swaths and patches of atmospheric interference. Methods to interpolate over these regions have been investigated and are detailed later in this chapter.

3.3 Data processing

To ensure that the data are used to maximum potential it has been necessary to find interpolation methods and software applications that suit each of these specific purposes. In the following two sections I discuss the methods used to interpolate surfaces to a resolution of 0.5 m followed by a discussion of selecting appropriate resolution for the dataset later on in the chapter.

The key aims for interpolation of the LiDAR point cloud are to create:

- surfaces that could be loaded and used efficiently in a 3-D visualisation and interpretation package
- a full DEM of the whole survey area at the highest possible resolution for the data

The requirements for these two key aims have resulted in needing to use different methods to create and utilise the DEM appropriately. The following sections will discuss both the requirements and the methods used.

3.3.1 3D Interpretation and Convergent Interpolation

A 3-D interpretation package allows for the accurate picking of the top and bottom edges of individual faults. Additionally, depending on the package, a surface can be easily rotated allowing the user to gain a full understanding of the interplay between faults and assisting with the identification of individual fault structures. One of the key issues with finding a suitable package was the sheer quantity of data in the LiDAR point cloud. Packages that can process and display surfaces in this way are resource intensive and restrictions in processor size and graphic display capabilities limited the size of data set that could be displayed and analysed. A number of applications were tested for usability (e.g. ER Mapper, ARC GIS) and Schlumberger's Petrel gave the best solution for 3-D fault analysis. It was necessary for the data to be split into smaller regions for processing (with a 3x3 km square being the maximum usable size of surface at 0.5 m resolution) and a background dataset was created that held the entire survey region as a series of 1x1 km square fully interpolated surfaces.

Petrel's convergent interpolation method was selected to create all the interpolated surfaces for 3-D fault analysis. This method uses a convergent gridder algorithm (Haecker, 1992) which takes a set of randomly distributed scatter points and computes

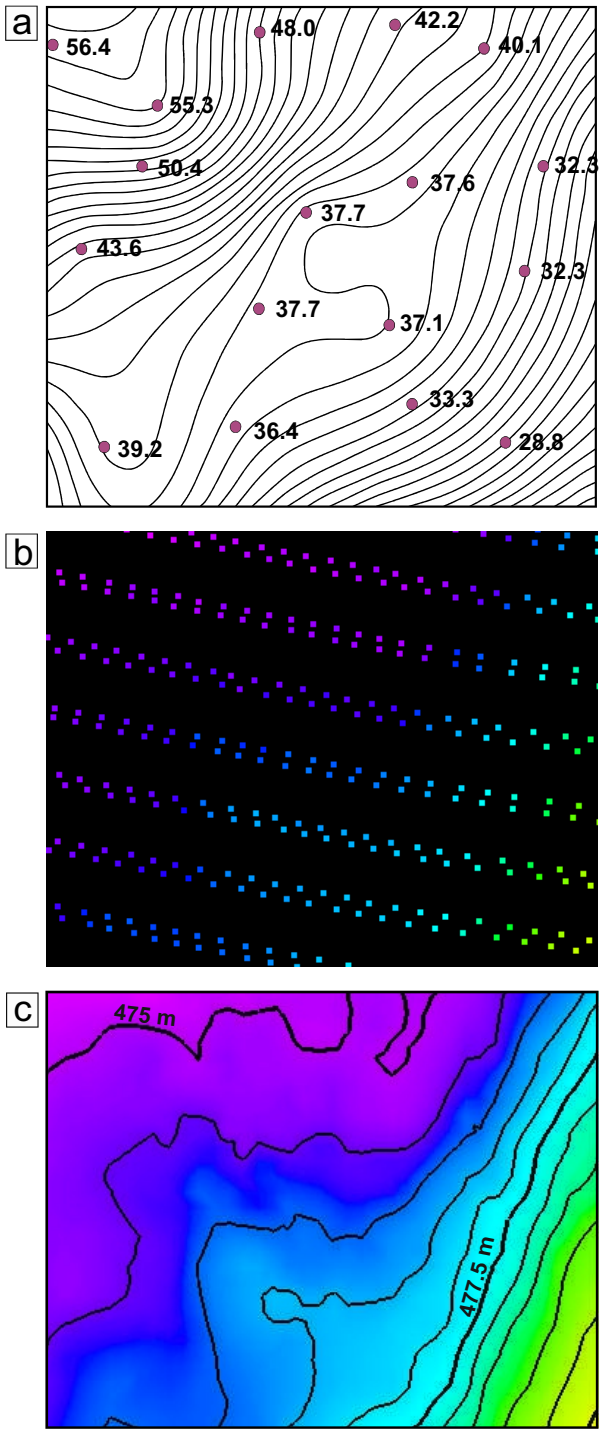

Figure 3.4: a) An example of the contours created using Briggs biharmonic (minimum curvature) smoothing around a series of data points (purple circles) to create an interpolated surface (some data points lie outside the field of view of the figure). This is a redrawn excerpt from results in Briggs (1974). b) and c) are an example of the minimum curvature algorithm applied to the LiDAR data using Petrel. b) contains a subset of original data points and c) is the interpolated surface.

the smoothest possible surface to match the given data. A coarse grid is initially applied to the data using a Taylor series projection which is then refined many times through a series of converging iterations, adding increased resolution with each iteration, smoothing using the Briggs biharmonic (minimum curvature) method (Briggs, 1974).

The minimum curvature interpolation method finds an optimal spline fit that minimises the total curvature, $C(u)$, of a surface, $u(x, y)$, whilst conditionally passing through the available observed data $u(x_i, y_i) = d_i$ with $i = 1, \cdots, n$. This was defined by Briggs (1974) as:

$$C(u) = \iint \left(\frac{\partial^2 u}{\partial x^2} + \frac{\partial^2 u}{\partial y^2} \right)^2 dxdy \tag{3.3}$$

With appropriate boundary conditions, this is equivalent to solving the bi-harmonic equation:

$$\left(\frac{\partial^2}{\partial x^2} + \frac{\partial^2}{\partial y^2} \right) \left(\frac{\partial^2 u}{\partial x^2} + \frac{\partial^2 u}{\partial y^2} \right) = 0 \tag{3.4}$$

With a grid spacing h and an interpolated value at grid point (i, j) of $u_{i,j}$, a system of linear equations can be obtained to minimise $C(u)$. An example of the resultant contours of an interpolated surface for a series of points using the minimum curvature method is shown in figure 3.4.

Examples of the surfaces created using Petrel's convergent interpolation method on the LiDAR point data are shown in figures 3.5, 3.6 and 3.7. Figure 3.5 is an example of how the interpolation managed (see figure 3.5b) over large and continuous holes in the LiDAR point cloud (see figure 3.5a) caused by gaps between flight acquisition swaths. These holes are the largest ones in the survey region and how an interpolation method managed these areas was a key indicator for choice of method, particularly for the full DEM (discussed in the next section). The surface interpolated over the hole appears smooth and reasonable for the surrounding area, it also compares favourably with the interpolation of this area in the full DEM (which is shown in figure 3.11a). Figure 3.6 shows regions of large, isolated holes, most likely the result of atmospheric interference, which again compares favourably with the DEM interpolation (3.11b). Figure 3.7 shows a region of high point density in the LiDAR point cloud and is actually representative of the point resolution and interpolated surface throughout the area used in the fault analysis covered in later chapters.

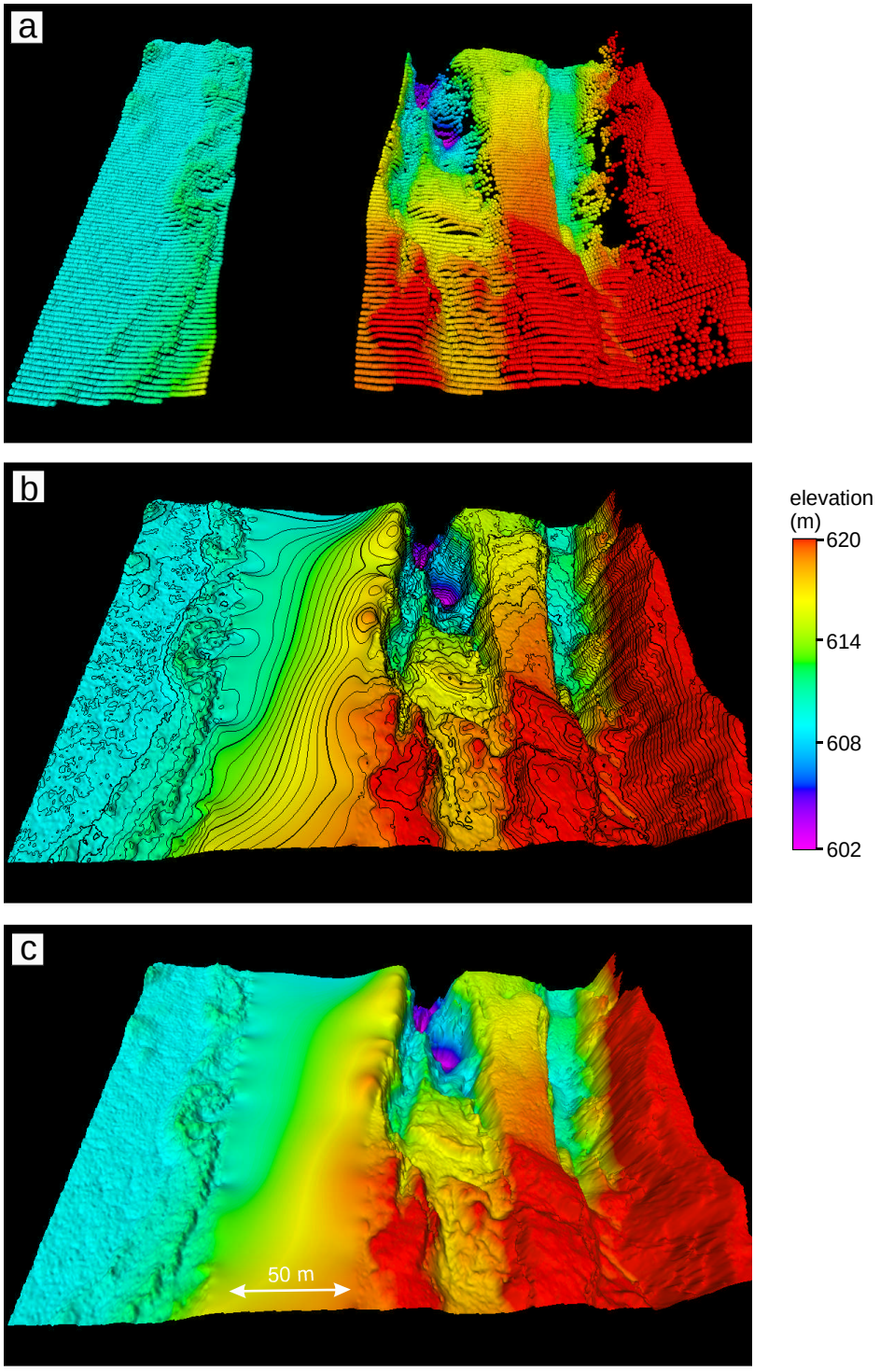

Figure 3.5: Showing the surface produced by Petrel's convergent interpolation over large continuous holes in the LiDAR point cloud where a) is the original point cloud, b) is the resultant interpolated surface with contours at every 0.5 m of elevation and c) is the interpolated surface without contours.

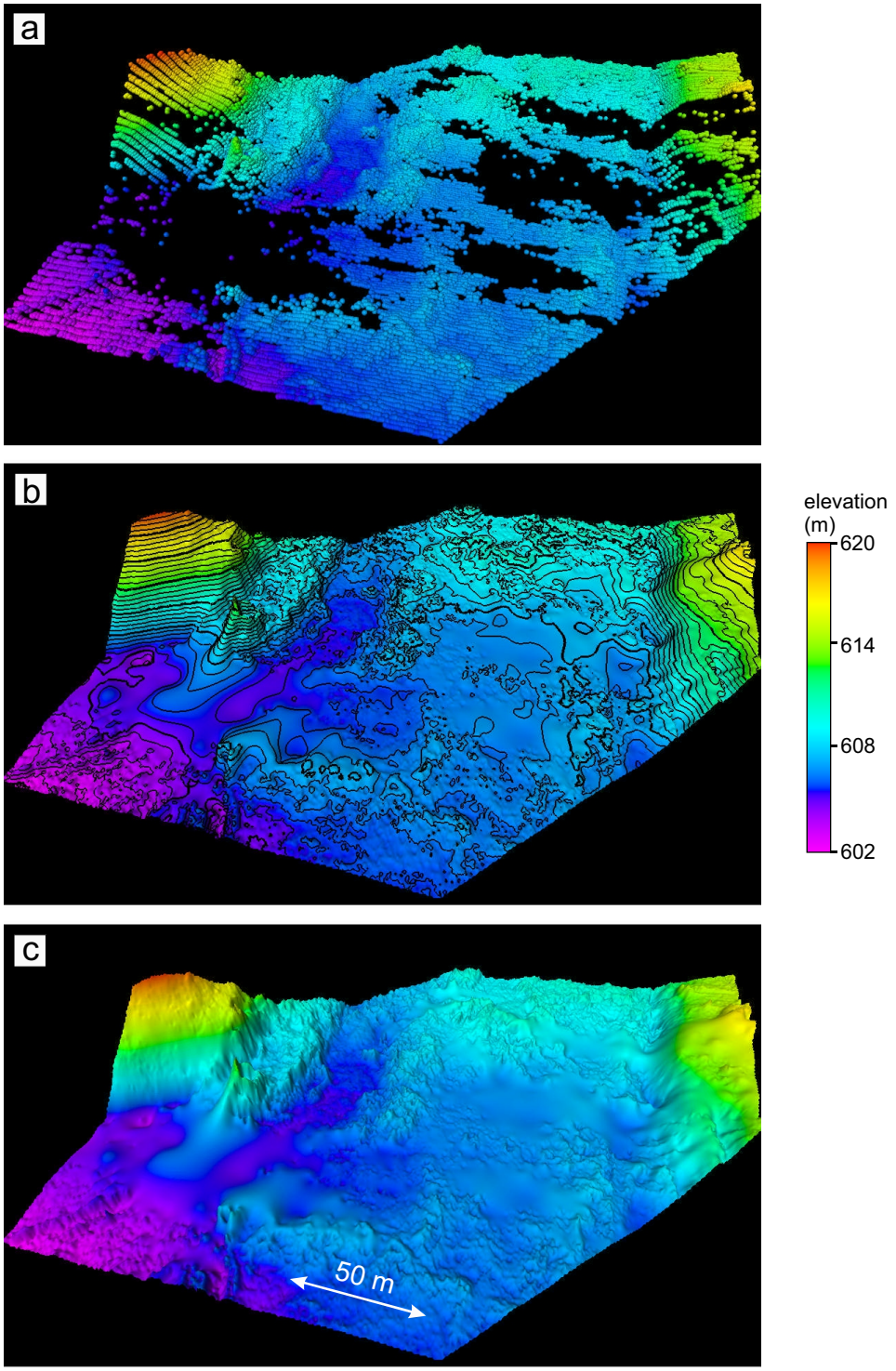

Figure 3.6: Showing the surface produced by Petrel's convergent interpolation over isolated holes in the LiDAR point cloud where a) is the original point cloud, b) is the resultant interpolated surface with contours at every 0.5 m of elevation and c) is the interpolated surface without contours.

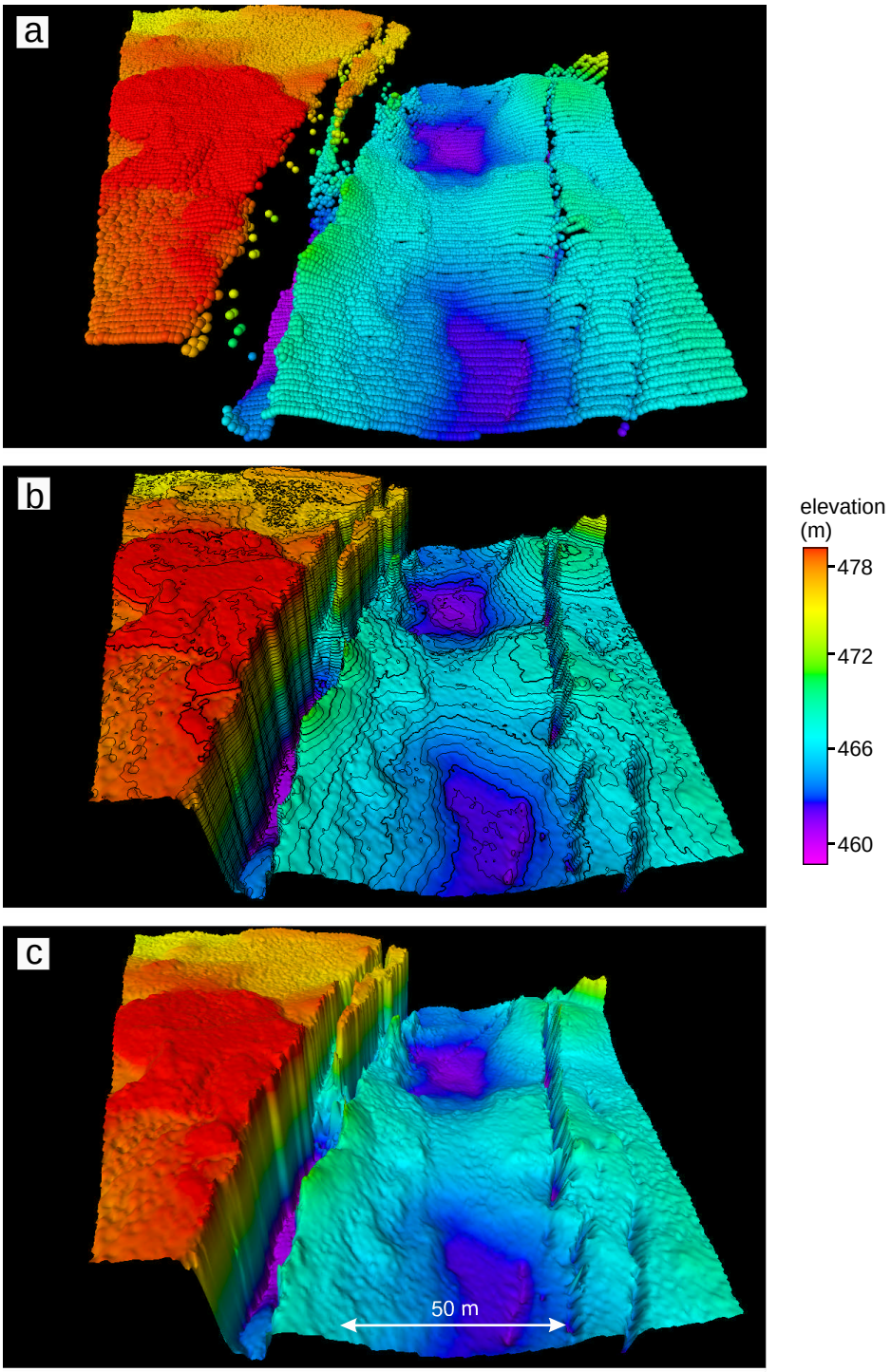

Figure 3.7: Showing the surface produced by Petrel's convergent interpolation over a region of high point density in the LiDAR point cloud where a) is the original point cloud, b) is the resultant interpolated surface with contours at every 0.5 m of elevation and c) is the interpolated surface without contours. The region of black in the point cloud is indicative of a rapid change in elevation (as can be seen in the surface in b) and c) rather than a horizontal hole in the point cloud.

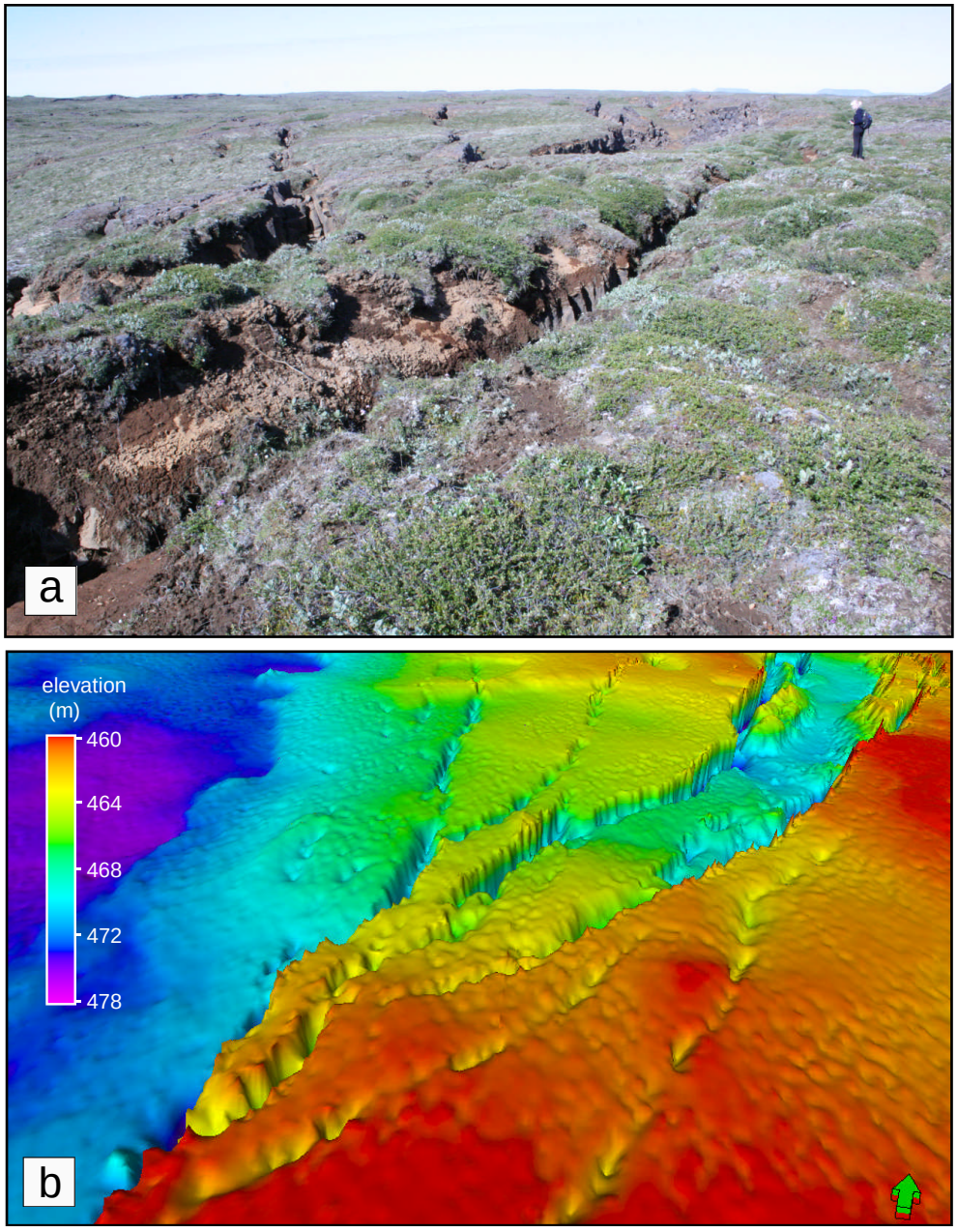

Figure 3.8: a) Shows an image of a horsetail splay found at the end of a large fault just north of the Krafla Fires lava flow, the interpolated LiDAR surface over the same region is shown in b).

A comparison between the interpolated LiDAR dataset and the actual surface can be seen in figure 3.8 where a small system of faults in a horsetail splay at the end of a large fault, shown in the photograph, can be seen clearly imaged in the LiDAR surface.

3.3.2 Digital Elevation Model and Nearest Natural Neighbour Interpolation

In addition to the surfaces created in Petrel for fault analysis, a DEM was created with the highest possible resolution provided by the LiDAR point cloud. Ideally the DEM was to be viewable as a single continuous surface by such packages as ER Mapper and Arc-GIS aiding the research in both this thesis and for future work that may need to use the full, high-resolution DEM of the Krafla swarm. To create the DEM it was necessary to find an interpolation method that was able to cope with not only variations in point cloud density but also sizeable holes in the order of 10s of metres wide created by gaps between flight swaths and atmospheric interference (where the original points are extracted in the post-acquisition processing prior to output to final xyz dataset).

As with the 3-D software packages, one of the restricting factors was the size of the LiDAR point cloud and the processing power needed to interpolate from point cloud to high resolution surface. Prior to interpolation I divided the dataset into smaller regions of 1 km^2 that could be easily processed and reconfigured to create a surface for the full survey region. Matlab produced the most promising results, I tested a number of possible interpolation methods using both the griddata and TriScatteredInterp functions on a 1 km^2 region of the LiDAR point cloud. I selected the test dataset as an area that contained a large number and variety of data holes to allow comparisons of how the interpolation methods coped with regions of low point density and across holes in the data. In addition the test data set contained some prominent geological features that would test the behaviour of the interpolation function on a surface with rapid elevation change. The point cloud used for testing can be seen in figure 3.9a.

The initial Matlab function I tested was ‘griddata‘ which has five possible interpolant options: linear, cubic, natural neighbour, nearest neighbour and v4 interpolation (where v4 is a Matlab specific interpolation), all of which use a variation of Delaunay triangulation (discussed further on in this section). I found the surfaces produced by all these functions to be poorly constructed with spurious errors and holes not present in the original point cloud. The function proved to have a known issue in using Delaunay

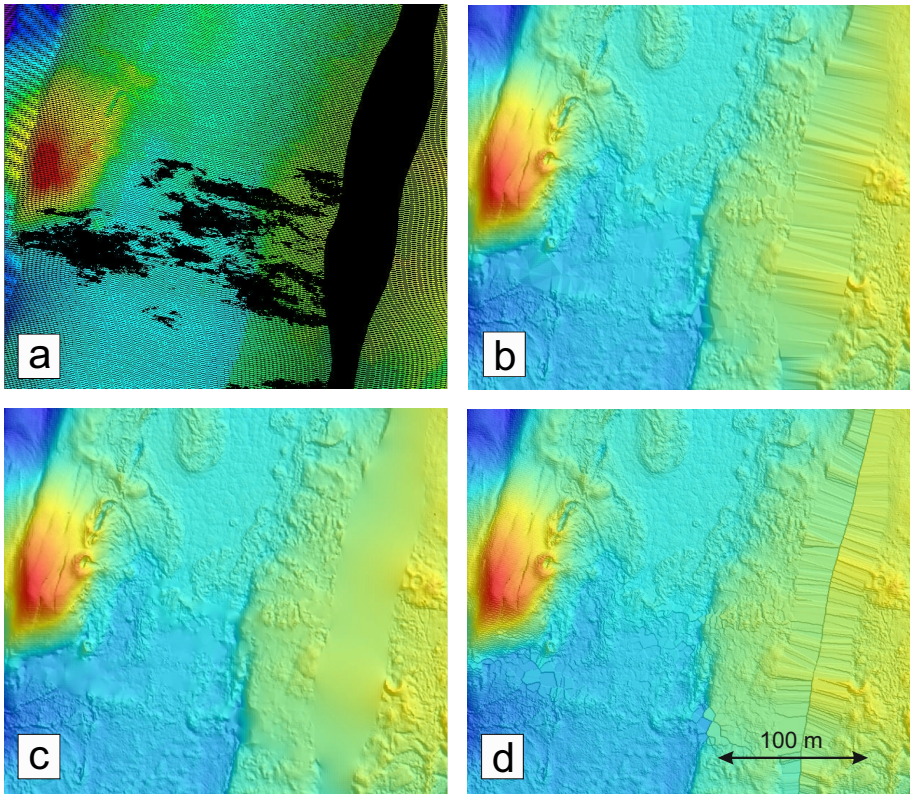

Figure 3.9: Comparing interpolation methods tested for creating the DEM. Shows a) the LiDAR point cloud used for testing containing holes due to both gaps between swaths (the long hole running from top to bottom) and atmospheric interference (the less regular holes at the bottom of the image). The interpolated surface produced by Matlab's TriScatteredInterp function which uses Delaunay triangulation with b) linear and c) nearest natural neighbour and d) nearest neighbour interpolation.

triangulation for processing large scale datasets such as the LiDAR dataset, resulting in the observed errors in the interpolated data. All five methods were tested with varying sizes of data and resolutions, to see if a reduction in processing created a better interpolation. However, even on datasets of 100 m^2 with a low resolution selection, there was no visible improvement to the interpolated data quality. Following on from this I researched other methods, including processing through GMT, the results from which also had poor data quality issues.

The relatively new function in Matlab called TriScatteredInterp offered a solution with three possible interpolant options: linear, nearest neighbour and natural neighbour

interpolation. This scattered data interpolation function uses the CGAL Delaunay triangulation which allows efficient interpolation of large datasets without the resulting errors seen from other interpolation functions. The triangulation for TriScatteredInterp is cached within the interpolant, rather than constantly re-calculated as in other functions, which means that the triangulation does not need to be re-computed each time a point is evaluated, resulting in making the interpolation much less memory intensive. The results of the three interpolation options can be seen in figure 3.9b,c and d. Whilst all three methods show good interpolation across regions of high point density, there are considerable differences in the way that the surface was interpolated across the holes in the data, with the natural neighbour interpolation showing the smoothest and visually the most accurate interpolation in all cases.

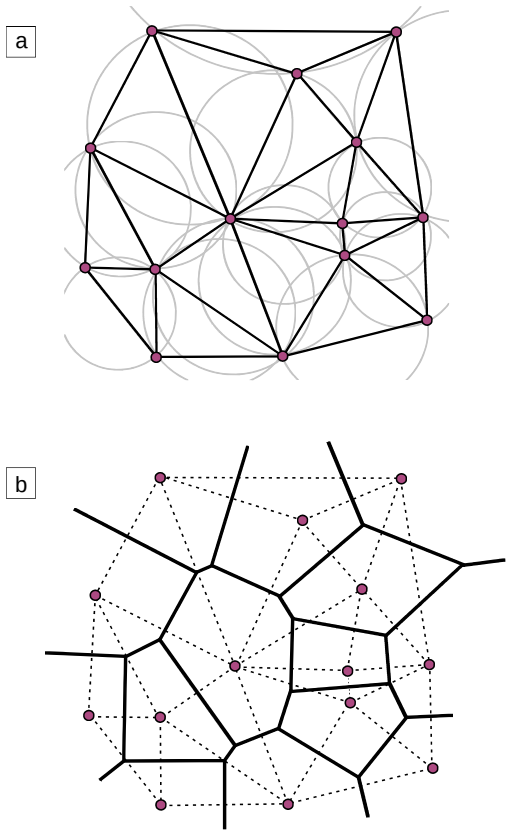

Figure 3.10: Shows the surface interpolated for a series of data points (purple circles) using a) delaunay triangulation and b) nearest natural neighbour interpolation where the Voronoi polygons are calculated from the perpendicular bisectors of the original delaunay triangulation (dotted lines) as shown a).

Natural neighbour interpolation is a Delaunay triangulation-based method that has an area-of-influence weighting associated with each sample point. It is a method that has been widely used in the area of geostatistics and performs well in both clustered and sparse data locations (Boissonnat and Cazals, 2000, Goodwin et al., 2006, Bater and Coops, 2009). In interpolation mathematics, the Delaunay condition for a set of points in a plane is such that no point in the set is inside the circumcircle of any triangle created by joining the points together. The interpolation method works by drawing up a set of lines connecting each point in the dataset to its natural neighbours. The interpolation is then performed on the triangular surfaces created based on the Delaunay condition (as shown in 3.10a).

Natural Neighbours interpolation is based on the concept that there is an implicit weighted dividing line between a pair of neighbours which, over a group of points, creates sets of irregular Voronoi polygons from which a formal relationship 'nearest natural neighbours' can be described (as shown in 3.10b). Natural neighbour interpolation was first formulated by Sibson (1981) and is described in 2D by the following equation:

$$G(x,y) = \sum_{i=1}^{n} w_i f(x_i, y_i) \tag{3.5}$$

where G(x,y) is the interpolated quantity at position (x,y), w_i are the weights and $f(x_i, y_i)$ are the known data at x_i and y_i.

Firstly a triangulated irregular network (TIN) is created by connecting each point in a set of scattered points to its nearest neighbour, satisfying the Delaunay criterion of triangulation mentioned earlier. A Voronoi polygon network is then created by perpendicularly bisecting the lines between points, forming closed polygons with the perpendicular bisectors. The network is then such that there is only one polygon created for each point within the network and its enclosed area is closer to that point than to any other point within the network.

The next step is to define the weight values (w_i). This is done using local coordinates to define the amount of influence or 'neighbourliness' any point within the network will have on the computed value of a chosen interpolation point. This is done by calculating the changes to each point's area of influence within a Voronoi network caused by introducing the new point into the network and recalculating the boundaries of the network. Only the points whose polygons have been affected by the temporary insertion

of the interpolation point, P_i, are used for the calculation of the value of P_i. A local coordinate is defined by relating the area shared by the new polygon defined by P_i and that of the original polygon for each of the original points. The greater the shared area, the larger the local coordinate for each point which results in a greater weight and influence upon the final value of P_i.

Some examples of the DEM produced using the nearest natural neighbour interpolation method at 0.5 m resolution are shown in figure 3.11. Figure 3.12 shows a comparison between the interpolation using Petrel's convergence interpolation and Matlab's natural neighbour interpolation, with interpolation over the large hole as shown in 3.5

3.3.3 Interpolation Resolution

One of the outcomes for the LiDAR data processing was to produce as high a resolution DEM as viably possible from the point cloud density. Prior to the acquistion of the LiDAR data the best available DEM was provided by the ASTER Global Digital Elevation Model (ASTER GDEM).The ASTER GDEM was acquired by the remote sensory device ASTER (Advanced Spaceborne Thermal Emission and Reflection Radiometer) onboard the Terra satellite launched into orbit around Earth by NASA in 1999. The ASTER dataset provides images in 15 different wavelengths, ranging in elevation resolution from 15 to 90 m, with the near-infrared (as used in the LiDAR survey) having a resolution of 15 m, with measurements taken at 30 m intervals. A comparison between the ASTER GDEM and the LiDAR DEM (processed at 0.5 m resolution) is shown in figure 3.13

An understanding of the variability of the point density across the survey area is needed to ensure that the optimal resolution is used for interpolating the LiDAR point cloud. The coverage over the survey area is shown in points/m^2 in figure 3.14a showing a general coverage $>$ 1 point/m^2 over the main body of the survey area, with some regions of very low coverage in the wider swaths flown in the first survey that extend out either side of the main region. Increased coverage of 2 or more point/m^2 can be observed in regions that contain overlap of the flight swaths. This histogram in figure 3.14b shows the spread of the coverage across the survey, giving a mean value of 0.97 points/m^2 with a standard deviation of 0.55 points/m^2 and a maximum coverage of 5.4 points/m^2. The mean value includes the regions of low coverage around the edges of the survey and also in the wide flight swaths discussed earlier, and so it would be reasonable to aim for a

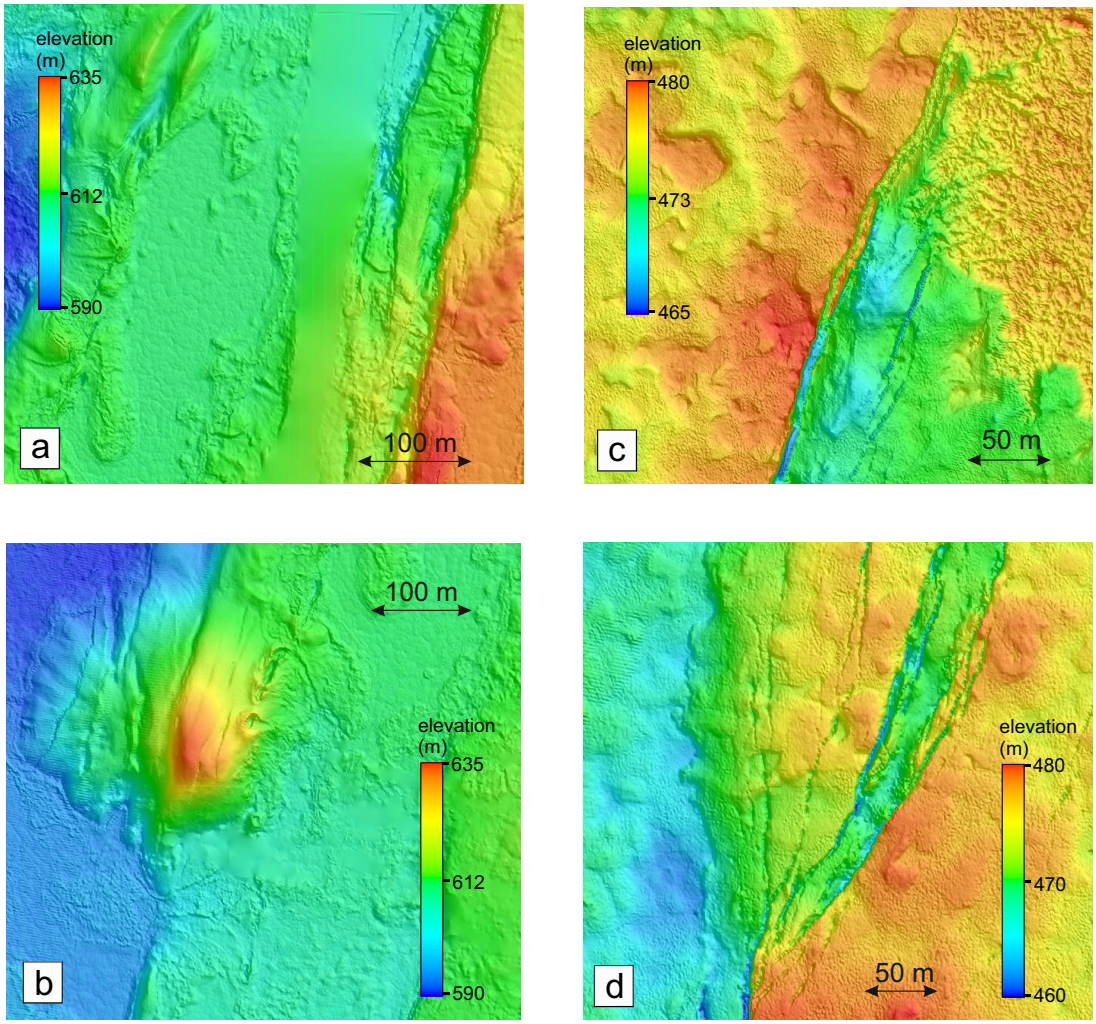

Figure 3.11: Surfaces created from LiDAR data using Matlab nearest neighbour interpolation function. The areas shown in a)-d) can be compared with the surface created by Petrel's convergent gridding interpolation method where a) is the region with a large gap in data between adjacent swaths as shown in 3.5a, b) is a region of smaller holes in the data possibly caused by atmospheric interference as shown in 3.6a, c) is a region of complete coverage where lava from the Krafla Fires (in the top right corner of the image) can be seen flowing along a large fault in the centre of the image, as shown in 3.7 and d) is the region of small faults shown in 3.8.

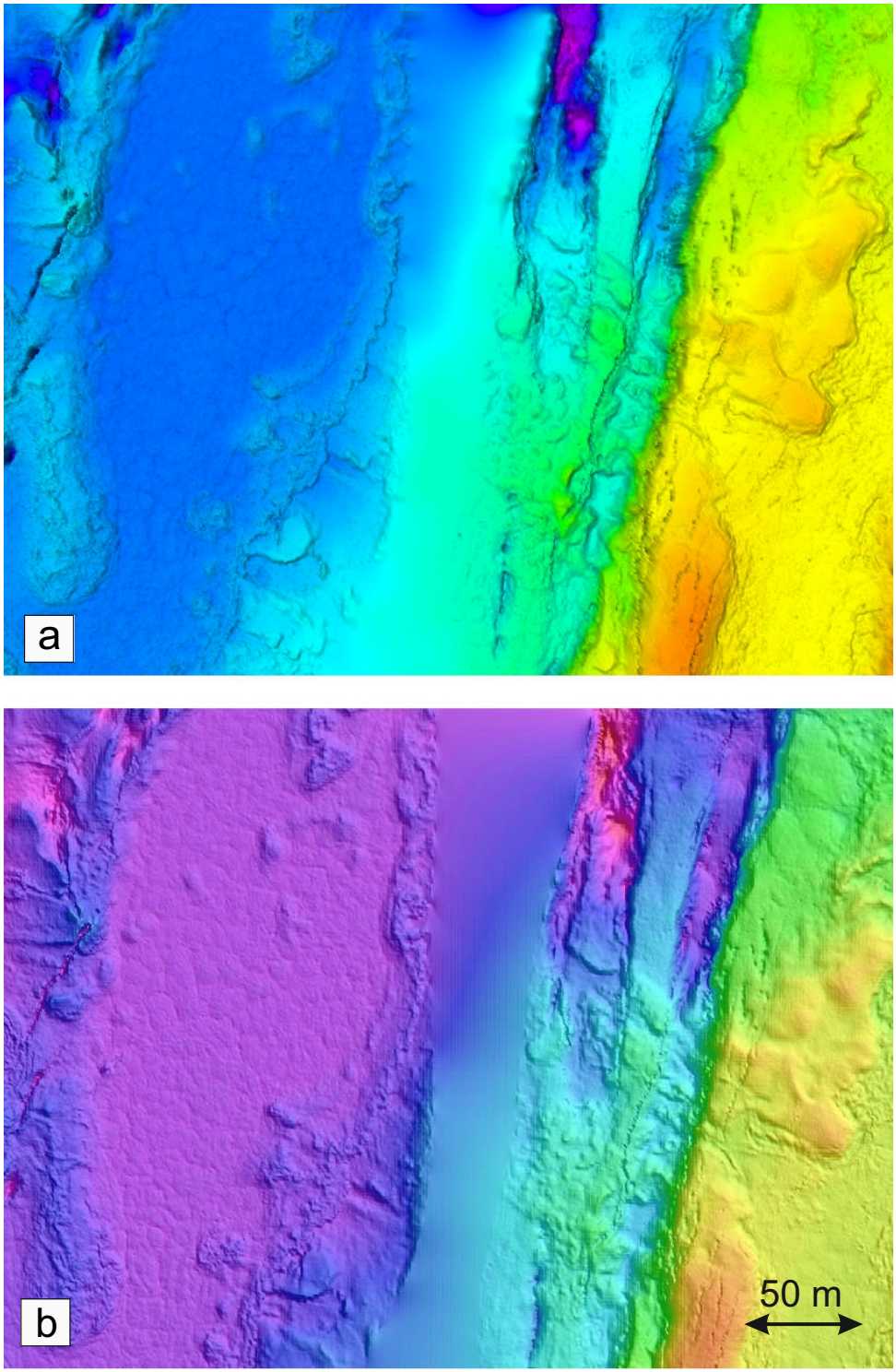

Figure 3.12: Comparison of interpolation methods over a large hole (hole as shown in figure 3.5) using a) Petrel's convergence interpolation and b) nearest natural neighbour interpolation (viewed in ER Mapper). Differences in colour between a) and b) are due to slightly different colour ranges in the two applications. Image is of a slightly wider area than shown in figure 3.5.

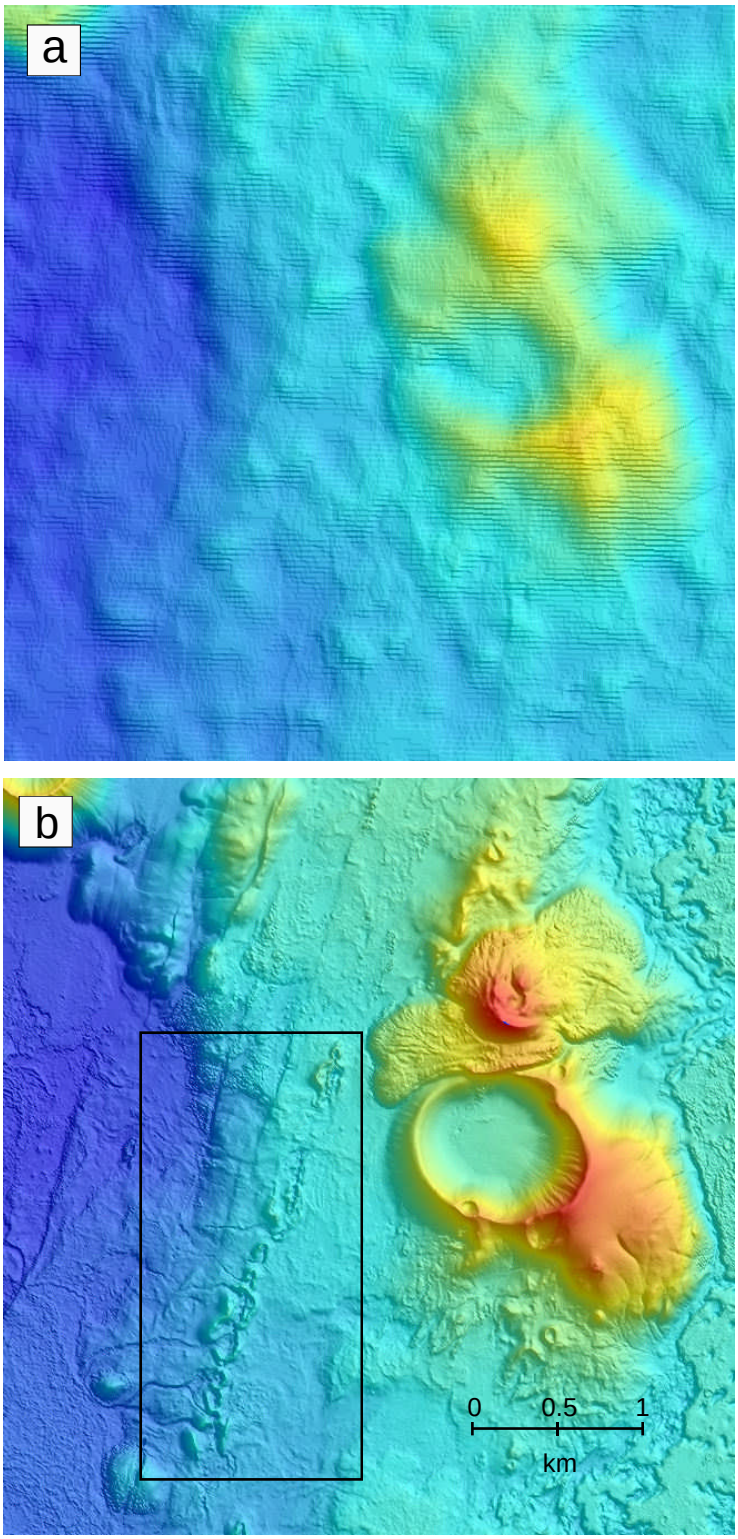

Figure 3.13: Comparison of data resolution between a) the ASTER GDEM and b) the LiDAR DEM processed at 0.5 m resolution.The boxed area in b) indicates the long feature of the Ludentarborgir fissure row (shown in figure 2.6. ASTER GDEM image produced with permission from METI and NASA.

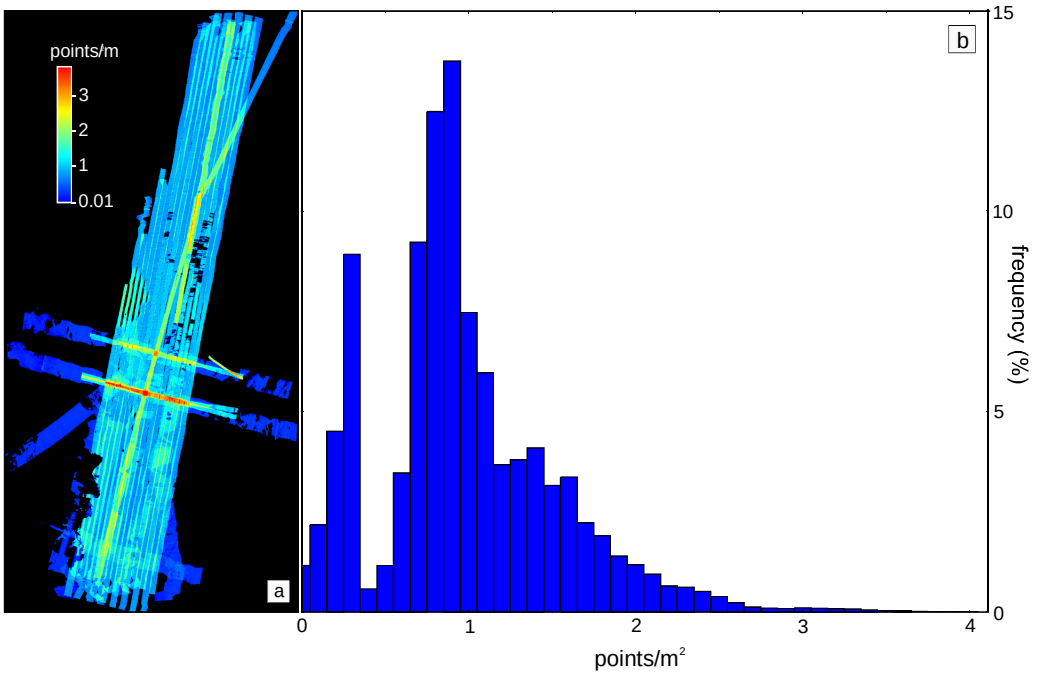

Figure 3.14: Density of LiDAR coverage over Krafla where a) shows a map of the LiDAR coverage over Krafla and b) is a histogram showing the frequency of LiDAR coverage in points/m^2

resolution of 1-2 points/m^2 in the main body of the survey area.

Figure 3.15 shows a section of the interpolated data, selected to represent an area with good average coverage (between 1-2 points/m^2) overlain with a scatter plot of the pre-interpolated data points. This region is also representative of the area that will be used in chapter 4 for in-depth fault analysis. The original data points in figure 3.15(1) show that the LiDAR data points are evenly distributed in densely populated rows running perpendicular to the direction of flight, a distribution associated with the rotation of the laser head. This distribution shows that in a region of good coverage there is an interleaving of densely populated (up to 4 points/m^2) and sparsely populated areas. To ensure that the elevation measurements in the densely populated areas are included in interpolation, a resolution of 0.5 m was selected, this would ensure that 4 points evenly distributed across a single m^2 would be included in interpolation. Smoothing over the more sparsely populated areas, for example a single point/m^2, would be the similarly interpolated at either 0.5 m or 1 m and should not be affected by the choice of higher resolution. Examples of interpolation using Petrel's convergent interpolation

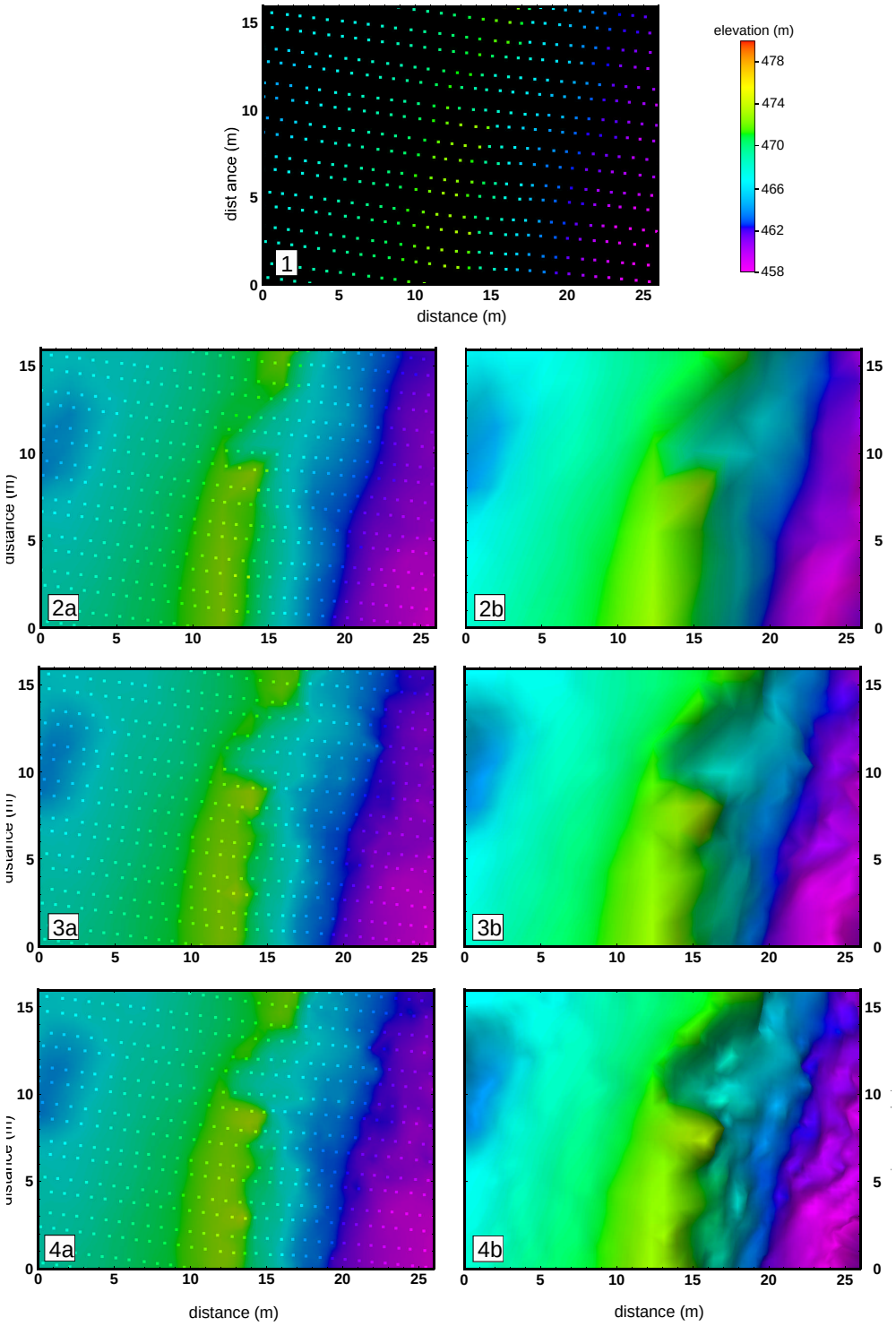

Figure 3.15: Comparing surface resolutions using the convergent interplation method. 1) Shows the original LiDAR points used for interpolation and 2), 3) and 4) show the interplation performed at 2 m, 1 m and 0.5 m resolution respectively. a) shows the 2-D interpolated surface overlain by the data points and b) shows the interpolated surface in 3-D. All surfaces produced using Petrel's convergence interpolation method.

at 2, 1 and 0.5 m can be seen in figure 3.15(2),(3) and (4) repectively, with each showing the 2-D interpolated surface overlain with the original points in (a) and the 3-D surface in (b). These images clearly show an improvement in accuracy over the three resolutions. Higher resolutions were tested showing minimal improvement in the surface detail beyond 0.5 m with any small improvements negated by the additional processing capacity needed to cope with the increased requirements.

3.4 Ground-truthing with dGPS

I performed a series of differential GPS (dGPS) surveys in July 2010 to allow ground-truthing of the LiDAR dataset. I acquired the surveys in accessible regions of the Krafla fissure swarm, with five surveys being completed as shown in figure 3.16. Regions were selected both as clearly defined structures in the LiDAR DEM and also for their spread across the survey area to provide tie-in across the LiDAR dataset. Unfortunately due to time constraints and difficult terrain, surveys were not acquired north of the caldera although I did spend time travelling throughout the northern section without the GPS equipment, examing signifcant features from the DEM to get a better understanding of the geological features.

A dGPS survey uses two receivers: the stationary base station which is used to tie the GPS satellite measurements to a stable local reference point and the roving station that moves around taking positional measurements. Real Time Kinematic (RTK) satellite navigation is used to increase the precision of positional data by using the base station as a reference station to provide real-time corrections which are then passed on to the roving station. The schematic shown in figure 3.17 shows the key features of a dGPS survey. For the purposes of this survey the base station position was known only to the accuracy of the initial GPS measurement taken at the start of each survey and selected as the stationary base station permanent location (usually accurate to a few metres). As the base station is stationary throughout each survey, the initial GPS reading can be assumed to be static for that location and the corrections calculated and passed on to the rover station allow an accuracy relative to the base station of a few centimetres.

A satellite signal acquires inaccuracies in travel time as it passes through the Earth's atmosphere and these errors are inevitably included in the final position calculation. However, as the location of the base station is already known, it is possible to extract the timing errors by calculating the difference between actual and expected signal travel

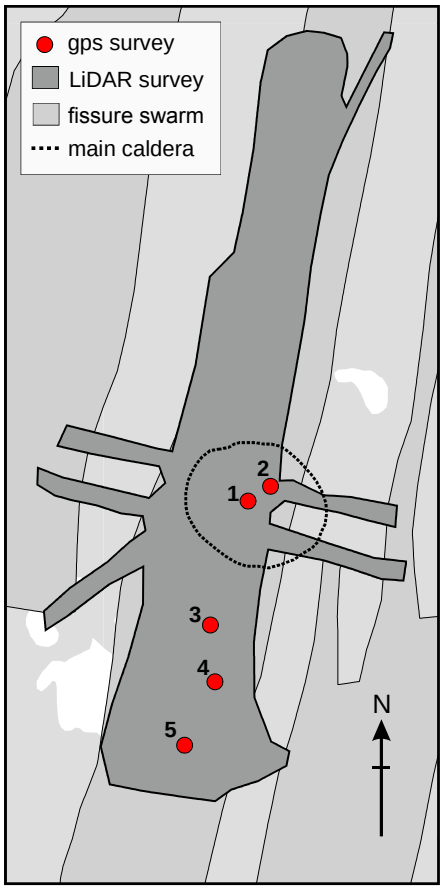

Figure 3.16: Map of the differential GPS survey locations, acquired in July 2010. The surveys are represented by the red circles and the LiDAR survey region is shown as the dark grey region.

time from the satellite. The base station receives signals from a minimum of four satellites for which it calculates the signal timing errors and subsequently transmits these by radio connection to the rover station. As the roving receiver is relatively close to the base station, the satellite signals it recieves will have travelled through the same slice of atmosphere and acquired the same errors. The rover station then applies the timing corrections to its received timing signals and calculates the rover location to a high level of accuracy.

For this survey the base station comprised a Trimble R7 GNSS system using a Trimble Zephyr Geodetic 2 ground plane antenna. The Trimble PDL450 radio attached to the base-station provided a radio modem data link that broadcasted the RTK data to the rover station. The rover station consisted of a Trimble R8 GNSS, able to recieve both the satellite and RTK corrections and the Trimble TSC2 controller. The Trimble

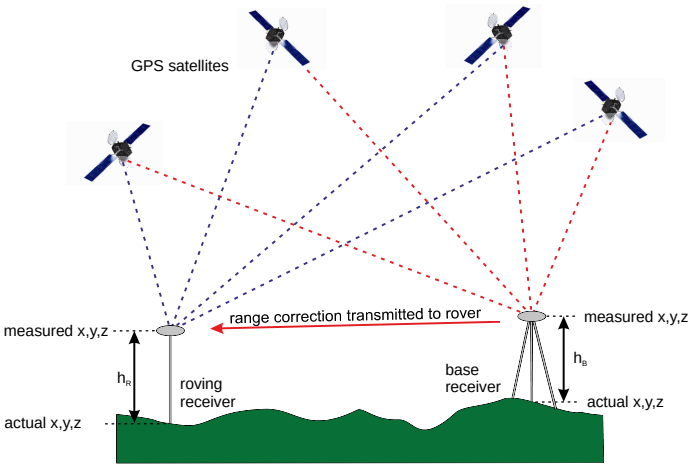

Figure 3.17: Schematic of differential GPS.

TSC2 is a hand held computer with integrated wireless bluetooth which allowed communication with both the R7 and R8, initialisation of both antennae, communication and recording of data.

The final positional data are stored in a Trimble specific format that can either be converted using the Trimble TSC2 controller to a more usable xyz format and exported via a USB connection, or imported using Trimble software which can be used to manipulate the data in a variety of ways from converting to alternative coordinate systems to creating models from the data.

3.5 Comparison of GPS and LiDAR

The positional data acquired in the dGPS surveys were converted to xyz format and imported into Petrel as point data for comparison with the LiDAR interpolated surface. The dGPS points from the five surveys can be seen as blue points in figure 3.18 overlying the corresponding LiDAR surface.

To examine any differences between the LiDAR and dGPS meaurements, the elevation data was extracted from the LiDAR DEM at the corresponding dGPS point locations using GMT. Figures 3.20a and 3.21a show plots of the elevation for dGPS and LiDAR at the same location, with the data sorted by LiDAR DEM elevation (not dGPS survey acquisition order). It can be seen that both survey 3 and 4 have what

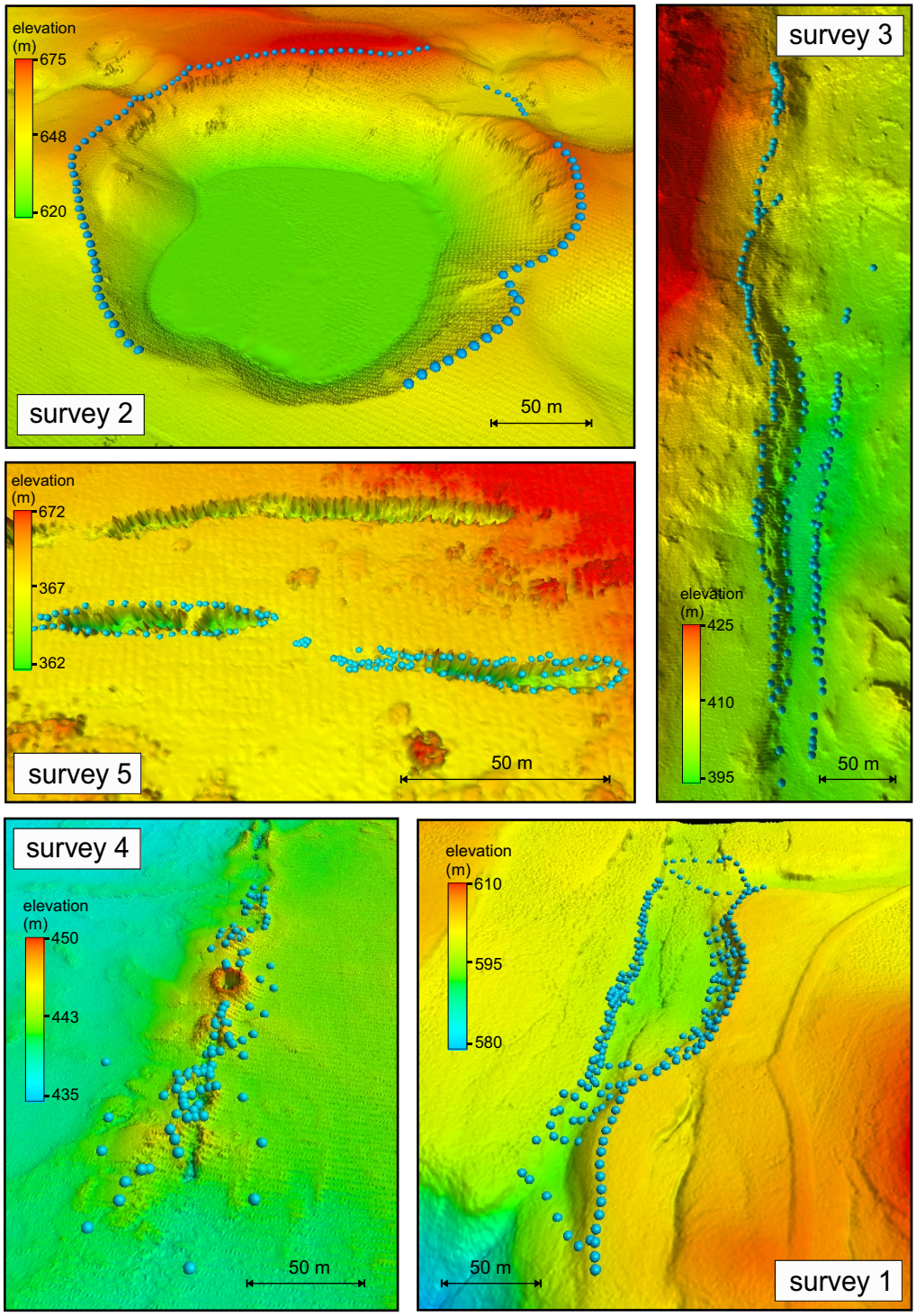

Figure 3.18: The dGPS surveys (points acquired in theses surveys are shown as blue circles) shown superimposed on the LiDAR surface at the same easting/northing locations.

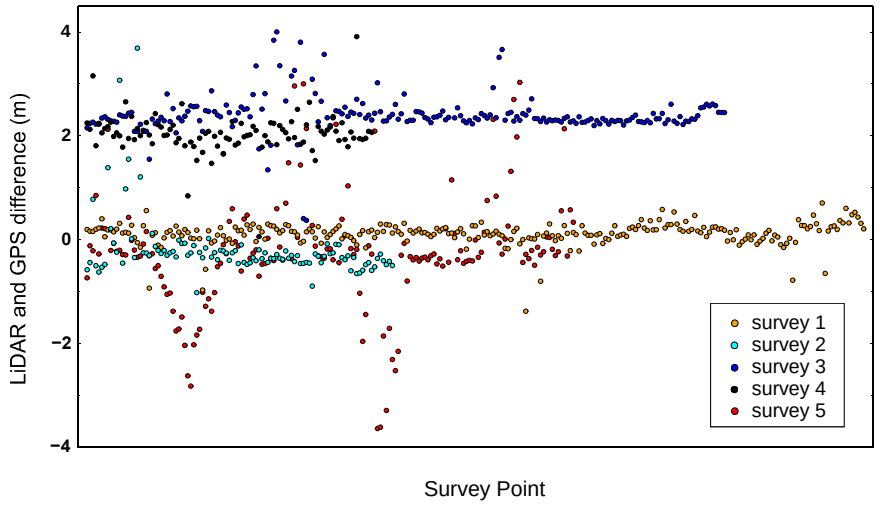

Figure 3.19: Plot of difference between GPS elevation measurements and elevation extracted from the LiDAR DEM for the same northing/easting position.

appears to be a systematic error of ∼2 m. This error is highlighted in figure 3.19 which shows the difference between the dGPS and LiDAR DEM elevation values for the same location. Survey 3 and 4 were acquired on the same day and as the other surveys do not show a similar systematic error, this error could be due to incorrect correction for the antennae height of either the base station or the roving station (which is ∼2 m). Allowing for correction of the systematic error it can be seen that the dGPS data ties in well with the LiDAR data.

Figures 3.20b and 3.21b show scatter plots for each survey with LiDAR elevation plotted against GPS elevation. In surveys 1-4 the scatter plots show very little scatter in the point distribution with points showing a 1:1 relationship between LiDAR and GPS with only a small deviation in the distribution.

Using the variation in the differences between the dGPS and LiDAR DEM elevation values I have calculated the mean difference values and their standard deviations are shown in the table 3.1. Assuming a systematic error of +2 m in survey 3 and 4 and adjusting the mean elevation difference accordingly, the dGPS and LiDAR surveys have a mean elevation difference of 0.05 m with a mean standard deviation of 0.61 m.

Some points from the dGPS survey do not have a good tie with the LiDAR DEM,

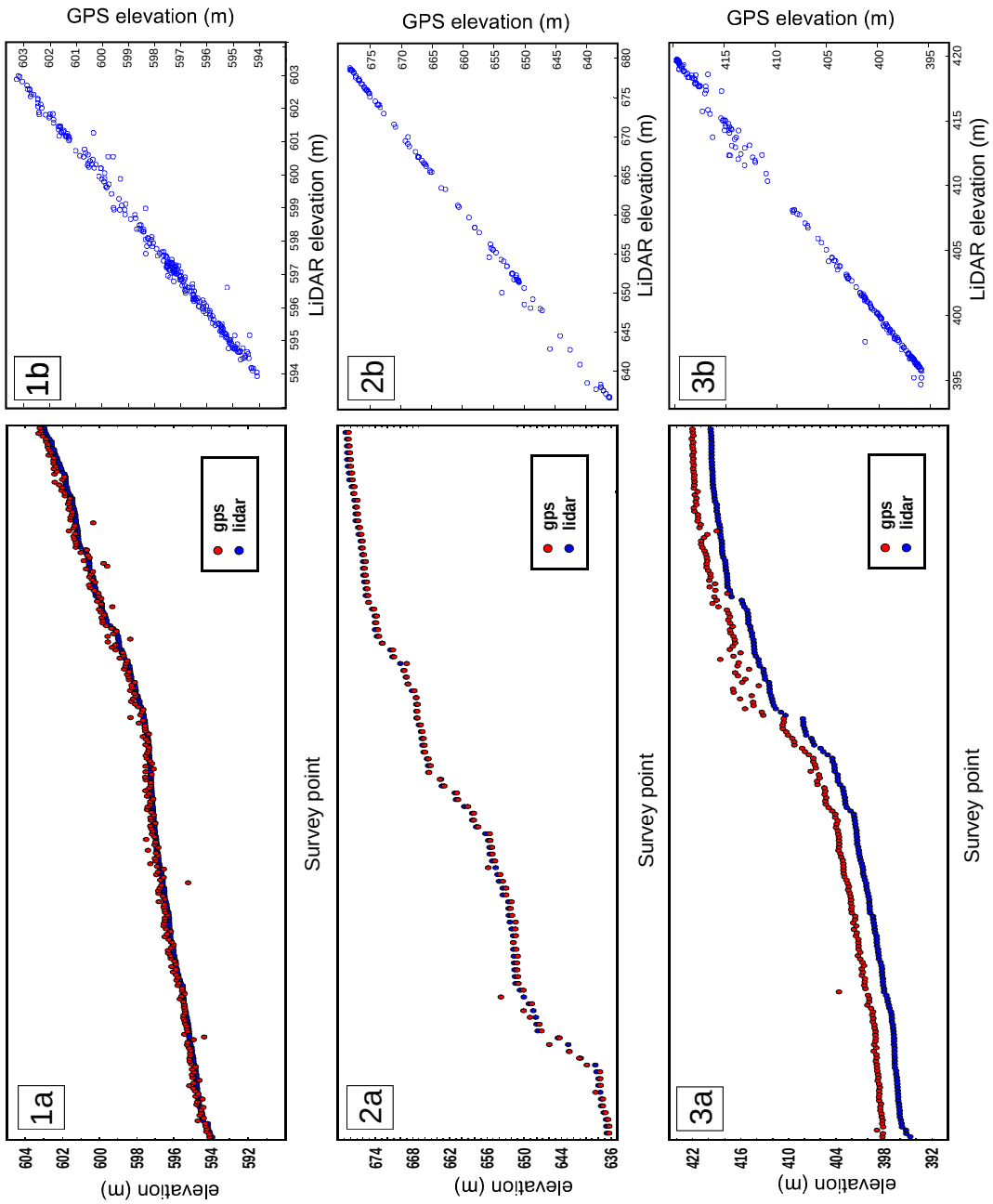

Figure 3.20: a) The dGPS elevation data for surveys 1-3 (shown in red) acquired in the field plotted alongside the elevation extracted from the LiDAR DEM (shown in blue) for the same northing/easting position (sorted by LiDAR elevation). b)
scatter plot of LiDAR elevation vs GPS elevation for each point in the GPS survey (and the corresponding LiDAR point at the same northing/easting location).

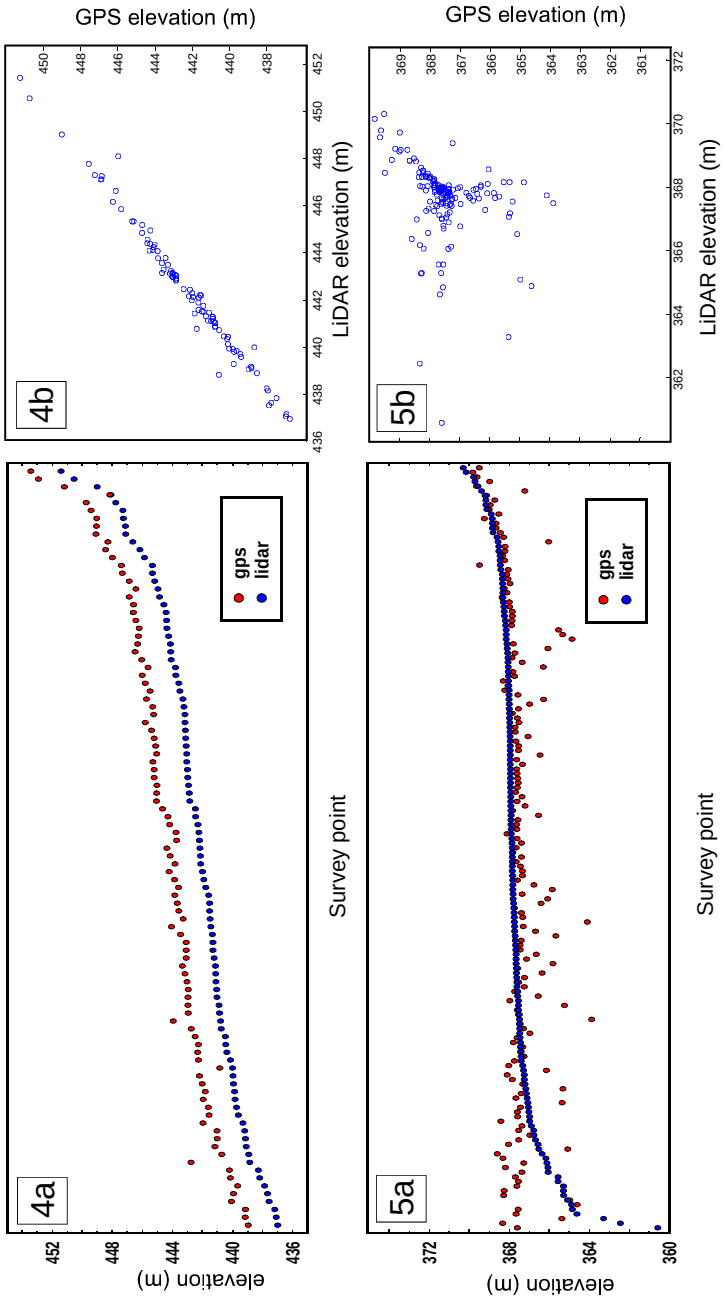

Figure 3.21: a) The dGPS elevation data for surveys 4-5 (shown in red) acquired in the field plotted alongside the elevation extracted from the LiDAR DEM (shown in blue) for the same northing/easting position (sorted by LiDAR elevation). b)
scatter plot of LiDAR elevation vs GPS elevation for each point in the GPS survey (and the corresponding LiDAR point at the same northing/easting location).

Table 3.1

dGPS survey	mean elevation difference (m)	standard deviation (m)	range of elevation difference min|max(m)
1	0.1170	0.2220	-1.3760 | 0.7060
2	-0.1880	0.6288	-1.0220 | 3.6850
3	2.4446	0.5098	0.3720 | 5.6510
4	2.0370	0.3897	0.0600 | 3.9100
5	-0.1598	1.3218	-3.6360 | 7.0030

with a maximum difference in elevation of ∼7 m observed in survey 5. The majority of points exhibiting large discrepancy are those measured very close to or on a rapid elevation change, where any error in the horizontal position of the dGPS coordinates would be most apparent as a mismatch in elevation values. Survey 5 shows the largest size and number of elevation mismatches, as this survey was taken around the edges of a deep fissure with a rapid cut-off at the fissure edges, these mismatches are most likely due to small errors in the horizontal coordinates rather than any underlying issue with the LiDAR data.

In the next two chapters I will primarily use the LiDAR DEM to measure fault length and displacement. This requires that the DEM provides a high level of relative accuracy between points on the fault (i.e. does not depend on the accuracy of the LiDAR DEM with respect to regions outside the LiDAR survey area). As the relative accuracy of the GPS points in a dGPS survey is very high, the low standard deviation between the LiDAR and GPS points signifies a corresponding level of relative accuracy in the LiDAR data.

Chapter 4

Fault Growth

4.1 Introduction

This study will consider the behaviour of the faults in the Krafla fissure swarm, attempting to identify a pattern in the growth of a fault from fissure to classically shaped fault. The resulting pattern will be presented as a model that acts as a preliminary phase of fault growth not accounted for in the published fault growth models.

Models of fault growth often consider the evolution of a fault only once it has achieved a classical fault shape (as shown in figure 4.1a) where the fault has zero vertical displacement at its tips with a gradual increase to a maximum vertical displacement, D_{max}, at the midpoint of its length, L. However, a large proportion of the faults I have measured in the Krafla fissure swarm retain often significant regions of fissure-like features that have very little vertical displacement (e.g. figure 4.1b). Observations of rifting during the Krafla Fires (Björnsson et al., 1979, Einarsson and Brandsdottir, 1978, Tryggvason, 1980, 1984) showed that many of the fractures in Krafla initiate as horizontal surface opening caused by dyke intrusion and evolve into structures with vertically displaced slip surfaces during subsequent rifting events.

There a three types of fracture, illustrated in figure 4.2, which can be separated into shear fractures (with slip surfaces) and extension or opening fractures (fissures, joints and veins). Extension fractures are fractures that show extension perpendicular to the walls and when they are filled with air or fluid they are referred to as fissures - a magma filled fracture is classified as a dyke. The fractures observed at the surface in Krafla are usually extensional fissures.

Fracture growth can be classified in the three different modes (see figure 4.3): Mode

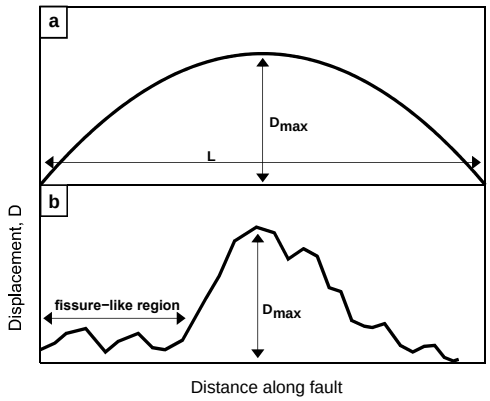

Figure 4.1: Shows a) the classic fault shape, with zero displacement at fault tips gradually increasing to maximum vertical displacement at the fault centre, b) an example of a fault in the Krafla fissure swarm, where regions of the fault exhibit fissure-like features that have very little vertical displacement.

I where there is extension of opening perpendicular to the crack, Mode II is slip (shear) perpendicular to the edge and Mode III is slip parallel to the crack (Fossen, 2010). It is possible to get a combination of these growth modes along a fracture and these are referred to as hybrid fractures. In order to move from a fracture structure to a faulted structure the fracture must acquire a slip surface.

The fractures in the Krafla fissure swarm show that vertical extension is acquired on fissures in the region, with a large number of structures that have a combination of faulted and fissure-like features along their length. Fossen (2010) considers vertically displaced fissures formed from open extension fractures in basalt in the Thingvellir fissure swarm, Iceland. Fossen (2010) suggests that the vertical displacement indicates a connection with underlying faults - this would be reasonable in Krafla as the extensional fractures are generally caused by dyking (e.g. Björnsson, 1985, Buck et al., 2006).

Shipton and Cowie (2001) identify that a measurable throw only occurs on a fracture once a through-going slip surface has developed. An illustrative model by Shipton and Cowie (2001) shows the development of a through-going slip-surface in sandstone and the consequent vertical displacement (see figure 4.4). Shipton and Cowie (2001) discuss the development from initial short, discontinuous slip-surface segments through to a single through-going slip surface that would allow an increase in throw.

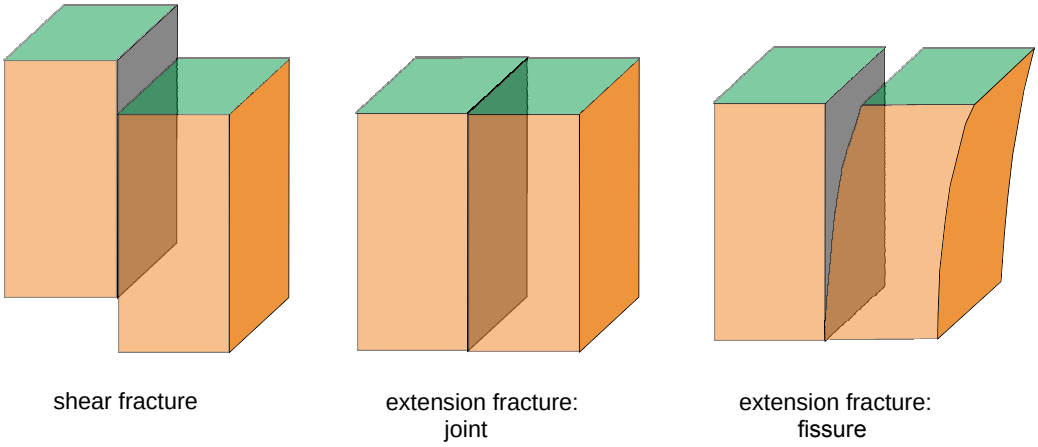

Figure 4.2: Illustration of the three types of fracture (redrawn from Fossen (2010).

There are two widely accepted models for fault initiation and growth (Kim and Sanderson, 2005): 1) a fault is a single smooth continuous surface of displacement discontinuity becoming larger as slip increases (e.g. Walsh and Watterson, 1987, Cowie and Scholz, 1992a) and 2) faults grow primarily by the linkage of individual segments (e.g. Peacock, 1991, Cartwright et al., 1995, Kim et al., 2000).

For model 1) there are several key examples that examine the relationship of D_{max} to L for faults growing in isolation, showing either an increase with L as D_{max} increases, such as shown in figure 4.5a, or maintaining a constant L as D_{max} increases, as shown in figure 4.5b, Walsh et al. (2002). The type 1) models have been developed further to account for fault growth by linkage (type 2 models) ((e.g. Peacock and Sanderson (1991),Cartwright et al. (1995)), where the initial growth of each component part of the linked fault is assumed to follow the growth models of faults in isolation up to the point that the stress accommodation between two faults is initiated and fault linkage occurs.

4.1.1 Fault Growth

A relationship between fault length, L, and displacement, D was proposed by Watterson (1986), which implies a description of fault growth over geologic time of the form:

$$D \propto L^n \tag{4.1}$$

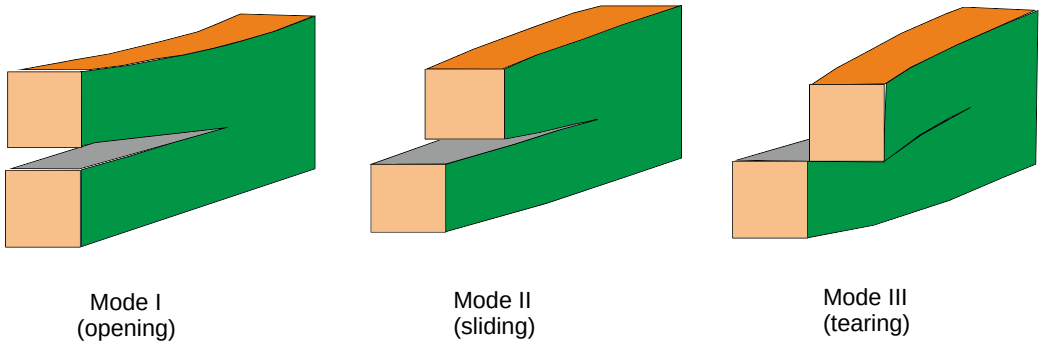

Figure 4.3: Illustration of the three types of fracture growth.

where n has been found to have a value between 1 and 2, with published results giving n=2 (Watterson, 1986, Walsh and Watterson, 1988), n=1.5 (Marrett and Allmendinger, 1991, Gillespie et al., 1992) and n=1 (Gudmundsson, 1992, Dawers et al., 1993). A summary of these results was made by Cowie and Scholz (1992a), in which it was acknowledged that the previous findings had come from a variety of settings, usually each from a single rock type, all of which would have its unique effect on the fault behaviour. Cowie and Scholz (1992b) proposed a model that accounts for differences in rock type and tectonic environment resulting in a varying constant of proportionality and a linear scaling relationship between D and L:

$$D = \frac{C(\sigma_o - \sigma_f)L}{\mu} \tag{4.2}$$

where μ and σ_o are the shear modulus and shear strength of the surrounding rock, σ_f is the frictional shear stress on the fault. The constant of proportionality, C, is dependent on the ratio $(\sigma_o - \sigma_f)/\mu$, in which both σ_o and μ vary with lithology and σ_o, σ_f and μ all vary with confining pressure.

The majority of individual study areas are usually restricted by a number of factors that cause bias to the results: (i) fault size range covers less than two orders of magnitude ; (ii) study area is within a particular rock type and tectonic setting, and (iii) only a small number of faults are measured. Gillespie et al. (1992), noted that these biases, along

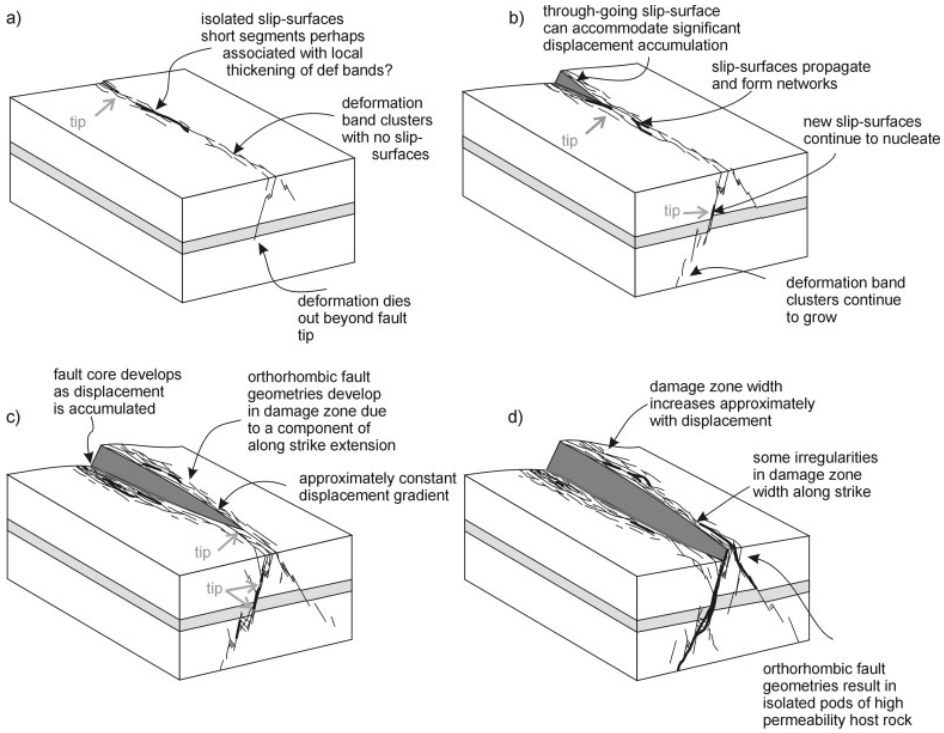

Figure 4.4: Illustration from Shipton and Cowie (2001) shows the evolution of a fault in the same block of rock through time. Illustration is based around the evolution of a fault in sandstone. Reprinted from Journal of Structural Geology, Vol 23, Shipton and Cowie (2001), Damage zone and slip-surface evolution over μ m to km scales in high-porosity Navajo sandstone, Utah, 1825-1844, ©(2004), with permission from Elsevier.

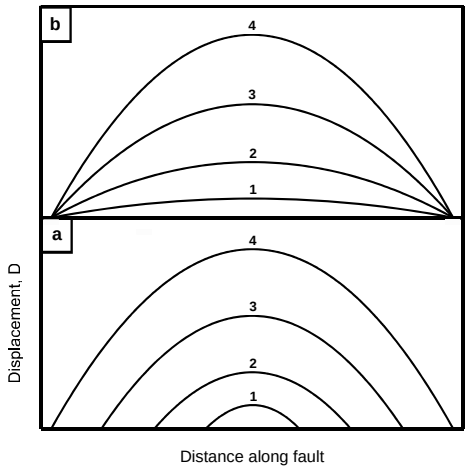

Figure 4.5: Some simplified fault growth models.

with differing errors in data acquisition, would introduce complications in identifying a simple D/L relationship when combining the individual studies as one large dataset. Ideally, to fully understand this relationship, a study of a large sample of faults, across the full range of fault size (from ∼1 mm to 100 km), in single tectonic and rock setting, would allow a more informed understanding of the D/L relationship.

A study by Bailey et al. (2005), using a 1300 km^2 fault map obtained from mined coal seams in the East Pennine Coalfield, allowed for the study of 7862 faults, with throws ranging from <1 to 180 m and lengths from 10 m to 16 km. The faults in the Bailey study were sampled at ∼100 m intervals for throw values. A proportion of the faults had low to no recorded throw values, these faults all being <200 m in length, and it was inferred that faults with trace length of less than 200 m were unlikely to have a maximum throw >50 cm, a value below the resolution of the map. The resulting maximum throw data allowed for an estimation of n∼1.22.

I have measured the length and displacement along 775 faults using the 0.5 m resolution DEM. I was able to pick a range of fault lengths covering three orders of magnitude, ∼10 m to ∼2000 m, and I used a sampling rate of between 2-5 m. Contrary to Bailey et al. (2005) it was found that many faults with lengths <200 m achieved a maximum throw >50 cm and these smaller faults have been included in the study.

4.1.2 The Krafla Fissure Swarm

The Krafla rift zone consists of the Krafla central volcano and caldera, and the fissure swarm that transects it (see figure 4.6b). The Krafla central volcano is the result of repeated eruptions, with the oldest measureable formations dated at around 200,000 years old (Saemundsson, 1991). The caldera formed during the interglacial period about 100,000 years ago, with the majority of ∼35 Holocene eruptions occurring in either the central caldera region or further south around Namafjall (Björnsson and Saemundsson, 1977). The fissure swarm is a 5-10 km wide and 100 km long region containing numerous eruptive fissures, faults and cracks (Hjartardóttir et al., 2012). Study area 1 (figure 4.6c) lies to the north of the main caldera and is dominated by a large lava shield, created by the eruption of the Theistareykir volcano to the west of the Krafla fissure swarm around 10,000 years ago. The area is characterised by large fissures and faults, many of which can be seen to cut straight through the shield layer. The most recent episode of magmatic rifting, the Krafla Fires, took place over a series of events between 1975-1984

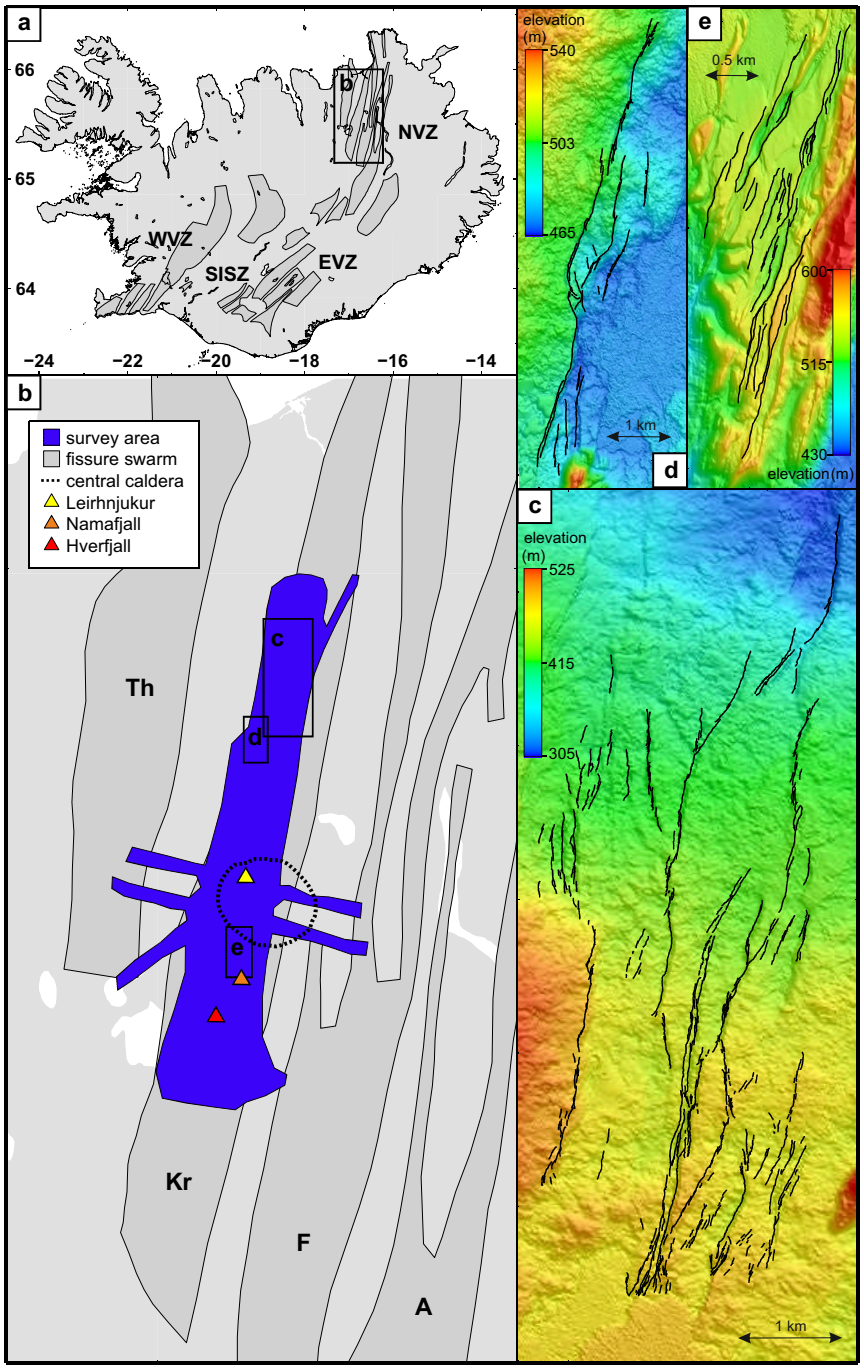

Figure 4.6: Map of Iceland denoting the 4 major zones, NVZ (Northern Volcanic Zone), EVZ (Eastern Volcanic Zone), SISZ (Southern Iceland Seismic Zone) and WVZ (Western Volcanic Zone). b) Shows the Krafla fissure swarm (Kr) and the survey area with surrounding NVZ fissure swarms Askja (A), Fremrinámar (F) and Theistareykir (Th). Boxes c), d) and e) show the faults picked and used for analysis in this study.

(e.g. Einarsson and Brandsdottir, 1978, Brandsdottir and Einarsson, 1979, Tryggvason, 1980, Opheim and Gudmundsson, 1989), where activity propagated mainly northwards after initiating at Leirhnjúkur in the central caldera.

The main structural features in the fissure swarm range from pure extension (tension) fractures through to well-developed normal faults. The main region of deformation is largely confined to a central zone of fissures, commonly flanked by normal faults forming a graben structure with steeply dipping exposed fault planes (Opheim and Gudmundsson, 1989, Gudmundsson, 1984). The fissure swarm consequently forms a set of graben structures with the central graben extending from north of Hverfjall up through the central caldera (Angelier et al., 1997) towards the coast, with the density of faults and fissures decreasing with increasing distance from the central caldera (Hjartardóttir et al., 2012). The larger faults in the Krafla fissure swarm have been active over many thousands of years, typified by the faults around study area 1, the result of numerous rifting events such as the Krafla Fires, rather than one single large event. Björnsson and Saemundsson (1977) concluded that a major rifting event occurs every ∼100 years in the NVZ, affecting only one of the five rifting segments per episode, giving on average an event every 500 years in each fissure swarm. With the 10,000 year old surface in study area 1, major faults could therefore be the result of ∼20 individual rifting events.

It is thought that the faulting in both submerged and emerged spreading ridges are driven by dyke propagation (e.g. Buck et al., 2006). Direct observation of this was possible during the 1975-1984 Krafla Fires rifting episode with around 20 individual diking events exhibiting effects on both the existing fault structures and in creating new structures (e.g. Opheim and Gudmundsson, 1989, Björnsson and Saemundsson, 1977, Einarsson, 1991a) resulting in a total crustal extension of ∼9 m and vertical deformation of ∼2 m (Björnsson et al., 1979, Tryggvason, 1984). Brandsdottir and Einarsson (1979) proposed that earthquake swarms observed during each individual diking event represented the movement of magmatic material below the surface. The majority of these were seen to propagate laterally from the central caldera at a rate of 1 to 2 m/s from the central magma source (Brandsdottir and Einarsson, 1979, Wright et al., 2012), which lies under the central caldera at depths of ∼3 km (Einarsson and Brandsdottir, 1978, Brandsdóttir et al., 1997, Tryggvason, 1980).

Opheim and Gudmundsson (1989) measured the length and strike of 1,083 fractures in the Krafla region using aerial photographs and maps. They defined normal faults as

those that had achieved a vertical displacement of >1 m and their results suggested that a fault needed to achieve a length of >∼200 m before any such vertical displacement occurred. They measured a total of 8 faults in the field, ranging from 350-3500 m with throw and width measurements made every ∼50 m (faults measured in aerial photographs were sampled every ∼25 m). They noted that pure tension fractures were the most common form of fracture in the Krafla fissure swarm and although some were associated with faults, either parallel to or branching off from them, many others appeared in isolation from main faults.

4.2 The fault dataset in Krafla

Typically the faults and fractures in Krafla did not present as simple standalone structures but as groups of often complex segmented structures. Combinations of fissures, faults and horsetail fractures at the end of large faults, with semi-breached relay ramps, rock collapses, debris and monocline structures on the hanging wall all made identification of individual structures problematic

Monocline structures were frequently a barrier to identifying the bottom cut-off of the fault. Figure 4.7 shows two examples of monocline structures in the Krafla fissure swarm. Figure 4.7a shows a long fault in the southern part of the fissure swarm, between Lake Myvatn and the Hverfjall tuff ring. This particular monocline structure has caves underneath it that contain geothermally heated pools. Figure 4.7b shows a fault typical of the large faults in the fissure swarm north of the caldera. The faults I picked and measured for this chapter were mainly in this region and the majority of larger faults in this region had monocline structures on the hanging wall. The throw for the faults in these situations was measured around the base of the monocline and projected back to the fault to give a value of throw on the fault. This particular fault was not used in the study as the far end of the fault lies underneath the 1984 lava flow (just visible in the far horizon).

Debris and collapsed structures at the bottom of the footwall on many faults (see figure 4.8a) presented problems with identifying the bottom cut-off. As with the monocline structures, measurements were made at the base of the debris and projected back to the fault to calculate throw. Collapse and fracturing at the top of the fault, particularly on larger structures, added complexity to picking the top cut-off of a fault (see figure 4.8b). Typically I made measurements at the point just behind the fracture

Figure 4.7: Photographs of some monocline structures on large faults a) to south of the caldera and b) in the northern fissure swarm just north of the 1984 lava flow.

or collapse. Horse-tail splays at the end of large faults (figure 4.8c) present an issue with identifying the fault tip of the main fault. In this particular case the continuity of the main structure was very obvious in the field, but without the geological markers available in the field, much more difficult to identify in the LiDAR DEM.

Figure 4.9 presents a series of images of fissures in the Krafla region. Fissures a) and d) are both in the far south of the fissure swarm. Figure b) is a fissure that extruded lava during the Krafla Fires - I was able to observe that the lava at the edge of the main lava flow had drained down into a fissure. Following this fissure for a distance showed the lava remerging as a seemingly seperate lava flow (see image in 4.9b).

Lava flows and extruded lava have prevented a number of large faults being included in the results, figure 4.10a shows the northern tip of the 1984 lava flow flowing into a series of large faults and fissures. Figure 4.10b shows lava extruded from fissures some distance away from the main lava flow.

Three examples of fault picks using the surface in Petrel are shown in figures 4.11, 4.12 and 4.13 which show picking along a monocline structure, a still intact relay between two faults and two en echelon fissures respectively. The top cut-off picks are shown in red and the bottom cut-off picks are shown in blue.

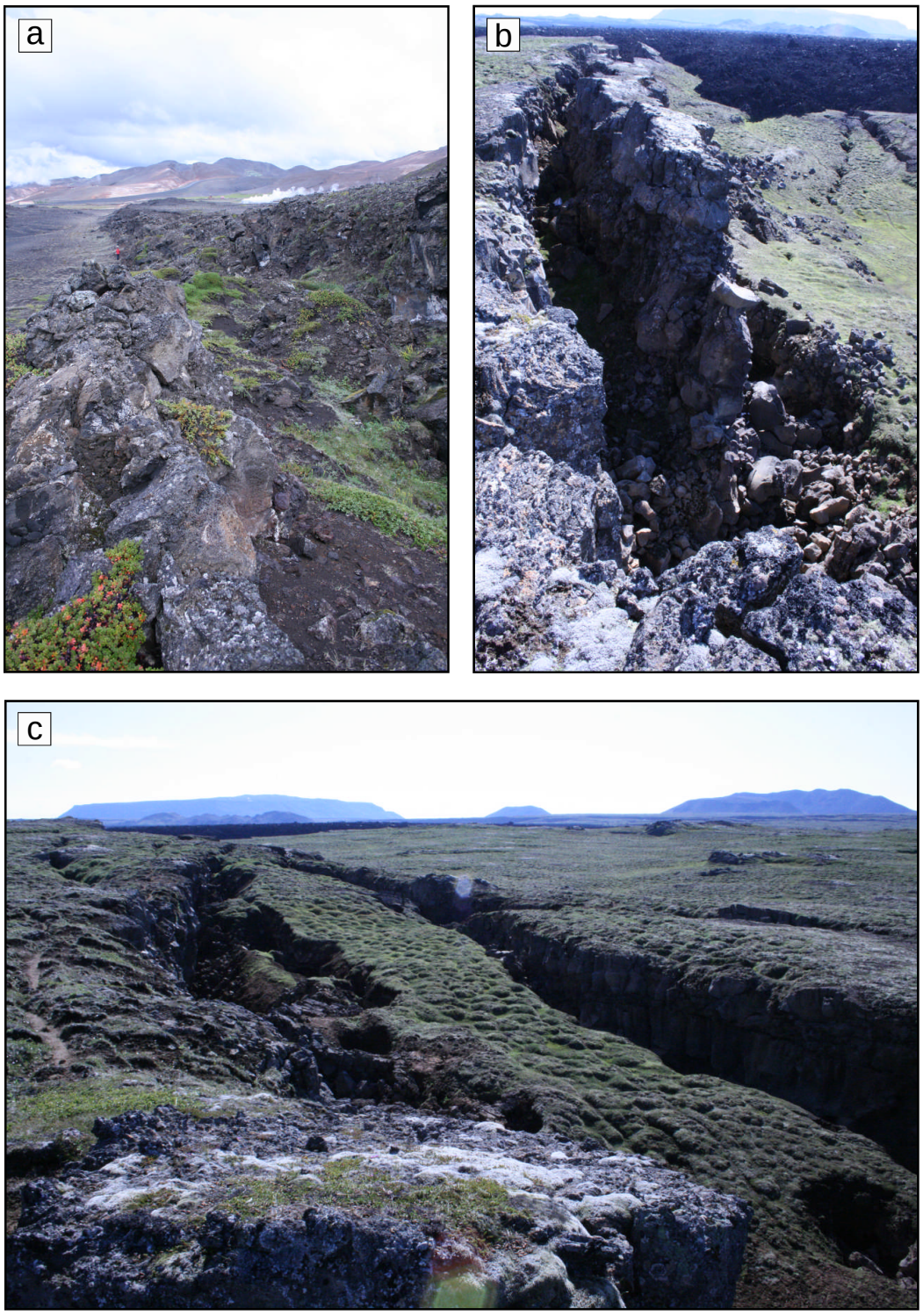

Figure 4.8: Photographs showing a) debris at the bottom of the footwall b) collapsing structure at the top of the fault and c) horse-tail splay at the end of a large fault.

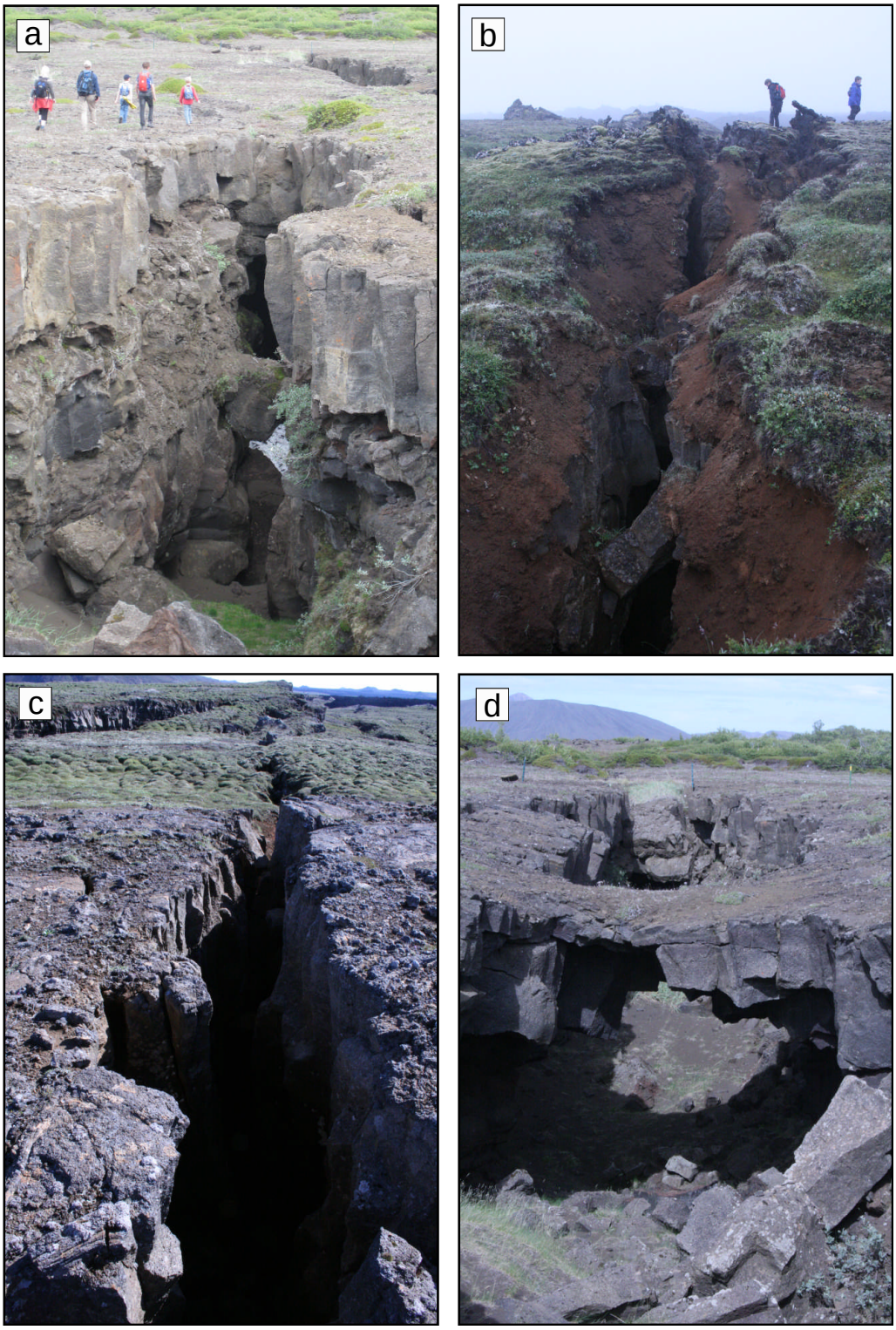

Figure 4.9: Photographs of 4 fissures in Krafla, a) and d) in the south of the fissure swarm and b) and c) in the north.

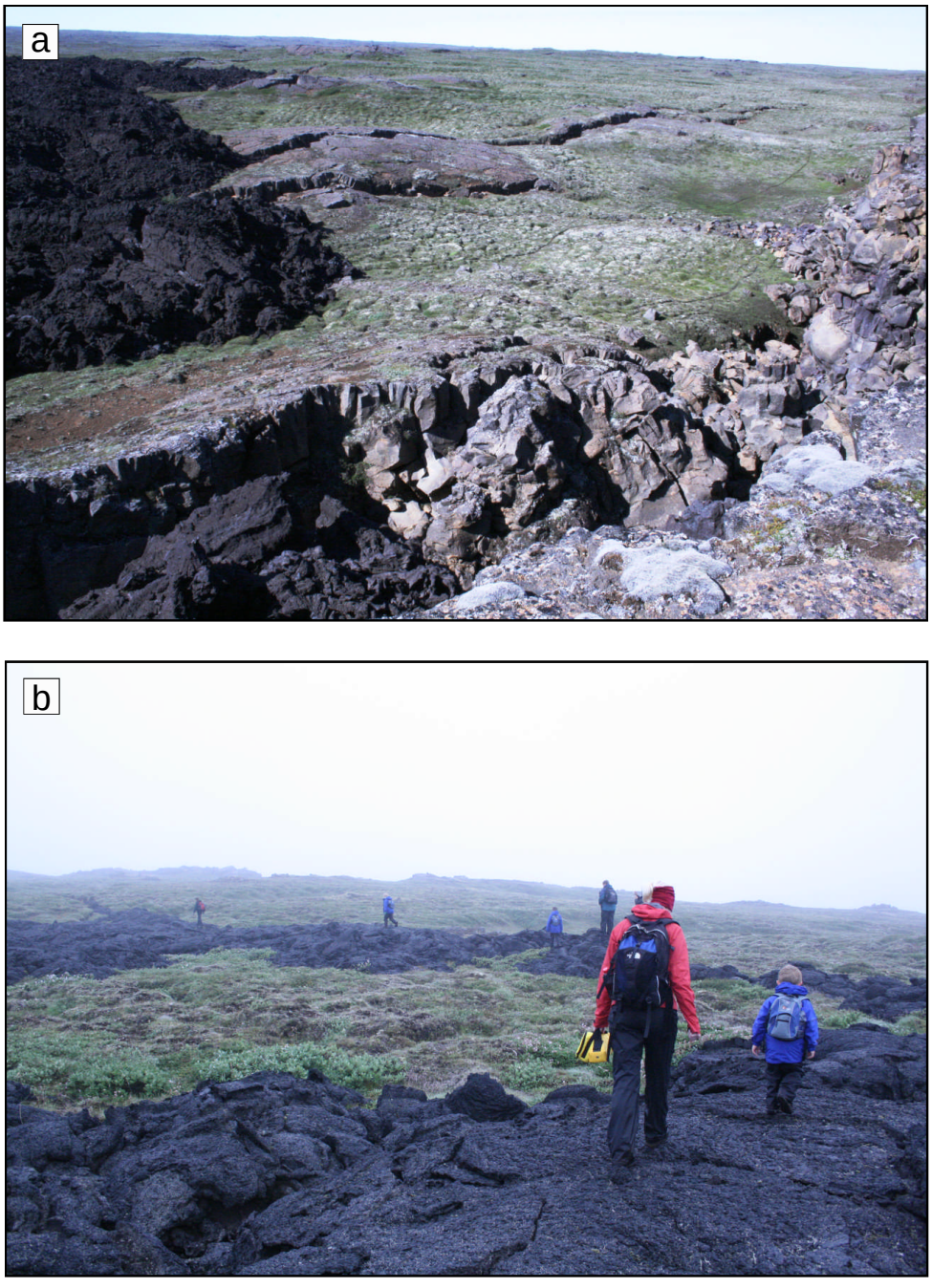

Figure 4.10: Photographs of lava a) flowing into and b) extruding out of fissures and faults.

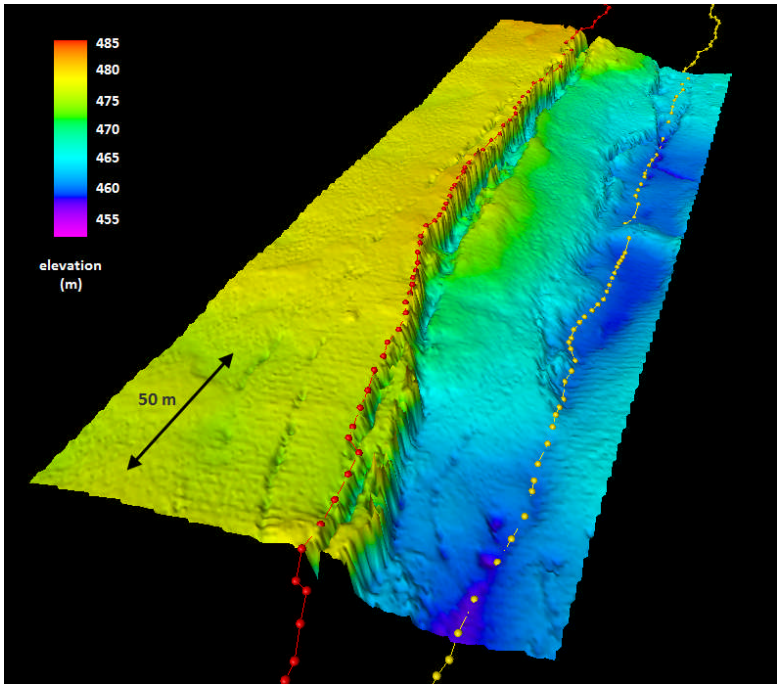

Figure 4.11: An example of fault picking along a monocline structure using the DEM produced in Petrel.

4.3 Fault Analysis - Length-displacement

The faults in the Krafla fissure swarm were analysed using the high resolution (optimally ~0.5 m) 1300 km^2 DEM created from the LiDAR point cloud discussed in the previous chapter. The high resolution of the dataset allowed for the detailed study of structures that would appear as single faults in lower resolution datasets, revealing a much more complex en echelon system of smaller faults, described as a segmented fault array by Walsh et al. (2003). According to Walsh these arrays start off as independent segments which, as they develop, interact kinematically with other structures to form a series of fault relay zones. The behaviour of these individual segments can be examined with the high resolution dataset and compared with the length-displacement of the array as a whole. A detailed study of the fault behaviour of a wide range of fault sizes across the Krafla fissure swarm has been made measuring the vertical displacement along 775 faults, with throws ranging from ~0.5-37 m, and lengths ranging from ~15-2,000 m. A map of the main group of faults picked is shown in figure 4.15

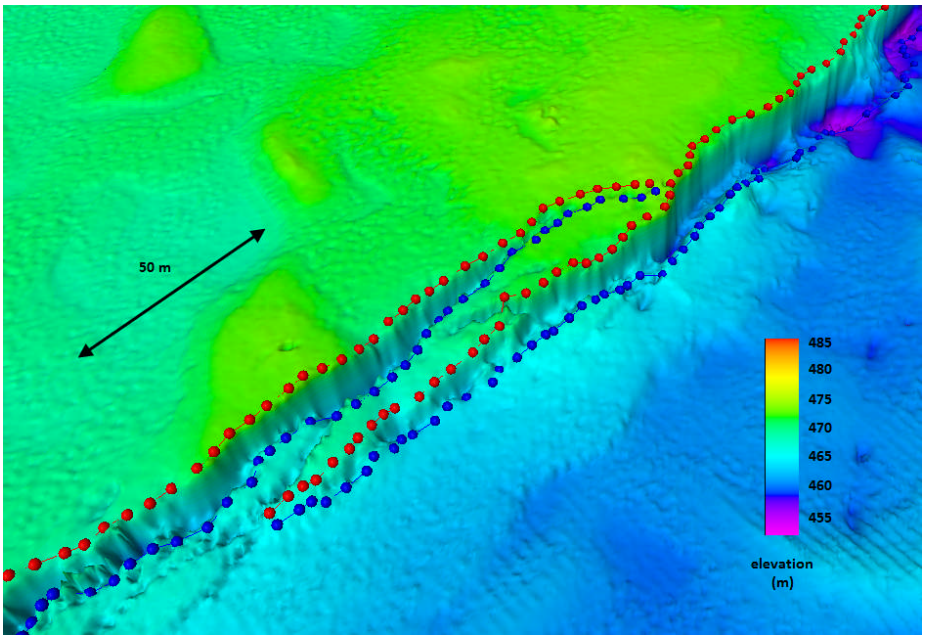

Figure 4.12: An example of fault picking along two faults separated by a barely intact relay ramp (made using the DEM produced in Petrel).

The faults selected for this survey are concentrated in a region of the fissure swarm north of the main caldera (see areas in figure 4.6c and 4.6d), an area on the eastern region of the caldera just north of the Viti crater and a region in the south of the main caldera (see figure 4.6e). Opheim and Gudmundsson (1989) suggested that the normal faults found in Krafla start off as a tension fracture and subsequently develop in to normal faults once they have attained a certain minimum depth and length, noting that most of the normal faults tended to grade into tension fractures at their ends, an indication of this evolution. To better understand if there is an evolutionary relationship between fissures with minimal vertical displacement and faults exhibiting large vertical displacements and classic length-displacement curves, I have identified and measured a full range of fault structures - from fissure to fully formed fault.

The fault data were extracted from the DEM using Schlumberger's Petrel software to both view the DEM in 3D and to manually pick the fault top and bottom cut-off points at ∼2-5 m intervals. Although Petrel does have the facility to perform fault prediction using a Rock Deformation Research (RDR) plugin, the complexity of the

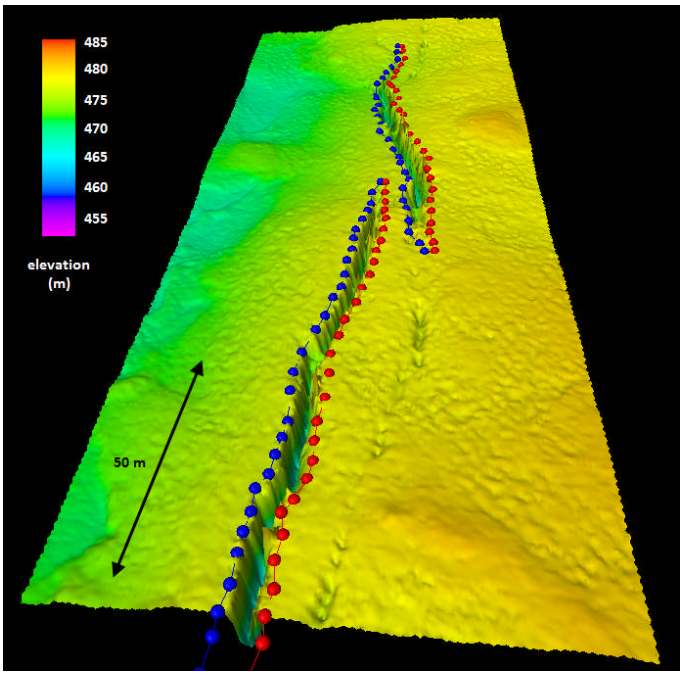

Figure 4.13: Showing picks along two en echelon fissures in the northern fissure swarm (made using the DEM produced in Petrel).

fault structures in the high resolution dataset made correct identification of both the fault tips and the true top and bottom cut-offs very difficult. As a result, all the fault picking was performed manually using the 3D rotation facility available in Petrel to examine complex regions as fully as possible.

The top edge of the fault was usually the most clearly defined and straightforward to locate, occasionally complicated by the presence of small fissures along the top edge or just behind the fault, as shown in figure 4.14a. For a profile through points A-A" in figure 4.14a and shown in figure 4.14a', the top pick on the foot wall was made behind the group of small fissures at point A", with a corresponding bottom-pick made at A. In this case, accounting for small amount of debris at the base of the fault, point A was picked at the point the hanging wall flattened out at the edge of the debris. A and A" were then used to calculate the throw, h, as shown in 4.14a'.

The bottom cut-off at the hanging wall was often less easily defined, obscured by features such as well formed slab-like monoclinal structures that connect the foot wall to the hanging wall, as shown in figure 4.14b, through to heaps of fractured material at

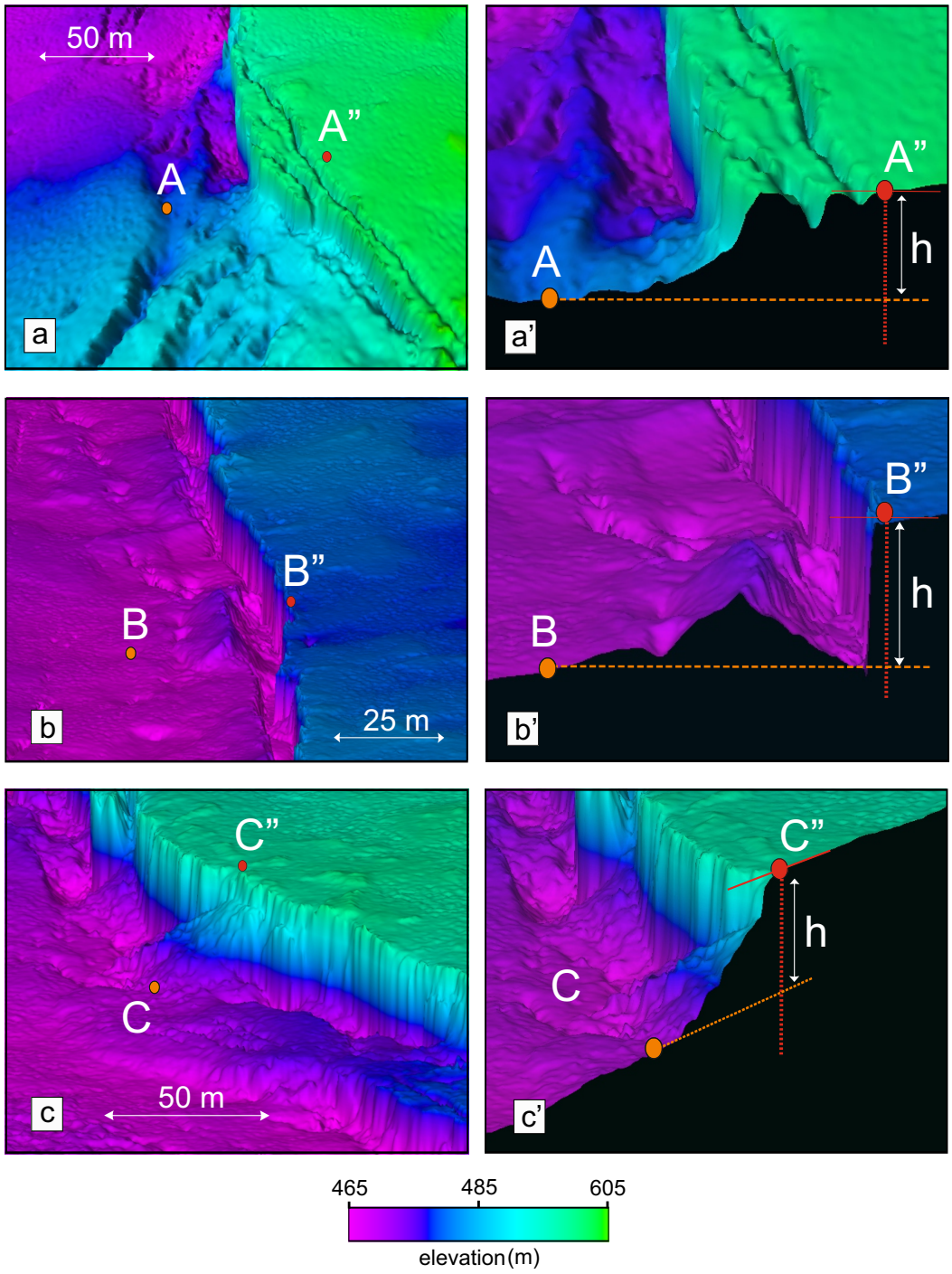

Figure 4.14: Some examples of physical issues that complicate picking. a) shows fractures at the top of the fault that hinder picking an exact cut-off for the top of the fault, the measured throw (h) between points A-A“ is shown in a’). b) shows large monocline structures on the hanging wall, the measured throw (h) between points B-B“ is shown in b’).c) shows debris from rockfalls obscure the cut-off for the bottom of the fault, the measured throw (h) between points C-C“ is shown in c’).

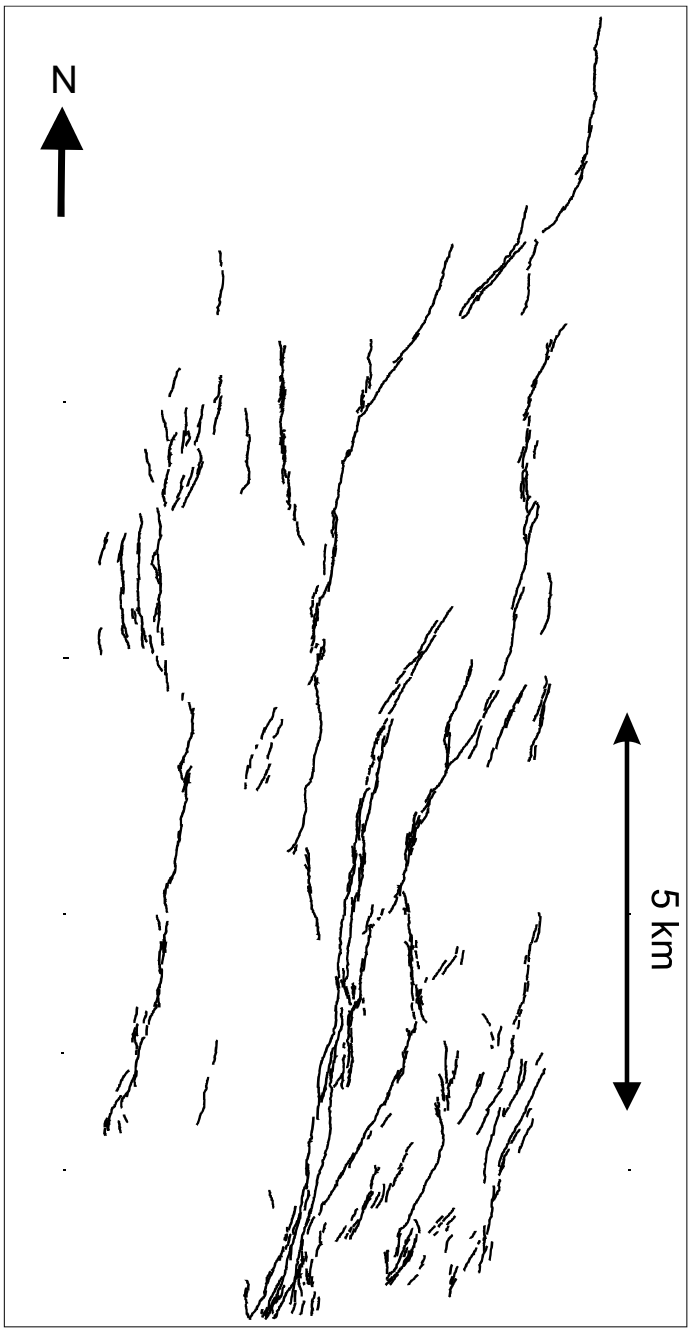

Figure 4.15: Map of the faults picked in the main region used for fault picking, to the north of the 1984 lava flow (location shown in figure 4.6).

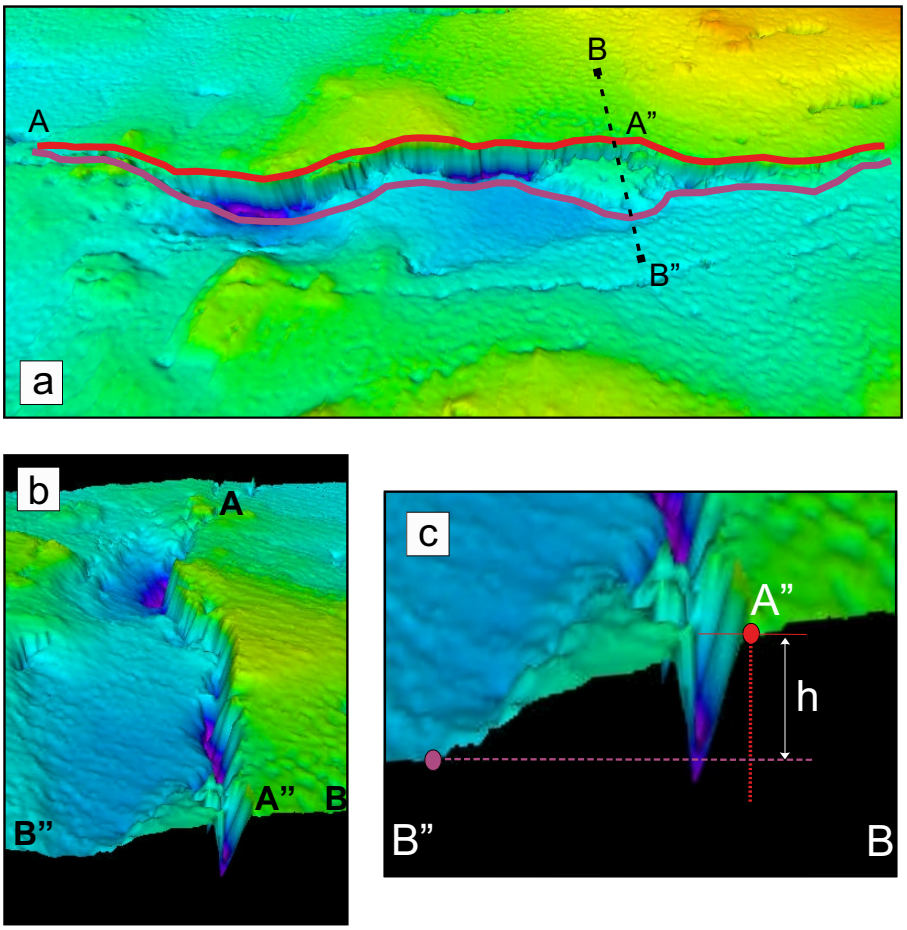

Figure 4.16: An example of fault picking in a) where the top and bottom cut-offs of the fault are shown by the red and purple lines respectively. The along-fault view is shown in b) with the cross-section B-B“, passing through a pile of debris at the footwall, at the bottom of the image. B-B” is shown in the schematic in c) showing the top and bottom picks (as red and purple circles) and the calculated throw, h.

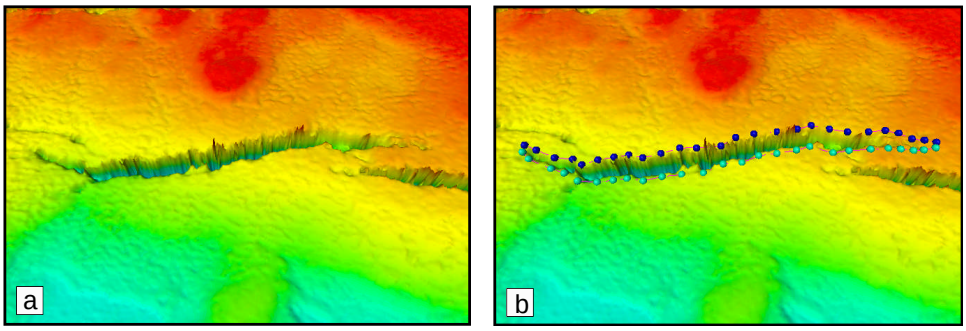

Figure 4.17: The mainly fissure-like (with very little vertical displacement) structure in a) is used to show how the faults have been picked. The top cut-off is picked (shown as blue circles in b)) followed by picking the corresponding bottom cut-offs, resulting in the same number of picks top and bottom.

the foot of the fault, shown in figure 4.14c. In these scenarios a pick was made at the lowest point of the monocline (as shown in figure 4.14b' at point B) or debris (as shown in figure 4.14c' at point C) and extrapolated in to the footwall to calculate throw, h. Figure 4.16 shows a fault with the top cut-off in red and the bottom cut-off shown in purple. It can be seen here that the bottom pick has taken into account the pile of rock debris (located at A") by picking a path around the base of the rock pile. The along-fault profile, from A-A", is shown in figure 4.16b with the cross-section through the rockfall, B-B", clearly evident at the bottom of the image. This cross-section is represented in the schematic in figure 4.16c, showing the bottom pick (purple circle) being extrapolated back to calculate the throw, h, of the fault. The process of picking the top and bottom cut-off points was repeated every ~2-5 m along the length of each fault to produce the full fault profile and extract the corresponding throw values.

An example of the process of fault-picking can be seen in figure 4.17 which shows a simple structure with only small amounts of vertical displacement (a good example of a fissure-like structure). As the top cut-off of a fault is usually the more easily distinguished, the structures have all been picked by selecting points along the top cut-off first (shown as the dark blue circles in figure 4.17b). The bottom cut-off is then picked (shown as light blue circles), to make a pair of points each with a corresponding top cut-off point. Where possible the bottom pick was made to take in to account any strike-slip there might have been by following any structural ties that might be visible in the fault profile, although generally there was either very little strike-slip or it was

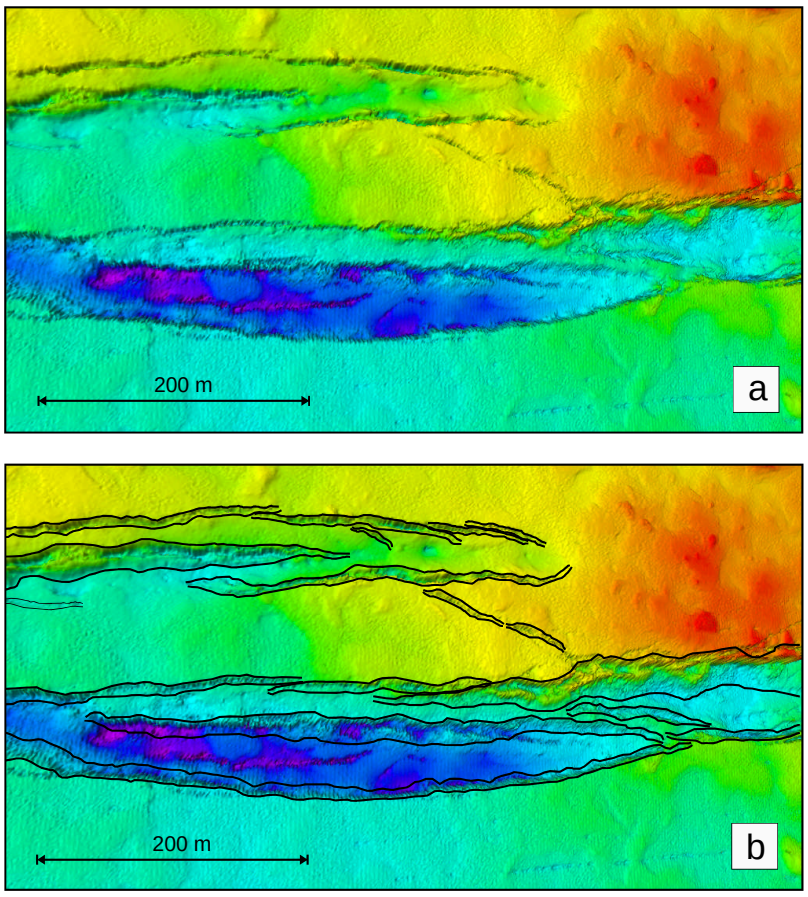

Figure 4.18: a) Shows an example of complex faulted structures in Krafla where normal faults form series of grabens and nested grabens 10s to 100s of m wide. The central graben floor is collapsed and riddled with smaller tension fractures and faulting. b) Shows the final picks for the top and bottom cut-offs of the faults (shown as black lines).

difficult to discern from the LiDAR data alone.

The high resolution data revealed the complexities of fault structure and interaction, often creating issues with the identification and definition of structural forms in the region. Many of the normal faults in the Krafla fissure swarm form series of grabens and nested grabens which can be 10s to 100s of m wide and in many the central graben floor is collapsed and riddled with smaller tension fractures and faulting (an example of this is shown in figure 4.18a with the final top and bottom cut-offs shown in figure 4.18b). With the width and complexity of these structures, it was problematic to distinguish between a large tension fracture and a faulted graben and assess at what stage they were at in evolving from tension fracture to normal fault. In the cases where the central volume had not collapsed and the resulting structure could obviously still be classified as a pure tension fracture, they were treated as such. In more complex evolved systems, the structures were interpreted as walls of a graben and they were measured as normal faults. It is possible that there is some misinterpretation due to incorrectly categorising these systems.

4.4 Results

Prior studies of the displacements of faults in this region have examined faults >200 m in length with a sampling rate every ~50 m. In Opheim and Gudmundsson (1989), normal faults are defined as fractures that have acquired a vertical displacement >1 m and their results indicated that a fracture had to attain a length of >200 m before any significant vertical displacement was found. With the 0.5 m resolution dataset a much higher sampling rate of between 2-6 m (with an average of 4.8 m) was used with z-axis data resolution accuracy of ~0.2 m, allowing for an examination of the displacement behaviour of much smaller fractures in an attempt to understand the relationship and evolution of fissures and fully formed faults. The length-maximum displacement data are shown in Appendix A, split into categories as discussed later in the chapter. The data have been compared with published length displacement data (e.g. Bailey et al., 2005) in figure 4.19.

Monte Carlo simulation about 21 points selected from the best fit linear relationship of the length/displacement data has been performed. The simulation calculated 100 possible random values for each point using a maximum error of 10 m in length and 0.5 m in displacement. This allows a comparison between the observed distribution of

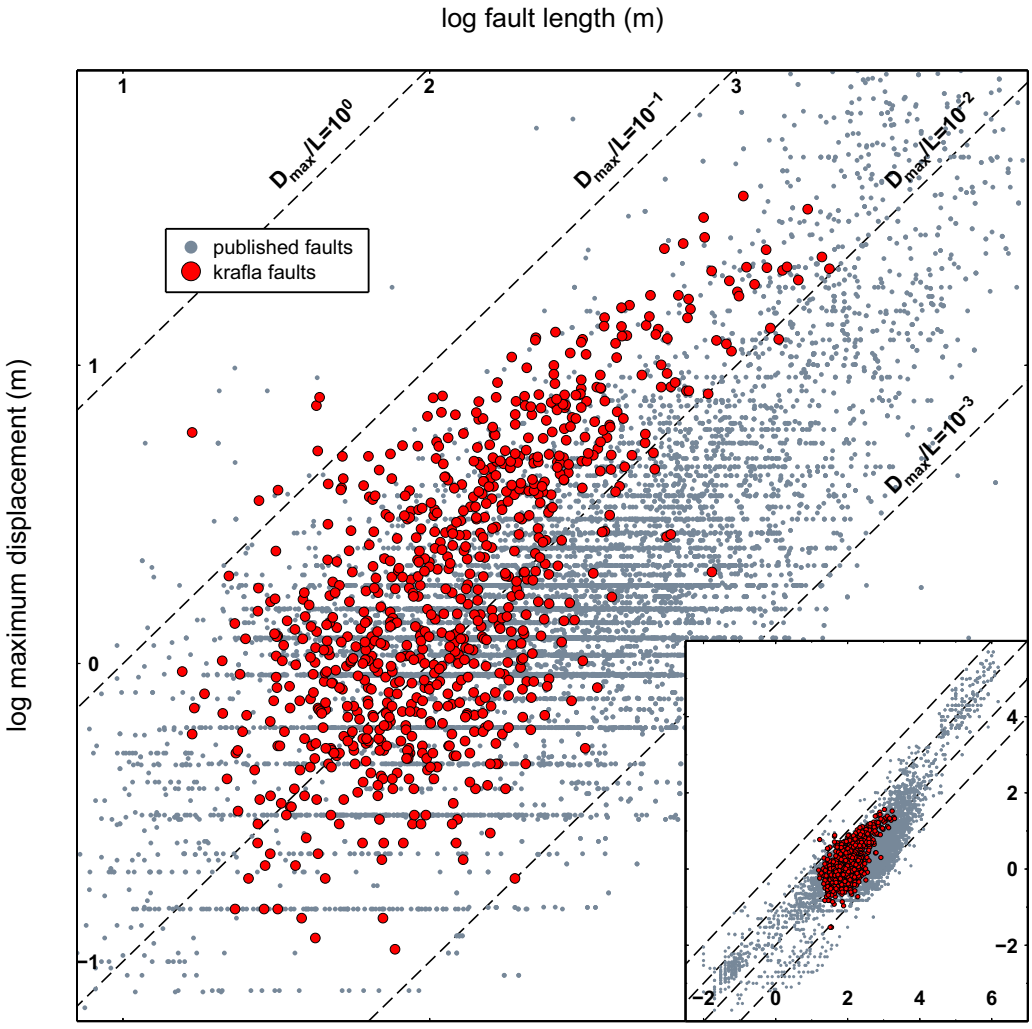

Figure 4.19: The Krafla fault length/maximum displacement data plotted along with published data from many sources (e.g. Aitkenhead et al., 1985, Villemin and SUNWOO, 1987, Opheim and Gudmundsson, 1989, Walsh and Watterson, 1988, Gillespie, 1991, Marrett and Allmendinger, 1991, Peacock, 1991, Gillespie et al., 1992, 1993, Dawers et al., 1993, Davison, 1994, Dawers and Anders, 1995, Cartwright et al., 1995, Jackson et al., 1996, Nicol et al., 1996, Schlische et al., 1996, Rowan, 1997, Fossen and Hesthammer, 1998, Bailey et al., 2005).

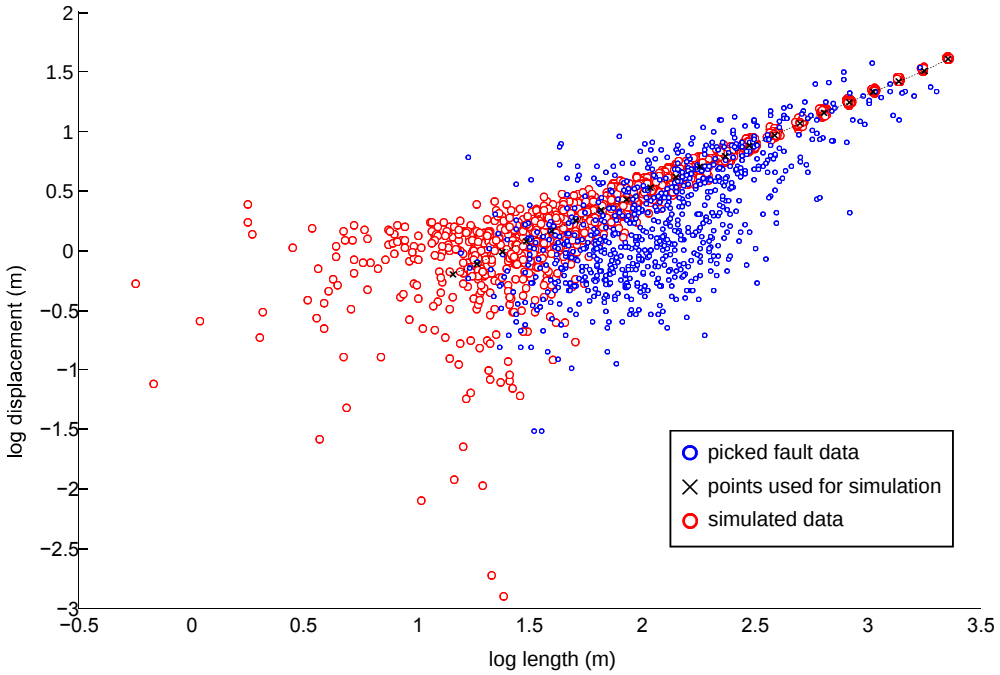

Figure 4.20: Comparison of distribution of the fault data (blue) with a simulated distribution calculated using monte carlo simulation using errors of 0.5 m for the displacement and 10 m for the length around points (black crosses) along the best fit gradient line of the picked distribution.

the picked length/displacement data with that produced as a result of measurement error (see figure 4.20). Whilst the distribution in the simulated data would account for some of the spread in the data (particularly for the smaller length/displacements) it is quite clear in figure 4.20 that the distribution is not entirely due to measurement error and that other factors account for the spread in the distribution.

To assess whether there is a pattern in the evolution of fissure to fault I have characterised each fault by the approximate percentage of its length/displacement profile that still exhibits a fissure-like appearance (here defined as the regions of the fault profile that have $\sim<1$ m vertical displacement). For this characterisation I have created 5 categories (as shown in 4.1: 1. 100% fissure - is a pure fissure, with the fault profile showing a fairly linear displacement along the fault with 100% of the displacement $\sim<1$ m (see figure 4.21b); 2. $\sim$75% fissure - has small regions ($\sim$25 %) of increased vertical displacement (see figure 4.21c); 3. $\sim$50% fissure (see figure 4.21d); 4. $\sim$25% fissure (see figure 4.21e) and 5. $\sim$0% fissure - the fracture is showing vertical displacement along

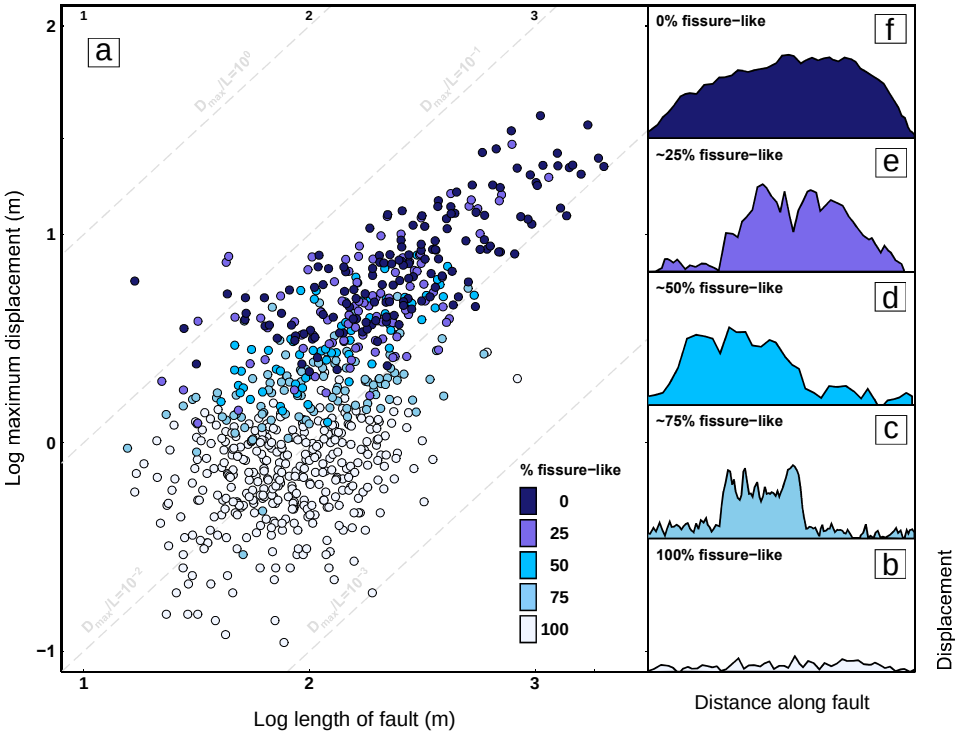

Figure 4.21: Shows a) The fault length vs maximum displacement for the full range of faults plotted with the fault length-displacement profiles categorised from 1-5, based on percentage of fault profile that is still fissure-like. Examples for categories 1-5 are shown in b)- f) respectively.

Table 4.1: Fault Categories

Category	% Fissure	Description
1	100	minimal vertical displacement across fault
2	∼75	∼ 25% of fault showing vertical displacement
3	∼50	∼ 50% of fault showing vertical displacement
4	∼25	∼ 75% of fault showing vertical displacement
5	0	vertical displacement across whole fault
5a	0	category 5 with classical fault profile
5b	0	category 5 with flattened fault profile
5c	0	category 5 with linked fault profile

its whole length, tending to zero displacement only at its tips (see figure 4.21f). The D_{max}/L for the Krafla dataset is shown in figure 4.21a with each of the faults coloured to show its respective category.

In addition, the fifth category (∼0% fissure) has been subdivided into three further groups as shown in figure 4.22. The subdivisions are 5a. where the displacement profile is smooth and represents the single fault profile (see figure 4.22b); 5b. the displacement profiles show large dips in vertical displacement along the profile (see figure 4.22c); and 5c. the displacement profile has a flattened appearance, with large regions of constant vertical displacement along its length (see figure 4.22d). The D_{max}/L of these subdivisions can be seen in figure 4.22a.

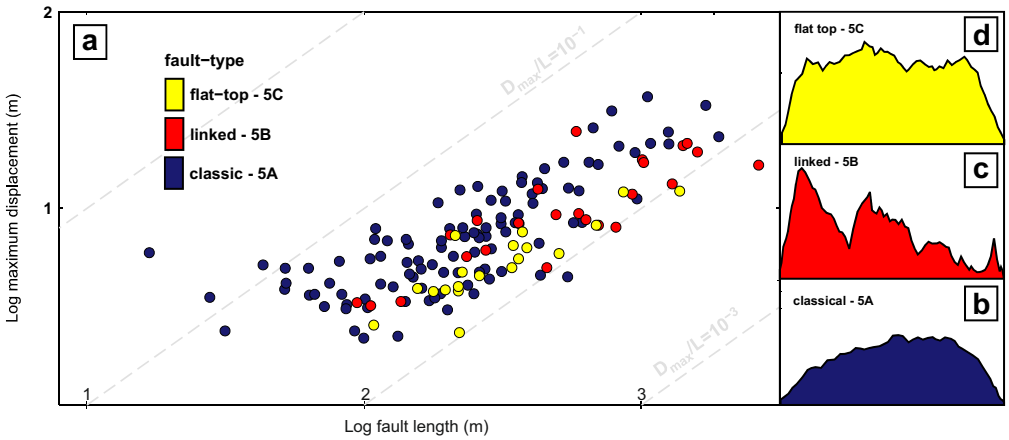

Figure 4.22: Category 5 faults are plotted in a) with a further three subdivisions for faults that have a profile with b) a classical fault shape, c) large dips in displacement across fault and d) large flat regions of high displacement.

The category 5b faults (containing large dips in the displacement profiles) are here

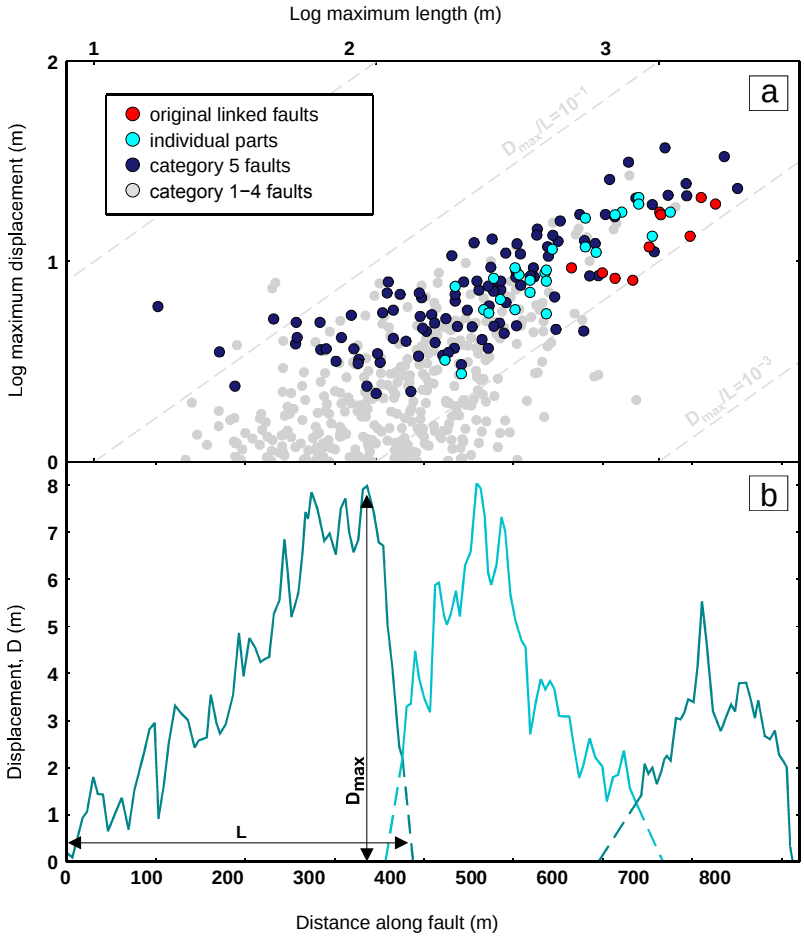

Figure 4.23: A selection of possible linked faults (red) have been broken down in to their possible original faults (cyan). The length/maximum displacement has been plotted for these shown alongside the category 5 faults (dark blue).

considered to possibly represent linked faults, where the dips represent the regions between the original faults that are in various states of linkage. The displacement profiles for a selection of these have been broken down in to their possible original fault segments (e.g 4.23), with each fault segment being extrapolated to represent the original fault profile with length L. The resulting D_{max}/L has been plotted in figure 4.23(cyan), alongside the linked faults (red) and the other category 5 faults (dark blue).

A location map of the faults is shown in figure 4.24 with each fault coloured to show its category. The northern area of the fissure swarm, as shown in figure 4.24a, shows a large proportion of faults presenting a displacement profile in the categories 1-4. Whereas the region just to the south of the main caldera, as shown in figure 4.24b, shows

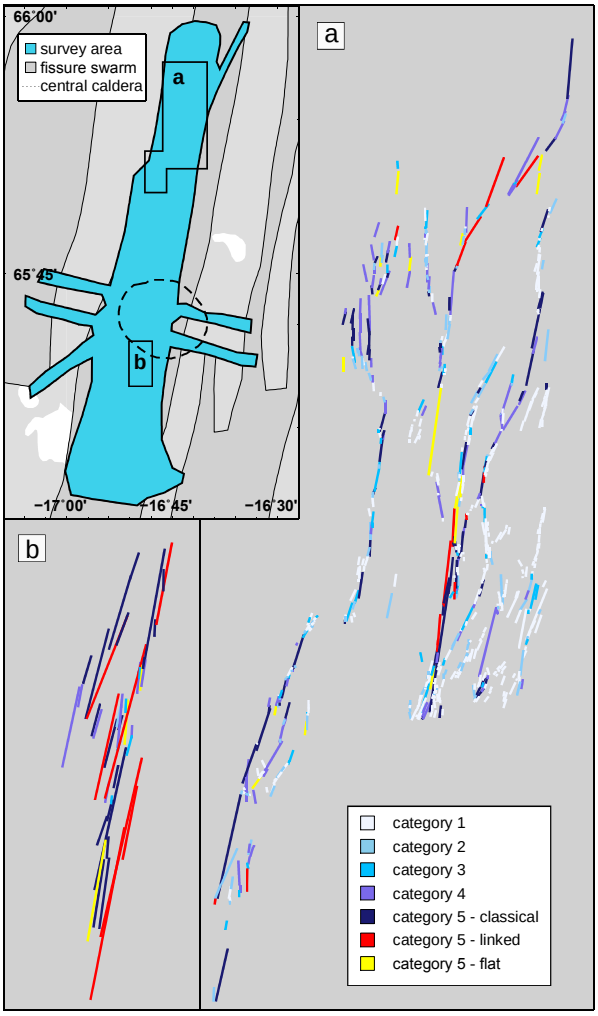

Figure 4.24: Location map of the categorised faults from 1-5 with category 5 shown subdivided into categories 5a, 5b and 5c

very few fissure-like faults, with the majority of fault profiles presenting a displacement profile of 5a-c.

4.5 Discussions and Conclusions

I suggest a model of fault growth, as shown in figure 4.25, which encompasses the pattern of growth from fissure to fully displaced fault as observed in the categorised D_{max}/L data (figure 4.21). The model maintains a constant length, L, whilst the fault still has fissure-like regions, with an increasing maximum displacement, D_{max} as stress is accommodated by vertically displacing non-displaced regions of a fault. It is possible

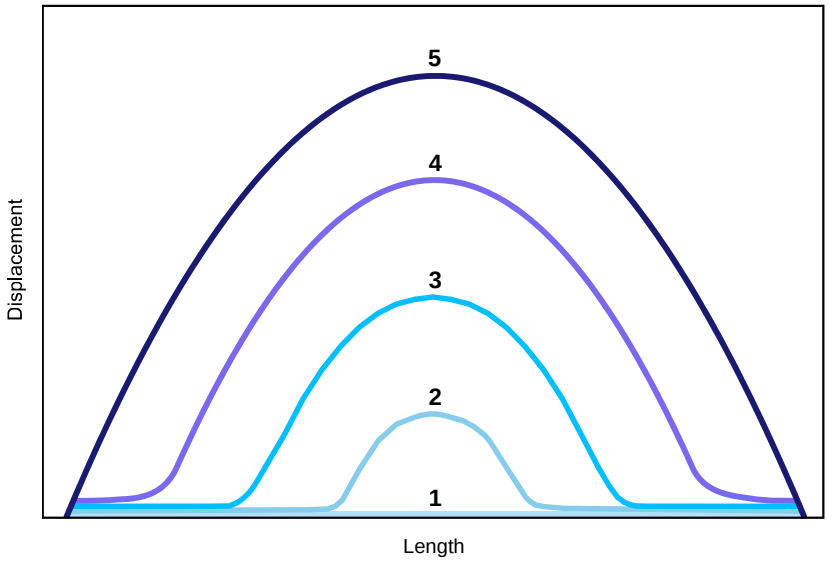

Figure 4.25: a) Shows the proposed model of growth from fissure to fault, showing fault categories 1-5. Here the length, L, remains constant after the original fissure (category 1) and stress is further accommodated by vertical displacement (categories 2-4) to the point the fault achieves a classical vertical displacement profile (category 5).

from the results that there is increasing L with increasing D_{max}. However, the length-displacement plot shows that there is a maximum length boundary to which the fissure structures can exist. This suggests that a fissure that has a maximum possible length has to evolve into a fully evolved fault before it can grow further in length, implying that stress is more easily accommodated by increasing vertical displacement up to the point a fault reaches a classical fault shape. This model is idealised with D_{max} at the centre of the fault, in reality the location of D_{max} does not present an obvious pattern, the fissure-like regions were always seen to extend from the fissure-tips but proportions at either end of the fault were seen to vary. The model can be incorporated as an early stage of fault growth for current models which presently only model behaviour of a fault once it has acquired the classical D/L profile. An illustration of the stages in growth from fissure to fault is shown in figure 4.26.

Of the category 5 faults shown as subcategories in figure 4.22, the 5B (linked) faults tended to have a lower D_{max} than the 5A (single faults) of the same length. This occurs because the 5B faults actually acquire the D_{max} of the original shorter, pre-linked faults. I observe that the majority of the pre-linked faults in a 5B fault had achieved both a classical fault shape (as shown in 4.23b) and that they had a maximum D/L for their

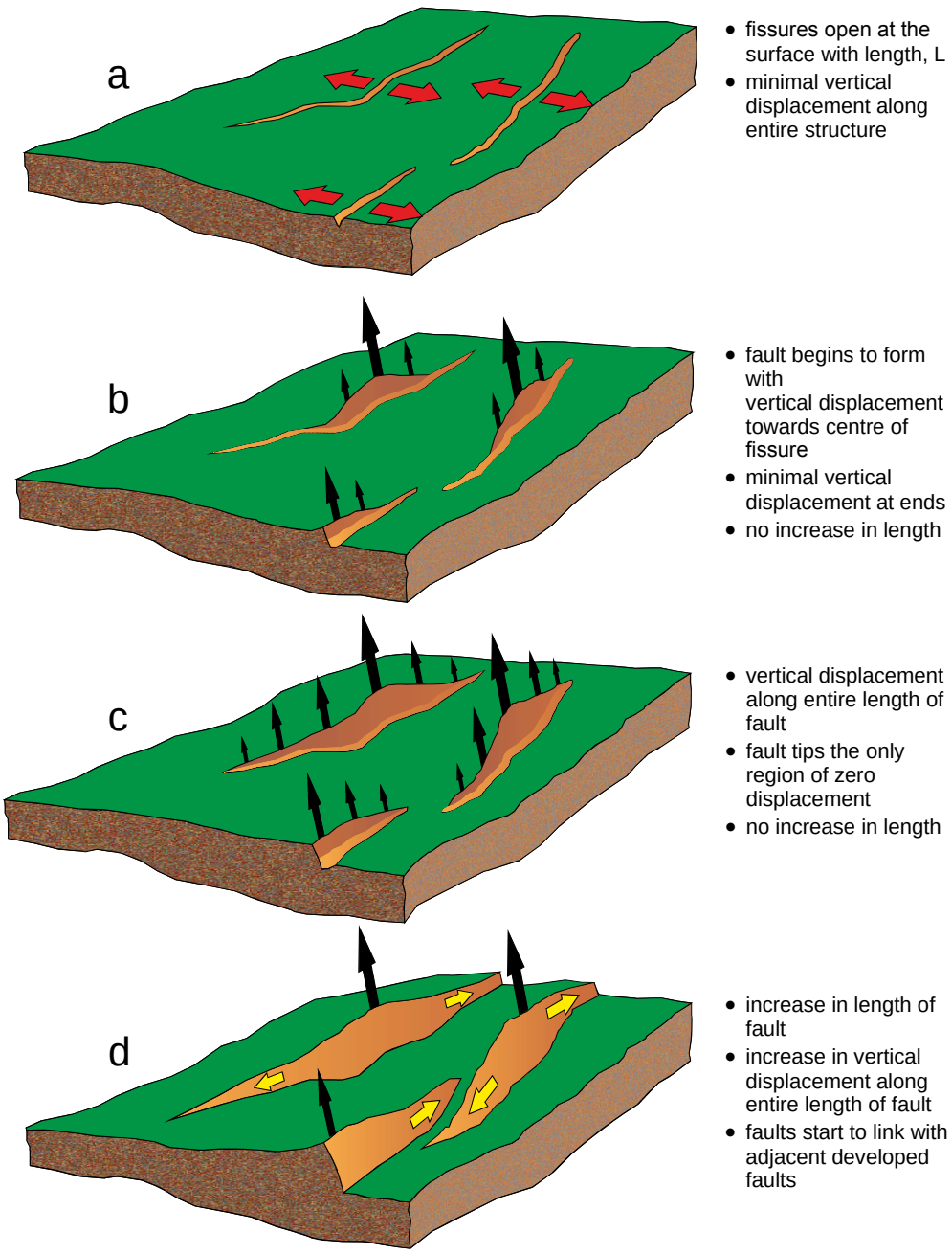

Figure 4.26: Illustration showing the stages of growth from fault to fissure. a) Fissures appear at the surface with minimal vertical displacement, b) stress is accommodated by vertical displacement, the tips of the fault remain fissure-like and there is no increase in the length of the structure, c) the structure has continued to displace vertically to become a fully formed fault, showing vertical displacement from tip-to-tip, d) the fully formed fault begins to accommodate stress by growing in length and continuing to displace vertically.

extrapolated lengths prior to linkage (as shown in figure 4.23a). I suggest that a fault can most easily accommodate stress by displacing regions that are still fissure-like, and that a fault would be more likely to accommodate stress by linkage once it has reached the maximum displacement for its fault length with no regions of zero displacement (with the exception of the fault tips).

In a number of previous studies it has been suggested that faults <200 m in length exhibit very little vertical displacement and were discounted from results. In this study the DEM allowed for the profiling of many structures <200 m with not only vertical displacements >0.5 m but in some cases fully evolved classical fault shapes. Many previous studies sampled data at much larger intervals than the 2-6 m sample interval used here(e.g. Bailey et al. (2005) at 100 m and Opheim and Gudmundsson (1989) at 25-50 m). The increased sample interval and resolution reveals structures that whilst small, account for a considerable amount of vertical deformation across the fissure swarm.

The D_{max}/L results from this work fit within the spread of the published data for comparable fault lengths. However, previous studies would likely not include fissures and partially fissured faults, so when considering only the category 5 faults in this study, the results sit at the high end of the D_{max} for comparable fault lengths. Studies using lower resolution datasets would not reveal the intricacies of fault segmentation, with single faults at low resolution actually being composed of multiple faults, resulting in a lower D_{max} to fault length trend than that found in high resolution data. As it is possible that data resolution could account for some of the spread in published results, an examination of the effects of resolution on fault analysis is presented in the next chapter.

Chapter 5

Resolution

5.1 Introduction

In the exploration industry, fault structure analysis is used to not only identify possible regions of hydrocarbon entrapment but also to understand and predict regions of fluid flow in order to locate ideal sites for wells and hydrocarbon extraction. Relay zones between faults can offer regions of high fluid flow. However, the resolution of the seismic data used for fault interpretation restricts the ability for interpreters to identify regions that contain relay zones that are smaller than the resolution of the data. This chapter will use faults picked using a resampled, low resolution DEM to compare with the faults found at high resolution in chapter 4. From this I will show that it is possible to identify whether a single fault picked at low resolution is actually a segmented fault, with regions of relay zones, based on the location of the fault's D_{max}/L within the published distribution.

Current understanding of the displacement/length (D/L) relationship of faults is a result of the consolidation of numerous published studies (e.g. Aitkenhead et al., 1985, Walsh and Watterson, 1988, Gillespie et al., 1993, Davison, 1994, Dawers and Anders, 1995, Cartwright et al., 1995, Jackson et al., 1996, Nicol et al., 1996, Rowan, 1997, Fossen and Hesthammer, 1998, Bailey et al., 2005). As discussed in chapter 4, each individual study is limited by the tectonic setting, rock type and the resolution of the data which further limits the fault sample size and fault length range (Gillespie et al., 1992).

Gillespie et al. (1992) noted that these limitations would introduce complications in identifying a simple D/L relationship when combining the individual studies as one

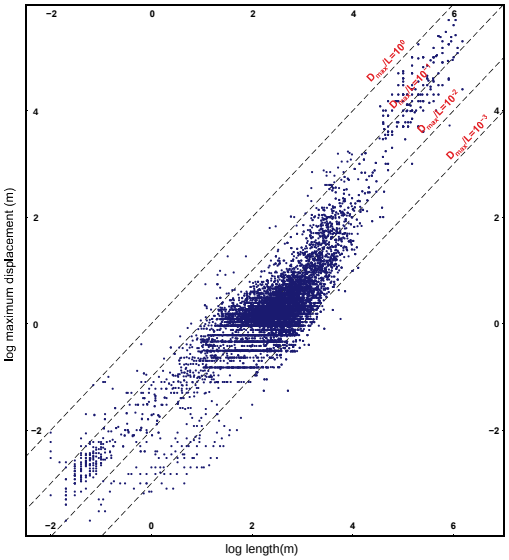

Figure 5.1: Plot of the published D_{max}/L datasets as shown in Bailey et al. (2005).

large dataset. The combined published dataset shows D_{max}/L to vary between 10^0 and 10^{-3} as shown in figure 5.1 (Bailey et al., 2005).

Additionally, the definition of what the measured fault comprises varies from study to study, either by choice or as forced by resolution limitations making it impossible to identify smaller discrete structures. For example, in Cartwright et al. (1995) the measured faults all contained segmentation, but a choice was made to measure the length of the entire fault system as a single fault rather than presenting the D_{max}/L of each individual segment. Whereas studies such as Dawers et al. (1993) noted the presence of en echelon segmented faults and presented,as separate entities, the D_{max}/L of those faults that showed little evidence of linkage to their neighbouring faults. Figure 5.2 compares the D_{max}/L results for a number of published datasets (Villemin et al., 1995, Opheim and Gudmundsson, 1989, Krantz, 1988, Walsh and Watterson, 1987, Dawers et al., 1993, Peacock, 1991, Muraoka and Kamata, 1983, Schlische et al., 1996, Scholz and Cowie, 1990, Wilkins and Gross, 2002, Walsh et al., 2002), highlighting how each study follows its own discrete trend within the confines of the overall D_{max}/L published distribution.

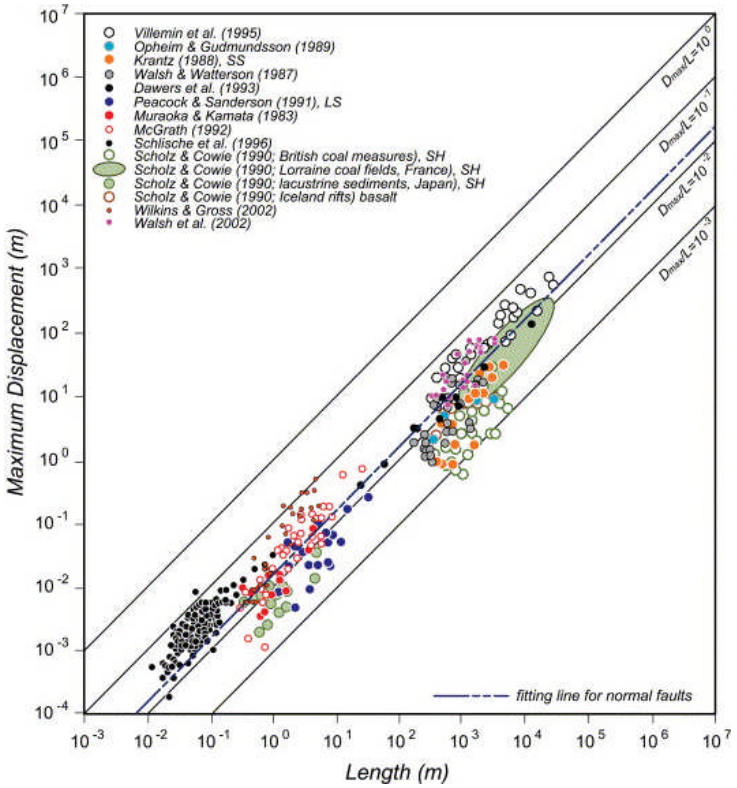

Figure 5.2: Comparison of a number of published D_{max}/L datasets, figure from Kim and Sanderson (2005). Reprinted from Earth-Science Reviews, Vol 68, Kim and Sanderson (2005), The relationship between displacement and length of faults: a review, 317-334, ©2005, with permission from Elsevier

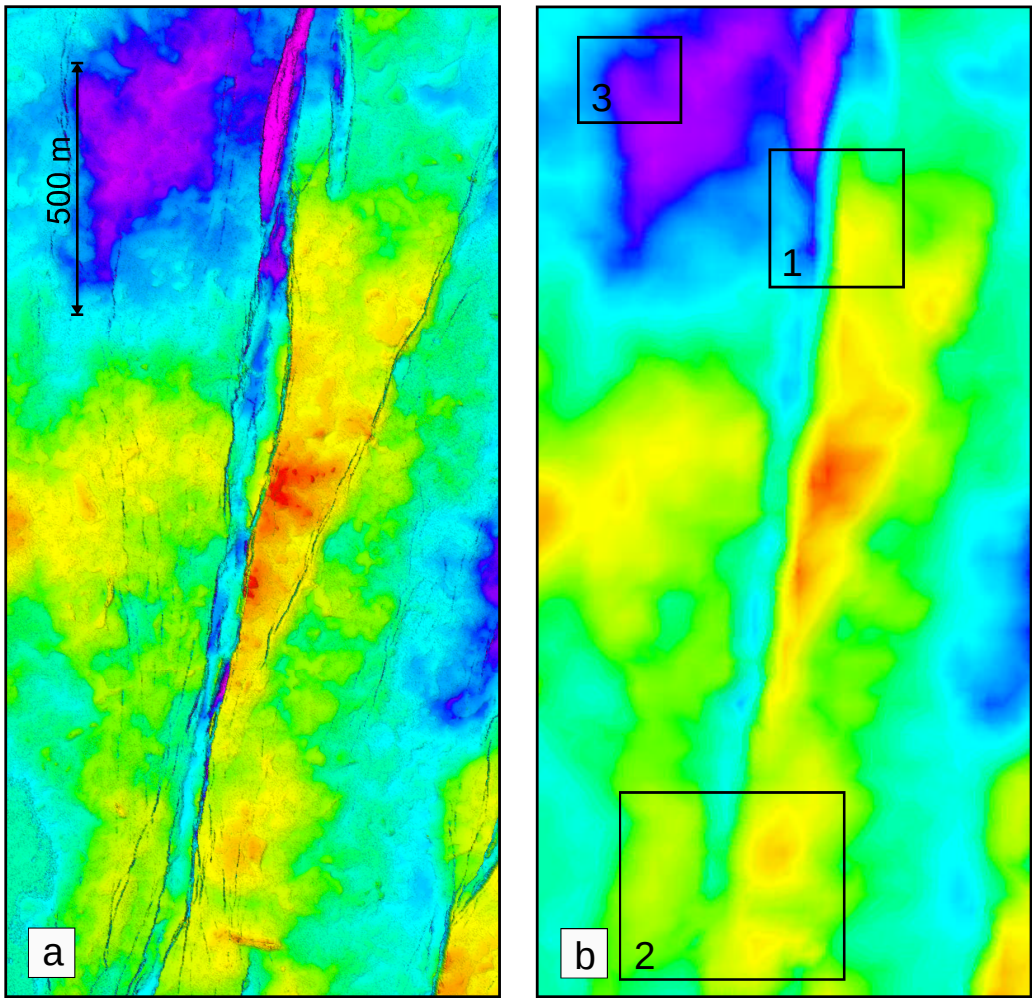

Figure 5.3: A region just north of the Krafla Fires lava flow is shown to compare the resolvable fault detail in a) the 0.5 m resolution DEM and b) the 30 m resolution DEM. Enlarged images of boxed areas 1, 2 and 3 are shown in 5.4.

5.2 Resolution and the displacement/length relationship

To examine the effect that data resolution has on the spread of D_{max}/L results and the consequent interpretation of the D/L relationship, the LiDAR point data was resampled at 10 m and 30 m resolution. Using the Petrel convergent interpolation algorithm (as described in chapter 3) the resampled datasets were processed to create two lower resolution DEMs (at 10 m and 30 m respectively) which were then used to measure faults in addition to those measured using the original 0.5 m resolution surface as discussed in chapter 4. Figure 5.3 shows a comparison of the 0.5 m resolution surface in figure 5.3a, taken over the region of the fissure swarm just north of the Krafla Fires lava flow, with the 30 m resolution surface of the same region. In this figure it can be clearly seen that a complex and segmented fault system that is easily observable at 0.5 m resolution is resolved as just a few much larger faults in the lower resolution surface. Figure 5.4 shows the boxed areas in figure 5.3b magnified to give a more detailed view of the two different resolution surface.

A total of 90 and 40 individual faults were identified and measured from the 10 m and 30 m resolution DEMs respectively. Figure 5.5 shows the location of the faults picked at 30 m and 0.5 m resolution, with figure 5.5c displaying those picked at 30 m resolution and figure 5.5d,e and f those picked at 0.5 m resolution. The faults highlighted in red will be used later in this chapter to examine systems of faults at different resolutions.

Figure 5.6 shows the D_{max}/L for all of the fault profiles picked at 10 m and 30 m resolution alongside both the 0.5 m resolution fault data presented in chapter 4 and those of the published data as shown in figure 5.1. The D_{max}/L data for the 10 m and 30 m resolution fault picks are shown in Appendix B and Appendix C respectively.

Figure 5.7 shows the 0.5 m resolution fault separated into the data five main categories as defined in 4. The figure shows that the category 1 faults, where the faults are still in a fissure-like form, cover the entire spread of the distribution. As the faults develop through the categories it shows that the spread of data decreases, tending towards the upper boundary of the published distribution as the faults become more fully formed.

Figure 5.8 shows only the category 5 fault D_{max}/L data (the faults are all fully formed faults tending to zero only at the fault tips), alongside the 10 m and 30 m resolution and published datasets. This figure shows that by varying the data acquisition

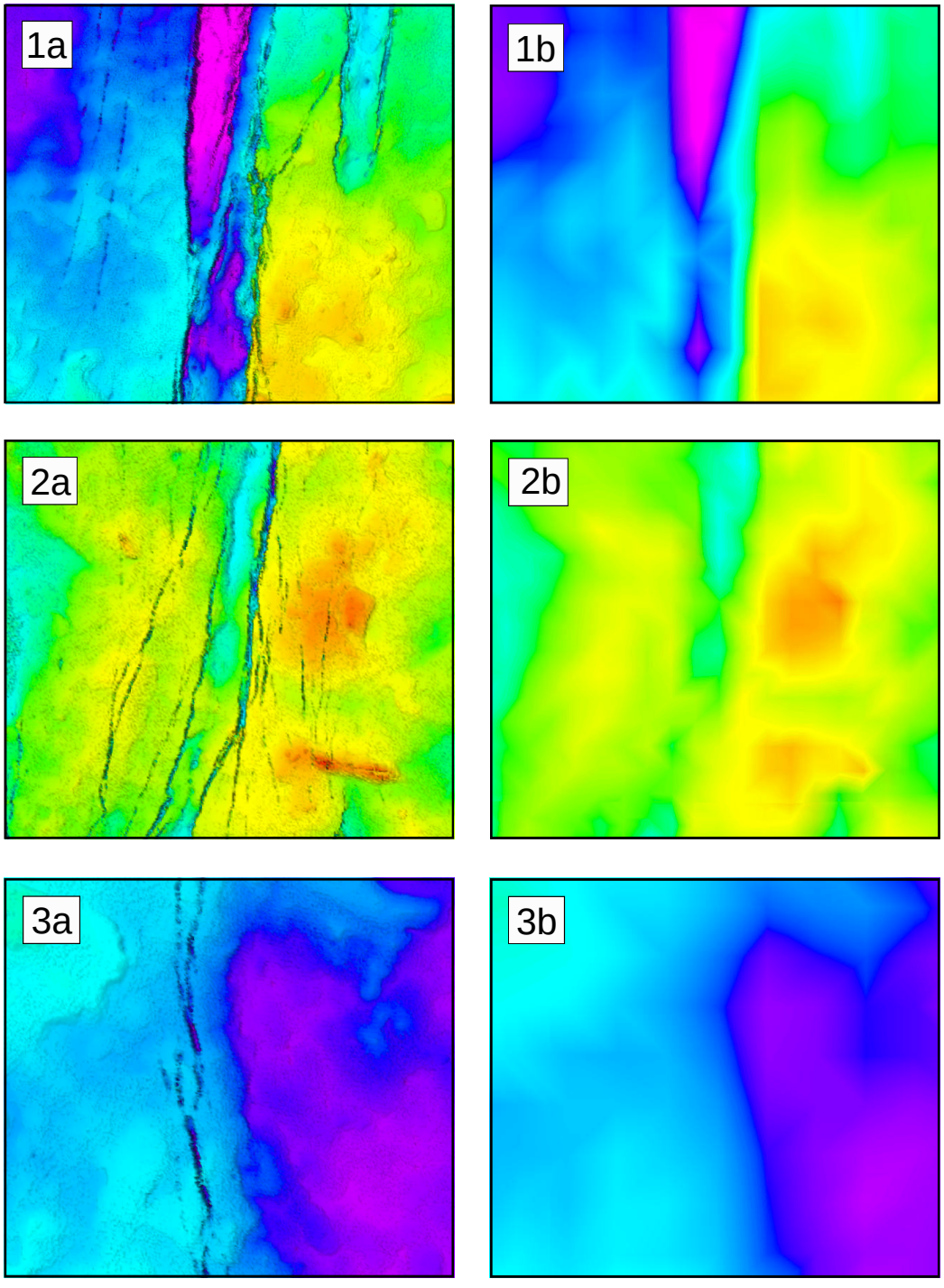

Figure 5.4: Images 1), 2) and 3) represent the boxes areas 1, 2 and 3 from 5.3 with the a) and b) images showing the DEM at 0.5 m and 30 m resolution respectively.

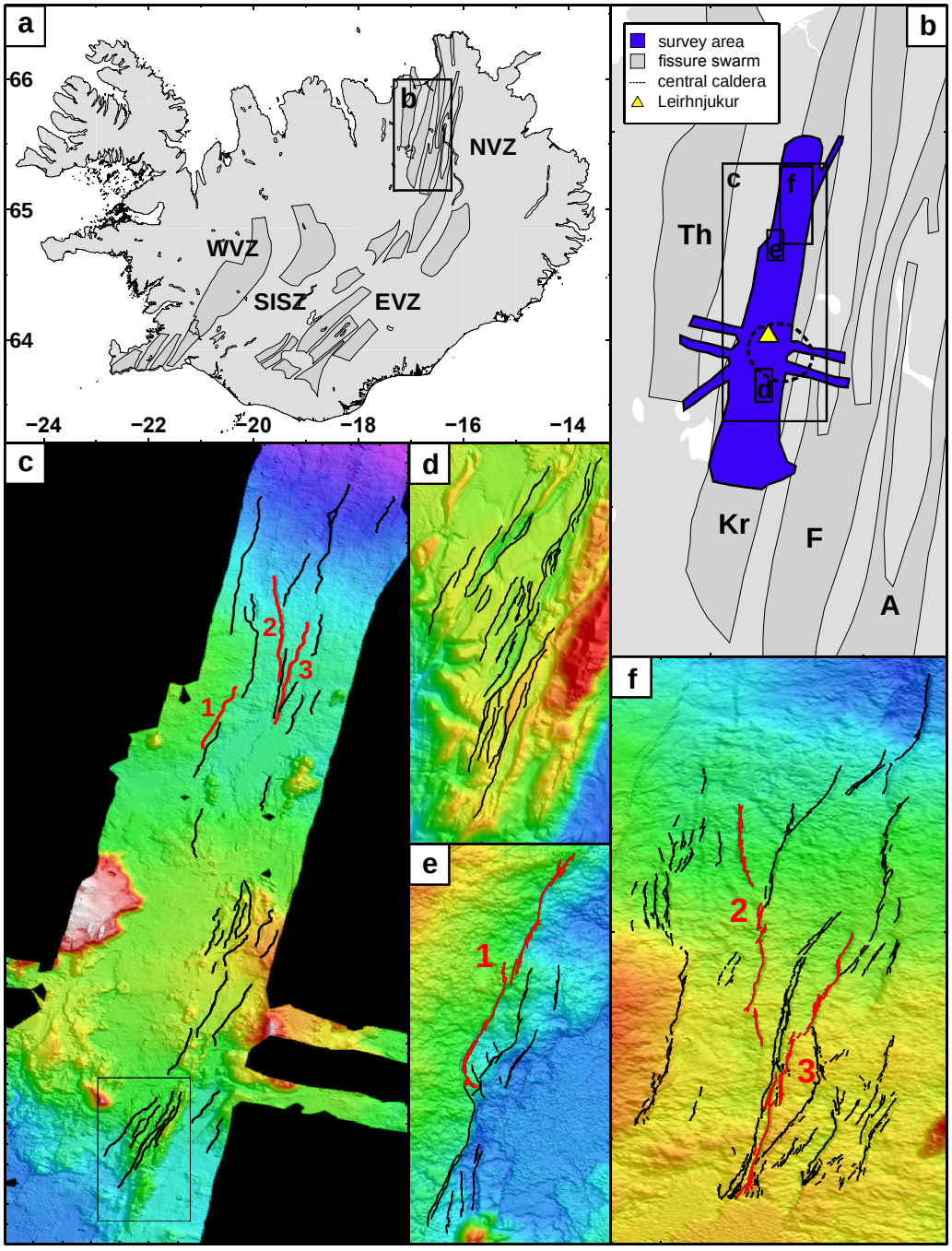

Figure 5.5: a) and b) show a Location map for the faults picked at 30 m and 0.5 m resolution, where the boxed areas in b) represent the regions in which faults were picked at c) 30 m resolution and d), e) and f) at 0.5 m resolution. The boxed area in c) indicates the location of the region shown in d) and boxes e) and f) are the regions containing the red faults 1,2 and 3 in c).

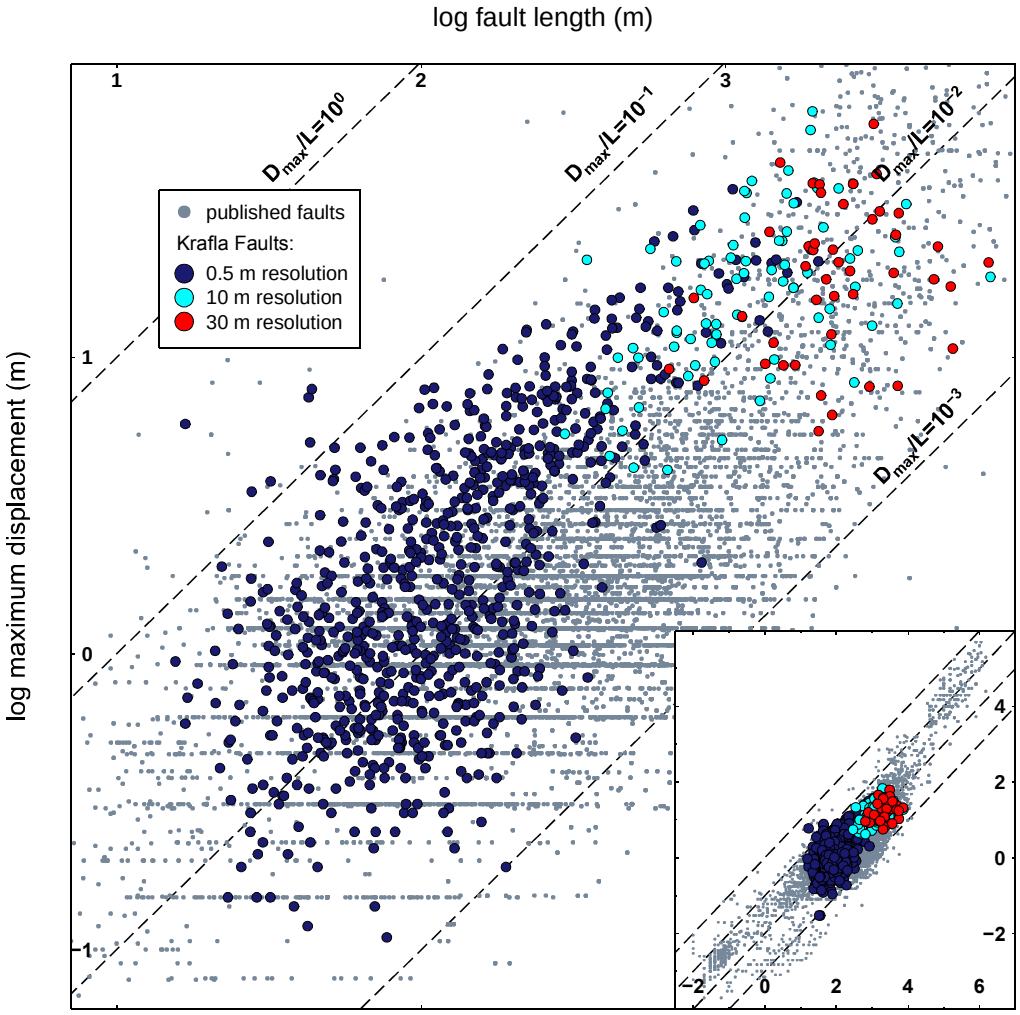

Figure 5.6: Shows D_{max}/L of Krafla faults as compared with the published data. The blue, cyan and red results are picked from 0.5 m, 10 m and 30 m resolution surface respectively.

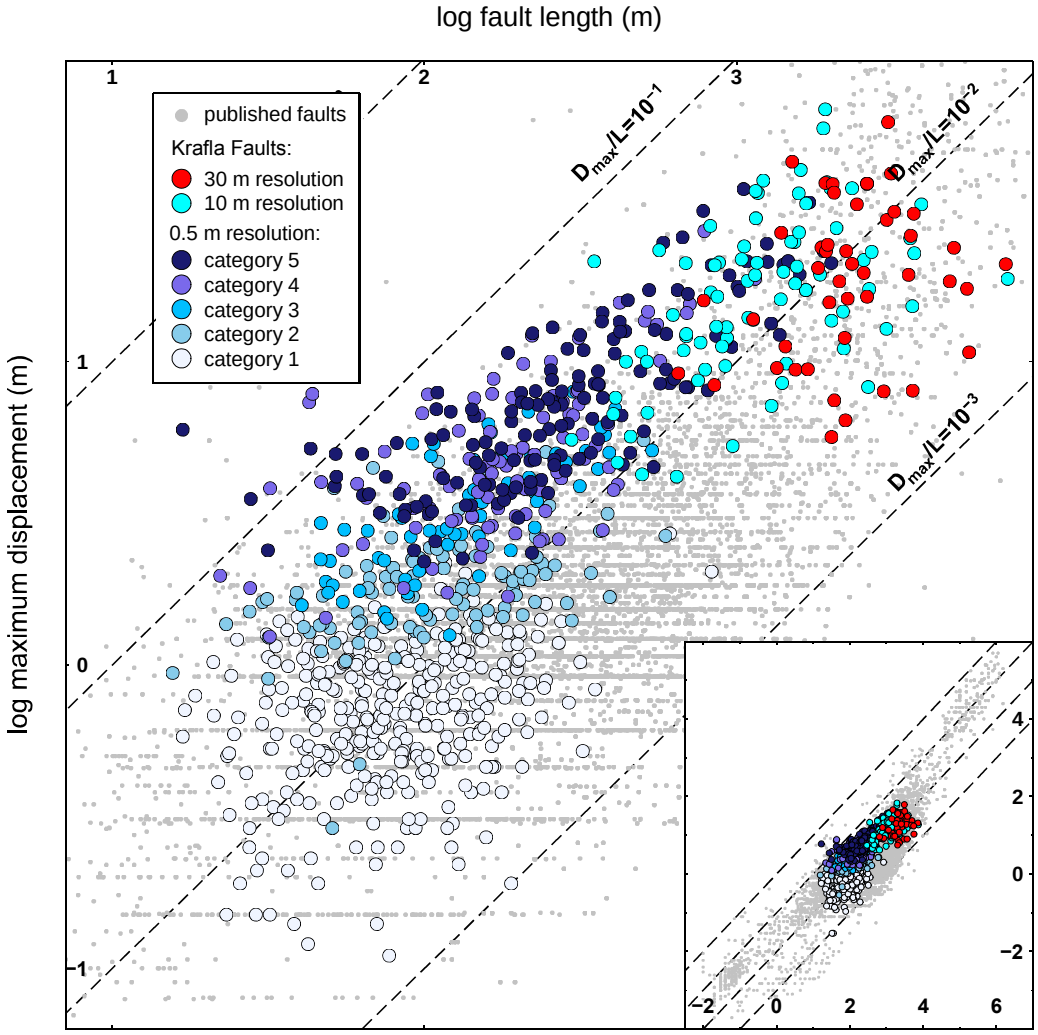

Figure 5.7: Shows D_{max}/L of Krafla faults as compared with the published data. Here the 0.5 m resolution faults are coloured by their categories as defined in chapter 4, the cyan and red results represent faults as picked from 10 m and 30 m resolution surfaces respectively.

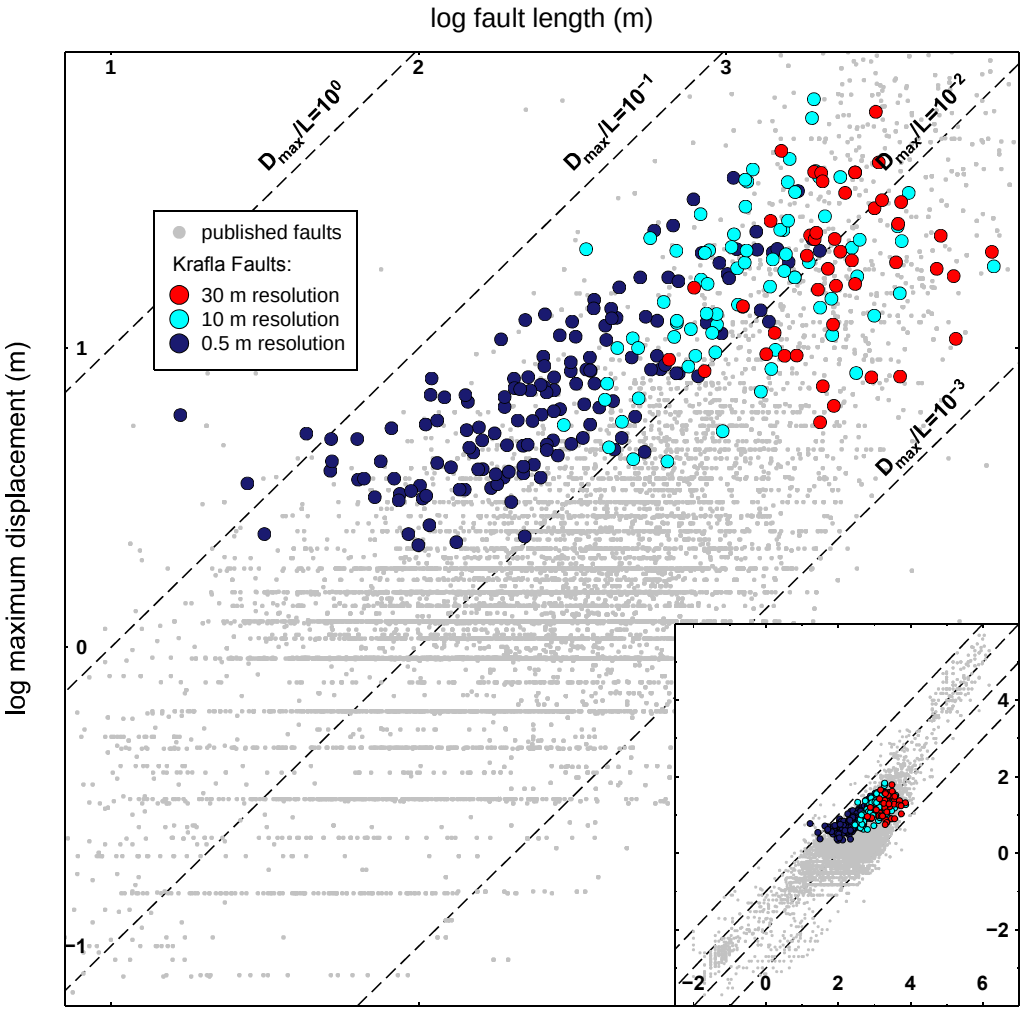

Figure 5.8: Shows D_{max}/L of Krafla faults as compared with the published data. The blue, cyan and red results are picked from 0.5 m , 10 m and 30 m resolution surface respectively. The 0.5 m resolution data includes only faults defined as category 5 faults in chapter 4

resolution the resultant D_{max}/L values give trends for each resolution that together cover the spread in results of the combined published data. The highest resolution picks, where it has been possible to measure segmented faults as separate entities, show a D_{max}/L relationship that follows the upper boundary of the published dataset between $D_{max}/L = 10^{-1}$ and $D_{max}/L = 10^{-2}$. The 30 m resolution picks, where the fault profiles represent anything from a single long well-developed fault through to an entire fault system composed of many shorter segmented faults, show a wider spread across the distribution that reaches down to the lowest boundary where $D_{max}/L = 10^{-2}$.

5.3 Resolution and fault system analysis

To better understand the implications of acquiring fault data at differing resolutions a comparison between the results for a select group of faults has been made. Three long faults profiled in the 30 m resolution dataset were selected, as shown in red in the figure 5.5c as faults 1, 2 and 3. These faults will be referred to in this section as fault systems 1, 2 and 3. The faults profiled along the same region of deformation using the 10 m and 0.5 m resolution DEMs were identified, the 0.5 m resolution picks for fault systems 1, 2 and 3 can be seen highlighted in red in figure 5.5e and f. Table 5.1 details the number of faults profiled for each of the fault systems.

Table 5.1: Table showing the number of faults picked for each of the fault systems using 30 m, 10 m and 0.5 m resolution DEMs

	Number of faults at			
Fault System	30 m resolution	10 m resolution	0.5 m resolution	Length of system (m) (m)
1	1	1	57	3400
2	1	2	50	5500
3	1	2	76	5400

All three fault systems were selected from faults picked in the north of the fissure swarm, with fault system 1 located along the western edge of the fissure swarm and fault system 2 and 3 both within the the main central group of faults in the fissure swarm. Fault systems 1, 2 and 3 are shown in figures 5.9, 5.10 and 5.11 respectively, with the faults picked at 0.5 m and 30 m resolution shown in a) and c) respectively. To allow a comparison between the 0.5 m and 30 m resolution measurements of vertical displacements along the fault system, the individual fault measurements were projected onto a best-fit line along each fault system. The vertical displacement profiles of each

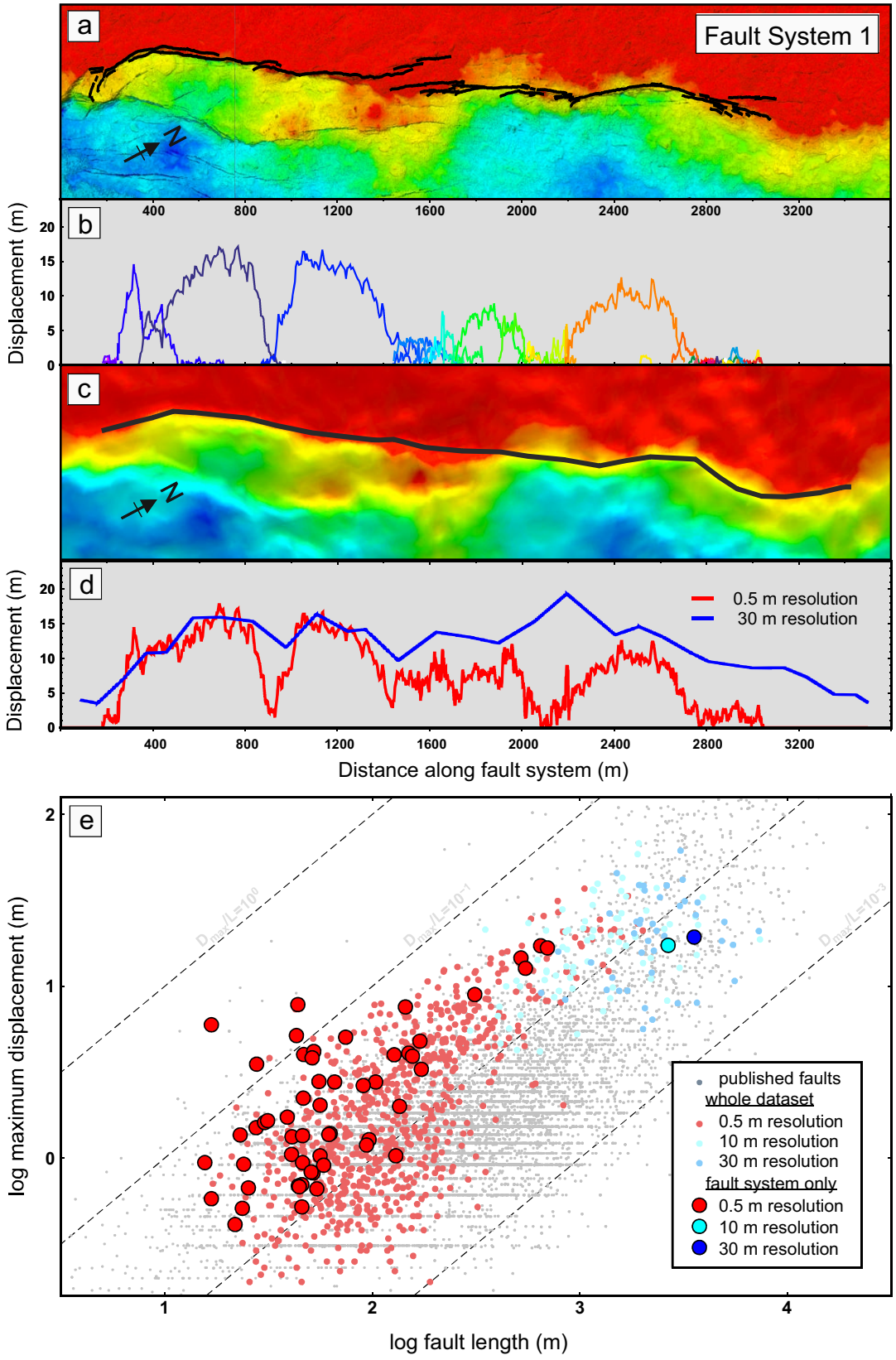

Figure 5.9: Fault system 1. The 0.5 m resolution DEM for the fault system region can be seen in a) with the faults picked for the fault system shown in black and the profiles for these fault are shown in b). The 30 m resolution DEM and the single continuous fault for fault system 1 is shown in c). d) Shows the cumulative displacement profile of all the faults picked at 0.5 m (red) plotted alongside the 30 m resolution fault profile (blue). e) D_{max}/L for all the faults picked for the fault system at 30 m (blue), 10 m (cyan) and 0.5 m (red) resolutions are shown alongside the entire Krafla and published data.

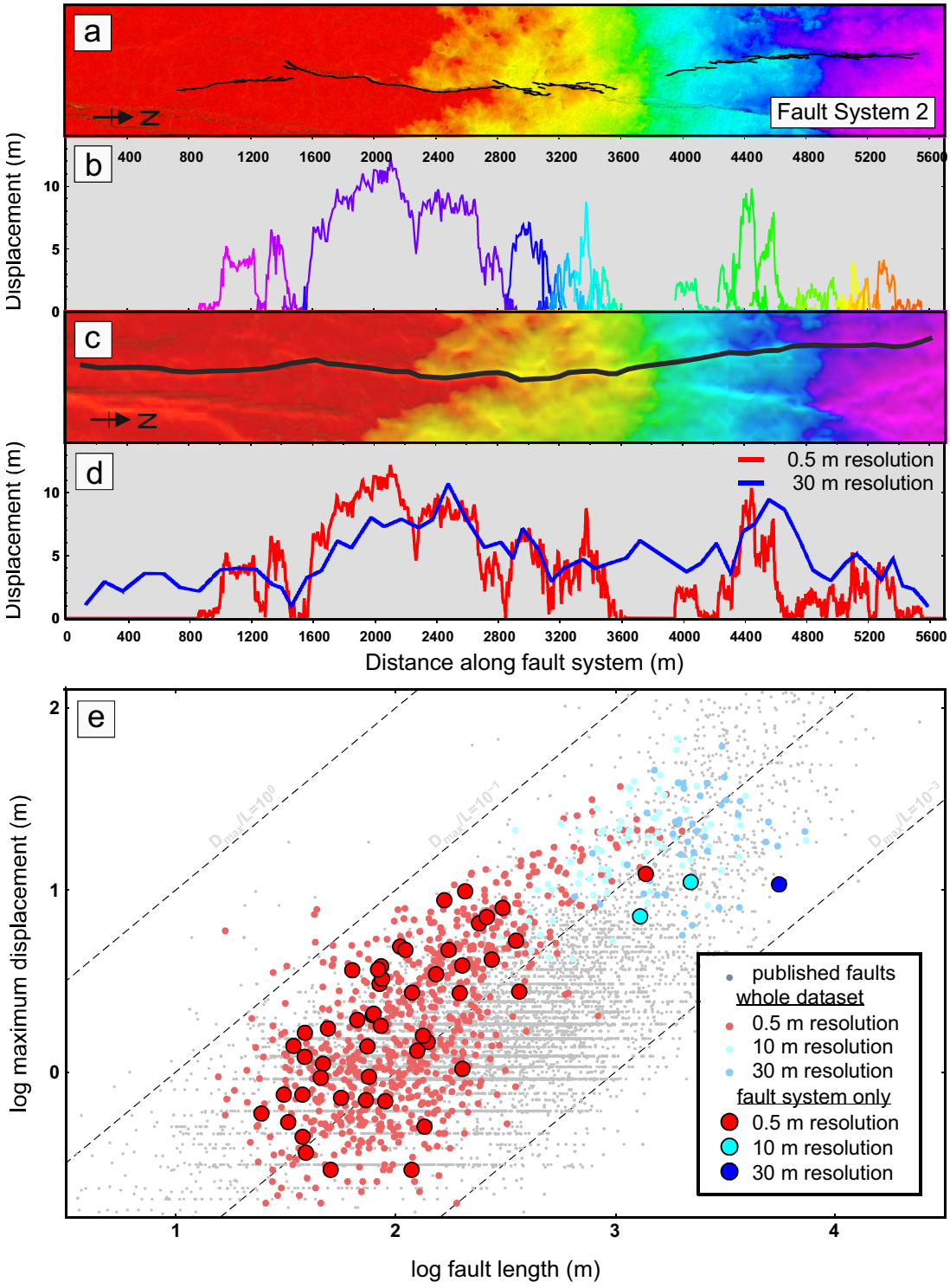

Figure 5.10: Fault system 2. The 0.5 m resolution DEM for the fault system region can be seen in a) with the faults picked for the fault system shown in black and the profiles for these fault are shown in b). The 30 m resolution DEM and the single continuous fault for fault system 1 is shown in c). d) Shows the cumulative displacement profile of all the faults picked at 0.5 m (red) plotted alongside the 30 m resolution fault profile (blue). e) D_{max}/L for all the faults picked for the fault system at 30 m (blue), 10 m (cyan) and 0.5 m (red) resolutions are shown alongside the entire Krafla and published data.

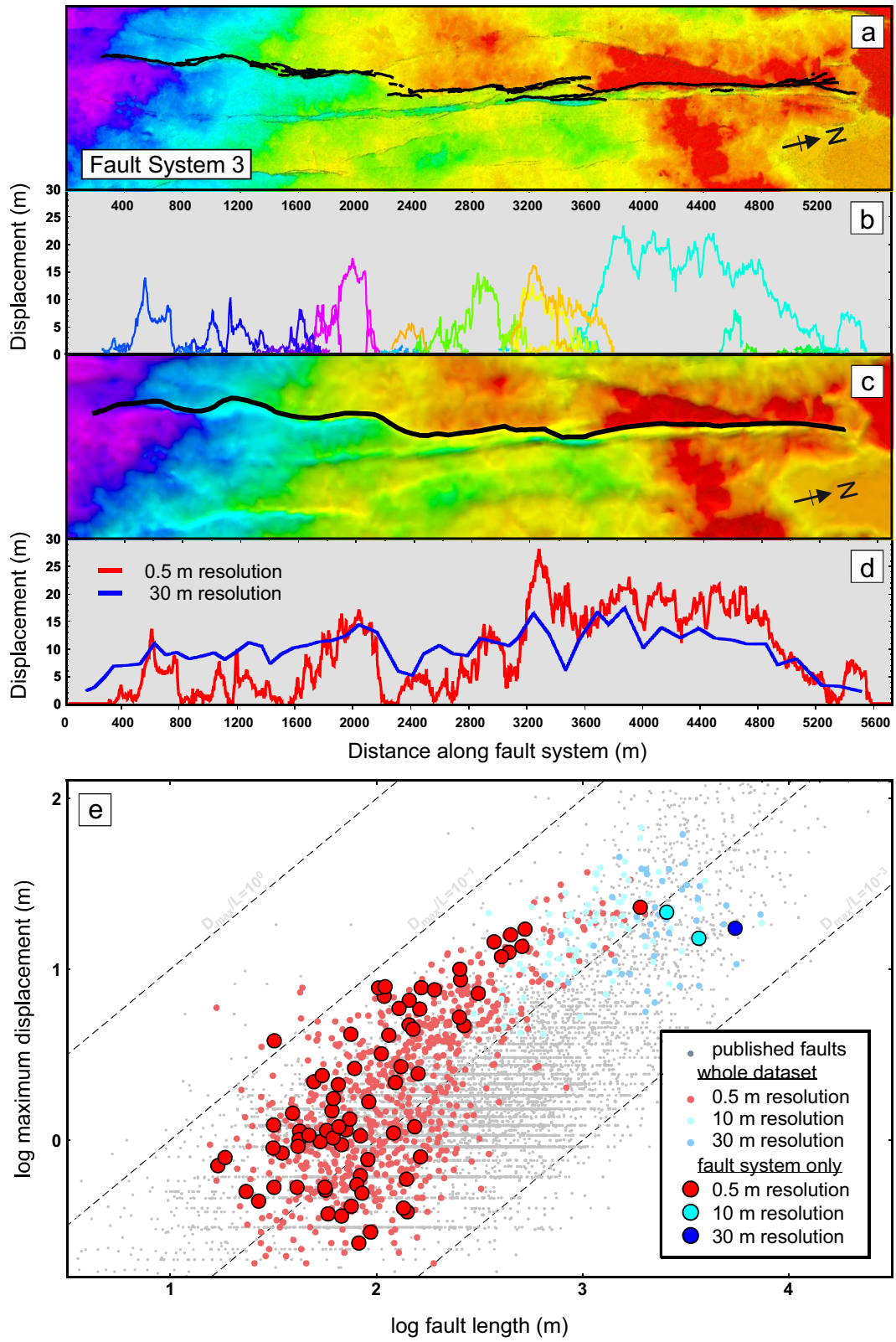

Figure 5.11: Fault system 3. The 0.5 m resolution DEM for the fault system region can be seen in a) with the faults picked for the fault system shown in black and the profiles for these fault are shown in b). The 30 m resolution DEM and the single continuous fault for fault system 1 is shown in c). d) Shows the cumulative displacement profile of all the faults picked at 0.5 m (red) plotted alongside the 30 m resolution fault profile (blue). e) D_{max}/L for all the faults picked for the fault system at 30 m (blue), 10 m (cyan) and 0.5 m (red) resolutions are shown alongside the entire Krafla and published data.

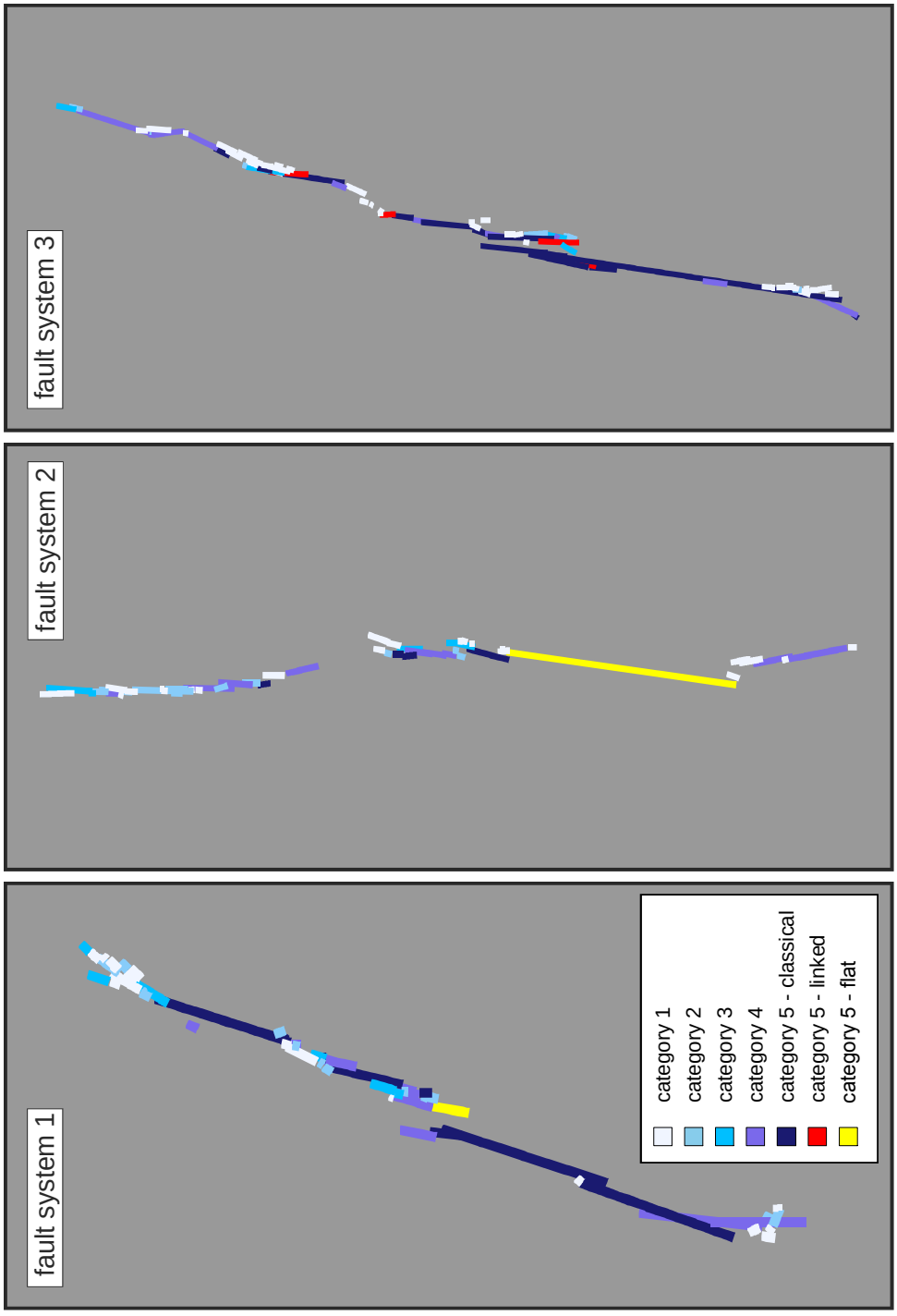

Figure 5.12: Plots showing the categories of the faults within each of the fault systems (for faults picked using the 0.5 m resolution DEM).

of the 0.5 m resolution faults, projected onto the best-fit line, are shown in b) of figures 5.9, 5.10 and 5.11. The vertical displacement profiles for the 0.5 m resolution faults were then summed at every 0.5 m along the best-fit line to produce a cumulative vertical displacement plot that could be directly compared to the 30 m resolution vertical displacement (shown in d) of figures 5.9, 5.10 and 5.11 as red and blue lines respectively). The D_{max}/L plot for each of the fault systems is shown alongside the Krafla data and the published dataset in e) of figures 5.9, 5.10 and 5.11.

The D_{max}/L plots for all three fault systems (figures 5.9e, 5.10e 5.11e) show a similar distribution of faults, with a small number of long fully developed faults and a distribution of smaller faults that mimics the distribution of the entire Krafla 0.5 m resolution fault data. Fault system 1 does show a slightly narrower distribution than the other fault systems, with D_{max}/L tending towards the higher limits of the published data. The category of individual faults within each fault system are shown in figure 5.12.

The 10 m resolution picks showed very similar results to the 30 m resolution pick for fault system 1, the length of the measured fault was seen to be shorter for the 10 m resolution, most likely because the end of the fault was more accurately measured in the higher resolution surface. In both fault systems 2 and 3 a major gap or relay zone observed in the 0.5 m resolution surface was also identified in the 10 m resolution surface.

5.4 Discussion

If the faults had been picked using only one surface resolution then the dataset for Krafla would have been constrained to a small region of the full distribution of the published D_{max}/L dataset, as seen in many of the published datasets shown in figure 5.2. However, measurements for the Krafla faults over the three different resolution surfaces (0.5 m, 10 m and 30 m resolution) produce D_{max}/L results that span the entire distribution of the published datasets, for the range of lengths measured.

The level of detail in the 0.5 m resolution surface allows individual faults to be correctly identified giving a true value of D_{max} for the fault length. The resultant D_{max}/L produces a distribution for the fully formed category 5 faults that lies in the higher limits of the published distribution. The 30 m resolution fault profiles, whilst in some cases being correctly identified single faults, often represent whole fault systems of segmented faults. In this case, L would represent the length of the entire 'fault system' and D_{max} is a measure of the segment with the largest vertical displacement. This agrees with the spread of the 30 m resolution D_{max}/L which produces faults from the highest to lowest limits of the published distribution. An example of this can be seen in the fault system comparisons of D_{max}/L for 0.5 m and 30 m resolution fault profiles. The 30 m faults, for all three of the fault systems, each has a D_{max}/L that lies towards the lower boundary in the published distribution.

To further examine the 30 m resolution D_{max}/L figure 5.13 compares two regions of faults. A region of faults to the south-east of the caldera (shown in yellow) is almost entirely composed of category 5 faults when measured at 0.5 m resolution, wheras at 30 m resolution the majority of measured faults either maintain the single fault profile or at the most two to three of the faults observed at the higher resolution. These are shown in figure 5.13a to have a much higher D_{max}/L than those for the many-segmented fault systems discussed earlier in the chapter (shown in purple in figure 5.13a and b).

One conclusion from this data is that a fault (category type 5) measured with a D_{max}/L ratio at the high end of the published range is most likely to be a single fault and a fault that has a D_{max}/L ratio at the lowest end of the published range is probably a fault system composed of many segmented parts that have not been identified due to restrictions in data resolution. Using the published distribution as reference it could be possible to identify the composition of a measured fault by establishing its position

within the distribution.

A test for this would be to compare this study with the resolution (and corresponding D_{max}/L locations) for the published studies (such as those shown in figure 5.2). However, as discussed at the beginning of the chapter, various factors such as variety of choice in how the faults were represented (e.g. Cartwright et al. (1995) presenting segmented faults as a single fault and Dawers et al. (1993) presenting all segments as seperate entities) and variations in the reporting of data resolution methodology, made direct comparisons difficult. Further studies in other tectonic environments using methods similar to the research presented here would help establish if the published distribution can be realistically used to identify segmented fault systems from single faults measured at low resolution.

The comparison between the 0.5 m and 30 m resolution fault profiles, for the three fault systems studied, shows that the low resolution surface allows for identification of the larger fault system, possibly outlining the location of a larger/longer fault underlying the 10,000 year surface. If this is the case, the high resolution fault data for the three fault systems possibly show the surface expression of the re-activation of the underlying large fault. However, these smaller surface faults, whilst possibly linked to an underlying fault, can still be considered effectively independent of the underlying large structure when examining the growth of a fracture from fissure to fault (as presented in chapter 4). The surface faults would be expected to grow independently as a newly formed fault, where any displacement on the structure, either horizontally or vertically, is caused by stress reaching sufficient levels for slip to occur, irregardless as to the origins of the original stress.

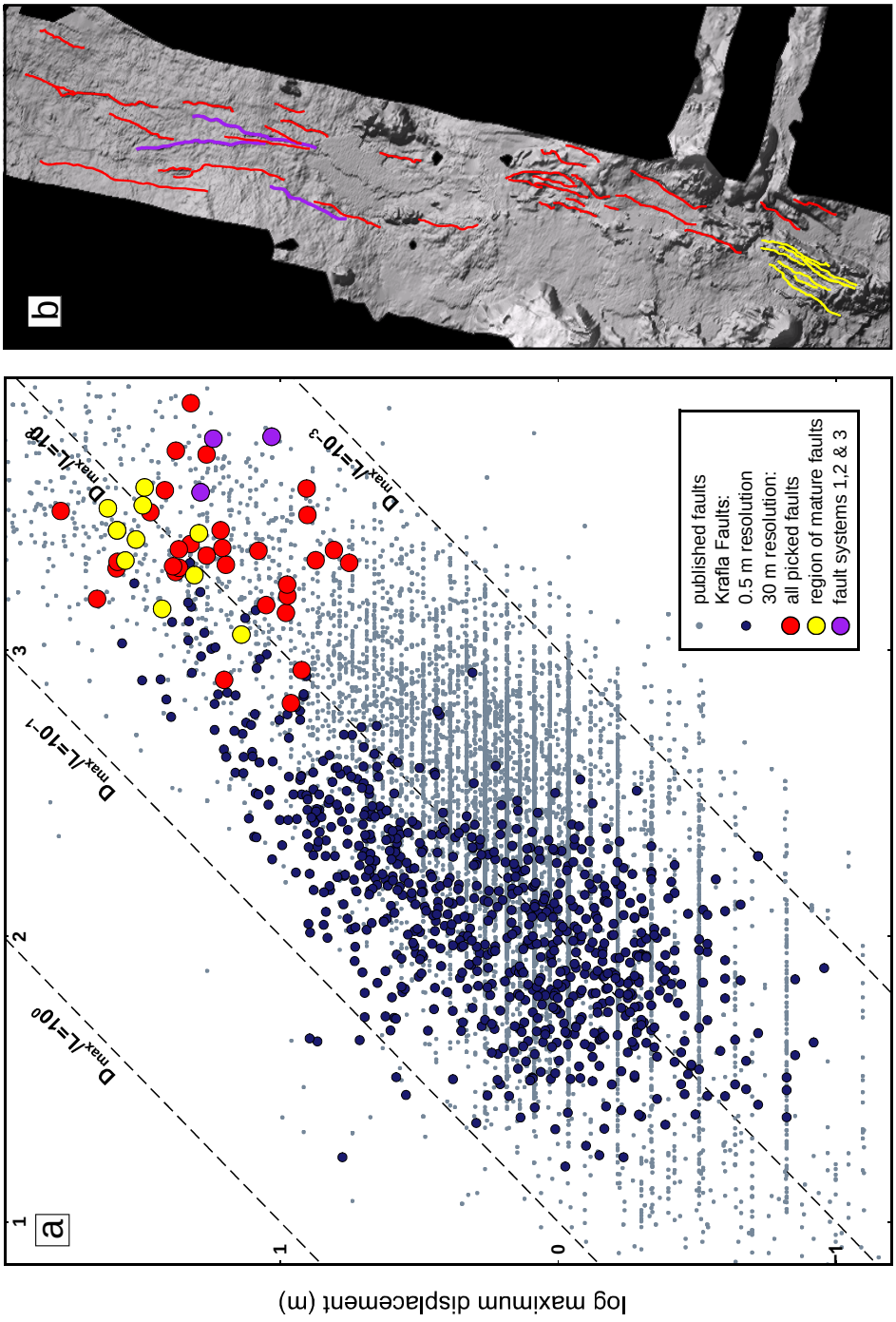

Figure 5.13: Showing a comparison of the position on the D_{max}/L published distribution for faults picked using the 30 m resolution surface. Faults shown in yellow in a) and b) are a select group of faults composed of only a few large fully-formed faults in the 0.5 m resolution surface. Faults shown in purple in a) and b) are the three fault systems from earlier in the chapter, composed of many much smaller faults and fissures (from 50-90 separate components) in the 0.5 m resolution surface. The faults shown in red are the remaining faults picked at 30 m resolution.

Chapter 6

Present-day deformation in the Northern Volcanic Zone

6.1 Introduction

Geodetic acquisition methods such as space-borne interferometric synthetic aperture radar (InSAR) have developed over the last several decades to become techniques with which millimetre-precision surface displacement data can be obtained over large study areas. To better understand surface deformation (e.g. during inter-, post- and co-event deformation), InSAR time series are commonly interpreted to obtain changes in rates of inflation, deflation and horizontal motion in key areas such as the surface above the recently erupted magma chamber, or to estimate average displacement rates using the cumulative results of the series over a wider area. This study aims to better understand changes in the rates of displacement both along and across the whole Krafla fissure swarm by using the incremental changes in the InSAR time series to examine any fluctuations in displacement rates over time and whether an average displacement rate fully encompasses the behaviour of a post-seismic rifting region. In addition, this study will similarly examine the inter-seismic Askja fissure swarm to identify regions of the fissure swarm that may not be fully represented by an average rate map.

6.1.1 Post- and inter- event deformation

A rifting cycle consists of three main phases: co-event, post-event and inter-event (e.g. Sigmundsson, 2006a). Co-event deformation usually yields centimetres to metres of surface displacement and, provided satellite coverage, atmospheric and surface conditions allow, is readily quantifiable with InSAR. Co-event deformation and has been the sub-

ject of many recent studies, for example Haiti (e.g. Calais et al., 2010),Canterbury,New Zealand (e.g. Elliott et al., 2012), and L'Aquila, Italy (e.g. Walters et al., 2009), allowing the deformation behaviour during the co-event phase to become well documented. There have been a number of published InSAR studies of land-based magmatic co-event rifting episodes, with the many published studies of the major rifting episode between 2005-2009 in Afar, Ethiopia (e.g. Wright et al., 2006, Grandin et al., 2009, Hamling et al., 2010) and studies such as the Biggs et al. (2009) InSAR examination of immature rifting in Tanzania. These can be combined with results acquired using other data acquisition methods, such as those acquired during the Krafla Fires rifting episode (e.g. Brandsdottir and Einarsson, 1979), to help build an understanding of magmatically induced rifting.

The post- and inter-event phases of the rifting cycle typically present much smaller displacements than those found in the co-event phase and noise limitations encountered in InSAR can present problems in identifying these small amounts of deformation. Using time series made from a large number of interferograms can help reduce issues with noise and allow for identification of patterns in deformation over time (e.g. Hooper et al., 2009, Ofeigsson et al., 2011). As a result of such processes as deflation or re-inflation of shallow magma chambers, additional slip from aftershocks and viscous relaxation of the crust and upper mantle, short-term post-event deformation directly following a co-event episode can be quite sizeable, with many of these processes continuing for many years, particularly the effects of viscous relaxation. Post-event deformation has been the focus of a number of InSAR studies, examining displacement decay times and average displacement rates from multiple interferometric inputs (e.g. Wright et al., 2012, 2013). Post-event studies range from short-term observations from the months directly after a co-event episode, e.g. (Árnadóttir et al., 2005), to several years, e.g. 3 year study of Afar (Nooner et al., 2009) and 4 year studies following the 2000 earthquakes in South Iceland (Jónsson, 2008), and the Manyi earthquake, Tibet (Ryder et al., 2007) through to much longer studies such as the 7 year study following on from the Landers earthquake, California (Fialko, 2004). As satellites carrying interferometric equipment have been providing coverage for time spans now reaching in to decades, it is becoming possible to monitor patterns in both post- and inter-event behaviour for longer and longer periods, enabling the identification of longer-term fluctuations and characteristics.

Studies of inter-event behaviour provide increased understanding of how strain is

being accommodated between major seismic events and could potentially identify areas of accumulated strain that could present potential future seismic hazard. InSAR time series have been used to examine inter-event deformation in numerous studies such as along the Denali fault, Alaska (Biggs et al., 2007), Tibet (e.g. Wright et al., 2004, Elliott et al., 2008, Wang et al., 2009), and San Andreas fault, California (Fialko, 2006).

Using an InSAR time series that spans 16 years of deformation, I will examine the post-event behaviour of the Krafla fissure swarm and inter-event behaviour of the Askja fissure swarm using the incremental displacements through the series to observe changes in characteristics of displacement.

6.1.2 Post-rifting deformation: Krafla

A number of key studies of post-event surface deformation have been made in the Krafla region following on from the Krafla Fires final event in 1985. The behaviour of the central caldera and more explicitly its shallow magma chamber from which magma extruded during the Krafla Fires, has been one focus.

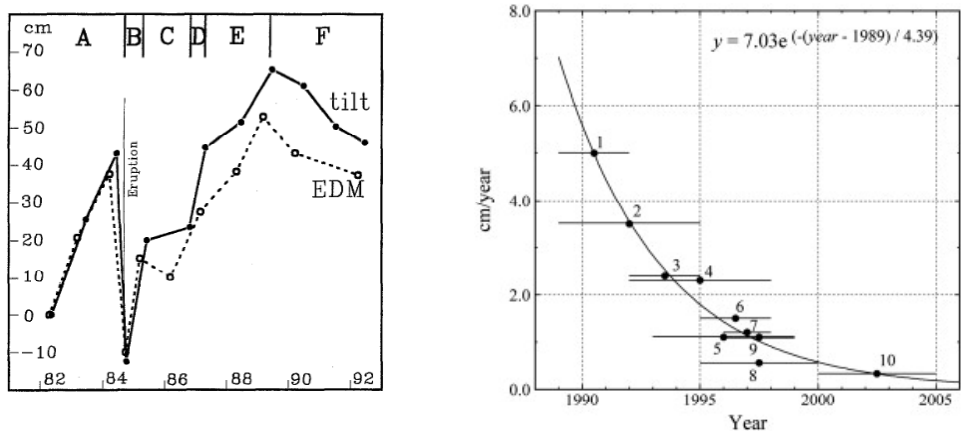

(a) (b)

Figure 6.1: Co- and post-seismic deformation of surface over the Krafla magma chamber with a) showing results from 1982-1992 Tryggvason (1994) (reprinted from Bulletin of Volcanology, vol.56, Tryggvason (1994),Surface deformation at the Krafla volcano, North Iceland, 1982–1992,98-107, ©1994, with permission from Springer) and b) showing results from 1989-2005 as compiled by Sturkell et al. (2008) from various published sources (Tryggvason, 1994, Björnsson and Eysteinsson, 1998, Sigmundsson et al., 1997, Henriot et al., 2001, Ágústsson, 2001, de Zeeuw-van Dalfsen et al., 2006, Sturkell et al., 2008)(reprinted from Journal of Volcanology and Geothermal Research, vol. 177, Sturkell et al. (2008), Multiple volcano deformation sources in a post-rifting period: 1989-2005 behaviour of Krafla, Iceland, constrained by levelling, tilt and GPS observations,405-417, ©1994, with permission from Elsevier).

Tryggvason (1994) measured the post-event surface deformation over the magma chamber using a tiltmeter and electronic distance measurements (EDM), from 1982-1992, capturing displacement during the final co-rifting event and the consequent post-event deformation as shown in figure 6.1a. As a continuation to this, Sturkell et al. (2008) collated results of published studies by (Tryggvason, 1994, Björnsson and Eysteinsson, 1998, Sigmundsson et al., 1997, Henriot et al., 2001, Ágústsson, 2001, de Zeeuw-van Dalfsen et al., 2006, Sturkell et al., 2008) which observed displacement over varying time periods between 1989 and 2005 using a variety of techniques: levelling, tilt, GPS, InSAR. Sturkell et al. (2008) was able to establish a relationship from the data, shown in figure 6.1b, where the rate of subsidence of the surface, dh(t)/dt during the post-rifting period decayed as follows:

$$\frac{dh(t)}{dt} = 7.03e^{-t/\tau} \tag{6.1}$$

where t is the number of years since 1989 and τ is a decay constant in years (with $\tau = 4.39$ years for the 1989-2005 time period).

A series of GPS campaigns were undertaken in 1987 (Foulger et al., 1987), 1990 (Jahn, 1990) and 1992 (Heki et al., 1993). The campaigns consisted of a network of ∼40 GPS points mainly concentrated within the Krafla volcanic system with a sparser distribution providing coverage over a wider region. Foulger et al. (1992), Heki et al. (1993), Hofton and Foulger (1996), Pollitz and Sacks (1996) used the horizontal and vertical displacement vectors from the GPS to constrain and provide best-fit models of the deformation field in Krafla. Foulger et al. (1992) identified a spatially varying deformation field that had a maximum expansion rate close to the rift of ∼6 cm/year between 1987-1990 (compared with the average plate motion in northeast Iceland of ∼1.8 cm/year).Hofton and Foulger (1996) further identified that the maximum expansion rate had decreased to 4.5 cm/year when averaged between 1987-1992 implying a reduction in the deformation rate between 1987 and 1992.

Studies of post-event displacement over the wider fissure swarm have been made, with Sigmundsson et al. (1997) using InSAR from 1992 to 1995 to identify ∼ 24 mm/yr subsidence over the shallow magma chamber combined with ∼ 7 mm/yr along-axis subsidence. Henriot et al. (2001), Henriot and Villemin (2005) observed a steady rate of deformation over Krafla using InSAR time series between 1992-2000, providing average displacement rates over the region, suggesting that the main component of ground motion is vertical and giving a maximum ground subsidence of 2.4 cm/yr. de Zeeuw-

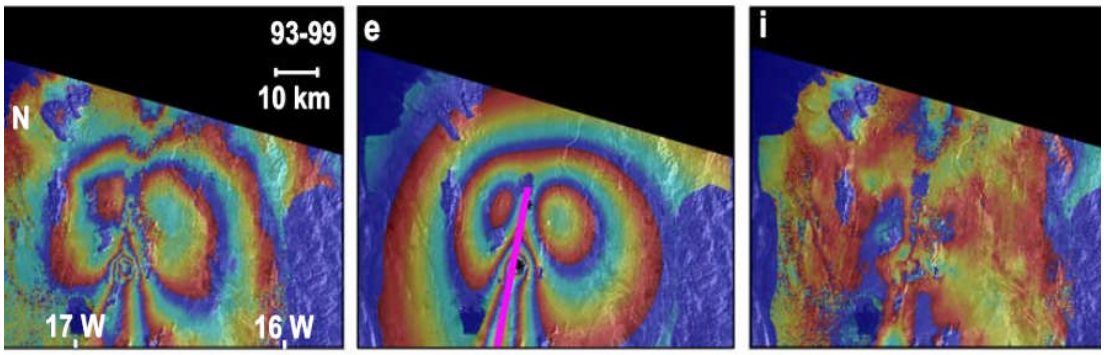

Figure 6.2: An excerpt from figure in de Zeeuw-van Dalfsen et al. (2004) showing a) the interferogram from 1993-1999, e) best fit model including two Mogi sources and tensile dislocation along-axis (shown in purple), i) the residuals remaining after subtracting the model from the interferogram. Reprinted from Geophysical Research Letters, vol. 31, de Zeeuw-van Dalfsen et al. (2004), Satellite radar interferometry 1993-1999 suggests deep accumulation of magma near the crust-mantle boundary at the Krafla volcanic system, Iceland, ©2004, with permissin from Wiley.

van Dalfsen et al. (2004) used 4 interferograms from 1993-2000 to obtain a model of the deformation behaviour of the fissure swarm and caldera, identifying three main regions of deformation: as with Sigmundsson et al. (1997) both localised concentric deformation in the centre of the caldera and linear deformation aligned along the major axis of the swarm were identified. de Zeeuw-van Dalfsen et al. (2004) proposed the along-axis deformation to be the result of a combination of post-rifting relaxation and plate spreading. Additionally de Zeeuw-van Dalfsen et al. (2004) described a more widespread concentric deformation ∼15 km north of the caldera that suggested inflation covering a circular area ∼50 km in diameter. de Zeeuw-van Dalfsen et al. (2004) modelled all three deformation processes together, using a deflating Mogi-source at 2.4 km depth and an average volume change of $-0.31x10^6 m^3 yr^{-1}$ for the shallow magma chamber and a yearly along-axis opening decaying from 3.4 cm/yr to 2.5 cm/yr over 1993-1999. They identified the widespread inflation signature as an inflating Mogi source at a depth of 21 km and a volume change of $25.9x10^6 m^3 yr^{-1}$ (see figure 6.2).

6.1.3 Inter-event deformation: Askja

The Askja volcanic system consists of at least three calderas within the central volcano, bisected by the fissure swarm oriented along the plate boundary at $N16°E$. The

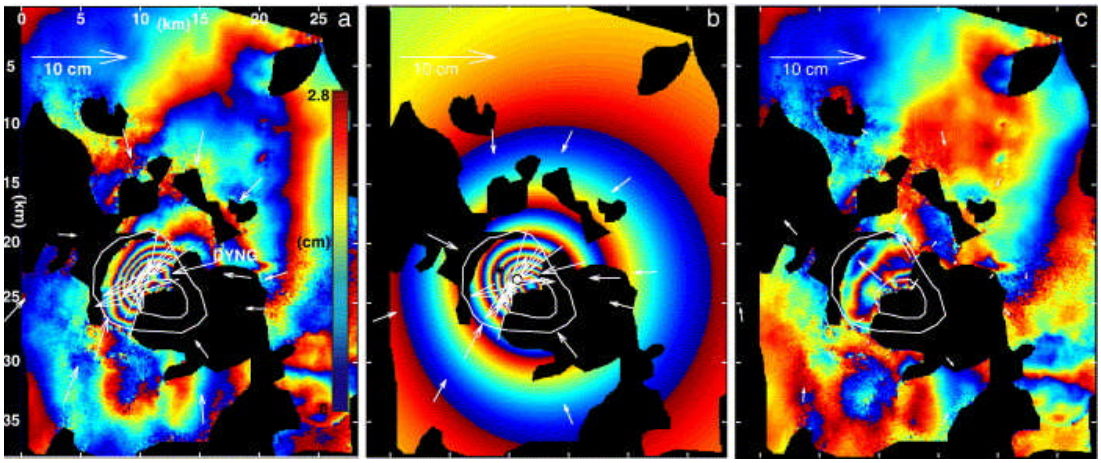

Figure 6.3: Figure from Pagli et al. (2006) showing a) the interferogram with GPS displacements (white arrows) b) the best fit model including a shallow ellipsoidal source and a deep Mogi source, c) the residuals remaining after subtracting the model from the interferogram. Reprinted from Journal of volcanology and geothermal research, vol.152 , Pagli et al. (2006), Deflation of the Askja volcanic system: constraints on the deformation source from combined inversion of satellite radar interferograms and GPS measurements,97-108, ©2006, with permission from Elsevier.

most recent major rifting episode in Askja occurred between 1874-1875 (Sigurdsson and Sparks, 1978) with smaller eruptions between 1921-1929 (Sigvaldason, 1979) and in 1961 (Thorarinsson and Sigvaldason, 1962), and is considered to be in the inter-event phase of the rifting cycle.

As with Krafla, the deformation behaviour in the central volcanic region is of primary focus. Major studies of the area initiated with a series of levelling measurements in Askja's main caldera, taken yearly between 1966-1972 and from 1983 onwards. Tryggvason (1989) observed a period of subsidence between 1968-1970 followed by a period of inflation between 1970-1972. Since measurements restarted in 1983 the caldera has continuously deflated. To model the deformation behaviour of the main caldera Sturkell and Sigmundsson (2000) used the levelling data from 1983-1998 and GPS from 1993-1998, identifying a model that broadly fitted a Mogi point source located near the centre of the caldera at a depth of 2.8 km.

Using a set of 10 interferograms between 1992-2000, Pagli et al. (2006) noted that subsidence was not confined to the caldera and observed deflation of the fissure swarm up to 25km from the central volcano. Pagli et al. (2006) proposed that a revised

model in which an ellipsoidal source at 3 km depth could accommodate the majority of the caldera subsidence, with an additional source at greater depth to accommodate subsidence in the fissure swarm (shown in figure 6.3). Sturkell et al. (2006) similarly proposed a two source model using Mogi point sources for both, suggesting a 16.2 km depth for the deep source. de Zeeuw-van Dalfsen et al. (2013) supported the two source model using micro-gravity data alongside GPS and InSAR deformation data. They observed that the net micro-gravity showed a decrease from 2003-2007, followed by an increase from 2007-2009, and that these changes did not produce an observable affect on the subsidence of the caldera. de Zeeuw-van Dalfsen et al. (2013) suggested that the changes in micro-gravity were due to magma movement and/or possibly a cap in the geothermal system, and that this needed to occur at depth as it did not create and change in deformation at the surface.

Sturkell and Sigmundsson (2000) observed that subsidence rate decayed from an average of ∼10 mm/yr between 1983-1991 to an average of ∼7 mm/yr between 1991-1998 and with additional results available between 1998-2003; Sturkell et al. (2006) proposed that the data between 1983-2003, shown in figure 6.4 followed an exponential decay function as follows:

$$y = -49.8 + 45.7e^{-(year-1983)/\tau} \tag{6.2}$$

where τ is the decay constant in years (τ = 39 years for this time period).

6.2 InSAR - How it works

Synthetic Aperture Radar (SAR) is a remote sensing technique that uses space-borne microwave frequency radar to accurately measure target topography and, by using Interferometric Synthetic Aperture Radar (InSAR) techniques, changes in the target topography over time. Following the launch of SAR-capable Earth observation satellites the technique has grown in the last couple of decades from early interferometric studies such as Zebker and Goldstein (1986) and Zebker et al. (1992) to being applied to a large range of surface deformation studies. Research into co-seismic deformation (e.g. Massonnet et al., 1993, Zebker et al., 1994, Peltzer and Rosen, 1995, Wright et al., 2006, Biggs et al., 2009, Hamling et al., 2010), volcanic deflation and inflation (e.g. Massonnet et al., 1995, Rosen et al., 1996, Pagli et al., 2012) and glacial motion (e.g.

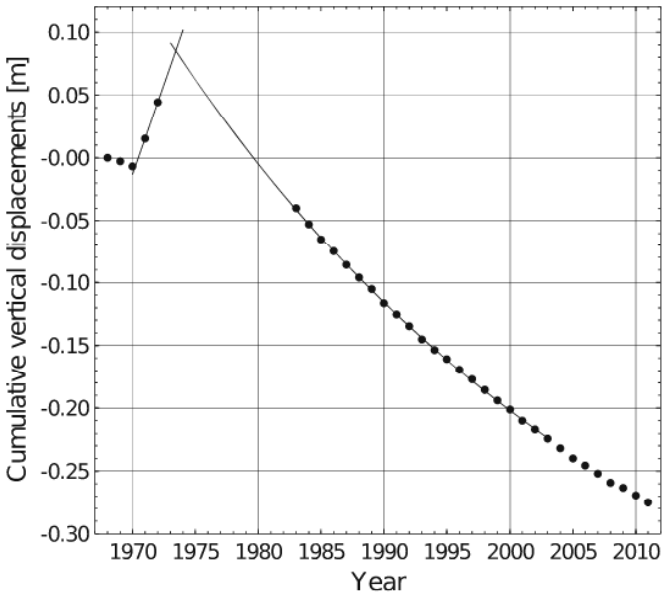

Figure 6.4: Yearly levelling data from 1968-1972 and 1983-2011 show decay in subsidence rate, figure from Sturkell et al. (2006), de Zeeuw-van Dalfsen et al. (2013). Reprinted from Bulletin of volcanology, vol.68 , Sturkell et al. (2006), 1983-2003 decaying rate of deflation at Askja caldera: Pressure decrease in an extensive magma plumbing system at a spreading plate boun dary, 727-735, ©2006, with permission from Springer.

Goldstein et al., 1993, Gourmelen et al., 2011) are just a few of the many examples in which SAR and InSAR have been used to examine and answer geophysical questions that had previously not been possible due to limitations in resolution and accuracy of more conventional tools.

SAR transmits microwave frequency electromagnetic waves towards a target on the Earth's surface and measures the reflected signal as an amplitude component, A, which measures the amount of backscatter energy received at the antenna, and a phase component, ϕ. With repeat satellite passes through time over the same target, the phase component can then be processed using interferometry to measure the phase difference between SAR images and hence any changes in topography as measured along the line-of-sight (LOS) of the satellite. Two examples of repeat-pass geometries can be seen in figure 6.5. Figure 6.5a shows a repeat-pass acquisition where the satellite has followed identical orbits for both passes and there has been a change in range (distance between the satellite and the ground) of δr between repeat passes. In this situation there is a change in the return signal path lengths, δr, that is recorded as a phase difference of the interferogram.

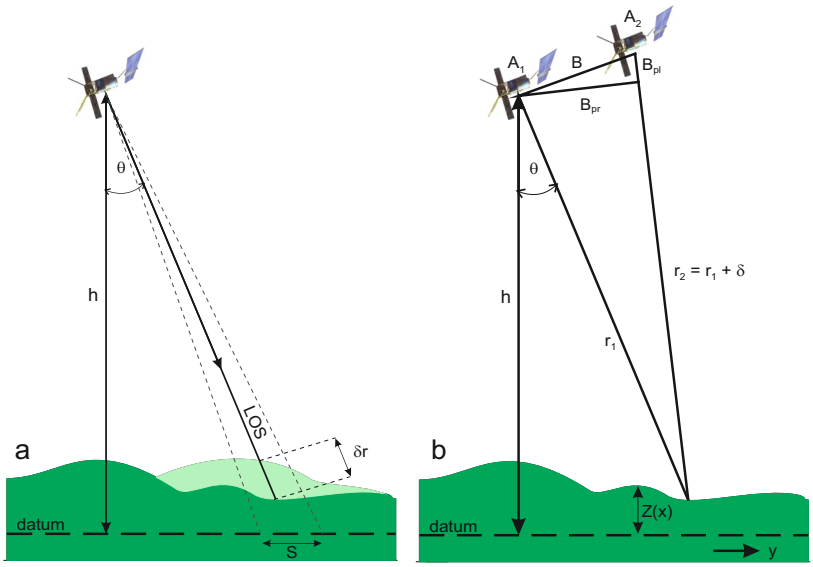

Figure 6.5: Geometry for a side-looking SAR satellite performing repeat passes with a) zero baseline difference between passes and a temporal variance in topography, and b) where there is no temporal variance of topography but a baseline difference, B, between passes. Figure from Garthwaite (2011), redrawn from Peyret et al. (2011) and Bürgmann et al. (2000).

Figure 6.5b shows the geometry for a repeat-pass where the orbits of the first-pass satellite, A_1, often known as the master, and the second-pass satellite, A_2, the slave, have varied by a distance, B, known as the baseline difference (e.g. Bürgmann et al., 2000). The components of the baseline are shown as the perpendicular baseline, $B_\perp$ and the parallel baseline $B_\parallel$, where variations in the perpendicular baseline, $B_\perp$ have been shown to have the greatest affect on the interferogram (this is discussed further in the section on orbital corrections). The resulting LOS path lengths, r_1 and r_2, have a measured difference of δ which will be recorded in the interferogram as a two-way phase-shift of:

$$\phi = \frac{4\pi\delta}{\lambda} \tag{6.3}$$

where λ is the wavelength of the radar.

In practice the repeat-pass geometry includes an aspect of both figure 6.5a, with the ground deformation and figure 6.5b, with a certain amount of baseline difference between orbits, and it is necessary to remove the component of phase caused by the orbital differences to extract the deformation component. In reality, the recorded component of phase, $\Delta\phi_{int}$ consists of not only the deformation phase signal, but also several sources of error that each present a possible change to the measured return phase signature.

The interferometric phase, $\Delta\phi_{int}$, is thus composed of a number of factors that combine together to produce the interferometric fringes of the final interferogram, as outlined in the following equation:

$$\Delta\phi_{int} = \Delta\phi_{def} + \Delta\phi_{topo} + \Delta\phi_{orb} + \Delta\phi_{atm} + \Delta\phi_{noise} \tag{6.4}$$

where $\Delta\phi_{def}$ is the phase representing the actual ground displacement along the satellite LOS. The other components of phase, $\Delta\phi_{topo}$, $\Delta\phi_{orb}$, $\Delta\phi_{atm}$ and $\Delta\phi_{noise}$ respectively the topographic, orbital, atmospheric and noise, will all need to be calculated/estimated and removed from $\Delta\phi_{int}$ to give $\Delta\phi_{def}$. A brief description of each of these components follow in the next section, continuing with the processing section which outlines how the majority of the unwanted components of phase are removed or compensated for to achieve the final interferogram.

6.3 Interferometric Phase

6.3.1 Orbital component of phase

The satellite can be affected by a number of forces, from atmospheric drag and ocean tides to gravitational effects from the Earth and other planetary objects, and whilst the satellite is able to make adjustments to its position to correct its orbit, it does not do this constantly and baseline differences can build up between acquisitions. For ERS and Envisat these can be 100s of metres (e.g. Bürgmann et al., 2000).

The rate of change of phase, ϕ, with respect to incidence angle, θ is dependent on $B_\perp$ as follows:

$$\frac{\partial\phi}{\partial\theta} \approx \frac{4\pi}{\lambda} \cdot B_\perp \tag{6.5}$$

Which results in the following phase ramp that can be calculated and removed from the original component of phase:

$$\frac{\partial\phi}{\partial\theta} = \frac{4\pi}{\lambda} \cdot \frac{B_\perp \cos\theta}{h} \tag{6.6}$$

The removal of the orbital component of phase is known as interferogram flattening and is discussed further in the data processing section. It should be noted that whilst the actual measurement of baseline difference is normally accurate to a few cm, for ERS satellites this is published as 10-15 cm cross-track and 5-7 cm radially (Scharroo and Visser, 1998), any error in the baseline measurement will cause an additional phase

difference that will not be accounted for in the above equation (Zebker et al., 1994). Whilst, within the range of error for the ERS satellite, this is a fairly small additional phase, when looking at small amounts of deformation such as those that occur in interseismic settings, this error may become a significant issue.

6.3.2 Topographical component of phase

An altitude change in the topography produces a phase change that is directly related to $B_\perp$ by the altitude of ambiguity, h_a. h_a is defined as the change in altitude that generates a phase change of 2π in the interferogram, and is shown to be inversely proportional to $B_\perp$ by the following equation (Hanssen, 2001):

$$h_a = \frac{r_s \lambda \sin\theta}{2B_\perp} \tag{6.7}$$

where r_s is the radar target distance of the slave image. This shows that with increasing $B_\perp$ an increasing number of fringes will be created for any given altitude range. Whilst the relationship in equation 6.7 allows the topographical phase component to be calculated using a DEM and removed, there is a limit to $B_\perp$, beyond which the topographic component will cause decorrelation of the interferogram. This is discussed further in the processing section.

6.3.3 Atmospheric component of phase

The troposphere and the ionosphere are the two layers of Earth's atmosphere that account for the majority of the atmospheric phase component, both introducing spatially and temporally varying elements of phase into the interferogram, with atmospheric water vapour in the troposphere providing the greatest contribution (Li et al., 2004). Changes in humidity, temperature and pressure are just a few of the possible environmental fluctuations that influence the effect of atmospheric water vapour on interferometric phase. There are two main effects on SAR radar propagating through the troposphere: a delay of the radar signal and a possible distortion of the propagation path (Rosen et al., 2000), both of which would influence the interpreted target elevation, with different influences for each SAR pass. The ionosphere is a region of charged particles that can can have a filtering effect on the frequencies of the SAR signal as they propagate through. Research into characterising the effect of both the troposphere and the ionosphere on interferometric phase is still ongoing (Freeman and Saatchi, 2004,

Meyer et al., 2006, Meyer and Watkins, 2011) and the possible phase component is not yet fully quantified. Various methods of atmospheric phase removal are discussed and tested later in this chapter in the $\pi-rate$ section.

6.3.4 Noise component of phase

Temporal or spatial variance of the target between the master and slave SAR images can cause a loss of coherence in the resulting InSAR output. In addition to the temporal changes caused by the atmospheric components, temporal changes can be caused by such things as seasonal variance in vegetation growth and weather-related issues such as snowfall. Variance in vegetation can also present a problem spatially with, for example, leaves on trees producing multiple point scatterers with a single pixel that do not actually represent the elevation of the ground target, with vegetation growth not only masking the ground target but also producing elevation error in the combined signal for that pixel.

Ideally to reduce issues with coherence, regions that have very little change temporally and spatially (such as rocky or urban areas that contain very little vegetation) give very good temporal coherence and can be coherent even over a number of years and the lack of vegetation also results in a minimised error from multiple point scatterers.

As vegetation coverage of a region increases, it is possible to improve coherence by selecting SAR images that offer the smallest temporal change possible - selecting images from the same time of year will give a predictable level of vegetation growth, for example a region of agricultural crops should have a similar level of growth at the same time each year, or selecting images in the winter only, when vegetation has died back. Some regions, such as in Iceland, are heavily affected by seasonal climate change with, for example, ground covered with heavy snow in the winter months. Taking SAR images from months not affected by adverse weather conditions would help maintain levels of coherence.

As many point scatterers combine within a single pixel, rapid spatial changes, such as those caused by vegetation, create noise in the resulting pixel signal. Performed after the topography correction has been applied, complex multi-looking (Goldstein and Werner, 1998) is a process of reducing this noise by averaging adjacent pixels in the raw interferogram. Averaging pixels does result in a reduction of resolution but provides an improved phase accuracy and coherence of the interferogram. For example, 4-looks

would be to take 4x4 pixels (in the case of ERS data, a pixel in the raw data represents 90x90 m of ground coverage) and average the result of all the pixels to replaced by one pixel 360x360 m. Working on the assumption that the phase changes over a greater distance than the new pixel resolution,this process should minimise random noise whilst keeping a strong phase signature.

The standard deviation of coherence, σ_{coh} gives a measure of the phase noise and is related to the variance on the phase by (adapted from Rodriguez and Martin (1992)):

$$\sigma_{coh} = (\frac{\lambda}{4\pi})\frac{1}{\sqrt{N_L}}\frac{\sqrt{1-\gamma^2}}{\gamma} \tag{6.8}$$

where N_L is the number of looks.

6.3.5 Deformation component of phase

With all the other components of phase removed the original phase, ideally the remaining phase component should be that of ground deformation of the ground target, as measured along the line-of-sight (LOS) of the satellite. This component of phase, $\Delta\phi_{def}$ is defined by:

$$\Delta\phi_{def} = \frac{4\pi\delta r}{\lambda} = \frac{-4\pi}{\lambda}\hat{l}\cdot u \tag{6.9}$$

where $\delta(r)$ is the range change between the master and slave LOS range, u is the ground displacement vector and $\hat{l}$ is the unit vector pointing from the target along the satellite's LOS. If it is possible to constrain the north-south and east-west horizontal displacement of the ground target, using the geometries of the satellite it is then possible to extract values for vertical displacement from the deformation component of phase. I will look to constrain horizontal displacement using GPS data using velmap software, this will be discussed later in the chapter.

6.4 ERS and Envisat Satellites

There are a number of available satellites producing SAR images over a range of frequencies, such as Radarsat-1 and -2, ERS-1 and -2 and Envisat all operating in C-Band, ALOS operating in L-Band and TerraSAR-X operating in X-Band. Due to data availability over Krafla as a result of compatibility between the satellite SAR frequency, orbits and track coverage, SAR images acquired by the satellites European Remote Satellite(ERS)-1, ERS-2 and Envisat were considered for this project (see table 6.1).

To examine the post-seismic and inter-seismic behaviour of the Krafla and Askja fissure swarms it is necessary to create as long and complete a time series as possible. Due to the limited lifespan of each of the individual satellites, it would be preferential to combine images from at least two of the three satellites.

Table 6.1: ERS-1, ERS-2 and Envisat.

Satellite	Repeat Cycle (days)	Wavelength (cm)	Operating Frequency	Coverage Period
ERS-1	35	6	C-Band	1991-2000
ERS-2	35	6	C-Band	1995-2011
Envisat	35	6	C-Band	2003-2012

Maintaining a sun-synchronous polar-orbit at an altitude of 780-790 km, their orbital paths planned to give the same ground track coverage and operating at similar C-band frequencies, the ERS-1, ERS-2 and Envisat satellites were designed to allow continuity of coverage and compatibility of recorded data across the lifespans of all three. (A small difference between the wavelengths of ERS and Envisat satellites means that they have to be processed seperately to produce an interferogram, but compatibility in track locations allow interferograms to be used together to produce a time series.) ERS-1 launched in July 1991, carrying a suite of instrumentation including the SAR, an altimeter radar and an infrared imaging sensor. ERS-2, carrying similar instrumentation to ERS-1 (with an additional atmospheric sensor) launched in July 1995. ERS-1 and ERS-2 maintained identical orbits, orbiting the earth every 101 minutes and completing a repeat cycle every 35 days. ERS-1 continued operations until March 2000 and ERS-2 until July 2011 (issues calculating Doppler values started in 2000 - this is discussed later in the chapter). Envisat launched in 2002, with the same orbit and repeat cycle as ERS-1 and ERS-2, carrying an increasingly advanced range of radar and optical instrumentation. The improved SAR (known as the Advanced Synthetic Aperture Radar, ASAR), whilst compatible with ERS-1 and ERS-2, had enhanced coverage with the selection of swaths of either 100 km or 400 km wide, improved incidence angle range and an increased number operational modes. Envisat continued operations until April 2012.

6.5 Selecting SAR Images

There are a number of factors that need to be taken into account when selecting suitable SAR images for processing into interferograms:

- availability and coverage of satellite tracks
- temporal changes in observed region
- baseline difference between SAR acquisitions
- doppler difference between SAR acquisitions

6.5.1 Selecting tracks

The ERS and Envisat satellites followed a near polar orbit imaging the Earth's surface both as they descended from north to south and ascended from south to north. As the Earth rotates along the equatorial plane, it was possible to acquire SAR images of the any given location with both ascending and descending tracks. For ERS and Envisat satellites, the SAR antenna is always pointed to the right-side of the track (known as the look-direction), giving ascending and descending tracks an east and west look-direction respectively.

There is good SAR coverage of Iceland with a choice of available tracks covering the Northern Volcanic Zone. I narrowed the tracks down to a possible four tracks that gave full coverage of both the Krafla and Askja fissure swarms with the two ascending tracks, 1 and 230, and two descending tracks, 9 and 281 as shown in figure 6.6. There is no need to be overly concerned with the effects of layering and shadowing for the region of study as the fissure swarms have relatively low slope angles. This study is not looking to constrain the deformation in the regions of high slope angle over areas such as the Askja caldera that are subject to both issues and would need a combination of both ascending and descending tracks to be able to fully quantify the deformation. As such, I only needed to select a single track, either descending or ascending, and my choice is based mainly on quantity and quality of available SAR images for each of the tracks. Of the four tracks, track 281 far surpassed the others on quantity of full coverage SAR images with sufficiently high repeat times to offer good resolution for a final time series. Track 281 provided continuous coverage from ERS-1, ERS-2 and Envisat and provided multiple possibilities for possible SAR pairings.

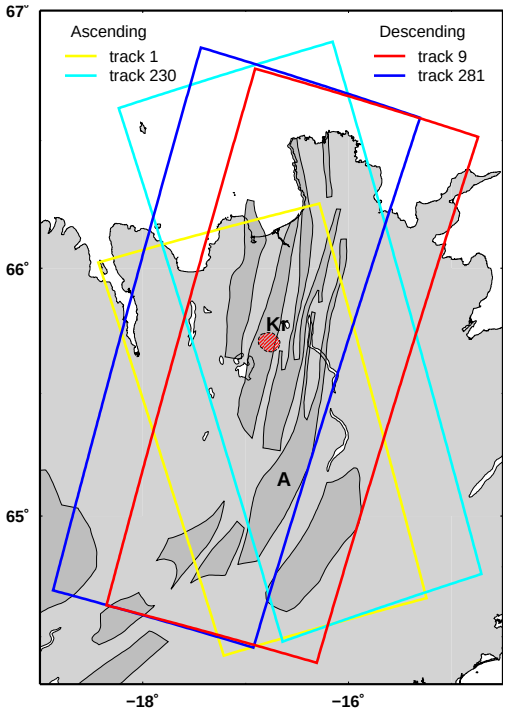

Figure 6.6: Showing the best available tracks for ERS-1, ERS-2 and Envisat over the Krafla (Kr) and Askja (A) fissure swarms. Descending track 281 was chosen for the quantity of good quality images that allowed for the longest and most complete time series across both Krafla and Askja.

6.5.2 Temporal changes

To further narrow down useable SAR images any temporal changes in the region should be taken into account. Iceland is subject to harsh conditions in the winter with heavy falls of snow covering the ground for many months, with central regions such as Askja having snow cover as early as September and remaining in place through to as late as early May. Vegetation is very low and slow growing in Iceland and whilst Krafla contains regions in the south and north of the fissure swarm that have very low-lying shrubs and the Askja fissure swarm is practically devoid of any vegetation at all. Thus noise due to multiple point scattering from vegetation is minimal and fairly constant through the summer season and should not present an issue for interferometric processing of SAR pairs from any time over the summer months. To account for the snow cover, I narrowed the available SAR images down to those from May to September only.

6.5.3 Baseline differences

The radar wavelength, λ has been shown in equation 6.6 to be inversely proportional to fringe frequency. If there is a phase change equal to or greater than 2π within the range resolution, $\Delta\rho$ (i.e. there is more than one phase change across a single pixel of the interferogram) then the phase is no longer well-defined and will result in decorrelation in the interferogram. Thus, there is a critical perpendicular baseline, $B_{\perp c}$ beyond which the interferogram will decorrelate, defined by the radar wavelength and the range resolution as follows (Rosen et al., 2000):

$$B_{\perp c} \propto \frac{\lambda}{\Delta\rho} \tag{6.10}$$

where it shows that the critical baseline scales linearly with the radar wavelength. It is important to take this in to account when selecting SAR image pairs for interferometric processing. In addition it was shown in 6.7 that the frequency of fringes created by the topographic component of phase increases with increasing baseline, which places an additional restraint on the size of the $B_{\perp}$. In practice for ERS C-band SAR, if $B_{\perp}$ is kept below ~500 m the effect of baseline difference on decorrelation caused by the orbital and topographic phase components is kept to a manageable level.

6.5.4 Doppler Shift

Due to the relative motion between the satellite and the ground target, there is a frequency shift known as the Doppler shift, between the transmitted and received signals. This shift in frequency is dependent on a number of factors: motion of the Earth and ground target, the look angle of the antenna and the satellite attitude, which is a measure of the satellite's velocity and position. Of particular importance to the creation of InSAR from SAR images is a consistent Doppler Centroid (DC) frequency, the centre frequency of the azimuth bandwith of the SAR image. The smaller the DC difference between the SAR pairs and hence the larger the percentage of azimuth spectral overlap of the images, the better the coherence of the pair. If the DC difference is too great the SAR pair will not be coherent, with total decorrelation occurring when the DC difference is equal to the azimuth bandwidth.

The attitude of both ERS-1 and ERS-2 was controlled by the Attitude and Orbit Control System (AOCS) whose nominal operating configuration used three gyroscopes

and digital earth and sun sensors. The AOCS minimised the doppler shift by steering the satellite using projected velocity vectors from earth models, adjusting the yaw of the satellite and tuning the receivers (Sunda et al., 2002).

At the start of 2001, three of the six on-board ERS-2 gyroscopes failed, followed by two more over the following year. To preserve the remaining gyroscope for emergencies, a new AOCS configuration was uploaded to ERS-2, which functioned without any functioning gyroscopes, operating in a gyro-less yaw steering mode called the Zero-Gyro-Mode (ZGM). ZGM made use of alternative on-board navigational systems to quantify the actual pitch, roll and yaw of the satellite and made adjustments based on a limited orbital dataset. The result was a much less stable attitude for the satellite, and an increased variance in the DC frequency. In establishing SAR image pairs for InSAR processing using ERS-2 images post 2001, it is necessary to consider the DC frequency and ensure that the DC difference is kept as small as possible.

Later in the chapter, figure 6.10 shows the pairings that I have processed for ERS-1 and ERS-2, based on a good combination of low baseline and doppler centroid difference. The pairs that have been successfully processed to produce a final interferogram are shown connected by red lines, with failed attempts at pairings shown connected by the grey lines. An interferometric pair can be made from any combination of ERS-1 and ERS-2 SAR images. Envisat SAR images have to be processed separately through to interferogram and in principle the interferograms from both ERS and Envisat can then be used together to create a time series. For the purposes of this research I have used the Envisat and ERS interferograms to create two separate time series and used the Envisat time series to verify the results of the ERS time series.

6.6 InSAR processing

I completed the processing of SAR images through to final interferogram using the ROI_pac (Repeat Orbit Interferometry package) software from the Jet Propulsion Laboratory, California Institute of Technology (Rosen et al., 2004).

All the possible stages of the ROI_pac processing flow can be seen in the schematic shown in figure 6.7. The following sections outline the key elements of the processing flow that have been used for creating the final interferograms in this study (for a more in-depth study of the interferometric processes and the algorithms used there are a number of good published sources available (e.g. Massonnet and Feigl, 1998, Rosen

et al., 2000, Bürgmann et al., 2000)).

In order to fully process a SAR pair through to final corrected interferogram it is necessary to have an appropriate digital elevation model of the track area to use for topographical corrections. It is possible to create a DEM from SAR images (Zebker and Goldstein, 1986). However, for this study I have obtained a full 90 m resolution DEM of Iceland from the Icelandic Land Survey made from a combination sources e.g. GPS-tracking, aerial photographs and SPOT-5 satellite images

6.6.1 SAR Image Formation

As discussed earlier, Doppler shift can cause a variation between SAR images of the azimuth frequency spectrum which can result in regions of non-common frequency that can cause image decorrelation of the interferogram. To minimise decorrelation ROI_pac uses the mean Doppler Centroid frequency to reprocess the two raw images to the same Doppler Centroid frequency. Although this results in a slightly defocused image, the coherence between the two SAR images can be much improved. Firstly, ROI_pac calculates the mean Doppler Centroid frequency, $f_c(r)$, using:

$$f_c(r) = \frac{(f_{DC_M}(r) + f_{DC_S}(r))}{2} \tag{6.11}$$

where $f_{DC_M}(r)$ and $f_{DC_S}(r)$ are the Doppler Centroid of the master and slave SAR images respectively. The baseline difference between the master and slave image orbits is then calculated and repeat orbit interferometry is performed using range and azimuth compression to create full resolution single look complex (SLC) images for both the master and the slave.

6.6.2 Image Co-Registration

Co-Registration ensures that the same range/azimuth is represented by the same pixel in both the master and slave images. It allows for compensation of a number of effects caused by differences in acquisition between the master and slave images: differing sensor attitudes, along and across track shifts, orbit skewing, different sampling rates and differing geometry due to change in view angle

To perform co-registration ROI-pac runs through a series of increasingly refined offset estimations to create a 2D field of offsets between the master and slave SAR images. The original offset estimate is made using orbits and various SAR image parameters

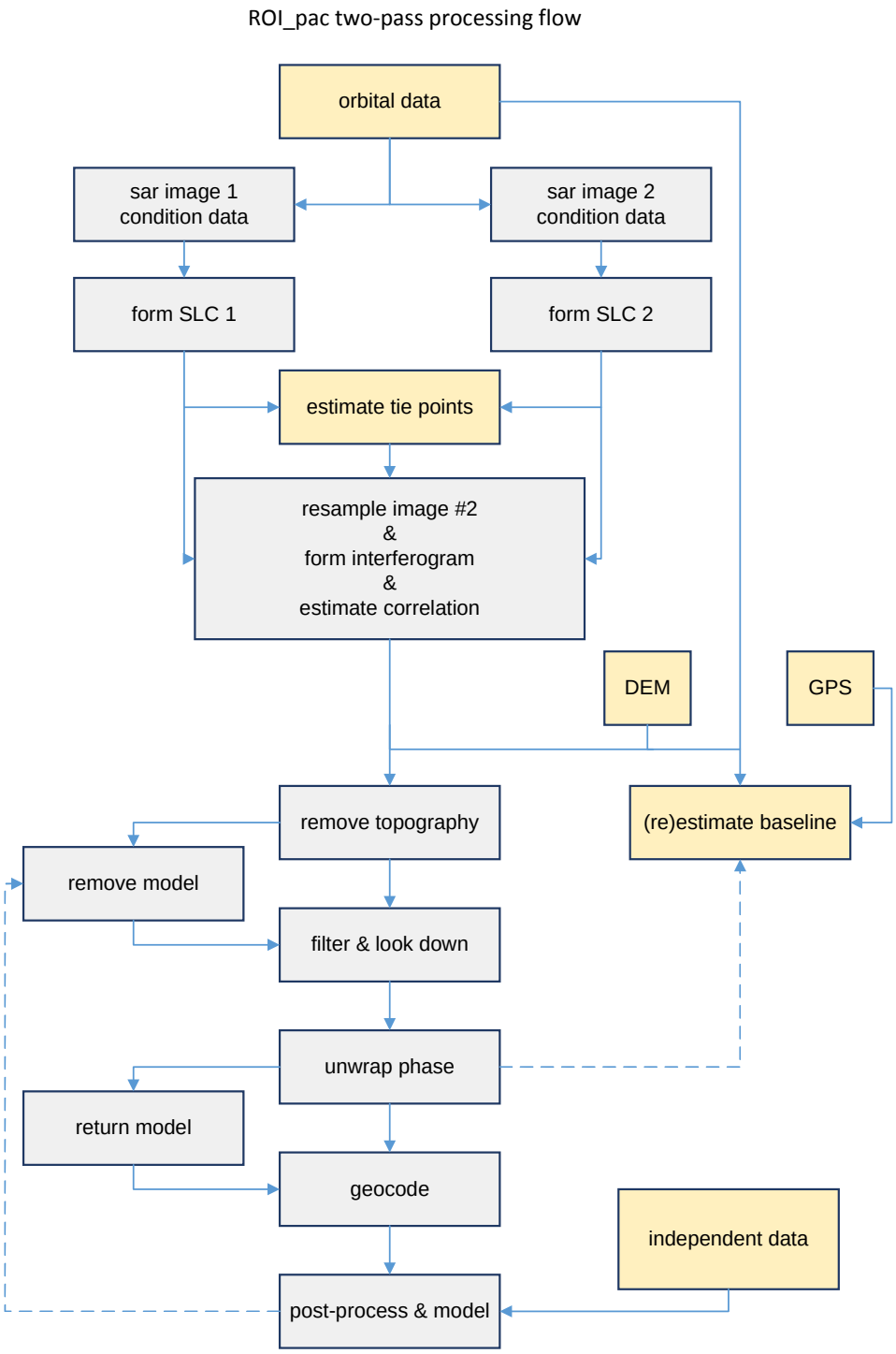

Figure 6.7: Schematic showing the ROI_pac processing flow.

which are then refined by gross matching and culling of points that are outside the fit (>0.5 pixels). A second finer matching is performed to further refine the offsets, with a first order affine transformation being applied to the results and the cull of points >0.08 pixels outside the fit. The slave image is then resampled using a second order polynomial function fit to the final culled offsets, creating a final slave image that is co-registered to the master image.

6.6.3 Create Interferogram

To create the raw interferogram from the master and slave image, each complex pixel of the master is multiplied by the complex conjugate of the slave pixel (Gabriel and Goldstein, 1988). The final raw interferogram still contains all the phase components outlined earlier: orbital, topographical, deformation, atmospheric etc, which will be removed at a later stage in the processing. An example of a raw interferogram can be seen in figure 6.8a.

6.6.4 Flatten Interferogram

The orbital component of phase, caused by baseline differences in the orbits of the master and slave images, is removed using a process called interferogram flattening (figure 6.8b). ROI_pac creates a constant elevation, curved Earth DEM which is then used alongside precise orbital data (we have used PRC orbital data for the ERS satellites) to calculate the expected phase value for the geometry of the orbit with respect to the curved Earth DEM. This phase value is then subtracted from the phase of the interferogram. The resulting interferogram still contains the topographical component of phase which will be removed further on in the processing sequence.

6.6.5 Correlation

Interferometric decorrelation can be caused by noise creating random changes in radar signal. This stage calculates the spatial correlation of the interferogram to use as an estimation of the interferometric coherence. A coefficient of correlation, γ, is calculated for each pixel, with a value between 0 (phase value is all noise) and 1 (phase value shows no noise), estimated as a weighted spatial average over an NxM pixel triangular weighted window. There is a lower limit on the size of NxM $\gtrsim\sim$ 4, below which the number of pixels averaged is so small that the correlation coefficient is usually overestimated,

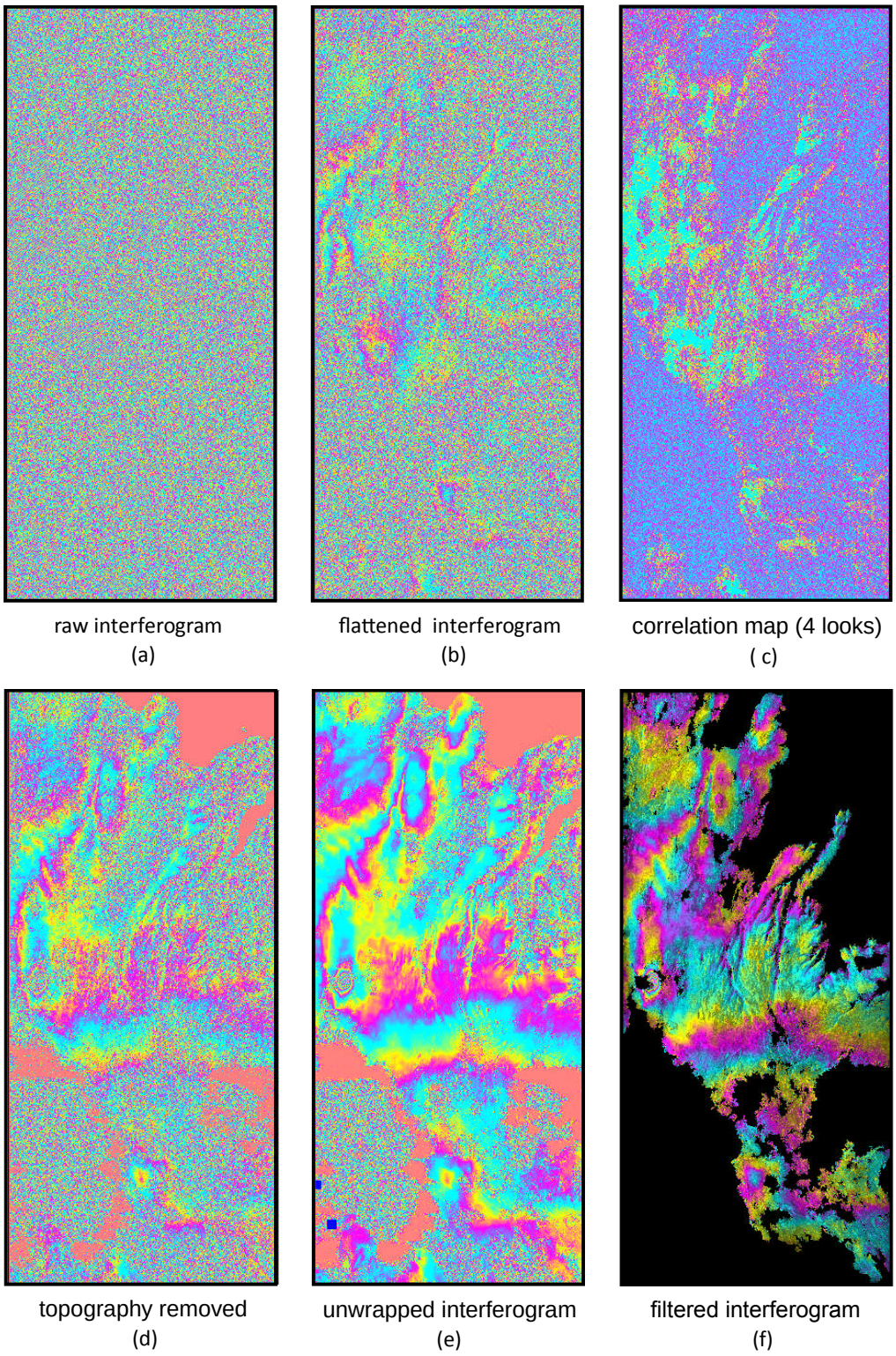

Figure 6.8: An example of the output for the key stages in the ROI_pac processing flow, using SAR image pair 2000-08-06 and 2004-07-11. a)- f) show the interferogram progress from the raw interferogram in a) through the removal of orbital phase (flattening) in b), the formation of the correlation map in c), the removal of the topographic phase in d), filtering in e) and the unwrapped interferogram in f). The final geocoding stage for this interferometric pair is shown in figure 6.9.

ROI_pac uses a default of 5x5 pixel window. An example of a correlation map is shown in figure 6.8c.

The correlation coefficient was is related to the standard deviation of the interferometric phase such that the smaller the value of the correlation coefficient, the larger the standard deviation of the interferometric phase, with larger values of standard deviation causing possible phase unwrapping issues in the latter stages of the processing sequence.

6.6.6 Remove Topography

The topographical removal is performed using the orbital geometries calculated from the orbital data with respect to an existing DEM of appropriate resolution. As in the flattening process, the orbital geometries can then be used to calculate the expected phase signature created by the topography of the ground target. This differs from the flattening procedure as it uses a real DEM containing topographical features (instead of a constant elevation DEM). This simulated phase is then subtracted from the interferogram (see figure 6.8d).

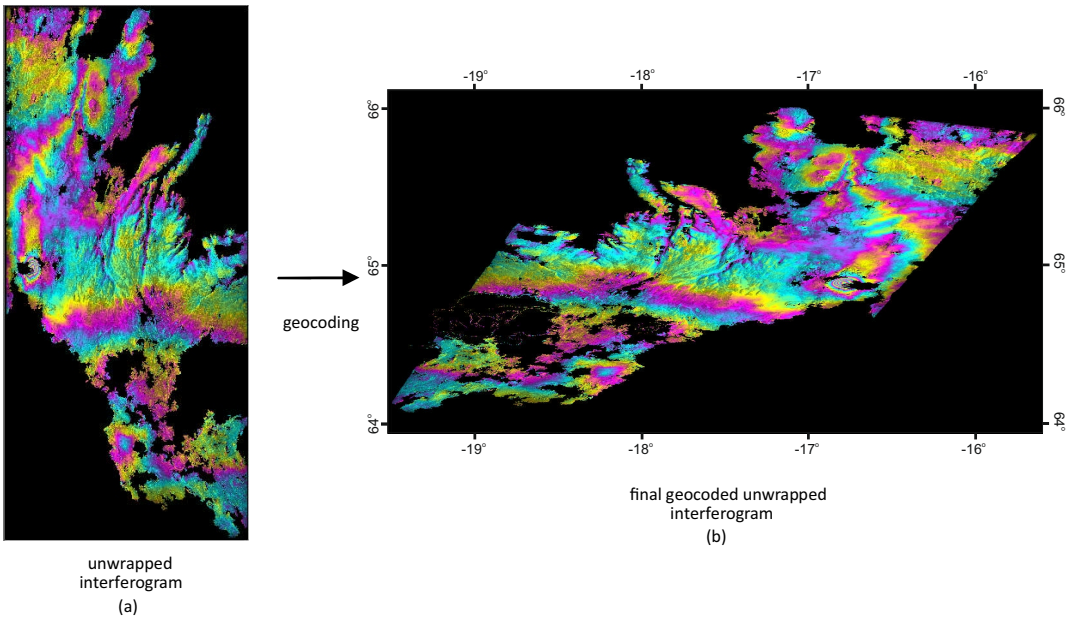

Figure 6.9: Geocoding: the unwrapped interferogram (a) is geocoded from radar coordinates into the geographic coordinates of the DEM to produce the final geocoded unwrapped interferogram.

6.6.7 Filtering

The filtering process first uses a method called 'power spectrum filtering' (Goldstein and Werner, 1998). Within a local area, the fringe frequency of interferometric phase will be dominated by a single frequency caused by the target backscatter with a broader band of less dominant frequencies associated with noise. The power spectrum filtering aims to filter out the noise from the local power spectrum, improving the signal to noise ratio by keeping only the frequency of the dominant surface backscatterer. The level of filtering used is controlled by the power spectrum exponent, α (with a value between 0 and 1). For interferograms with moderate correlation (γ >0.25), filtering can be moderate and a value of α in the range of 0.2 - 0.5 should be used. The value of α can be increased, resulting in a more severe filtering, for interferograms with low correlation. ROI_pac runs the power spectrum filtering with a default power spectrum exponent of 0.5. An example of a filtered interferogram is shown in figure 6.8e.

Following on from the power spectrum filtering, ROI_pac then creates a mask for the area of the interferogram that will be unwrapped in the next stage of the process. The mask is a combination of a coherence and a low amplitude mask, with the coherence mask based on the local phase variance (calculated from the filtered interferogram), and the amplitude mask designed to cut out pixels below a set amplitude threshold (default is $5.0e^{-5}$).

6.6.8 Unwrapping

Phase unwrapping is a stage that uses an algorithm to convert the fringes of an interferogram into an actual displacement. As the total phase difference between two points on an interferogram can be calculated by counting the the number of fringes between the two points, the number of fringes can then be converted into displacement using the wavelength of the radar. An example of an unwrapped interferogram is shown in figure 6.8f. The are several choices of unwrapping algorithms in ROI_pac and I selected the 'classic' branch cut unwrapping algorithm based around the algorithm presented in Goldstein et al. (1988). This option provides a more robust solution in terms of being correct in terms of the phase (Biggs et al., 2007). As a default the unwrapping procedure starts in the centre of the interferogram and works out across the coherent areas of the interferogram. If the centre of the interferogram is incoherent, it is possible to change the default starting point to a coherent area, in addition bridges can be made

to connect between coherent regions to ensure that all coherent areas are unwrapped.

6.6.9 Geocoding

Geocoding is the final stage for the interferogram in which the interferogram is resampled onto a uniform grid given by the reference ellipsoid (in our case given by the Iceland DEM) i.e. the unwrapped interferogram is geocoded from radar coordinates into the geographic coordinates of the DEM. An example of the resultant geocoded interferogram is shown in figure 6.9.

6.6.10 Interferograms

With the temporal weather conditions restricting the range of useable SAR images to those acquired from May to September, and after taking into account the baseline difference and doppler difference of all the available SAR images, I identified 106 possible pairs for the ERS-1 and ERS-2 satellites and processed through ROI_pac, see figure 6.10. Of these, I successfully unwrapped and geocoded 52 pairs to useable interferograms spanning from 30^{th} July 1992 through to 24^{th} August 2008. The final unwrapped and geocoded interferograms for the ERS SAR pairs can be seen in appendix D. In addition, I identified 23 possible pairs for the Envisat satellite and of these, I successfully unwrapped 11 pairs covering from 11^{th} July 2004 through to 13^{th} September 2009, see figure 6.11.

6.7 π-rate

$\pi-rate$ (Poly-Interferogram Rate And Time-series Estimator) is a software package that, given a set of unwrapped InSAR images for an area, is able to calculate both the incremental and cumulative time series and produce an average rate map for that area. Originally developed by Hua Wang (Wang et al., 2009), π-rate comprises the multi-interferogram method proposed by Biggs et al. (2007), topographically-correlated atmospheric delay corrections proposed by Elliott et al. (2008) and more recently, a number of algorithms including the variance-covariance matrix for large-scale interferograms as outlined in Wang et al. (2012).

A schematic of the π-rate processing flow can be seen in figure 6.12, a brief explanation of the key steps is given in the following sections,while more detailed overviews

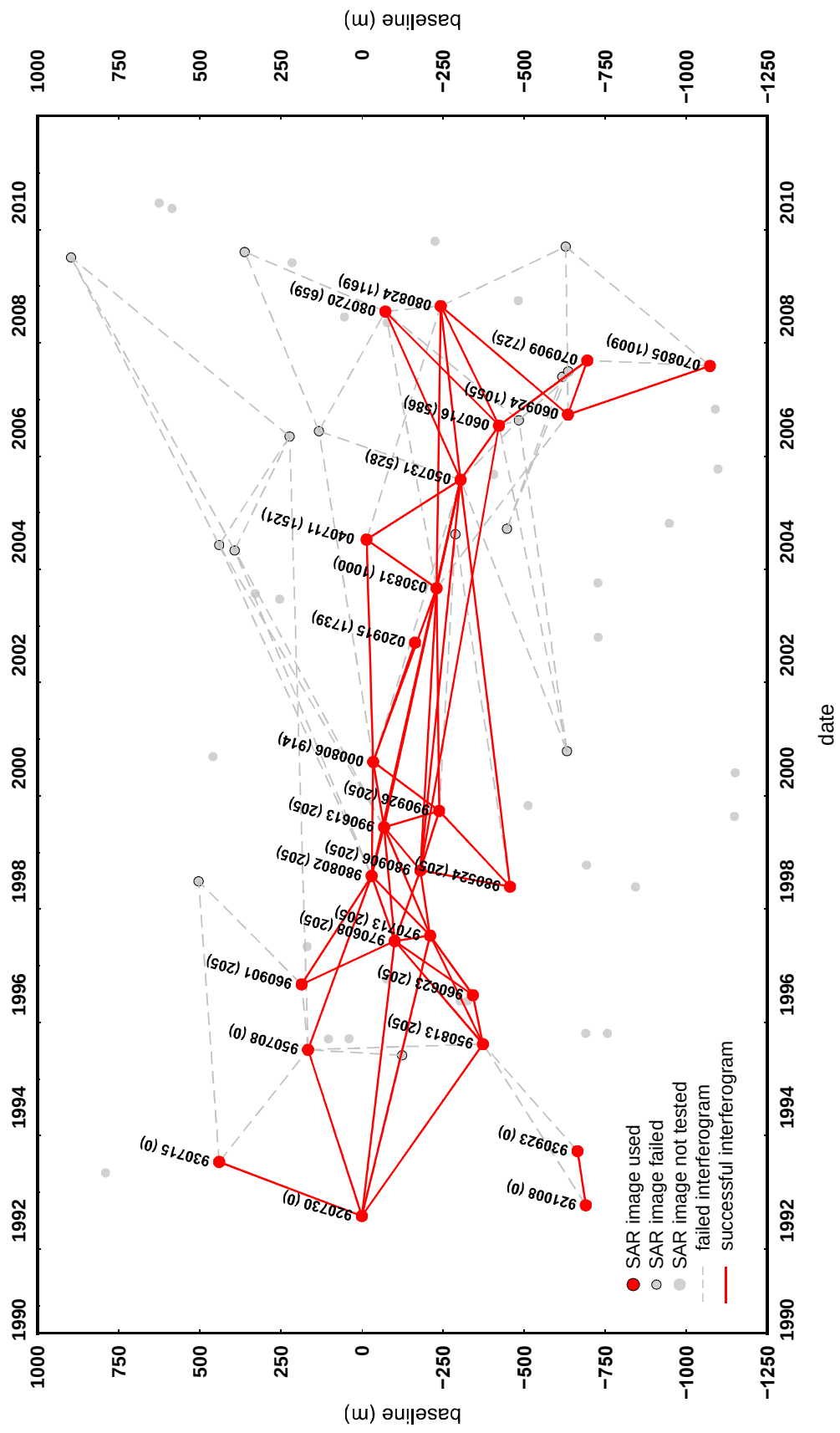

Figure 6.10: Plot of the baseline vs date of ERS-1 and ERS-2 SAR images for descending track 281 with the baseline and doppler shift relative to the first SAR image, 920730. Winter months have been excluded from any processing due to seasonal weather conditions, successfully processed interferograms are shown as red lines, SAR pairs that have not unwrapped successfully are shown by a grey dashed line.

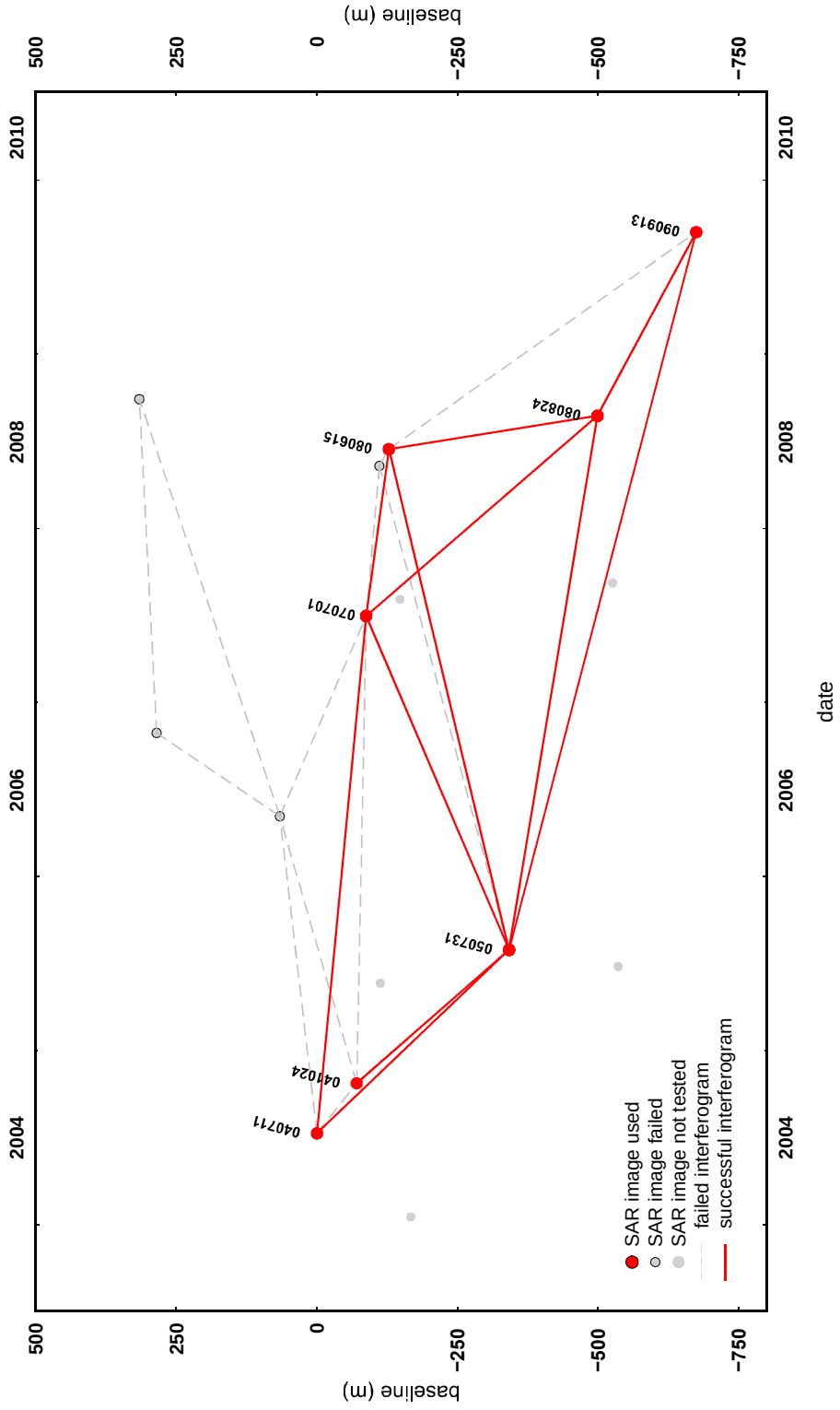

Figure 6.11: Plot of the baseline vs date of Envisat SAR images for descending track 281, with baseline values relative to the SAR image, 040711. Winter months have been excluded from any processing due to seasonal weather conditions, successfully processed interferograms are shown as red lines, SAR pairs that have not unwrapped successfully are shown by a grey dashed line.

of the methods and algorithms used in π-rate are given by Biggs et al. (2007), Elliott et al. (2008), Wang et al. (2009, 2012), Garthwaite (2011).

For processing in π-rate three interferogram groups were selected, these can be seen in figure 6.13. Group A was used for testing the various options for atmospheric correction available in π-rate and contained a select group of interferograms with the most complete coherent coverage over the largest possible temporal range. Group B was a group that expanded on Group A, including slightly less coherent interferograms to increase the number of epochs in the final timeseries and Group C included all available 52 interferograms (some of which offer only partial coverage of the region) to examine the effect on the quality of the final timeseries by including interferograms that had much smaller regions of coherency. A detailed list of the interferograms included in each group can be seen in Appendix E.

It is possible to apply a variety of masks during the various stages of the π-rate process. Masking over the whole time series or for just specific epochs, allows for removal of co-event and post-event deformation during the orbital and atmospheric error calculations ensuring that deformation is not removed or smoothed.

6.7.1 Minimum spanning tree algorithm

An adaptation of the minimum spanning tree (MST) algorithm (Kruskal, 1956) is used to calculate a connected chain of interferograms selected from a given group. It does this by giving the available interferograms a weighting value based on their coherence (the ratio of non-zero pixels) with the most coherent having the highest weighting. π-rate then calculates a path that is able to connect all the SAR acquisition dates in the group as a non-closed loop with the highest total weighting possible. The interferograms included in the final MST are referred to as the non-redundant observations and for most steps in π-rate only non-redundant observations are used. An example of the MST created by π-rate can be seen in 6.14 where 12 non-redundant interferograms are selected for the single MST calculated from the original 17 interferograms in group A. For Group B, with 36 interferograms, π-rate calculated an MST with 21 non-redundant interferograms, and for Group C, using 52 interferograms, an MST with 25 non-redundant interferograms.

An MST matrix is created based on the coherence value of each pixel - a threshold of coherent pixels is selected in π-rate and the adapted MST algorithm checks each

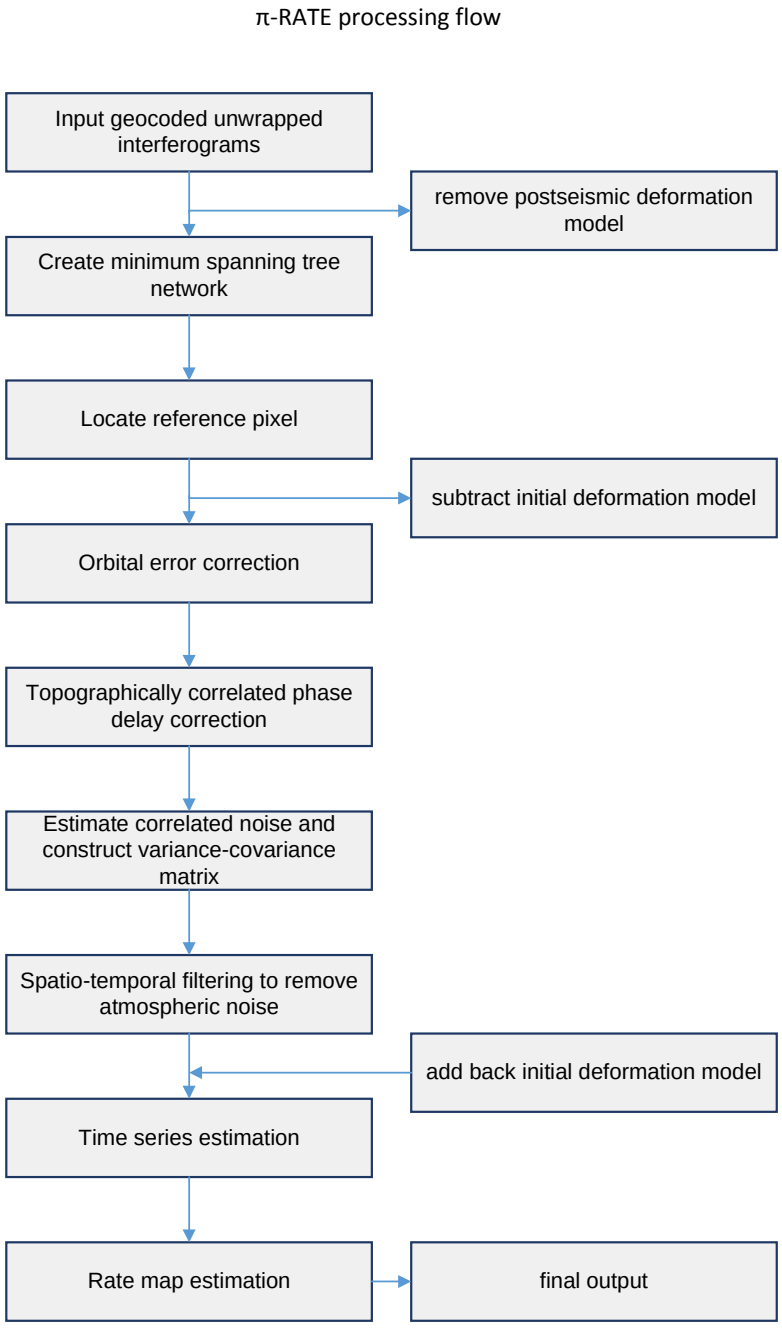

Figure 6.12: Schematic showing the π-rate processing flow.

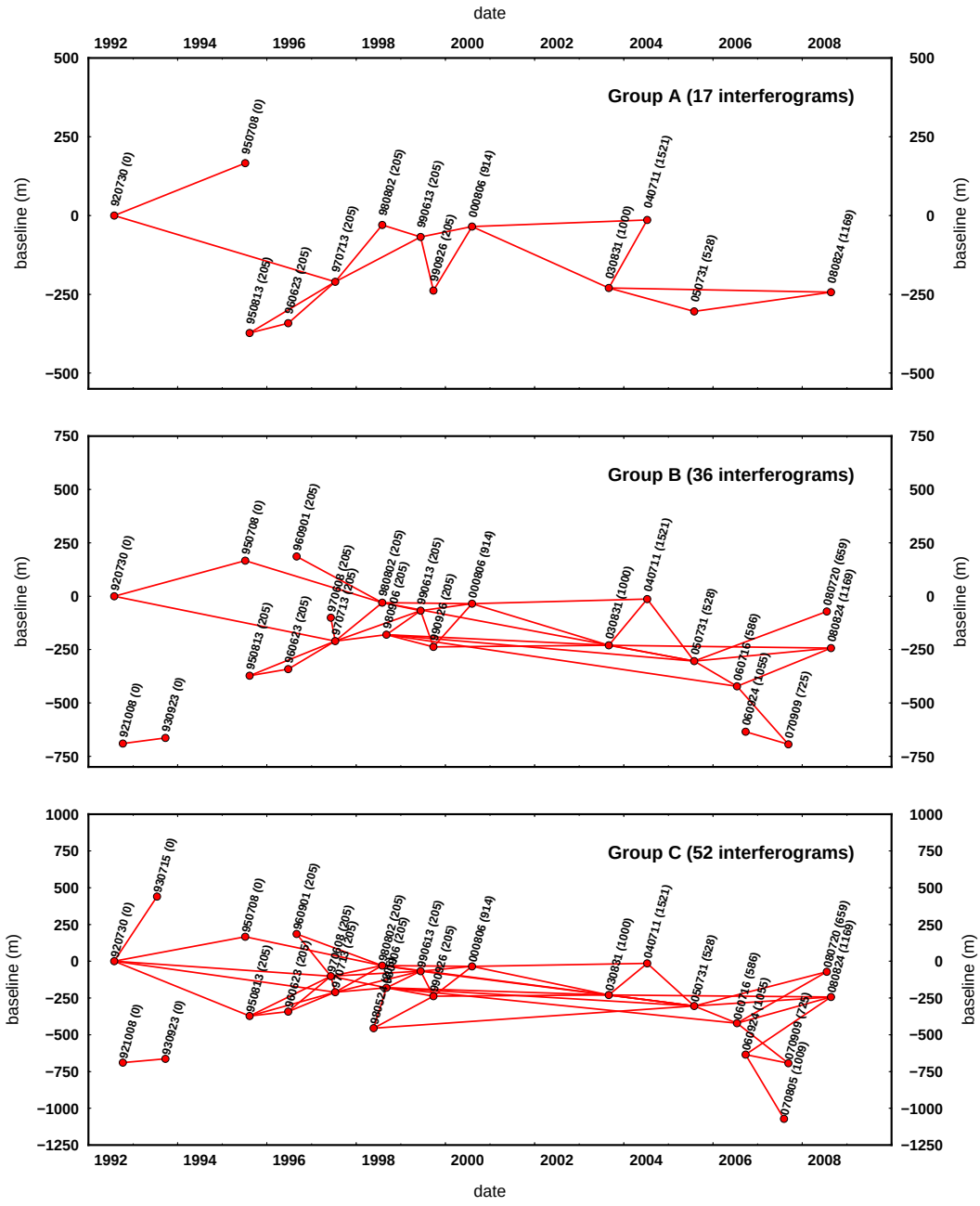

Figure 6.13: Plot of the baseline vs date of SAR images for each group of ERS interferograms processed through π-rate.

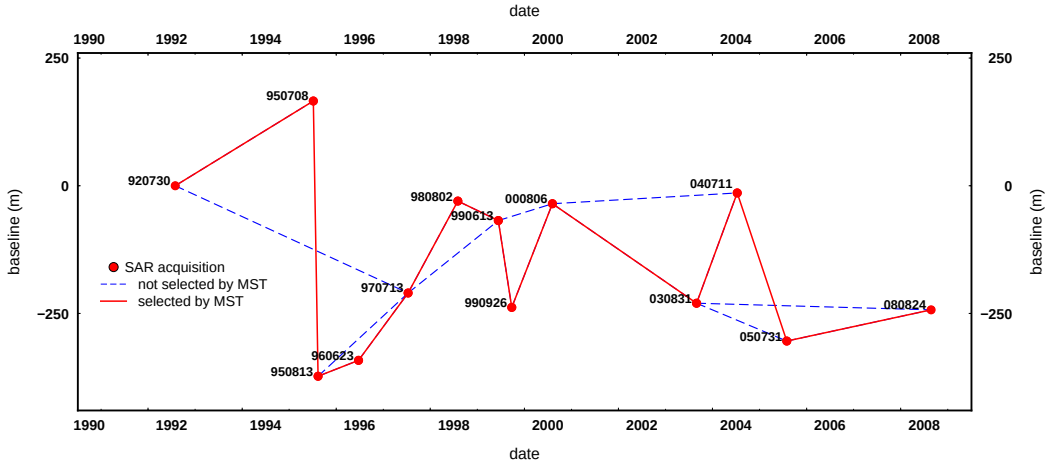

Figure 6.14: The minimum spanning tree (MST) selection of interferograms, here showing the first group processed through π-rate. With a total 17 interferograms the MST algorithm selected 12 interferograms (red solid lines) to create one MST with the redundant interferograms shown as a blue dotted line.

individual pixel through all the non-redundant interferograms. If the pixel is coherent in more interferograms than the threshold value then that pixel is given a value of 1 in the MST matrix and used in the time series calculation. If the pixel is coherent in less interferograms than the threshold value it is given a value of 0 in the MST matrix and the pixel is discarded in all non-redundant interferograms for calculating the time series.

Whilst it is usually recommended that the threshold is $\gtrsim 1/2$ the number of interferograms, for this study we are interested in the variance of displacement through the epochs rather than looking at extracting a final stack rate over the whole time series. As such, the threshold value was kept at a fairly low level to ensure that values that may have been coherent over just a few epochs were not removed because there might have been a lack of coherence at other stages of the time series.

6.7.2 Reference point

In a process similar to co-registration in ROI_pac, π-rate finds a reference point that has coherence for the greatest number of interferograms. The reference point is selected

from a series of tie-points which are tested across all the interferogram. The selection is based on the largest fraction of coherent pixels and the lowest phase variance within a small search window around each tie-point. As the reference point is used to calculate the orbital and atmospheric corrections with the mean value being applied across the rest of the data, where possible, the reference point is normally taken at the centre of the image to minimise the error in the average relative error calculation. The reference point can be recalculated at the orbital and atmospheric correction stages if needed, it is also possible to manually select the reference point.

6.7.3 Orbital error correction

Although the interferograms have orbital corrections applied during the ROI_pac processing, the optimum accuracy of the orbital data for ERS is 10-15 cm and 5-7 cm radially (Scharroo and Visser, 1998) and the interferograms still contain a residual orbital phase component. The orbital error correction used in π-rate is based on work by Biggs et al. (2007) that uses quadratic polynomial models based on a network of interferograms to calculate estimated orbital error. The network approach uses the idea that within a MST of interferograms, each acquisition will have been used to create several interferograms and that the orbital phase component of a single interferogram can be constrained using the related network of interferograms.

For the purposes of the network approach, is is assumed that in a single interferogram the long wavelength deformation is negligible (masks can be applied to remove areas where this is not the case), the atmospheric errors are short wavelength and that the long wavelength orbital phase contribution is the dominant signal. A beneficial side-effect of the orbital error correction is that it removes other sources of long-wavelength phase from the troposphere and ionosphere.

6.7.4 Variance-covariance estimation

A variance-covariance matrix (VCM) is estimated for use during the time series and rate map calculations. Both the time series and the rate map algorithms use least-squares inversions and the values in the VCM are used to appropriately weight each pixel for these inversions.

The variance-covariance value is a combination of the covariance as a measure of the temporal correlation between interferograms and variance as a measure of the temporal

variability of the data caused by noise. As the time series and ratemap inversions are calculated on a pixel-by-pixel basis, the spatial covariance is not taken into account for this VCM.

6.7.5 Atmospheric Correction

Atmospheric correction can be performed by either applying a combination of temporal high-pass and spatial low-pass filters or by using a Laplacian smoothing operator across the time series.

APS Temporal high-pass and spatial low-pass filters

The turbulent behaviour of the atmosphere is difficult to quantify as it varies unpredictably in both the temporal and spatial domains creating an atmospheric phase screen (APS) on the interferogram. Assuming that the APS is temporally random and spatially correlated, and that the tectonic displacement is usually temporally coherent, it is possible to use a temporal-spatial filter to calculate the APS using a raw time series of displacements. Although tectonic displacement can be as spatially well-correlated as the APS, as the filtering is firstly performed temporally and the subsequent spatial filtering is only performed on the component that has low temporal coherence.

The singular value decomposition (SVD) method, as used in the original SBAS method developed by (Berardino et al., 2002), is used to retrieve the temporal sequence from the raw time series. The SVD method creates any necessary connections across holes in the sequence caused by non-coherent pixels. The temporal sequence is then passed through a high-pass filter to leave only the components, such as the displacement, that are highly coherent in time. This highly coherent component is then removed from each epoch in the time series, leaving only the component with low temporal coherence. This is then passed through either a Butterworth or Gaussian spatial low-pass filter, leaving the spatially coherent component of the APS. This remaining component is then subtracted from the raw time series and the interferograms are recomputed.

In π-rate the high-pass filter can be either a Gaussian, Mean Filter or Triangular filter design, with a user selected high-pass cutoff value. The filter is designed around central point and the high-cutoff value is actually only half the filter length, so for example, if a high-cutoff value of 1 year is selected, the filter is actually 2 years and only components that are correlated for longer than 2 years will be removed.

Additionally, the low-pass filter does not have a fixed size, instead an estimate of filter cut-off is made for each acquisition by calculating the e-folding wavelength, α of a 1-D covariance function, where the covariance between pixels j and k, c_{jk}, is given by (Parsons et al., 2006):

$$c_{jk} = \sigma^2 e^{-d_{jk}/\alpha} \tag{6.12}$$

where σ^2 is the variance and d_{jk} is the distance between the pixels.

Laplacian smoothing

The Laplacian smoothing operator is applied during the time series analysis segment of the π-rate process, and is designed to apply a level of smoothing across the whole time series. This provides a consistent value of velocity across the time series and can also have the effect of smoothing out anomalies in the time series due to atmospheric error. The Laplacian smoothing operator, ∇^2, is related to the vector, d, that contains the displacement observations as follows (Schmidt and Bürgmann, 2003):

$$\begin{bmatrix} \mathbf{d} \\ 0 \end{bmatrix} = \begin{bmatrix} \mathbf{G} & B \\ \kappa^2 \nabla^2 & 0 \end{bmatrix} \mathbf{m} \tag{6.13}$$

where κ^2 is a measure of the weight of the smoothing factor as selected from the best fit weighted misfit versus solution roughness curve. The associated design matrix, $\mathbf{G}$ and model vector $\mathbf{m}$ are calculated from the time-spans and velocities between two SAR acquisitions, i and j, where, for the interferogram I_{ij}, $\mathbf{G}$ and $\mathbf{m}$ can be expressed as (Wang and Wright, 2012):

$$\mathbf{G}_{i,j} = [\underbrace{0}_{i-1} \underbrace{\Delta t_i \cdots \Delta t_{j-1}}_{j-i} \underbrace{0}_{n-j}] \tag{6.14}$$

$$\mathbf{m} = [v_1 v_2 \cdots v_{n-1}]^T \tag{6.15}$$

where t is the acquisition date, n is the total number of acquisitions, v_i is the velocity of the ith time-span. These can be simplified for linear displacement rates to:

$$\mathbf{G}_{i,j} = t_j - t_i \tag{6.16}$$

$$\mathbf{m} = \bar{v} \tag{6.17}$$

where $\bar{v}$ is the mean velocity.

Testing atmospheric correction method

Using the group A network of interferograms, a series of tests (shown in table 6.2) have been performed to establish the best method for atmospheric correction for this data. The results of the tests are shown for Laplacian smoothing in figure 6.15a and for spatio-temporal APS correction tests in 6.15b.

Table 6.2: π-rate testing for smoothing, Atmospheric (APS) vs Time Series Laplacian (TS) Smoothing

Test	Smoothing Type	Smoothing Factor	High Pass Method	High Pass Cutoff	Low Pass Method
1	None	-	-	-	-
2	TS	0.158	-	-	-
3	TS	0.100	-	-	-
4	TS	0.063	-	-	-
5	TS	0.040	-	-	-
6	TS	0.025	-	-	-
7	TS	0.016	-	-	-
8	TS	0.010	-	-	-
9	TS	0.006	-	-	-
10	APS	-	Gaussian	2	Butterworth
11	APS	-	Gaussian	3	Butterworth
12	APS	-	Gaussian	0.5	Butterworth
13	APS	-	Gaussian	1	Butterworth
14	APS	-	Gaussian	1.5	Butterworth
15	APS	-	Triangular	0.5	Butterworth
16	APS	-	Mean Filter	0.5	Butterworth
17	APS	-	Gaussian	0.5	Gaussian

A sharp change can be observed in the uncorrected displacement between July and August 1995 for points 1,3 and 4. This change represents a good point of reference to assess the efficiency of the tested smoothing methods. As there were no major events in either Krafla or Askja at that time, it is unlikely that the sharp change over such a short time period is due to a real surface displacement, and with point 2 (located in the Askja region), exhibiting very little change between July and August 1995, it suggests that the effect is localised and that the noise is possibly atmospheric. The test using laplacian smoothing can be seen to remove the sharp change well, however, looking across the whole time series regions of rapid change are smoothed that could very possibly be due to real surface displacement. This smoothing can be seen to be most exaggerated by the largest smoothing factor selected, 0.158 (test 2, represented by blue line in figure

6.15) which produces a smooth profile across the whole time series. Figure 6.16-(1c) shows the affect of using a much smaller smoothing factor of 0.016, where the resulting smoothed timeseries begins to represent more of a smoothed average displacement across the whole time series than a representation of the actual displacement in each epoch. Although Laplacian smoothing is an efficient way in which to remove noise from a time series there is also the risk that real displacement is being removed as well. As the aim is to examine changes in the rates of displacement over the time series (not to find the average for the whole time series) it is not appropriate to use this form of smoothing to remove atmospheric data. The spatio-temporal APS tests all show varying levels of correction of the sudden change in 1995, although none smoothed as dramatically as the Laplacian smoothing. The final selection for atmospheric correction was a high-pass gaussian filter with 0.5 year cut-off (1 year in total for both sides of the gaussian curve) and a low-pass butterworth filter. I selected this as it showed a middle ground in time series profiles, giving reasonable smoothing over the 1995 change whilst retaining most of the features of the original profile. Figure 6.16-(2b-c) shows how varying the length of the Gaussian high-pass filter from 0.5 year to 3 years has an effect on the resultant time series. Although the 3 year filter produces a cleaner image, as anything less than the length of the filter is subject to spatial filtering, a large amount of the deformation signal is lost along with the atmospheric noise. In comparison, figures 6.16-(2b) shows only small changes from the original unfiltered time series, cleaning up some regions of noise but ensuring that the deformation signal still remains.

As a note, when looking for average velocity rates across a time series, it is possible to apply Laplacian smoothing in addition to the temporal and spatial filters, however as we are looking to understand changes in displacement rates from epoch to epoch, this could present unrealistically smoothed data and make it difficult to identify any variance in rate through time.

6.7.6 Time-series analysis

There are three methods that can be used for time series analysis in π-rate: Laplacian smoothing, singular value decomposition (SVD) and B-Spline. I selected the SVD method to produce the time series (as discussed in the atmospheric correction section, I chose not to use any Laplacian smoothing to ensure that the actual surface displacement measured by InSAR remained as true as possible). As outlined earlier, the SVD method

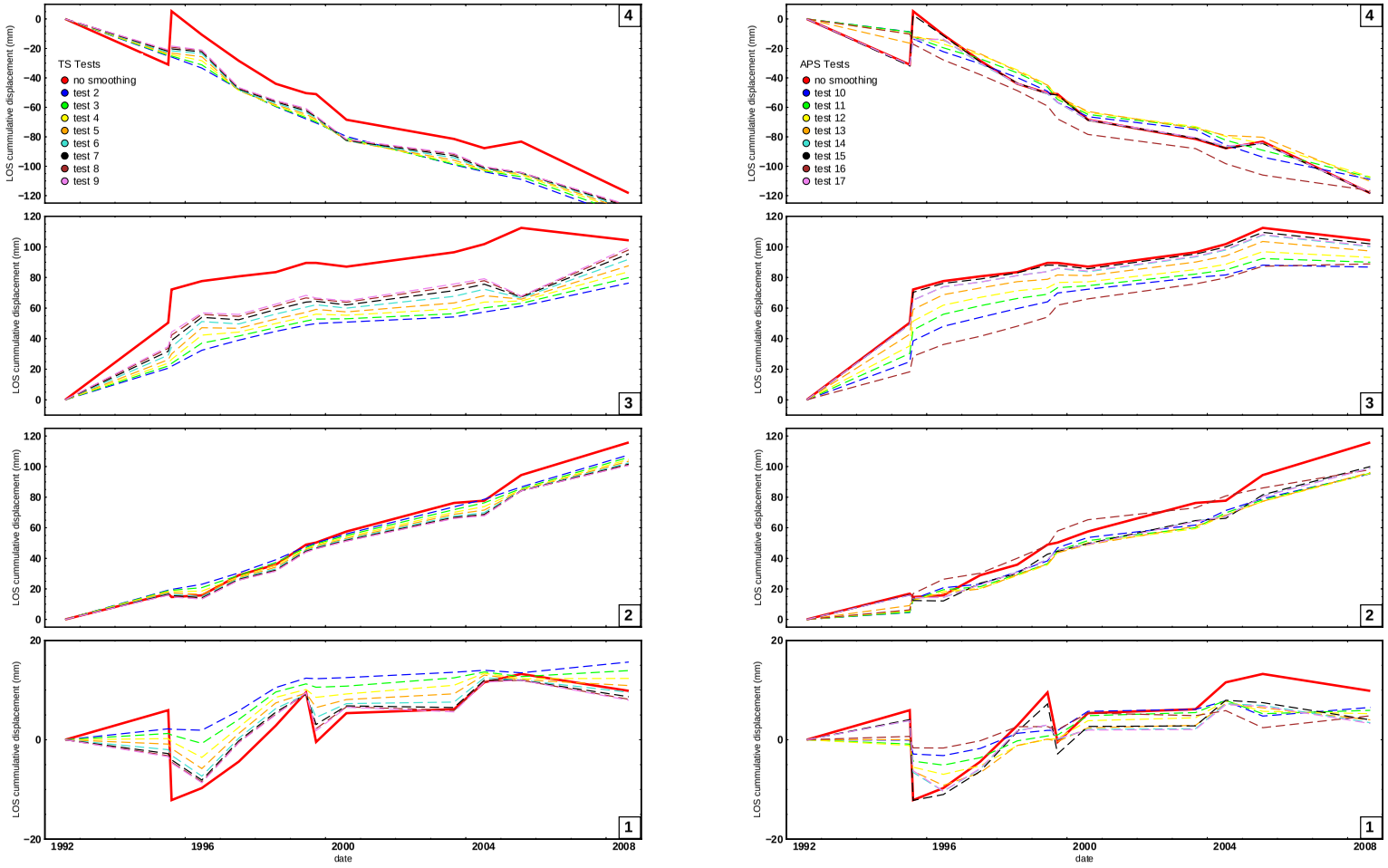

(a) (b)

Figure 6.15: π-rate smoothing tests performed on selected points 1-4 (as shown in figure 6.17), with a) tests performed using varying Laplacian smoothing factor applied during time series analysis and b) tests varying the temporal high-pass and spatial low-pass filter parameters during the APS atmospheric correction.

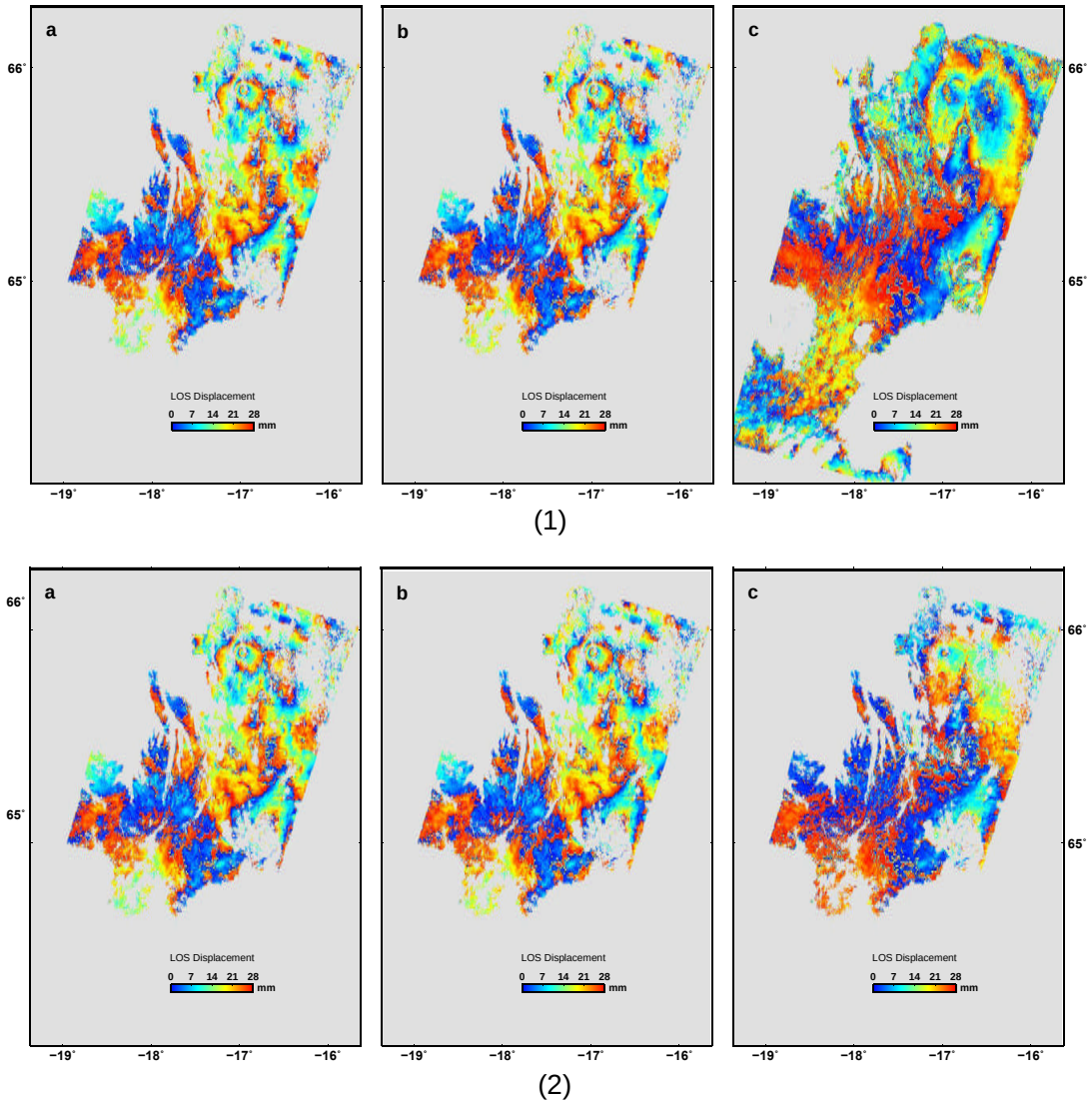

Figure 6.16: Comparing the results of atmospheric corrections applied to the time series segment 0050731-20080824 with (1) showing a) no correction or smoothing applied, b) APS correction applied using a 0.5 year Gaussian high-pass and Butterworth low-pass filters and c) Laplacian smoothing applied with a 0.016 smoothing factor, and (2) showing a) no correction or smoothing applied, b) APS correction applied using a 0.5 year Gaussian high-pass and Butterworth low-pass filters and c) APS correction applied using a 3 year Gaussian high-pass and Butterworth low-pass filters.

retrieves the temporal sequence from the now spatio-temporally corrected time series, creating any necessary connections across holes in the sequence. π-rate then produces both incremental and cumulative LOS displacement files (in .dat format) for each epoch in the sequence, along with a final average stack rate map for the whole time series.

6.8 Observations

I processed the three interferogram groups through π-rate using APS spatio-temporal atmospheric correction. As with the atmospheric testing, I selected points across the region of coverage to examine the outcomes of each of the groups. Figure 6.17 shows the final stack rate map (produced using group C interferograms) in which a region of average range increase (positive LOS displacement) can be observed over the Askja fissure swarm and also along the central axis of the Krafla fissure swarm. The lobes of average range decrease (negative LOS displacement) either side of the central axis of the Krafla fissure swarm can also be noted.

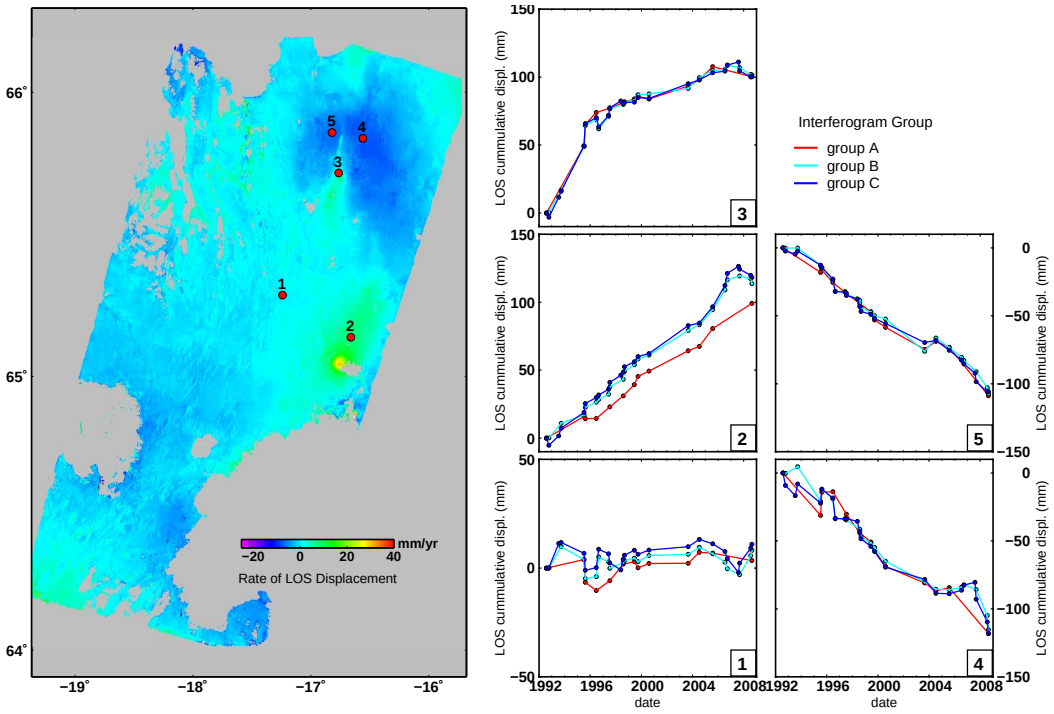

Figure 6.17: Stack rate map (as produced from the group C interferograms) and time series comparisons, for the extracted points 1-5, as produced by π-RATE for group A, B and C interferograms, using APS Gaussian high pass and low pass filters for temporal and spacial smoothing respectively. The time series for points 1-5 on the rate map are represented by the figures 1-5 respectively.

A range increase means that the distance between the satellite and the ground surface has increased and is generally assumed to represent a subsiding/deflating ground surface or an eastward motion. Equally, a range decrease means a decrease in distance between the satellite and the ground surface, representing an uplift/inflating ground

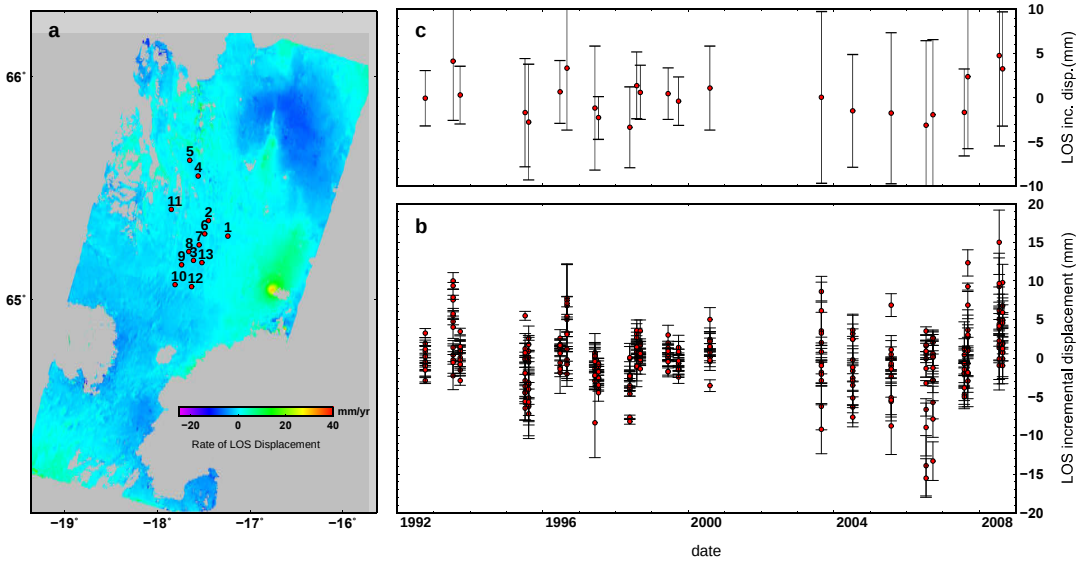

Figure 6.18: To calculate the variance in the displacement measurement taken from the interferogram in a window of $\pm 0.01°$ ($\sim \pm 1$ km) around a given point. a) shows the 13 points selected from the stack rate map, chosen in regions that have an average rate of 0 mm/yr, b) plots the the mean value of LOS displacement for each point window for each epoch, with the error bars showing the standard deviation of values across each window. c) shows the mean standard deviation for each of the 13 points across all epochs.

surface or a westward motion (for descending satellite tracks). Extraction of actual vertical displacement from LOS values is discussed in chapter 7. The five points selected represent: 1) a control zone where very little LOS displacement is observed in the final stack rate map, 2) a region of the Askja fissure swarm with high levels of range increase, 3) the central axis of the Krafla fissure swarm, showing range increase and with 4) and 5) taken from the lobes of range decrease respectively to the east and west of the Krafla fissure swarm.

A comparison of the three interferogram groups is shown in 6.17 where the profiles for each of the points can be seen in boxes 1-5. The three groups give displacement values that are in fairly good agreement, and although group A gives the smoothest profile, group C provides the largest number of epochs (24) to the time series giving the best opportunity to examine how the displacement behaviour varies with time. The time series produced by Group C has been used for the rest of this chapter.

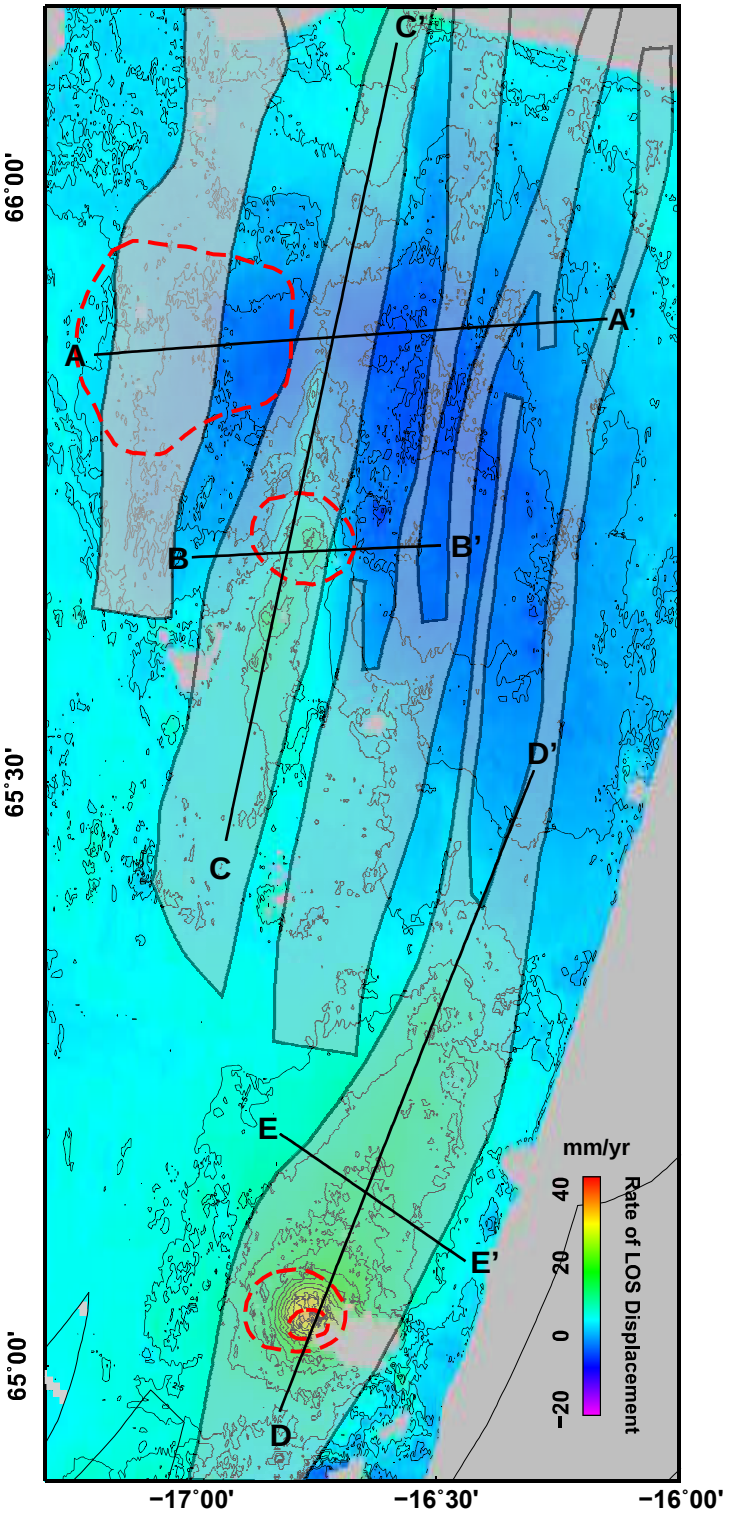

Figure 6.19: Profiles A - E from which time series of both the full profiles and a series of points along the section have been extracted. Profiles A-C are taken in the Krafla fissure swarm region and D-E cover the Askja fissure swarm region. Contour lines (thin black lines) denote a rate change of 2.5 mm/year, red dashed lines show calderas.

To quantify the uncertainty in the displacement measurement of a point and the values of the surrounding pixels, a sample of 13 points in regions of ∼0 mm/yr average displacement rate (as shown in the average rate map) have been selected (shown in figure 6.18a). The variance of all the pixels contained within a window of ±0.01° (∼ ±1 km, short-scale noise and coherence) surrounding each selected point was then calculated and then translated to standard deviation. The standard deviation for each point within an epoch can be seen in figure 6.18b and the average standard deviation for each epoch (shown plotted around the mean point value) can be seen in figure 6.18c. A maximum standard deviation of ±3 mm was found with an average standard deviation of ±1.5 mm across all the epochs

To examine displacement behaviour through time, I selected five profiles along and across rift (as shown in figure 6.19 as A-A‘ to E-E‘) with profiles A-C over the Krafla fissure swarm region and profiles D-E over the Askja fissure swarm, these are discussed further in the following sections.

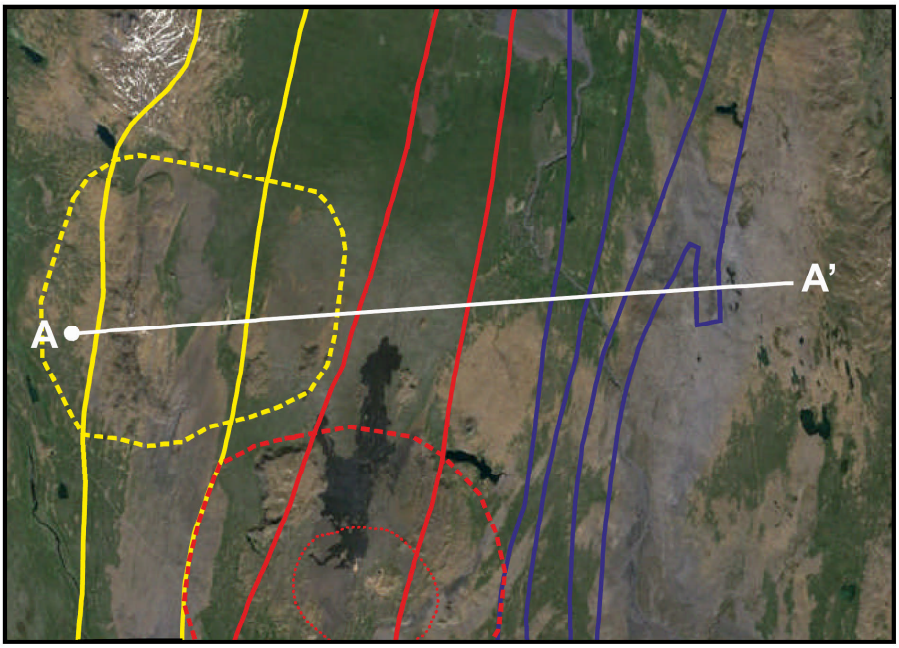

Figure 6.20: Map showing the location of profile A with respect to the Theistareykir (yellow), Krafla (red) and Freminamar (blue) fissure swarms and volcanic systems respectively represented by continuous and dotted lines (underlying image taken from Google Earth).The main lava flow from the Krafla Fires can be seen as the dark region in the image.

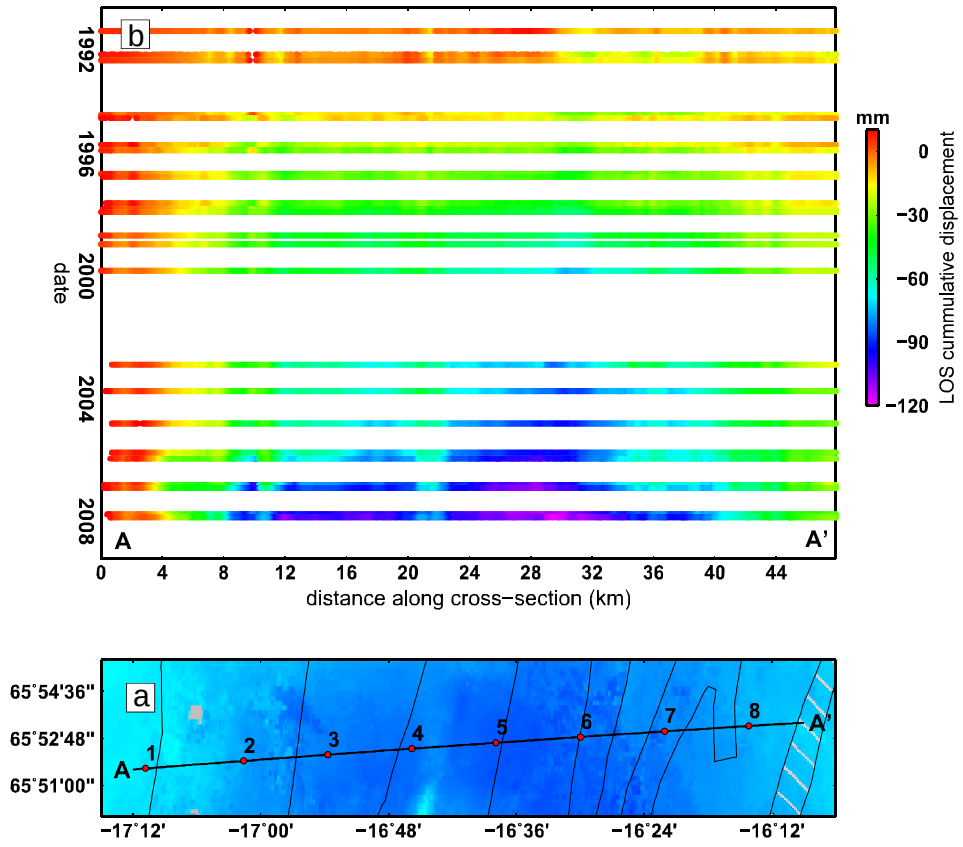

Figure 6.21: a) Map showing the location of Profile A (black line from A-A') on the stack rate-map (from figure 6.19) with the points 1-8 used for time series in figure 6.22. b) LOS cumulative displacements from 1992 through to 2008 for profile A.

6.8.1 Krafla Fissure Swarm

Krafla: Profile A

Profile A is a 50 km long profile that crosses the Theistareykir volcanic centre and the Krafla and Freminamar fissure swarms (shown in figure 6.20 by yellow, red and blue lines respectively). The profile cuts the fissure swarms at a perpendicular to the major rift axes, passing through both of the lobes of average range decrease (as seen in the stack rate map in figure 6.17). The Krafla section of the profile crosses the swarm just north of the 1985 lava flow in an area that was actively rifting during the Krafla fires.

For this profile (and the subsequent 4 profiles) I have extracted LOS displacement data for both the entire cross-section and also for 8 selected points along the profile (point locations shown in figure 6.21a alongside the cumulative LOS displacement values across the profile in 6.21b). The time series for each of the 8 points can be seen in

figure 6.22. The Envisat time series is plotted alongside the ERS time series to allow a comparison of results for the period of overlap between the two time series (between 2004-2008). Some of the points do not have an available Envisat time series as the profiles and points were selected from regions of continuous coverage in ERS time series. Some points may lie in regions without coverage in the Envisat time series (such as points 1 and 8 for profile A).

The time series in figure 6.22 make it possible to quantify displacement rate changes across profile A. The outermost points of the profile maintain a fairly constant rate of deformation, with point 1 lying to the west of the Theistareykir fissure swarm exhibiting very little deformation throughout the whole 16 year period and point 8 showing a reasonably linear rate of deformation of ∼-4 mm/yr.

Across points 2-7 there is a roughly similar trend in displacement rates split into three distinct time periods: 1992-1999, 1999-2004 and 2004-2008. Points 2-7 show a linear rate of displacement between 1992-1999, increasing in rate from the eastern edge of the Theistareykir fissure swarm across to the Krafla fissure swarm reaching up to ∼-8 mm/yr, decreasing again in the points out towards the Freminamar fissure swarm. Between 2000-2004 there is a period of relatively low displacement rate across all points of ∼-1-2 mm/yr. The final time period, from 2004 onwards, shows an increase in displacement rate initiating in the Theistareykir fissure swarm and out to the western edge of the Krafla fissure swarm, with a LOS displacement rate of ∼-13 mm/yr. The rate increase initiates later, around 2006/2007, in the more easterly points across the Krafla fissure swarm and out towards Freminamar.

Table 6.3: Time periods used for summing incremental LOS displacement for profile A.

Start	End	Length (years)
July 1992	Sept 1999	7
Sept 1999	July 2004	5
July 2004	Aug 2008	4

To examine these trends in LOS displacement along the entire profile I have summed the incremental LOS displacements for each of the time periods (see table 6.3). The summed LOS displacements are shown in figure 6.23.

The first summed time period (1992-1999) shows a trend that increases in negative cumulative LOS displacement from low displacement at either end of the profile

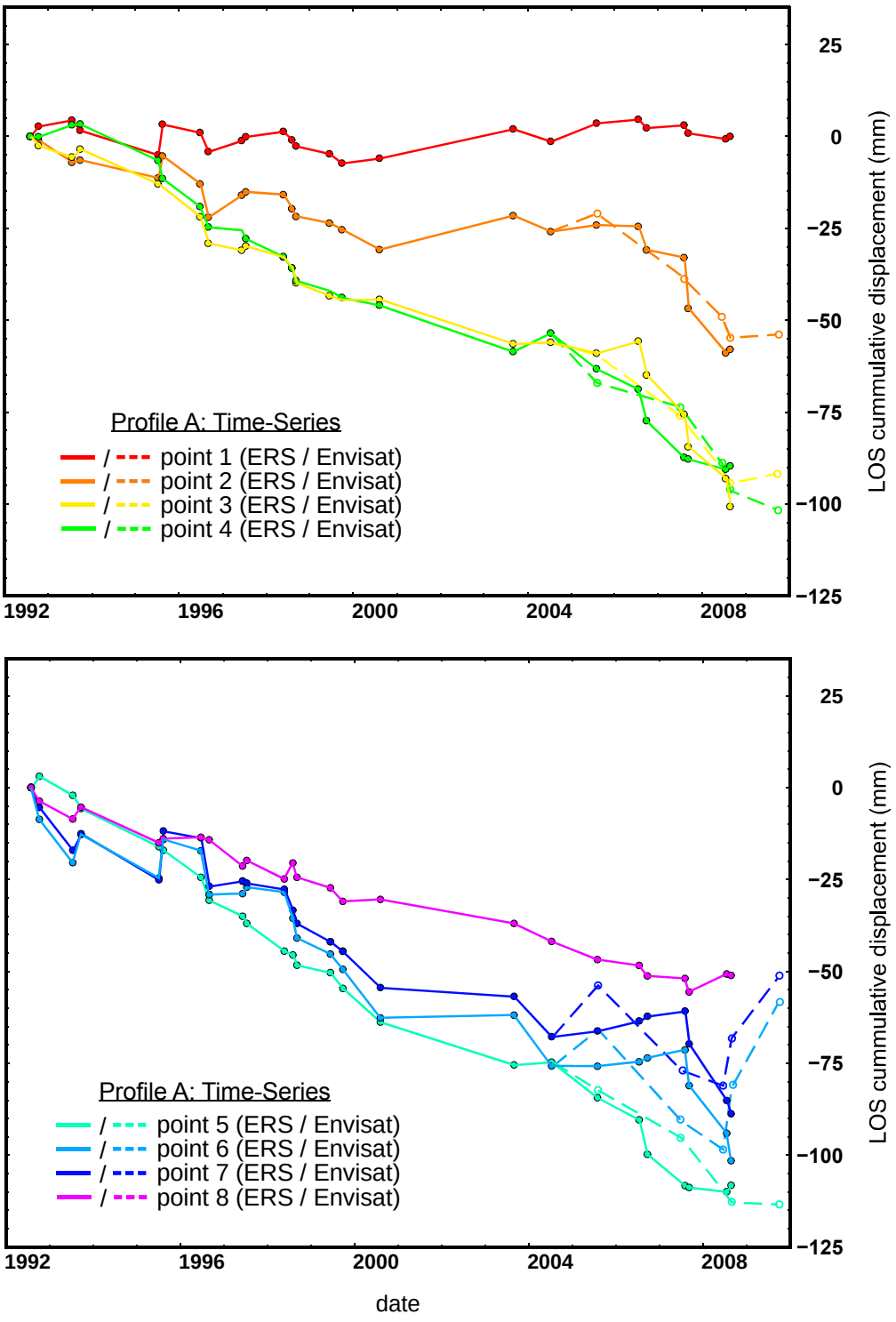

Figure 6.22: ERS (solid lines) and Envisat (dashed lines) time series plots for profile A, points 1-8 (as shown in figure 6.21a).

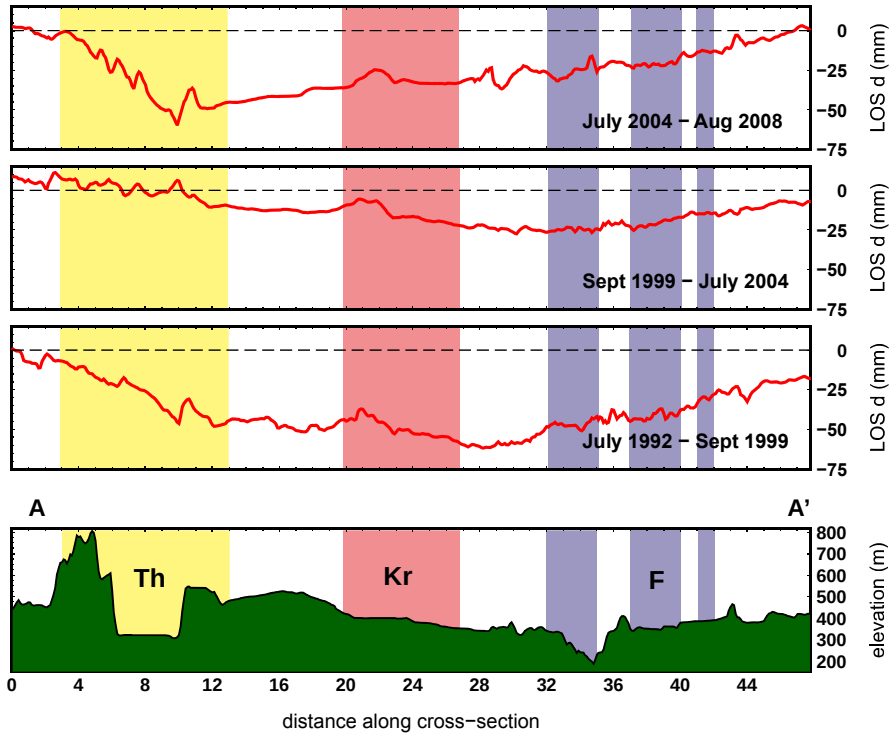

Figure 6.23: LOS cumulative displacements for profile A, over summed epochs as outlined in table 6.3, with topographical profile shown in green. The locations of the Theistareykir (Th) fissure swarm shown in yellow, Krafla fissure swarm (K) in red and Fremrinamar fissure swarm (F) shown in blue

through to a maximum at the centre of the profile. The maximum range decrease lies in the region between the Krafla and Freminamar fissure swarms. The roughly constant increase towards the centre of the profile suggests a long-wavelength displacement trend that runs across all three of the fissure swarms in this region of the NVZ.

The profile of the second summed time period (1999-2004) shows a much decreased level of displacement across the entire region. Although there is still evidence of the long-wavelength displacement trend across the profile, this time period shows that there has been a dramatic and consistent change in the displacement rate across all three fissure swarms.

There is a spike of increased range decrease at ∼10 km along the profile in both the first and last time periods. This region is located around the northern flanks of Mount Baejarfjall, an area in the Theistareykir volcanic zone noted to have particularly intense geothermal activity (e.g. Ármannsson et al., 1986). This spike could be due to increased negative surface displacement, but two additional factors should also be

considered: sub-surface geothermal activity could regularly produce surface displacement and regional topography shown in figure 6.23 could offer a 'trap' for inclement weather that could produce atmospheric interference, both producing spikes in the LOS displacement. However, the general trend in the third time-period (2004-2008) shows this region as the focus of range decrease, a significant change from the first time period, with LOS displacement increasing negatively across the whole region towards a maximum in this eastern region of the Theistareykir volcanic zone.

Across all three summed time periods there is a localised range increase (subsidence) ~21 km along the profile, this dip coincides with the central region of the Krafla fissure swarm and suggests that there is a shorter-wavelength displacement trend across the fissure swarm alongside the longer-wavelength displacement trend across the whole profile.

Krafla: Profile B

Profile B is a 24 km long profile taken at a perpendicular to the major rift axis, crossing the caldera in a region showing average range increase in the average rate map (as shown in figure 6.24a). The cumulative LOS displacements across the full profile are shown in 6.24b.

The location of Profile B provides displacement data that can be used as a comparison with published data from the caldera as shown in figure 6.1 (Sturkell et al., 2008). Additionally, the profile extends outside of the main caldera to allow an examination of the decay in the displacement rate with distance from the main focus of displacement. I selected the 7 points (locations in figure 6.24a) to provide time series both inside and outside the caldera. The caldera covers the region between ~7 and 15 km in the profile (as shown as the red striped region in 6.24a) and the LOS displacement within the caldera is shown by the time series points 3 and 4 (figure 6.25). These time series both show a range increase that is decaying with time - point 4 is the closest to the main area of deformation as seen in the average stack rate map and will be used here to represent the maximum LOS displacement for the caldera.

Displacement rates have been extracted from the LOS displacement curve for the point 4 time series and plotted as red points in figure 6.26. The displacement rates from published data (Tryggvason, 1994, Björnsson and Eysteinsson, 1998, Sigmundsson et al., 1997, Henriot et al., 2001, Ágústsson, 2001, de Zeeuw-van Dalfsen et al., 2006, Sturkell

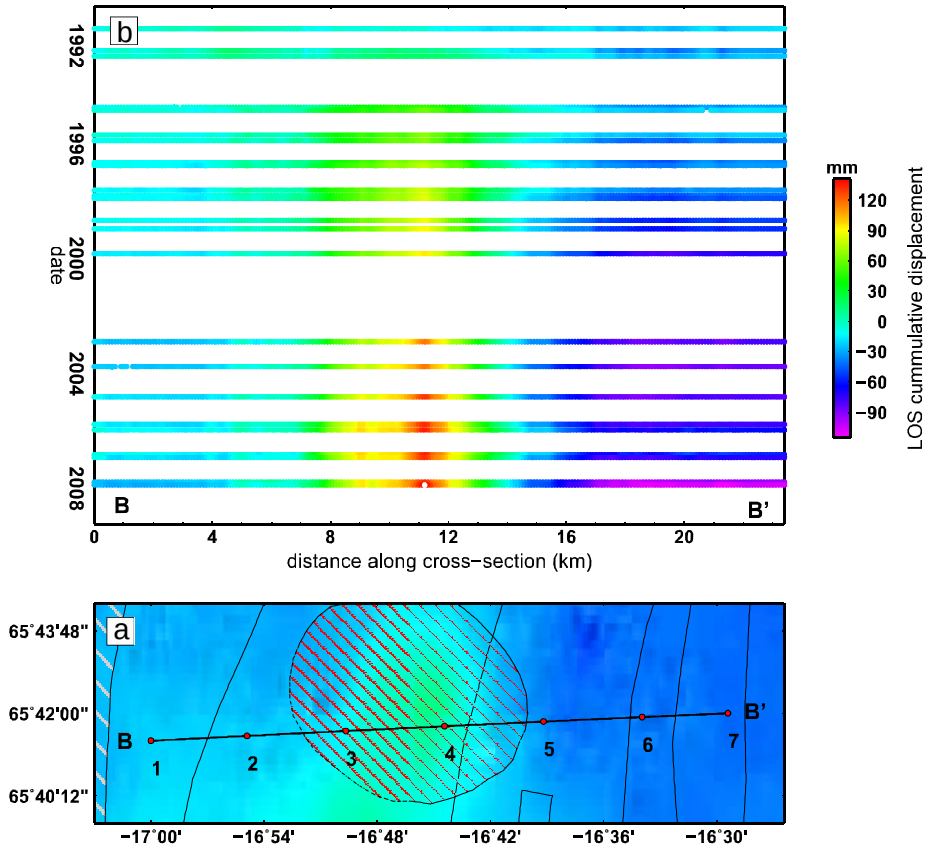

Figure 6.24: a) Map showing the location of Profile B (black line from B-B') on the stack rate-map (from figure 6.19) with the points 1-8 used for time series in figure 6.25. b) LOS cumulative displacements from 1992 through to 2008 for profile B.

et al., 2008), are shown as black points, with the best fit decay curve for the displacement of the caldera calculated by Sturkell et al. (2008) shown as a black dotted line. The LOS displacement rates are composed of both vertical and horizontal displacement and are therefore not fully representative of the true vertical displacement rate. However, the horizontal displacement component should be fairly small as compared to the vertical (discussed further in chapter 7) and the results can be considered a good approximation of vertical displacement rates for this comparison. Figure 6.26 shows that the decay rate of the LOS displacements has a good fit with the published data and the decay curve. Slightly lower values could be due to point 4 not being acquired at the same location as some of the published data (the published data being from a number of different sources, acquisition methods and locations).

The time series show that the range increase is confined to the caldera region, with points directly outside the western edge of the caldera exhibiting very little displacement

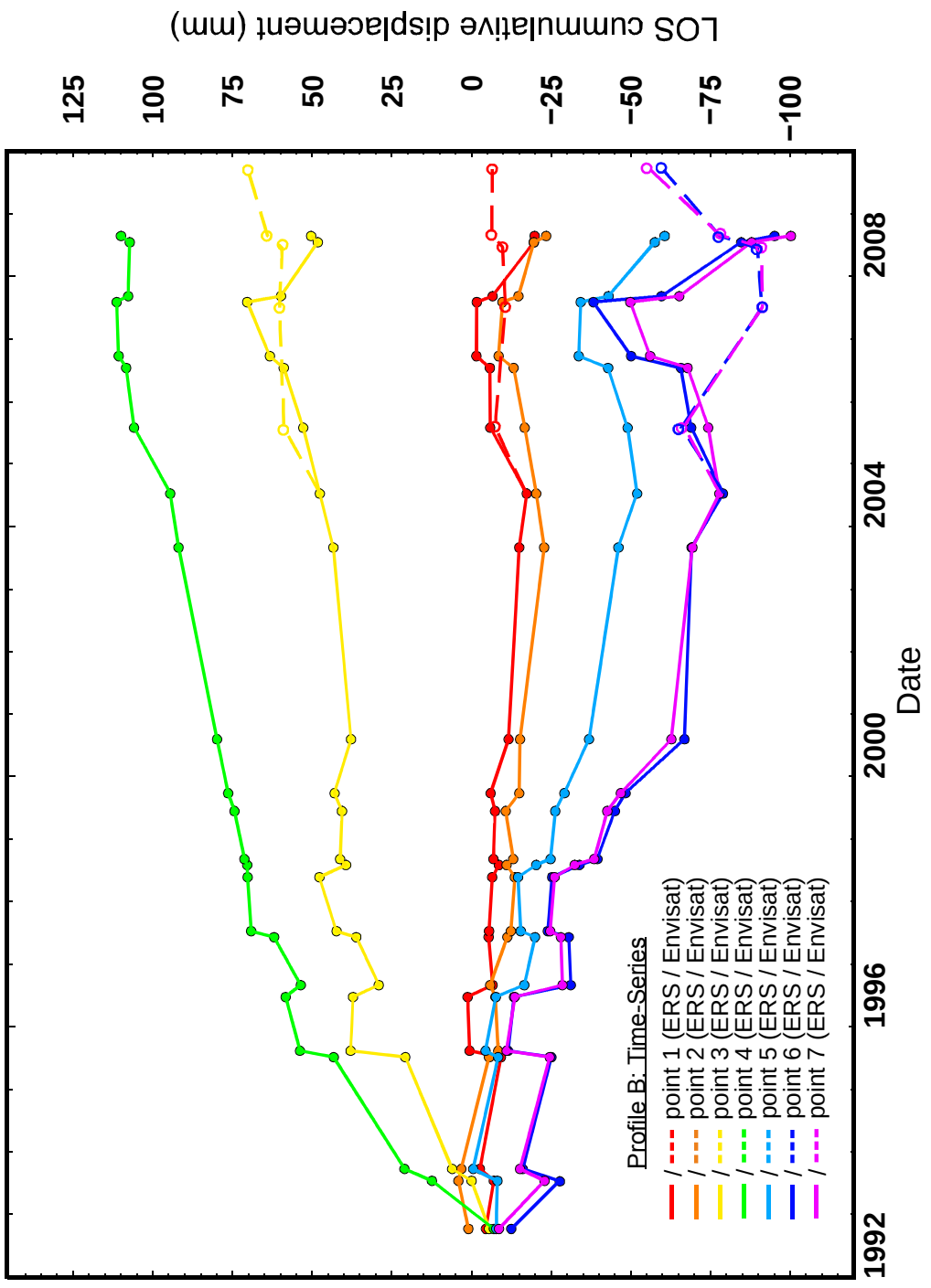

Figure 6.25: ERS (solid lines) and Envisat (dashed lines) time series plots for profile B, points 1-8 (as shown in figure 6.24a).

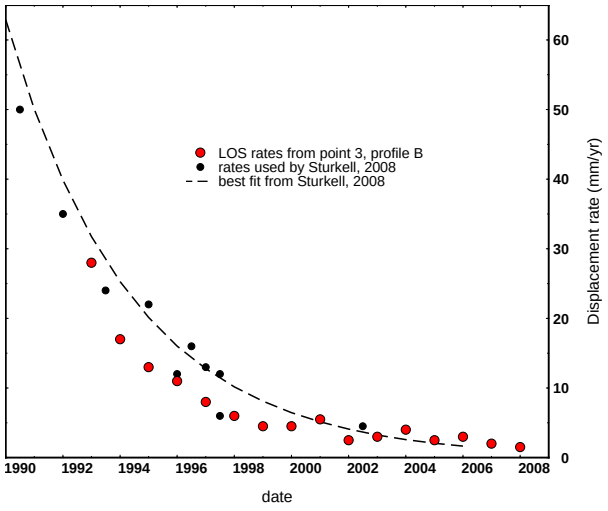

Figure 6.26: Comparison of the LOS displacement rates calculated from the displacement time series for point 4, profile B (see figure 6.25, shown as red points, with the results published by Sturkell et al. (2008) where the dotted black line is the best-fit decay curve calculated by Sturkell et al. (2008) and the black points are the displacement rate data used by Sturkell et al. (2008) from various published sources (Tryggvason, 1994, Björnsson and Eysteinsson, 1998, Sigmundsson et al., 1997, Henriot et al., 2001, Ágústsson, 2001, de Zeeuw-van Dalfsen et al., 2006, Sturkell et al., 2008).

throughout the 16-year period. Points to the east of the caldera initially show a similarly small amount of LOS displacement from 1992-1998, after which points 5-7 show some range decrease, increasing with distance from the caldera. To examine this behaviour across the whole profile I have summed the displacements across three time periods - from 1992-1998, 1998-2004 and 2004-2008 (see table 6.4). The summed displacement profiles are shown in figure 6.27.

Table 6.4: Time periods used for summing incremental LOS displacement for profile B.

Start	End	Length (years)
July 1992	Sept 1998	6
Sept 1998	July 2004	6
July 2004	Aug 2008	4

The summed profile from 1992-1998 clearly shows the range increase across the caldera, with the maximum displacement in the centre of the caldera decreasing with distance from the centre to the edges of the caldera. The range increase in the caldera, whilst still distinct, is much reduced in the 1998-2004 time period and is negligible between 2004-2008. This establishes that the decay of the displacement rate over time

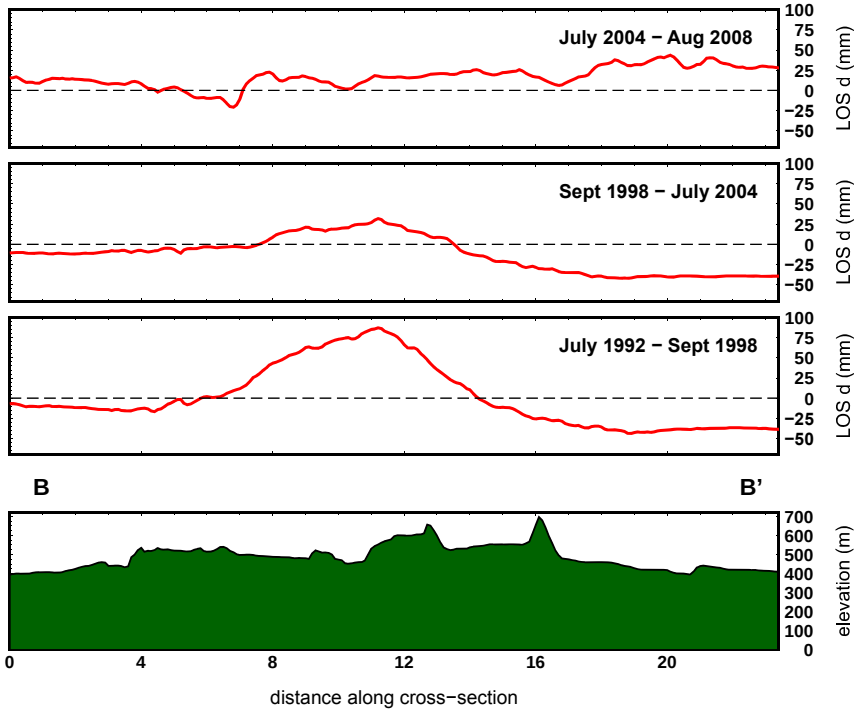

Figure 6.27: LOS cumulative displacements for profile B, over summed epochs as outlined in table 6.4, with topographical profile shown in green.

observed in both the point time series (figure 6.25) and published data (Sturkell et al., 2008) is occurring across the whole caldera portion of the profile.

The 2004-2008 time period, showing only small amounts of displacement across the whole profile, appears to be more erratic than the first two profiles, particularly from around the 16 km point onwards. The ERS time series show some disagreement with the Envisat time series, particularly for points 6 and 7, which could present some noise (possibly atmospheric) that has not been fully removed in processing.

Krafla: profile C

Profile C is a 76 km long profile taken along the major rift axis, passing through the main caldera from the south and continuing to the far north of the Krafla fissure swarm by the coast (shown in 6.28). The cumulative LOS displacements across the full profile are shown in 6.28b. I selected the locations of points 1-8 (shown in 6.28a) to give a representative view of along-axis displacement behaviour for the whole fissure swarm. The resulting time series of these points are shown in figure 6.29.

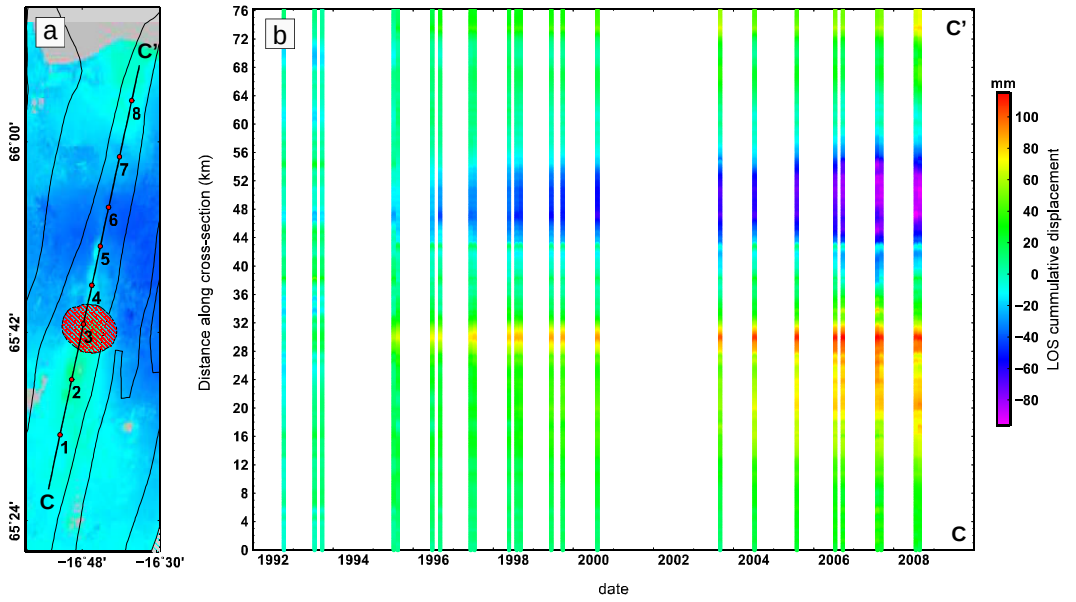

Figure 6.28: a) Map showing the location of Profile C (black line from C-C') on the stack rate-map (from figure 6.19) with the points 1-8 used for time series in figure 6.29. b) LOS cumulative displacements from 1992 through to 2008 for profile C.

In the time series plots (figure 6.29) for point 1, located in the south of the Krafla fissure swarm adjacent to Myvatn Lake, through to point 3, located in the central caldera, there is an overall range increase with displacement rates initially increasing with proximity to the caldera. Points 1 and 2, which both lie to the south of the caldera, show a reduction in the initial displacement rate over the same period as the caldera (point 3 for this time series and also for profile B discussed earlier). However, from 1996 onwards the LOS displacement rate at point 2 stops decaying and displaces at linear rate of ∼6 mm/year, in contrast to both points 1 and 3 which show decaying rate of displacement throughout.

Point 4, just north of the caldera, shows very little displacement throughout the entire 16 years, possibly at a transition point between displacement caused by the range decrease in the caldera and the much longer wavelength range decrease observed in profile A. Throughout the 16 years, points 5 and 6 show range decrease, as observed in profile A, with rate of displacement increasing with distance from the caldera to ∼-6 mm/year at point 6. In the north of the fissure swarm, point 7 shows very little displacement - marking a northern limit to the large lobes of range decrease observed

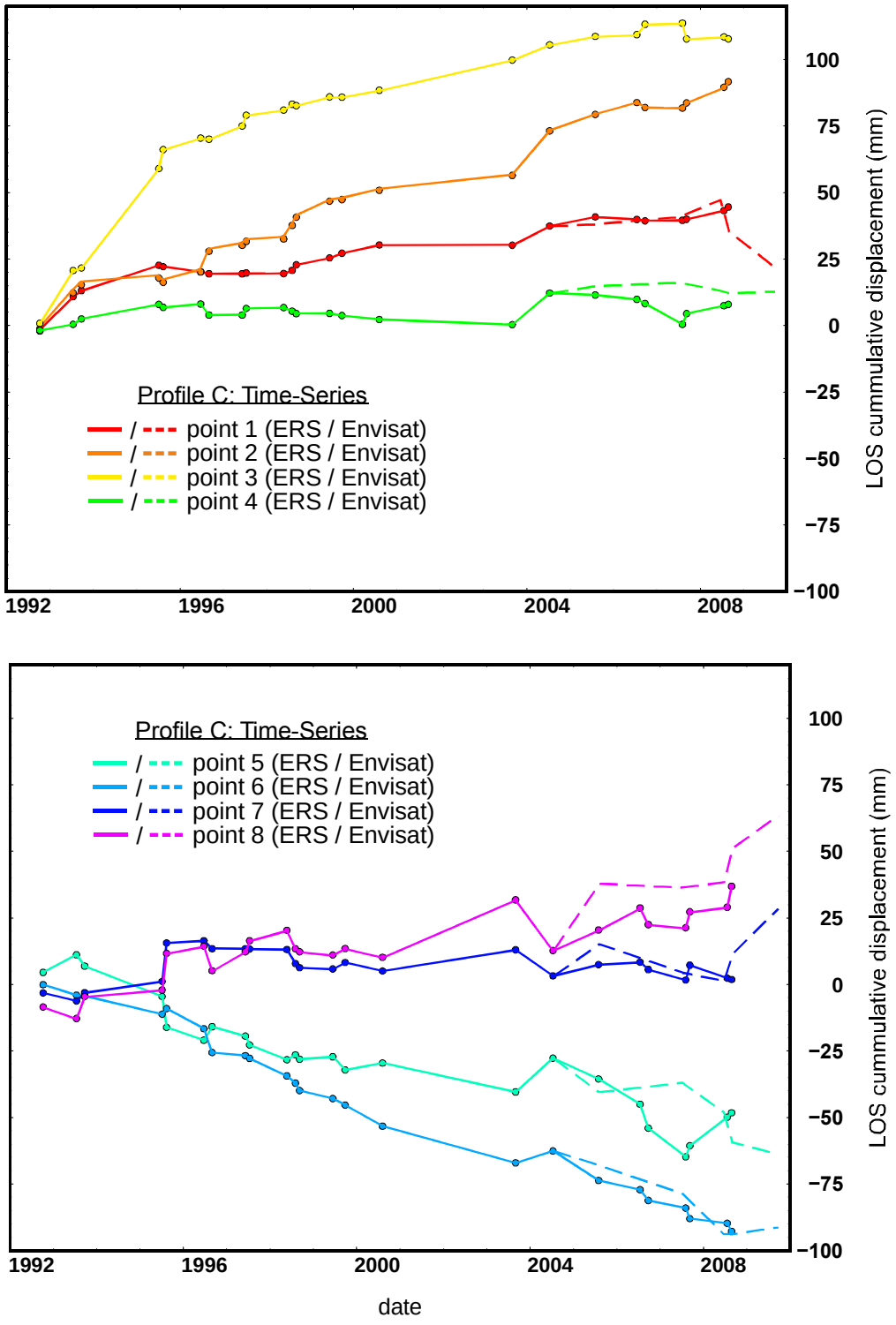

Figure 6.29: ERS (solid lines) and Envisat (dashed lines) time series plots for profile C, points 1-8 (as shown in figure 6.28a).

in the stack rate map (figure 6.19 (as well as profile A and points 5 and 6). Point 8 has a small amount of range increase that shows an increase in rate after 2004 in both the ERS and Envisat time series.

Table 6.5: Time periods used for summing incremental LOS displacement for profiles C, D and E.

Start	End	Length (years)
July 1992	Sept 1996	4
Sept 1996	Aug 2000	4
Aug 2000	July 2004	4
July 2004	Aug 2008	4

To examine the changes in rate of displacement between 1992-2008 across the entire profile, I have selected to create summed displacement plots for four equal time periods (see table 6.5). The summed displacement plots are shown in figure 6.30.

The first summed period (1992-1996) clearly identifies the range increase of the caldera, with a maximum displacement that decreased rapidly from the centre to the edges of the caldera. Outside the caldera to the south the displacement then decreases slowly with distance. To the north of the caldera the displacement changes to the range decrease seen across the wider northern volcanic zone (profile A), affecting an ~36 km along-profile region (from 36 km to 62 km on the profile). This possibly puts a constraint on the limits of the longer-wavelength displacement, with the far north of the profile showing range increase throughout.

6.8.2 Askja Fissure Swarm

Askja: profile D

Profile D is a 66 km long profile taken along the major rift axis, crossing the caldera in the south and continuing through to the far north of the fissure swarm (as shown in figure 6.31a. The cumulative LOS displacements across the full profile are shown in 6.31b. As for Krafla with profile C, I have selected the locations of points 1-8 (figure 6.31a) to provide a representative view of along-axis displacement behaviour for the whole fissure swarm. The resulting time series of these points are shown in figure 6.32.

The time series at point 1, located in the main Askja caldera, shows a substantial rate of range increase throughout the 16 years of observation. The time series shows two main changes in LOS displacement rate, from ~8 mm/year between 1992-1996

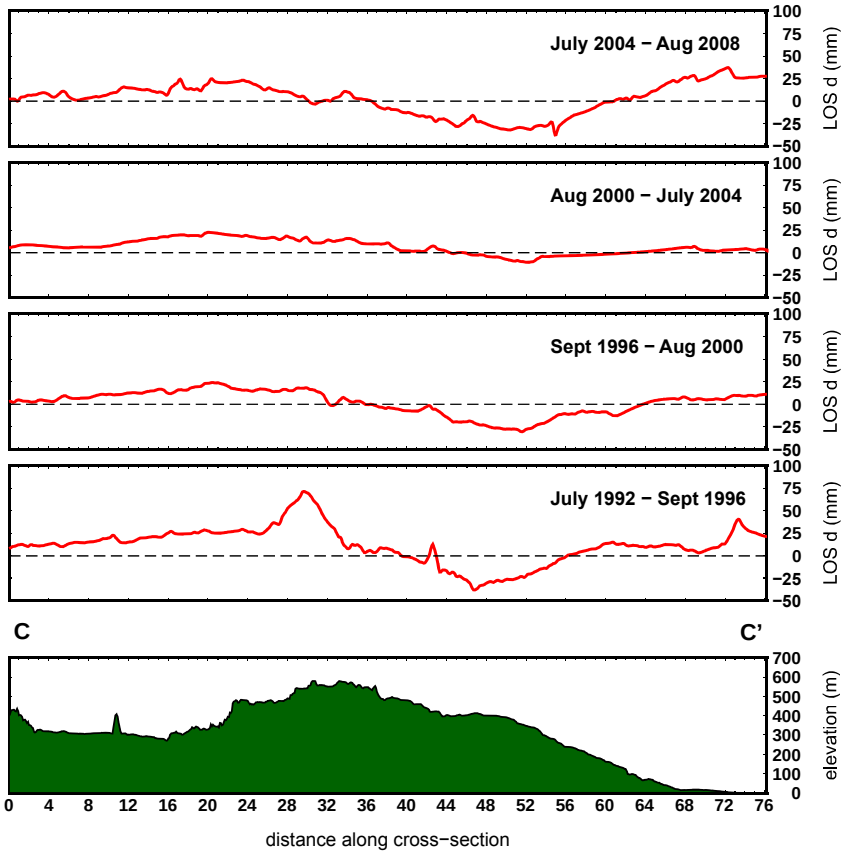

Figure 6.30: LOS cumulative displacements for profile C, over summed epochs as outlined in table 6.5, with topographical profile shown in green.

to ∼30 mm/year from 1996-2006 and then slowing to ∼15 mm/year from 2006-2008. This agrees with subsidence data from InSAR presented by de Zeeuw-van Dalfsen et al. (2013) that shows a deformation rate of just under 30 mm/year from 2000-2001 and a decreased rate of ∼15 mm/year during the 2008-2010 time period.

Looking along the rift axis, the time series show that the displacement rate generally decreases with distance away from the main volcanic centre, with point 6 showing very little displacement at all. An exception to this is point 5 which has a greater displacement rate than point 4 - although this is largely due to a period (between 1993-1995) of range decrease at point 4 after which range increase is slightly higher than at point 5. By point 7 there is a range decrease that increases from point 7 to point 8.

A number of points show a dip in the time series around 2003. This could be a genuine surface displacement measurement, but as this change is for a single epoch in the time series (and shows a return to the general trend in displacement rate in the

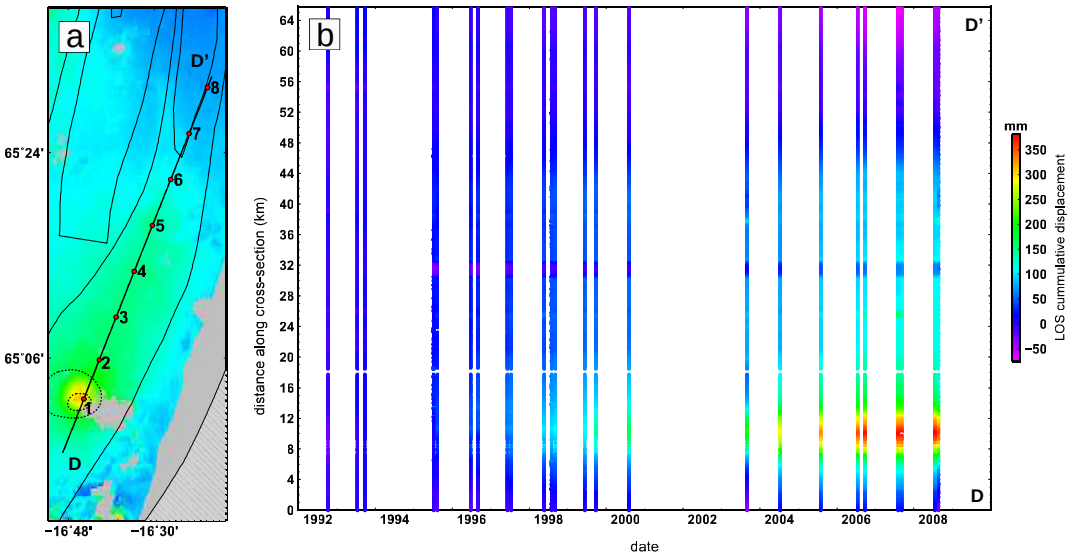

Figure 6.31: a) Map showing the location of Profile D (black line from D-D') on the stack rate-map (from figure 6.19) with the points 1-8 used for time series in figure 6.32. b) LOS cumulative displacements from 1992 through to 2008 for profile D. Main calderas shown by black dashed line.

following point) it is most likely due to noise in the interferogram. The displacement rate change for this epoch would best be validated by using other tracks over the same region to produce additional interferograms and time series between 2000 and 2003, from which a trend in displacement rate would be more apparent. Additionally, the ERS time series shows a dramatic change in the displacement rate in 2008 - the Envisat time series from 2008 onwards continues to follow the long-term trend of the earlier ERS time-series and would lead to the assumption that the last few epochs in the ERS time series could be affected by noise.

To examine trends in displacement rate across the whole profile, I have summed the LOS displacements across the equal time periods as outlined for profile C in table 6.5.

The summed plots show displacement over the volcanic centre very clearly, with range increase across the main caldera in all four time-periods. A change in LOS displacement rate in the caldera is apparent with the 1996-2000 and 2000-2004 plots reaching a maximum average of ∼35 mm/year and ∼30 mm/year respectively in the caldera, much greater than the ∼15 mm/year in the 1992-1996 and 2004-2008 time

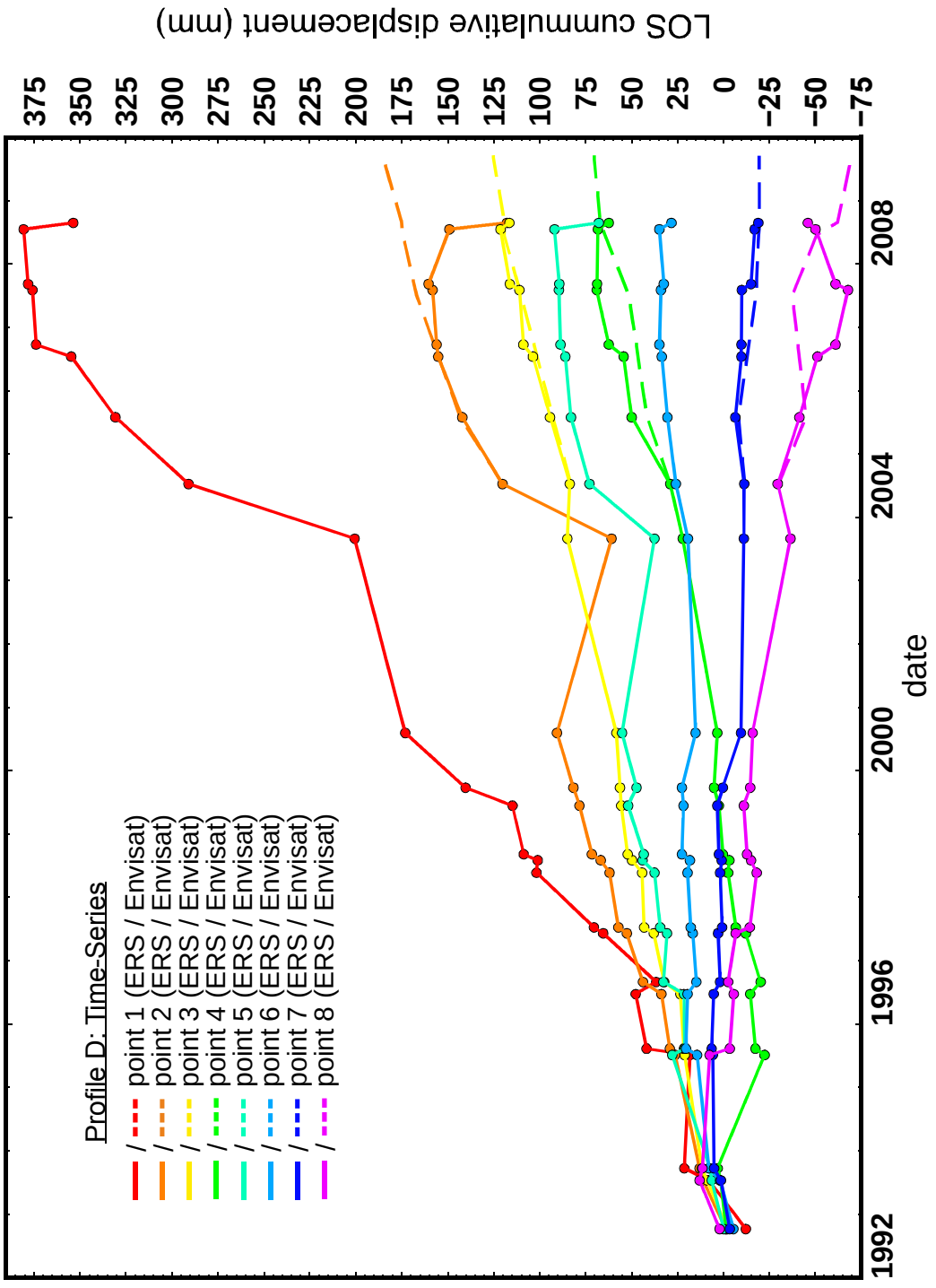

Figure 6.32: ERS (solid lines) and Envisat (dashed lines) time series plots for profile D, points 1-8 (as shown in figure 6.31a).

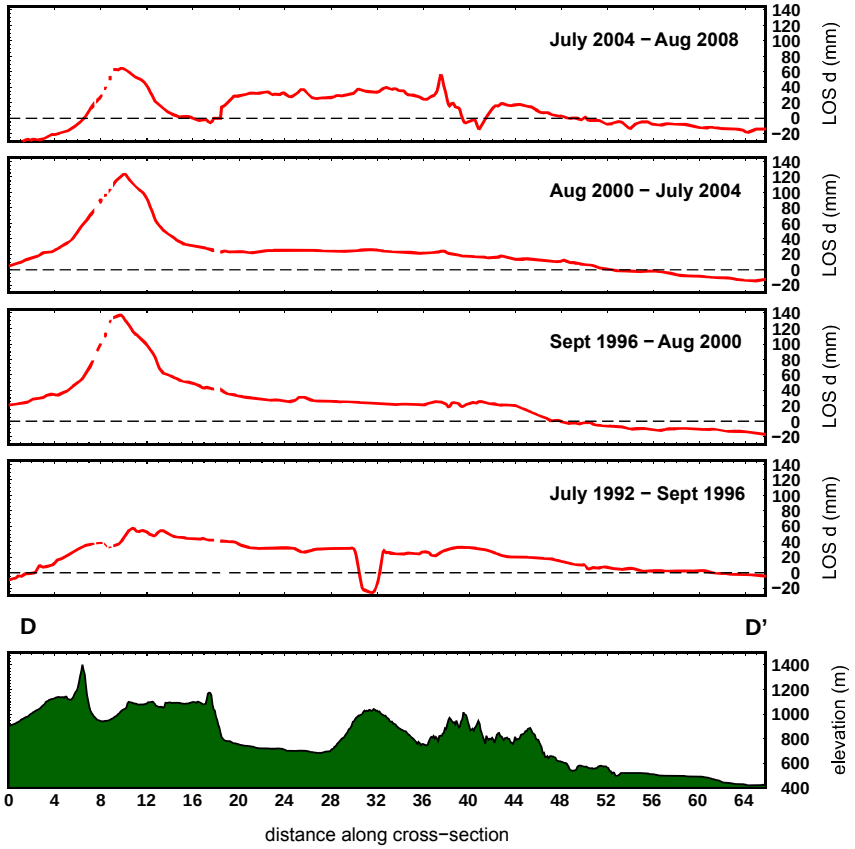

Figure 6.33: LOS cumulative displacements for profile D, over summed epochs as outlined in table 6.5, with topographical profile shown in green.

periods. Outside of the main caldera the fissure swarm displaces at a consistent rate throughout the 16 year period, with displacement rate decreasing smoothly with distance from the caldera. An increase in the displacement rate within the caldera does not appear to greatly affect displacement rate outside the caldera, Instead, the profiles show that the decay in displacement rate between the centre and the edge of the caldera increases.

The final summed time-period does not present as smooth a profile as the other three time-periods, particularly in the fissure swarm outside the caldera. The time series (figure 6.32) for a number of points had a dramatic change in displacement rate for the last two epochs, which did not compare well with the available Envisat data and is possibly the result of noise in the data. The final summed time-period is shown broken down into two parts, 2004-2007 and 2007-2008, in figure 6.34. These plots show a smoother profile for 2004-2007 that is more comparable with the other summed time-

periods, highlighting that variations in the 2007-2008 data may be due to noise and values from the Envisat data would possibly be more reliable.

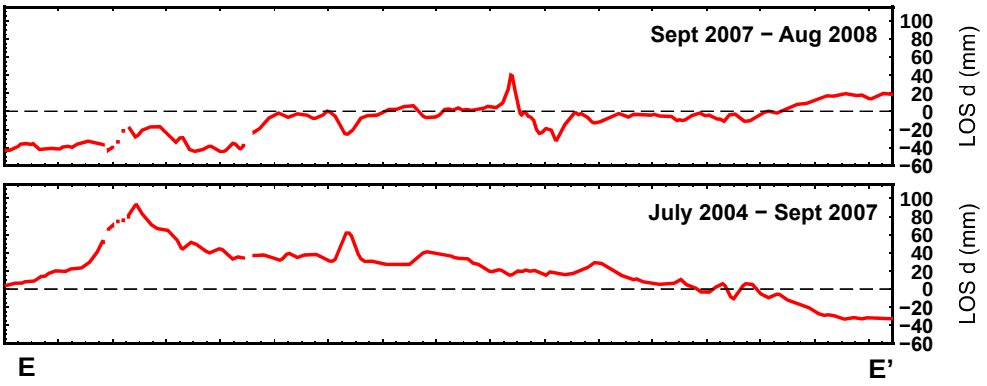

Figure 6.34: The summed time-period 2004-2008 has been broken down into two parts: 2004-2007 and 2007-2008.

Askja: profile E

Profile E is a 22 km long profile taken at a perpendicular to the major rift axis, crossing the fissure swarm to the north of the main caldera (see figure 6.19 and 6.35a). I have selected 8 points (figure 6.35a) to give a representative view of across-axis displacement behaviour of the fissure swarm. The resulting time series of the selected points are shown in figure 6.36

The time series shows a gradual increase in the average displacement rate for each time series from point 1 at the western side of the fissure swarm through to point 4 at its centre. The average rate then decreases back down again from points 5 through to 8. All of the locations show a change in displacement behaviour from 2004 onwards, particularly from 2006 where the western side of the fissure swarm shows an increase in positive LOS centred around point 3 which has a rate of $\sim$+22.5 mm/yr from 2006-2007 followed by a range decrease from 2007-2008, again at a maximum at point 3. Over the same period, points 6,7 and 8 on the eastern side of the fissure swarm experience the opposite, with an increase in negative displacement followed by a switch to range increase, both at a maximum at point 8 on the outermost eastern edges of the fissure

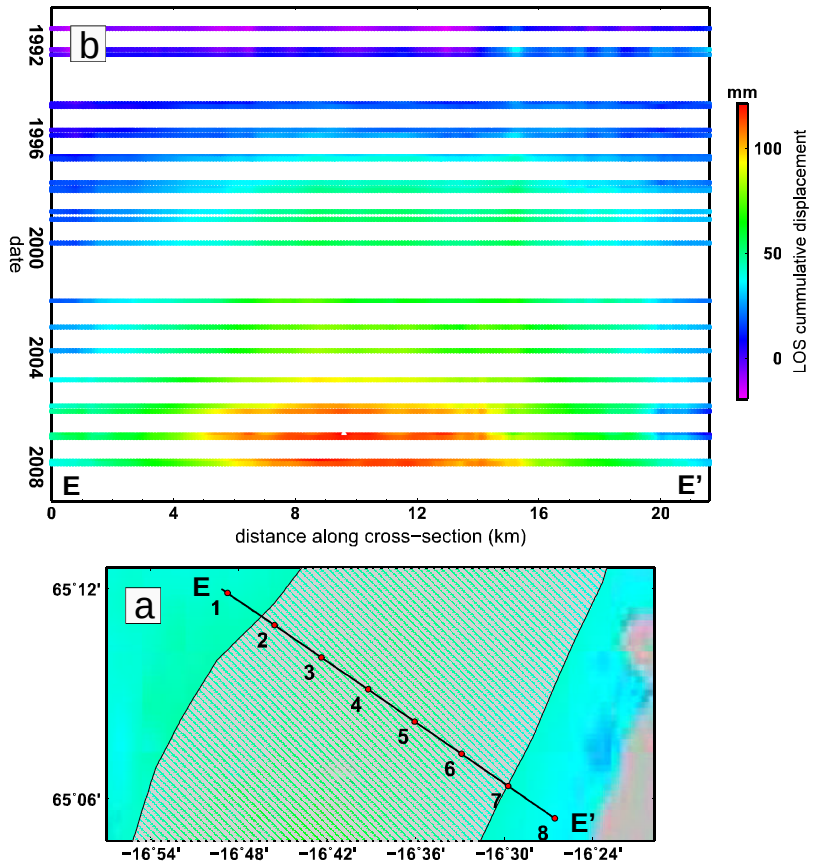

Figure 6.35: a) Map showing the location of Profile E (black line from E-E') on the stack rate-map (from figure 6.19) with the points 1-8 used for time series in figure 6.36. b) LOS cumulative displacements from 1992 through to 2008 for profile E.

swarm. These changes in displacement can be seen in the summed profiles in figure 6.37 which also highlight a period of quiescence prior to this period of activity.

To examine trends in displacement rate across the whole profile, I have summed the LOS displacements across the equal time periods as outlined for profile C in table 6.5.

The four summed time-periods show a constant rate of displacement across the entire 16 years, with a LOS displacement rate that increases smoothly from the edges of the fissure swarm to its centre, a distribution that remains consistent through time. The rate change observed within the caldera in profile D does not appear to have any influence on the rate of LOS displacement in the fissure swarm at this point.

As with profile D, the final summed time-period is noisier than the other three periods. The ERS time series for 2006 onwards show a lot of fluctuation in displacement whereas the Envisat time series gives more stable results that follow the general trend

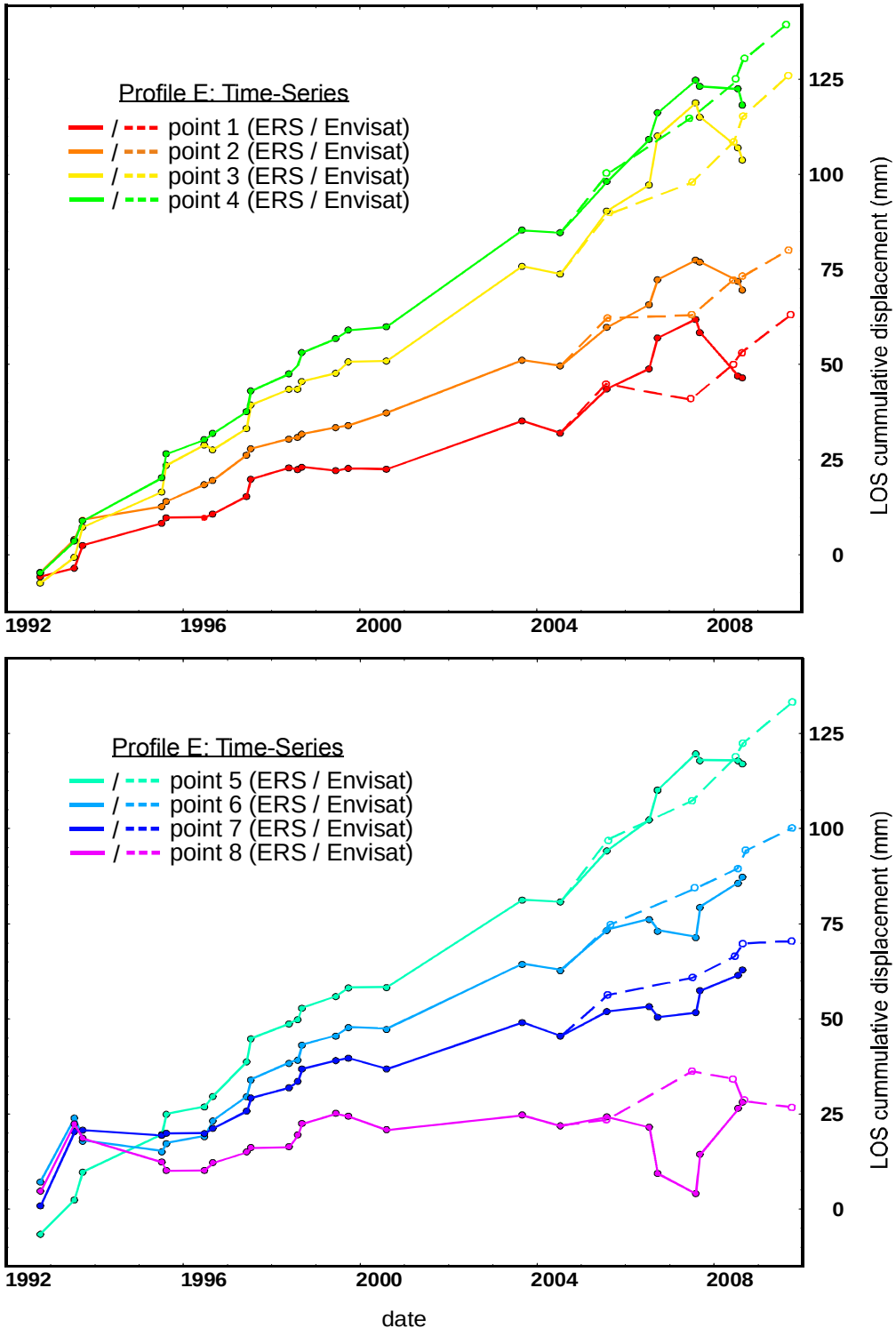

Figure 6.36: ERS (solid lines) and Envisat (dashed lines) time series plots for profile E, points 1-8 (as shown in figure 6.35a).

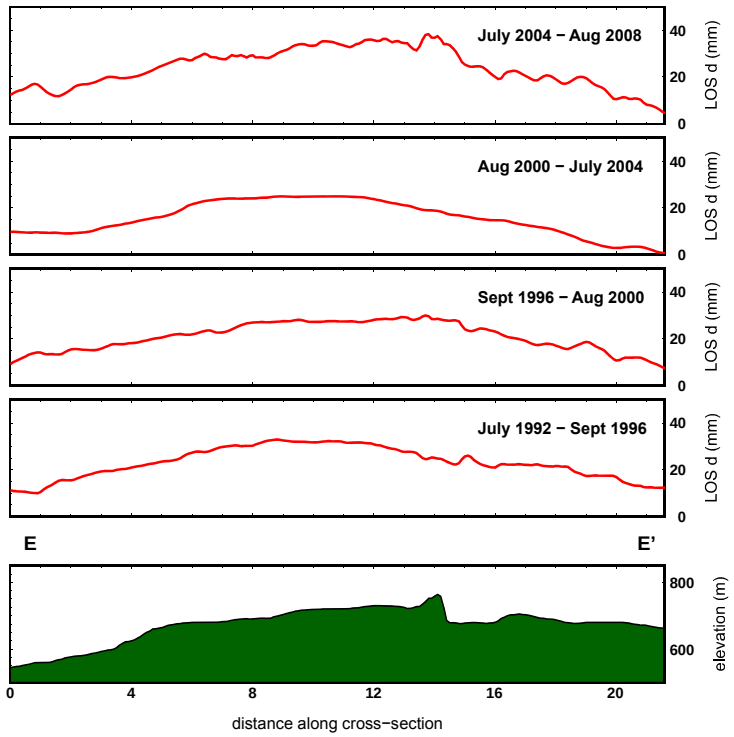

Figure 6.37: LOS cumulative displacements for profile E, over summed epochs as outlined in table 6.5, with topographical profile shown in green.

in displacement followed by the ERS time series up to 2006. It is most likely that there is noise in the ERS time series post-2006 and that the Envisat data is more reliable at this point.

6.9 Discussion and conclusion

Whilst it is useful to use π-rate to create an average LOS displacement rate map from a series of interferograms, it is important to understand that the average rate may not be a continuous rate throughout the time covered by the rate map. Using time series plots for selected points in the rate map, I was able to identify trends in displacement rates and confine episodes of displacement to within certain time-periods. Summing along-profile LOS displacement for all epochs within each time-period made it possible to identify displacement behaviour through time both along- and across-axis for both the Krafla and Askja calderas and fissure swarms.

Using time series and summed displacement plots I have been able to constrain the time durations of active surface displacement in the northern NVZ. The Krafla region

incurs surface displacement from three possible separate sources. Initially there is a localised short-wavelength surface deflation focused around the Krafla caldera, combined with a long-wavelength surface inflation focused further north between Krafla and Freminamar fissure swarms. A third long-wavelength surface inflation, focused at the Theistareykir volcanic centre, becomes prevalent at the latter end of the 16-year observation period.

de Zeeuw-van Dalfsen et al. (2004) modelled two possible Mogi sources in Krafla. A deflating Mogi-source at 2.4 km beneath the main caldera and an inflating source at a depth of 21 km lying ∼15 km north of the caldera. I observe that the shallow deflating source beneath the caldera is seen to decay from 1992 through to 1996, by which time the surface deflation is very small. The longer wavelength surface inflation between the Krafla and Freminamar fissure swarms, is seen to inflate through the same time, with an inflation signature lasting through to 1999. The cross-axis profile implies that the deeper source modelled by de Zeeuw-van Dalfsen et al. (2004) lies to the east of, rather than directly below, the major axis of the Krafla fissure swarm. Alternatively, the long-wavelength signature could be a residual effect of post-rifting - as this inflation signature disappears by 1999 this is a distinct possibility.

Between 1999 and 2004 there is a period of quiescence showing very little surface displacement across the northern NVZ. In 2004 a longer-wavelength surface inflation signature commences. However, this time the focus of the inflation has migrated to beneath the Theistareykir central volcano. The long-wavelength signature would imply a deeper source than that causing the deflation in the Krafla caldera. This agrees with results from studies made by Metzger et al. (2011) who modelled inflation over Theistareykir from InSAR pairs produced whilst examining the Tjornes Fracture Zone (at the northern end of the Theistareykir fissure swarm). Metzger et al. (2011) modelled the uplift signature, centred at the Theistareykir central volcano, using a Mogi source in an elastic half-space. Metzger et al. (2011) constrained the location of the Mogi source at a depth of 8.5 km below the central volcano.

Further south in the NVZ, the Askja fissure swarm showed decreased range (inflation) rates that were constant through time both along- and cross-axis and appeared to be largely unaffected by changes in displacement rate in the caldera. Inflation rate cross-axis increased smoothly from both the western and eastern edges to a maximum inflation rate at the centre of the swarm. The along-axis profile showed the fissure

swarm to decrease in range increase smoothly with distance from the caldera to a range decrease (subsidence) at the far north of the fissure swarm ∼52 km from the caldera centre. The subsidence appears to be part of the long-wavelength displacement centred in the north of the NVZ. The Askja caldera does not maintain a constant rate of displacement throughout the 16 year period. Changes in displacement rate can be constrained to three time periods: 1992-1996, 1996-2004 and 2004-2008 with maximum inflation rates of ∼8 mm/year, ∼30 mm/year and ∼15 mm/year respectively. de Zeeuw-van Dalfsen et al. (2012, 2013) presented a consistently decaying rate through time between 2000-2009, however the results in de Zeeuw-van Dalfsen et al. (2013) were the result of an average rate measured over long time-period interferogram pairs (e.g. 2003-2008). Using a time series produced from many smaller epochs has made it possible to more readily observe changes in rate through time.

Errors caused by noise in the interferograms can misrepresent the amount of displacement. Using time series makes it easier to identify the general trend across epochs and identify epochs that contain possible noise. Producing time series for the same location using different satellites (such as ERS and Envisat), or, if sufficient interferogram pairs are available, creating time series that use different group of interferograms across the same time-span, would help with the identification of incorrect displacement values.

Chapter 7

Long- and short-term deformation in Krafla

7.1 Introduction

In this chapter I shall use horizontal GPS velocities measured during GPS campaigns in the NVZ (Árnadóttir et al., 2009, Jouanne et al., 2006) to remove horizontal displacement from the InSAR time series and extract the vertical displacment values for Krafla over the 16-year period from 1992-2008. The vertical displacement can then be used to calculate rates of displacement over the short-term and will be compared with the displacement observed in the long-term over the region covered by the LiDAR survey.

I will examine the region of subsidence to the north of the main Krafla caldera, as observed in the InSAR in the previous chapter, by taking profiles through the InSAR vertical displacement and directly comparing them to features in the LiDAR DEM.

Finally, using a series of profiles extracted from the LiDAR DEM, I will measure the total throw for regions of faulting across the fissure swarm and calculate the total horizontal opening perpendicular to the major rift axis.

7.2 Vertical displacement using InSAR

7.2.1 Velmap

The range changes recorded by the interferograms are a measurement of ground displacement along the line-of-sight (LOS) of the satellite, with the LOS being along the direction between the satellite and the point being mesasured on the ground. The range change is therefore a combination of ground motion in the horizontal (north-south and

east-west) directions, and also in the vertical direction. To examine the characteristics of vertical displacement in the region, I will remove the horizontal components of the LOS measurement and adjust for the angle of the LOS as follows:

$$d_v = \frac{1}{u_v}(d_{LOS} - d_e u_e - d_n u_n) \tag{7.1}$$

where d_{LOS} is the LOS displacement, d_v, d_e and d_n are the components of displacement in the vertical, e-w and n-s directions; and u_v, u_e and u_n are the vertical and horizontal components of the unit vector u_d along the LOS from the ground, as shown in figure 7.1. The unit vector can be calculated as follows:

$$u_d = -\sin\theta \cdot \cos\beta) \cdot (u_e) - \sin\theta \cdot (-\sin\beta) \cdot (u_n) - \cos\theta \cdot (u_v) \tag{7.2}$$

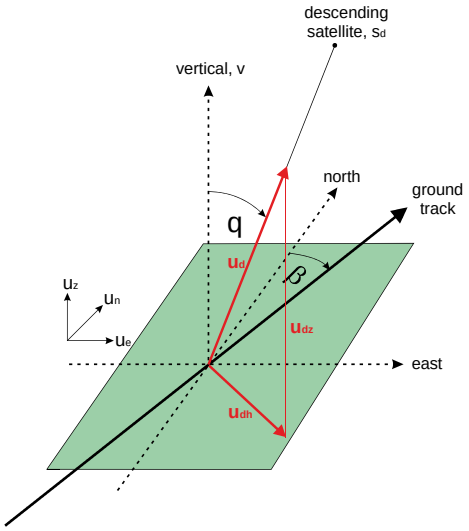

Figure 7.1: Showing the horizontal and vertical components of the LOS displacement for the descending satellite, S_d, redrawn from Catalão et al. (2011)

Velmap is a tool that given GPS velocities, d_{gps}, and InSAR LOS average displacement rates, d_{sar}, is able to calculate a 3-dimensional velocity field of the given area by

solving the following linear equations:

$$\begin{bmatrix} G_{sar} & G_{orb} & G_{atm} \\ G_{gps} & 0 & 0 \\ \kappa^2\nabla^2 & 0 & 0 \end{bmatrix} \begin{bmatrix} m_{vel} \\ m_{orb} \\ m_{atm} \end{bmatrix} = \begin{bmatrix} d_{sar} \\ d_{gps} \\ 0 \end{bmatrix} \tag{7.3}$$

where ∇^2 represents the Laplacian smoothing and κ represents the smoothing parameter whose value is guided by the required level of solution roughness versus the weighted residual misfit. G_{orb} and G_{atm} represent the orbital and atmospheric errors in the InSAR (the GPS data does not contain either orbital or atmospheric errors). Velmap fits the data to an arbitrary triangular mesh and by assuming a linear velocity within each triangle, it creates a velocity surface based on the available points within the mesh. For a more complete description, see England and Molnar (1997, 2005), Wang and Wright (2012).

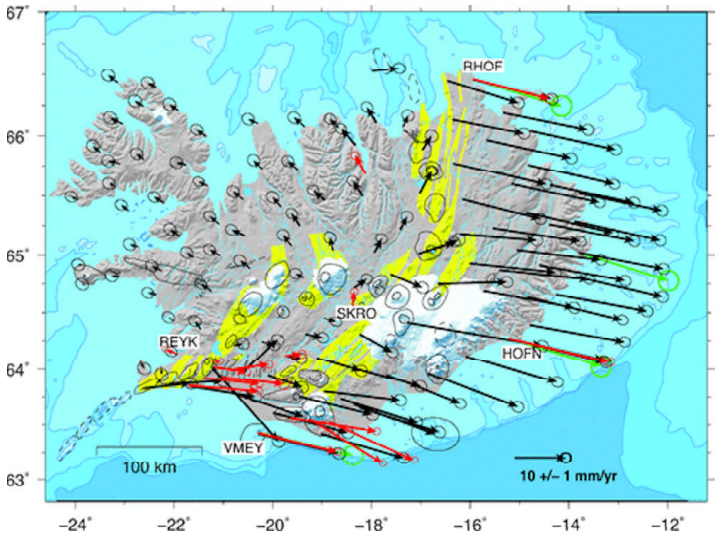

Figure 7.2: Map of horizontal GPS velocities for Iceland from 1993-2004 as published in (Árnadóttir et al., 2009). The velocities are relative to a stable North America, with GPS measurements from ISNET taken between 1993-2004 (black arrows) and from CGPS stations across Iceland taken between 1999-2004 (red arrows). Reprinted from Geophysical Journal International, vol. 177, Árnadóttir et al. (2009), Glacial rebound and plate spreading: results from the first countrywide GPS observations in Iceland, 691-716, ©2009, with kind permission from Wiley.

For the purposes of this work I will use *velmap* for interpolation of the GPS data only:

$$\begin{bmatrix} G_{gps} \\ \kappa^2\nabla^2 \end{bmatrix} m_{vel} = \begin{bmatrix} d_{gps} \\ 0 \end{bmatrix} \tag{7.4}$$

The resulting interpolation is given in horizontal north-south, horizontal east-west and vertical velocities (if using). We can then subtract the horizontal displacement rates from the horizontal from the LOS displacements produced by $\pi{-}rate$ to give a high resolution vertical displacement.

The horizontal GPS velocities have been taken from the published GPS dataset Árnadóttir et al. (2009), produced from a combination of the ISNET GPS data acquired over the time period 1993-2004 and a continous GPS survey of Iceland acquired over the time period 1999-2004, see figure 7.2. A profile of the GPS velocities taken through the Krafla Volcanic Centre is shown in 7.3

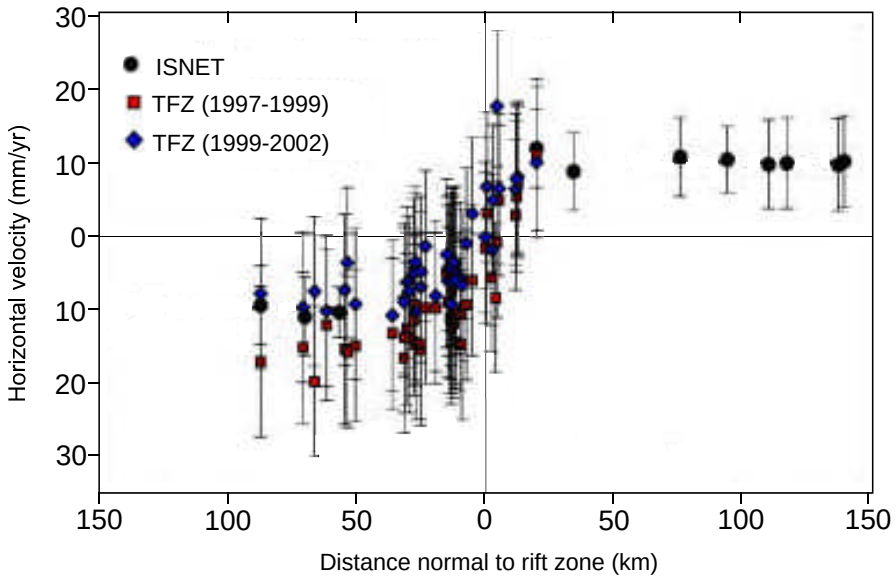

Figure 7.3: Showing the horizontal GPS velocities along a profile perpendicular to the fissure swarm in the region to the north of the main caldera. Velocities are the result of the ISNET campaign from 1993-2004 (Árnadóttir et al., 2009) and the Tjornes Fracture Zone (TFZ) GPS campaigns in 1997, 1999 and 2002 (Jouanne et al., 2006) (figure taken from Pedersen et al. (2009). Reprinted from Earth and Planetary Science Letters, vol. 281, Pedersen et al. (2009), Rheologic controls on inter-rifting deformation of the Northern Volcanic Zone, Iceland, pages 14-26, ©2009 with permission from Elsevier.)

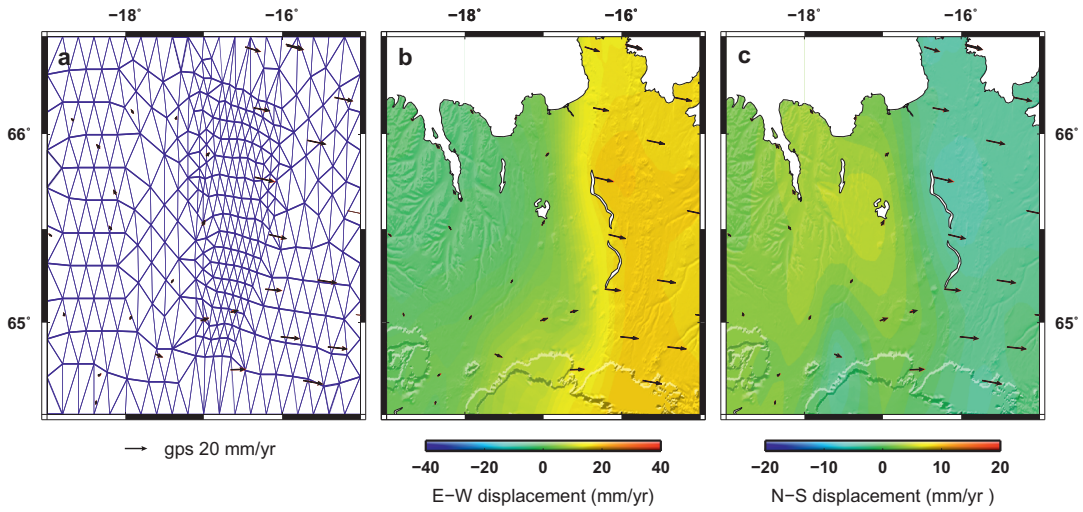

Figure 7.4: Interpolating GPS velocities using velmap where a) shows the interpolation mesh created using GiD, the GPS velocities are shown with the black arrows. The resulting interpolated horizontal displacement rate maps are shown for b) the E-W horizontal displacement and c) the N-S horizontal displacement.

As a default, velmap uses Delaunay triangulation to create the interpolated rate map. However, as the GPS data available for the region are sparse, the resulting surface is not good. I created a non-uniform mesh using the GiD software, with a finer mesh over the region covered by the InSAR track (see figure 7.4a). This mesh was then imported into velmap and the GPS velocities were interpolated across the mesh producing displacement rates for the E-W and N-S horizontal displacement and the vertical displacement. The horizontal rates can be seen plotted as the interpolated surface in figure7.4b and c.

7.3 Vertical displacement north of Krafla main caldera

There is a region of range increase north of the caldera visible in the stack rate maps in the previous chapter. This deflation signature is localised within $\sim$ 2-3 km (see figure 7.5) and as such implies a shallow source. I have extracted the vertical displacement from the InSAR for 12 profiles that cut across the deflating region (figure 7.5) with some taken to the north of the signature. I have compared these cross-sections with the LiDAR DEM (figure 7.7), which shows that the deflation signature coincides with the 1984 lava flow.

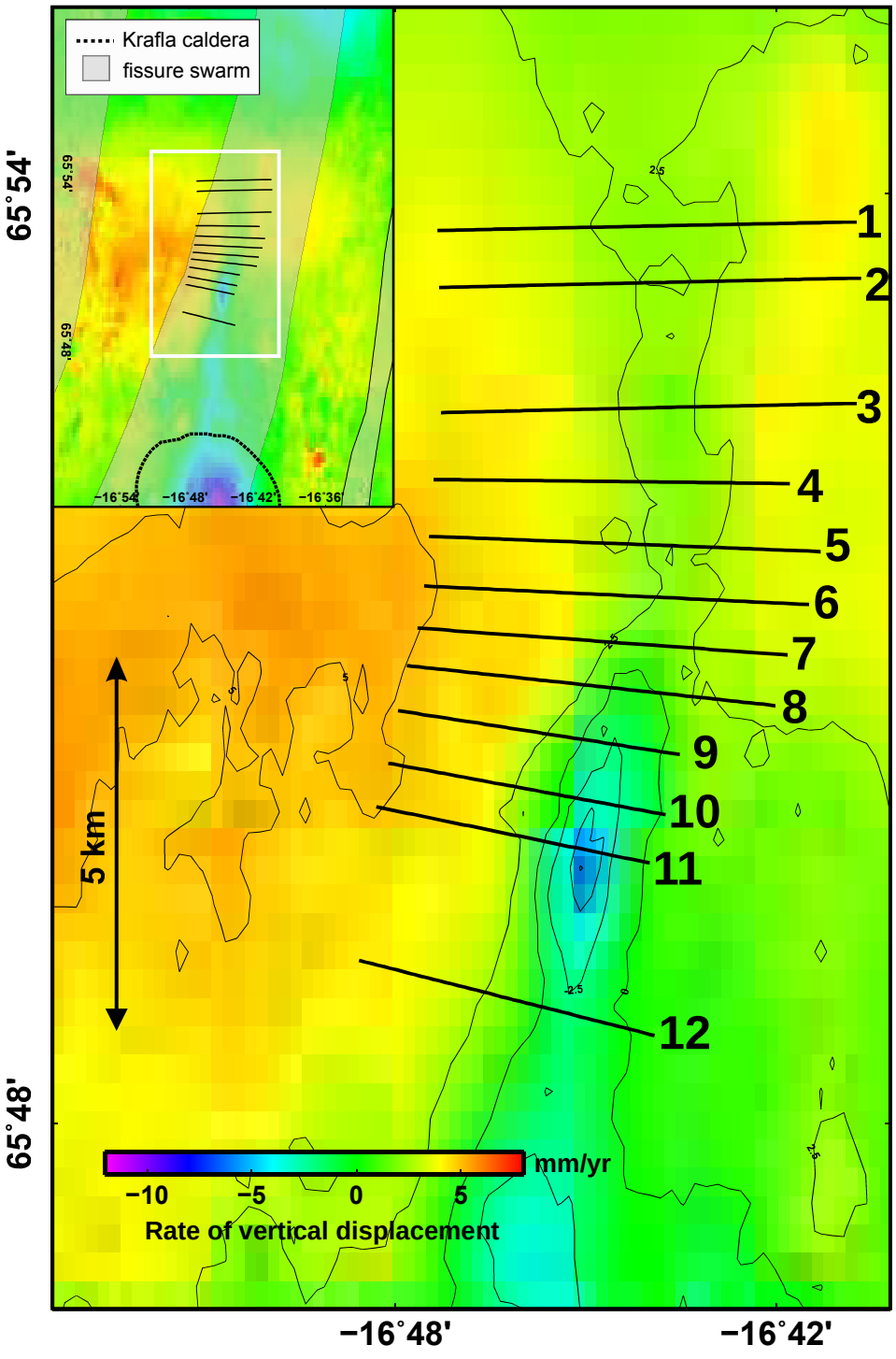

Figure 7.5: InSAR stack rate map of selected cross-sections used to compare InSAR cumulative vertical displacements with actual surface features in the LiDAR DEM. Inset map shows the wider area with the subsidence in the Krafla caldera at the bottom centre. White boxed area shows the region shown in the main map.

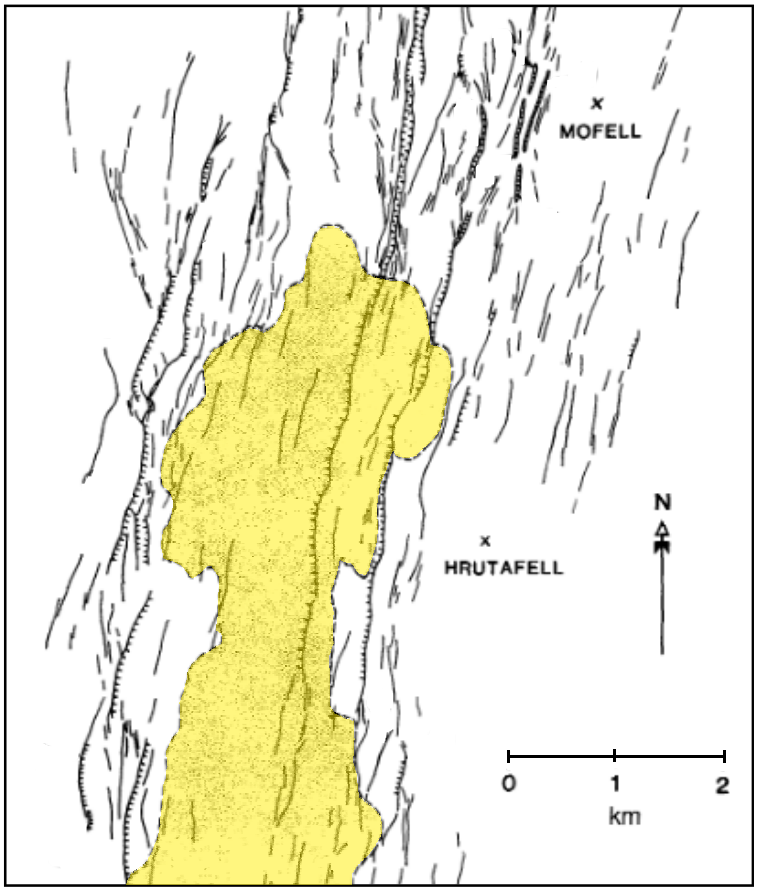

Figure 7.6: Map taken from (Opheim and Gudmundsson, 1989) showing faults now buried by the Krafla Fires lava flows (yellow area). Pre Krafla Fires fault data was acquired from 1960 aerial photographs. Reprinted with kind permission from Geological Society of America Bulletin, vol. 101, Opheim and Gudmundsson (1989), Formation and geometry of fractures, and related volcanism, of the Krafla fissure swarm, northeast Iceland, 1608-1622, ©1989.

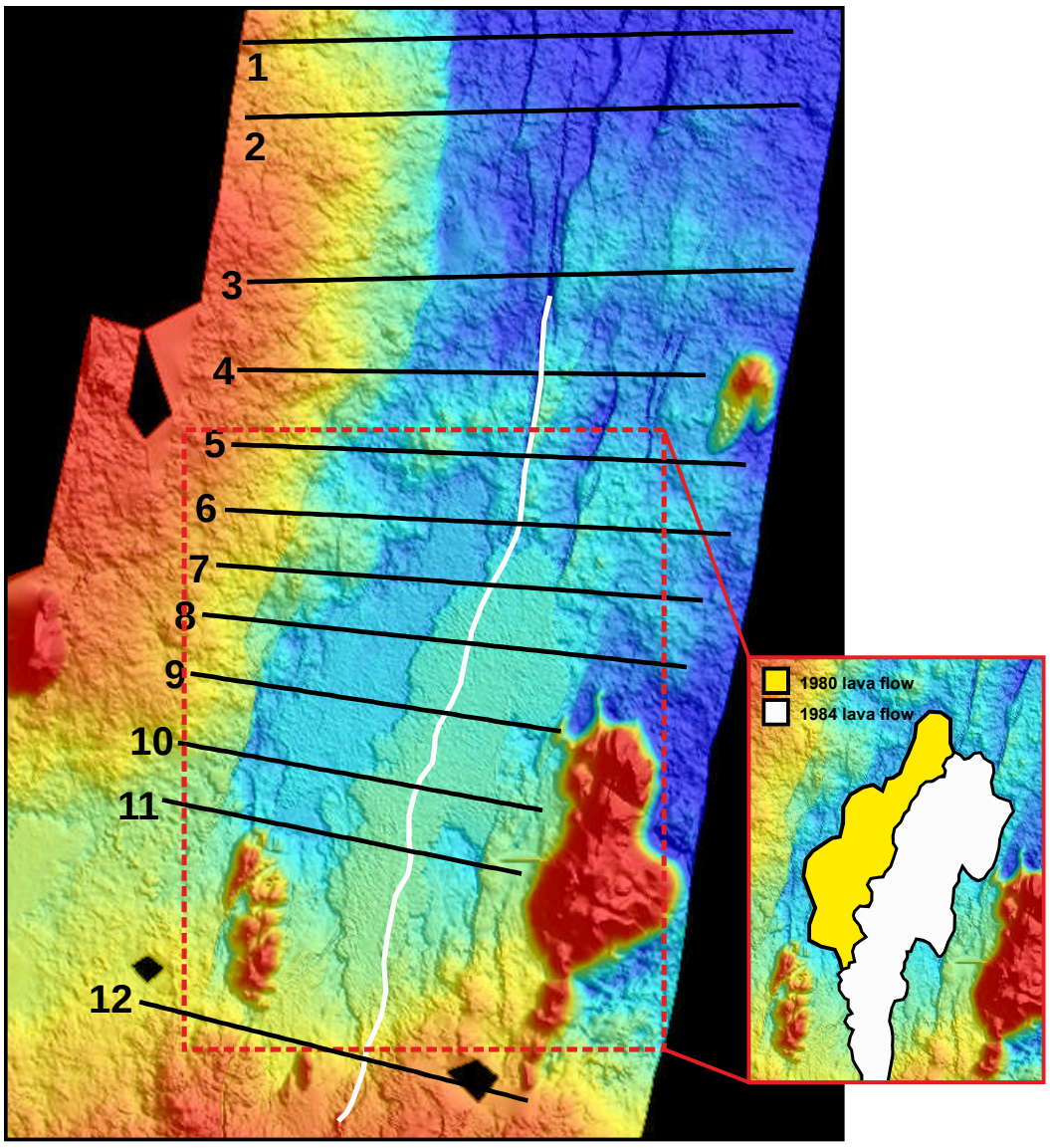

Figure 7.7: Map of selected cross-sections used to compare InSAR cumulative vertical displacements with actual surface features in the LiDAR DEM. White line denotes the location of the large fault system partially covered by the Krafla Fires lava flows. Inset image details the location of the 1980 and 1984 lava flows.

Figure 7.6 shows the location of faults beneath the Krafla Fires lava flow. Of particular interest is the long fault system visible in the LiDAR DEM just to the north of the 1984 lava flow. This fault system continues south in figure 7.6 towards the main caldera for some distance beneath the lava flow and coinciding with the location of the localised surface displacement. The fault system has been marked on both the map in figure 7.7 and the profile plots in figures 7.8, 7.9 and 7.10.

Using the summed epochs selected for the Krafla region in the previous chapter and shown in table 7.1 it is possible to identify the short-wavelength signature within the longer wavelenth signature of uplift identified in this part of the NVZ in the previous chapter. Initially I have plotted all 12 profiles using the first summed period only (from July 1992 to Sept 199), these plots are shown in figure 7.8. Additionally, the location of the lava flows for both 1980 and 1984 are shown. The plots show that the deflation signature completely dies out in the profiles north of the lava flow. They also show that the deflation signature increases in size through to profile 11 and then decreases in profile 12. According to the 1960s map (figure 7.6) the underlying fault ends just south of profile 12.

Table 7.1: Time periods used for summing incremental LOS displacement.

Start	End	Length (years)
July 1992	Sept 1999	7
Sept 1999	July 2004	5
July 2004	Aug 2008	4

To examine the behaviour of the deflation over time, and to see if there has been any change in displacement rate, I have used the profiles over the lava only (profiles 7-12) to make comparison plots of the summed vertical displacements. I have used all three summed periods as outlined in table 7.1. Plots are shown in 7.9 and 7.12.

The amount of displacement in each summed epoch has been extracted (see figure 7.11) and converted into a rate of displacement. The rates of displacement have been plotted in figure 7.7.

The results show that the short-wavelength signature is focused over the 1984 lava flow and the underlying fault signature. Lava flows contract and subside by both mechanical and thermal processes as they cool (Toombs and Wadge, 2012) with a rate of subsidence that is related to both the thickness of the flow and the time since the flow

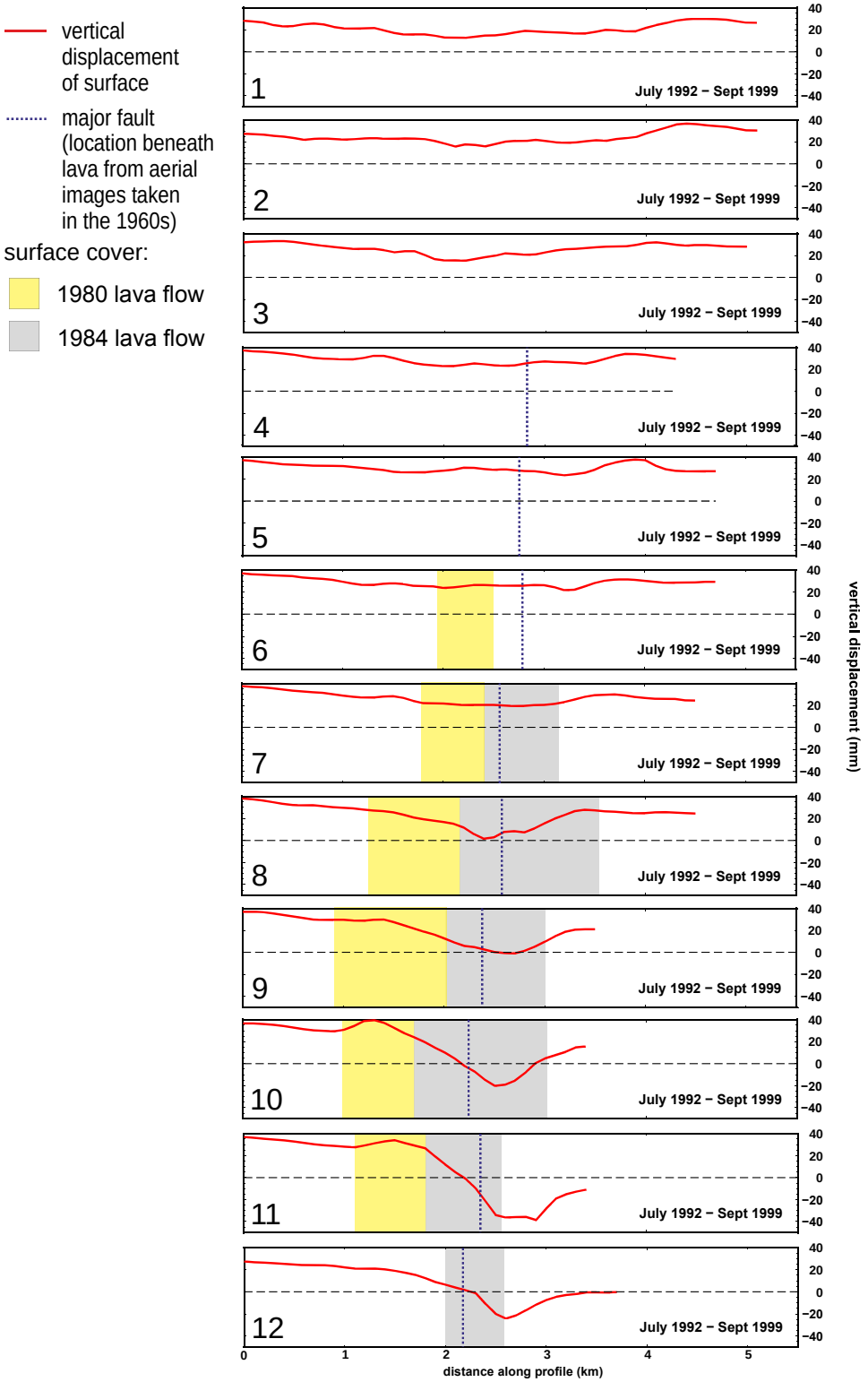

Figure 7.8: Vertical displacement plots over Krafla Fires lava flow from 1992-1989. Profiles are 1-12 as shown in figure 7.7.

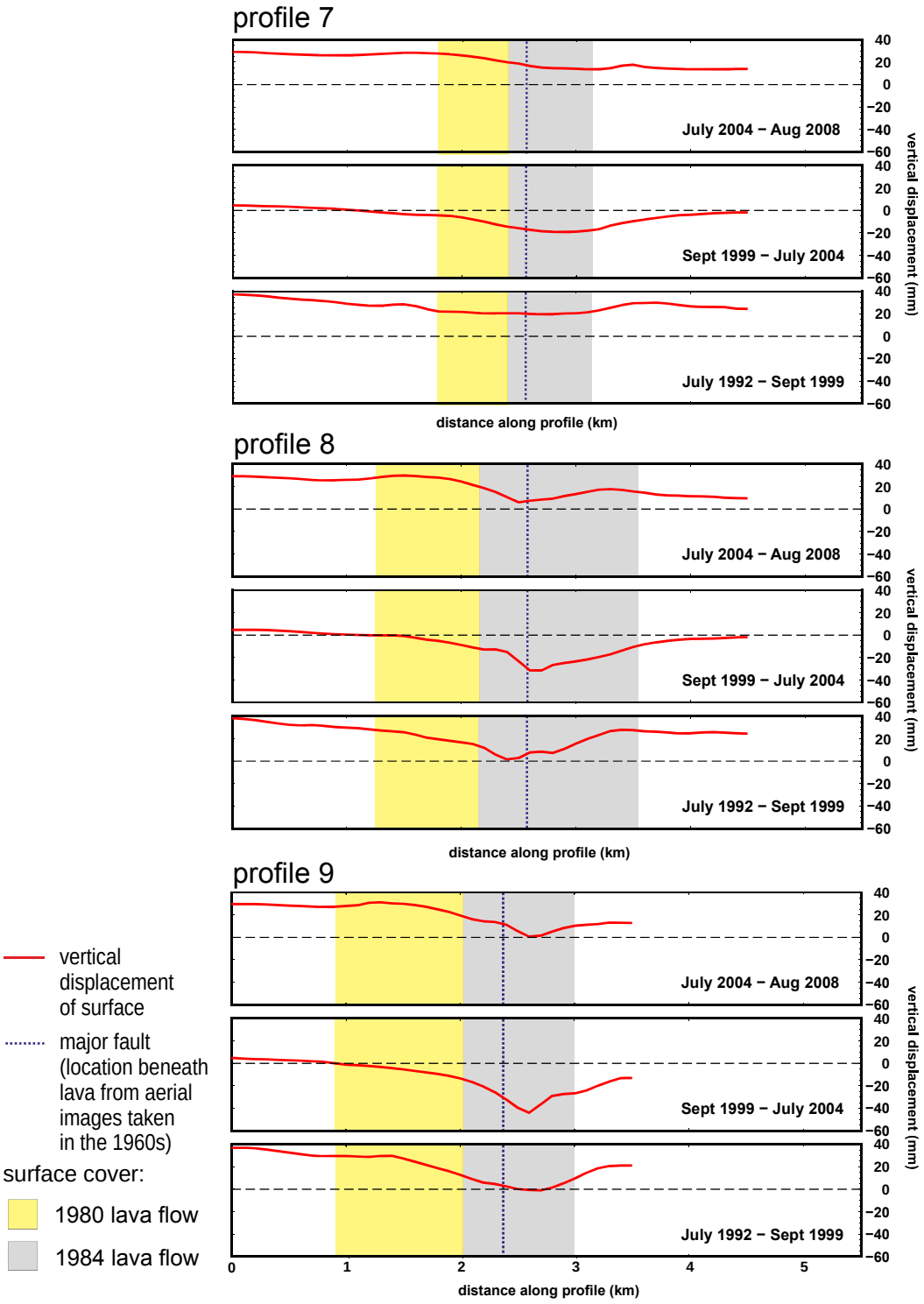

Figure 7.9: Cumulative vertical displacement plots for summed time periods (see table 7.1 over Krafla Fires lava flow. Profiles are 7-9 as shown in figure 7.7. Blue dotted line denotes the location of the major fault underlying the lava flow - location of fault identified from aerial images taken in the 1960s (see figure 2.5 in 2).

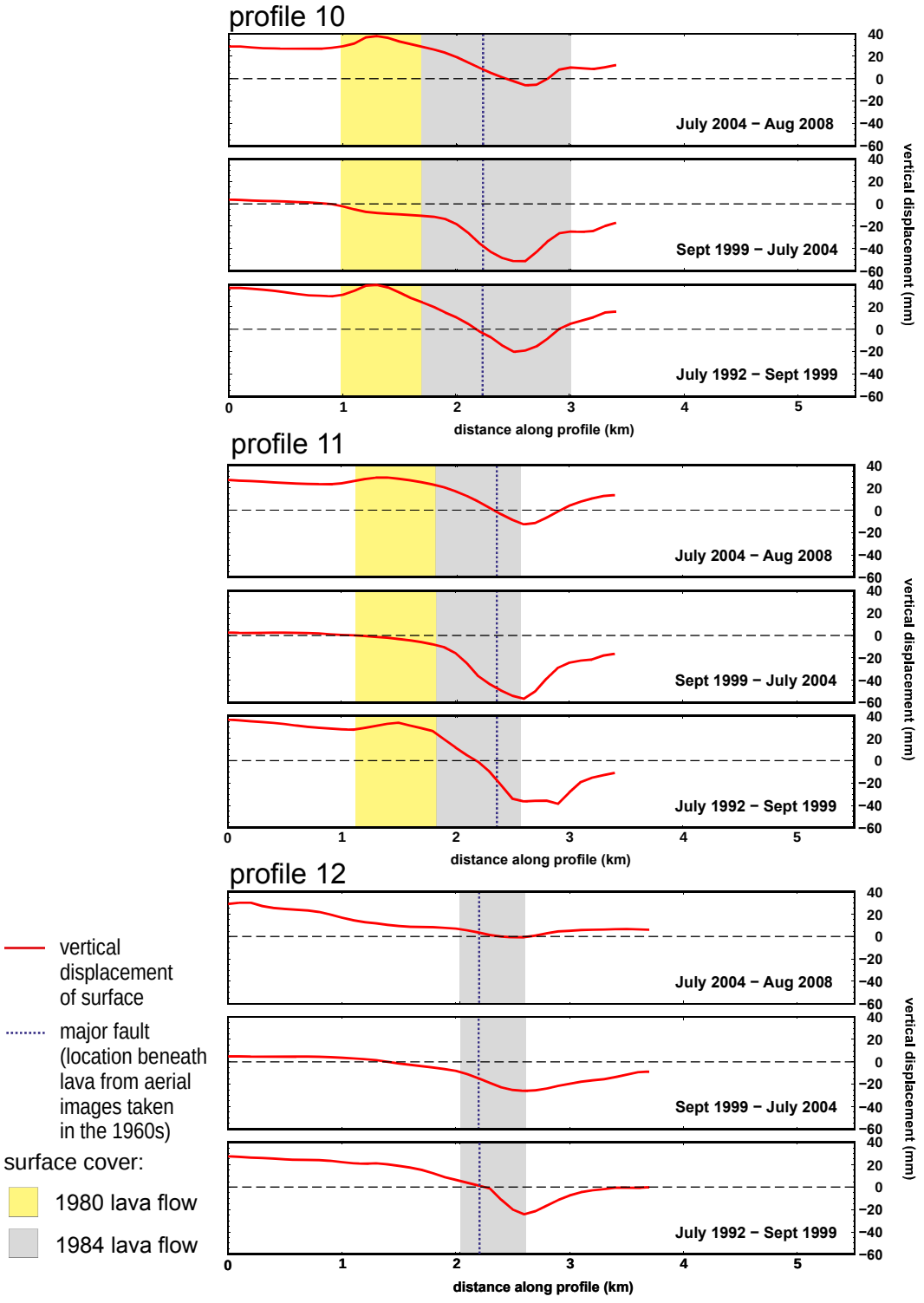

Figure 7.10: Cumulative vertical displacement plots for summed time periods (see table 7.1 over Krafla Fires lava flow. Profiles are 10-12 as shown in figure 7.7. Blue dotted line denotes the location of the major fault underlying the lava flow - location of fault identified from aerial images taken in the 1960s (see figure 2.5 in 2).

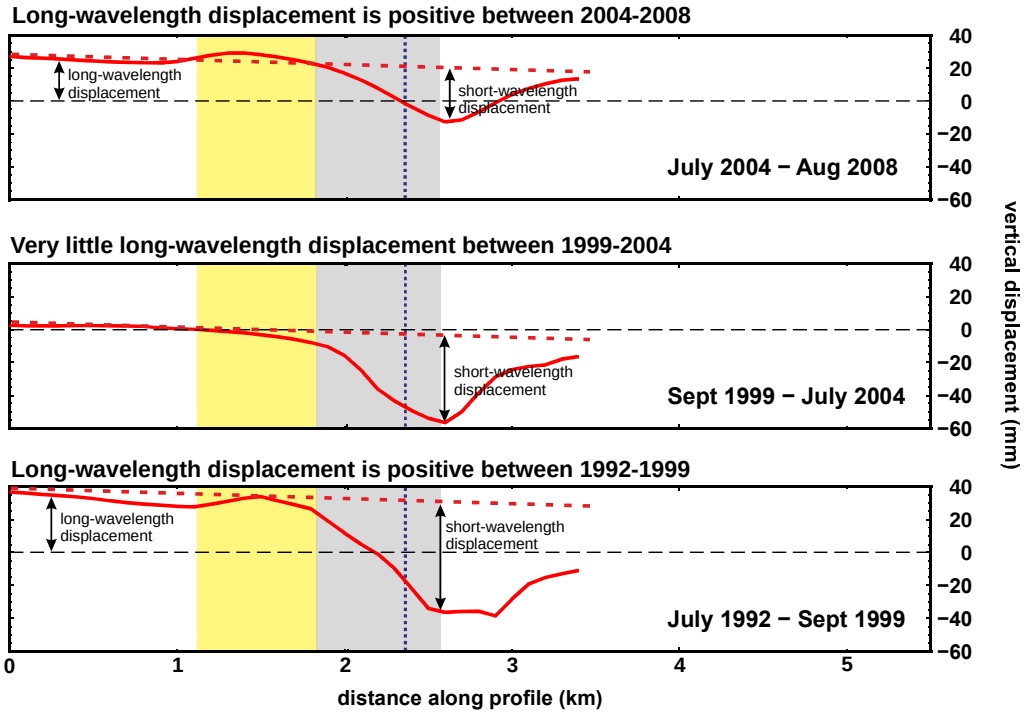

Figure 7.11: Removing long wavelength displacement from displacement profile to extract short-wavelength displacement. Approximate long-wavelength trend is shown as dotted red line. Profile 11 from figure 7.7 is used as an example displacement profile.

was emplaced (Stevens et al., 2001). Profiles 7, 8, 9 and 12 also show a reduction in rate over time which would imply that the lava thickness is small enough that the rate of subsidence through cooling and settling is starting to decay with time. However, profiles 10 and 11 do not show a decrease in rate maintaining a deflation rate of ∼10 mm/year, which would imply that the thickness of the lava is great enough at these locations that the cooling and settling is maintaining a near constant rate. Briole et al. (1997) noted that lava in Etna, with a maximum thickness of 10 m, subsided at 2.5 cm/year with an exponential relaxation time of 3.5 years (using a Maxwell visco-elastic relaxation time). Tryggvason (1986) documented the 1984 lava flow as having covered an area 24 km^2 area with a volume of $\sim 10^8\ m^3$ and an estimated average thickness of ∼5 m. Figure 7.13 is a schematic that shows the relative thickness to the hanging wall side of the fault, which adds the depth of the throw to the average depth of the the lava flow.

Figure 7.7 shows that the 1984 lava flow has a fairly continuous elevation across its surface. This implies that any underlying faults are completely submerged as they do

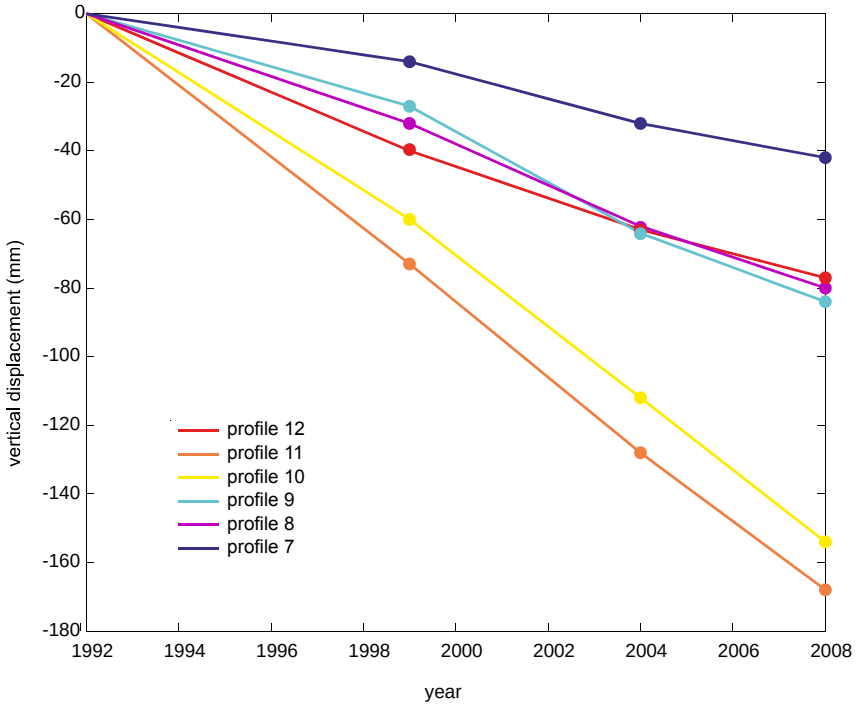

Figure 7.12: Plot of vertical displacement over the 1980/1984 lava flows with rates measured at the point of maximum vertical displacement. Vertical displacement taken from profiles 7-12 (as shown in figures 7.5 and 7.7).

not show as a surface feature in the lava. In the LiDAR DEM the large fault structure buried beneath the 1984 lava flow is part of a large fault system going north that has a throw of ∼5-8 m in the region close to the northernmost point of the lava flow, reaching throws of up to 30 m further north. It is possible that the fault has similar throw underneath the lava and this depth would account for there still being a subsidence signature 30 years after the lava's emplacement.

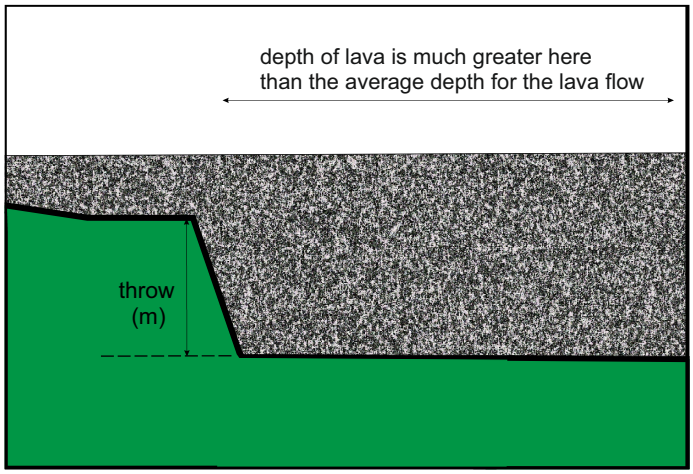

Figure 7.13: A schematic showing the change in depth of lava flow across a fault, showing the increase in depth on the hanging wall side of the fault.

7.4 Horizontal opening in Krafla fissure swarm

In this section I will use the LiDAR DEM to extract fault throw and fissure opening measurements from which I will examine how much of the plate spreading rate is accomodated by rifting events alone. I have taken four profiles 1-4, shown on the map in figure 7.5 in the previous section.

From these I have measured the total throw on each of the faulted structures showing vertical displacement across the DEM surface. The DEM surface and related throw data for each profile are shown in figures 7.15 for profiles 1 and 2 and 7.16 for profiles 3 and 4. I have also measured the angle of dip at over 35 locations to get an approximation of the dip angle on faults in the region. A histogram of these measurements is shown in figure 7.14 from which the average dip angle is $\sim$70-75^o. Using the dip angle I have converted the total measured throw into horizontal opening on the fault. As the sub-surface dip on a fault may be much shallower than at the surface, I have also calculated the opening on a fault with much smaller dip (45^o).

As a large amount of horizontal opening is accomodated by fissure opening, I have also measured the opening across all the fissures in each profile. These have been added to the opening calculated from the throw. All the results are shown in table 7.2.

The total horizontal opening across the fissure swarm ranges between 74-148 m for a 75^o dip and between 100-171 m for a 45^o dip. As all four profiles have been taken over

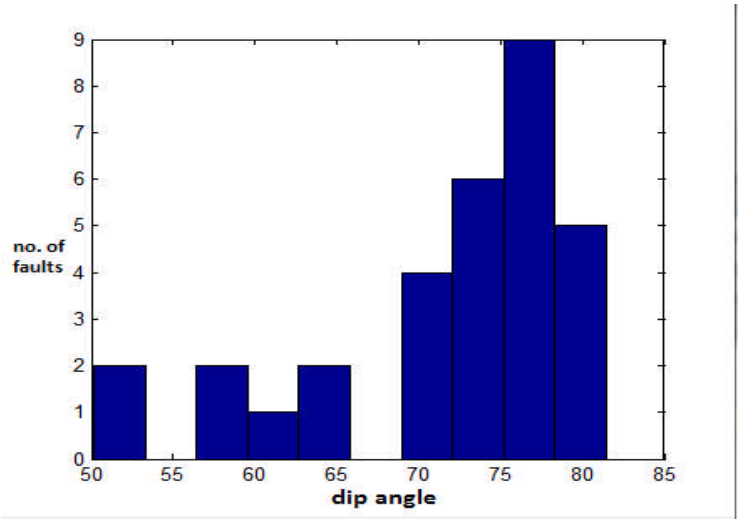

Figure 7.14: Histogram of dip on faults in region north of the Krafla Fires lava flow

the 10,000-year-old lava flow in the northern part of the fissure swarm, it is possible to assume that all the opening at the surface has occured in the last 10,000 years. This means that Krafla acommodates 10-17 mm/yr of extension in the NVZ and is the dominant structure. The Krafla rifting event produced ~9 m of horizontal opening and assuming that all rifting events in Krafla produce a similar amount of opening, Krafla would have experienced between 8 and 20 rifting episodes in the last 10,000 years.

The plate spreading rate in the Iceland region is ~19 mm/year which over 10,000 years would mean that 190 m of total plate spreading would need to be accommodated at the plate spreading centre. Even the maximum opening value does not accommodate all the opening needed. This either implies that the strain is being accommodated outside of the major rifting events in a slower, less intrusive manner. Or, more likely, that the strain is being accommodated across all the fissure swarms that lie in a line perpendicular to the plate spreading axis. For this region of the Krafla fissure swarm the en echelon style of the surrounding fissure swarms means that there is overlap with both the Theistareykir fissure swarm and the Frerinamar fissure swarms and that some of the strain is being accommodated by the other two fissure swarms.

An examination of the horizontal opening over the other two fissure swarms would help answer the question as to whether strain is being completely accomodated by rifting episodes.

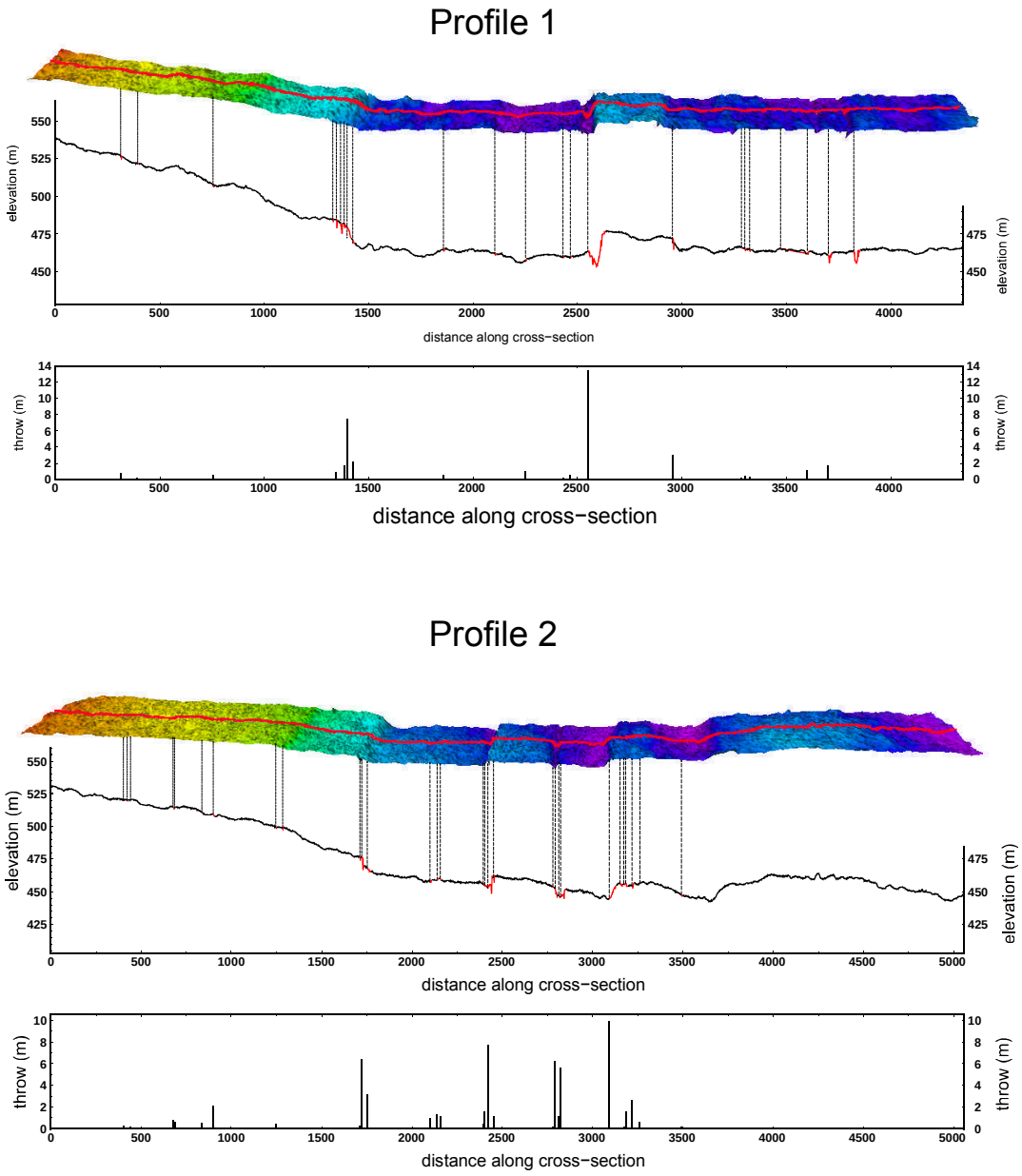

Figure 7.15: Cross-section 3 and 4 used to calculate throw and horizontal opening. Each profile consists of a DEM plot of the surface with the red line showing the profile, below this is a plot of the elevation across the profile, with the red sections showing the areas of vertical displacement by faulting - the throw was extracted for these sections and is plotted in the bottom plot.

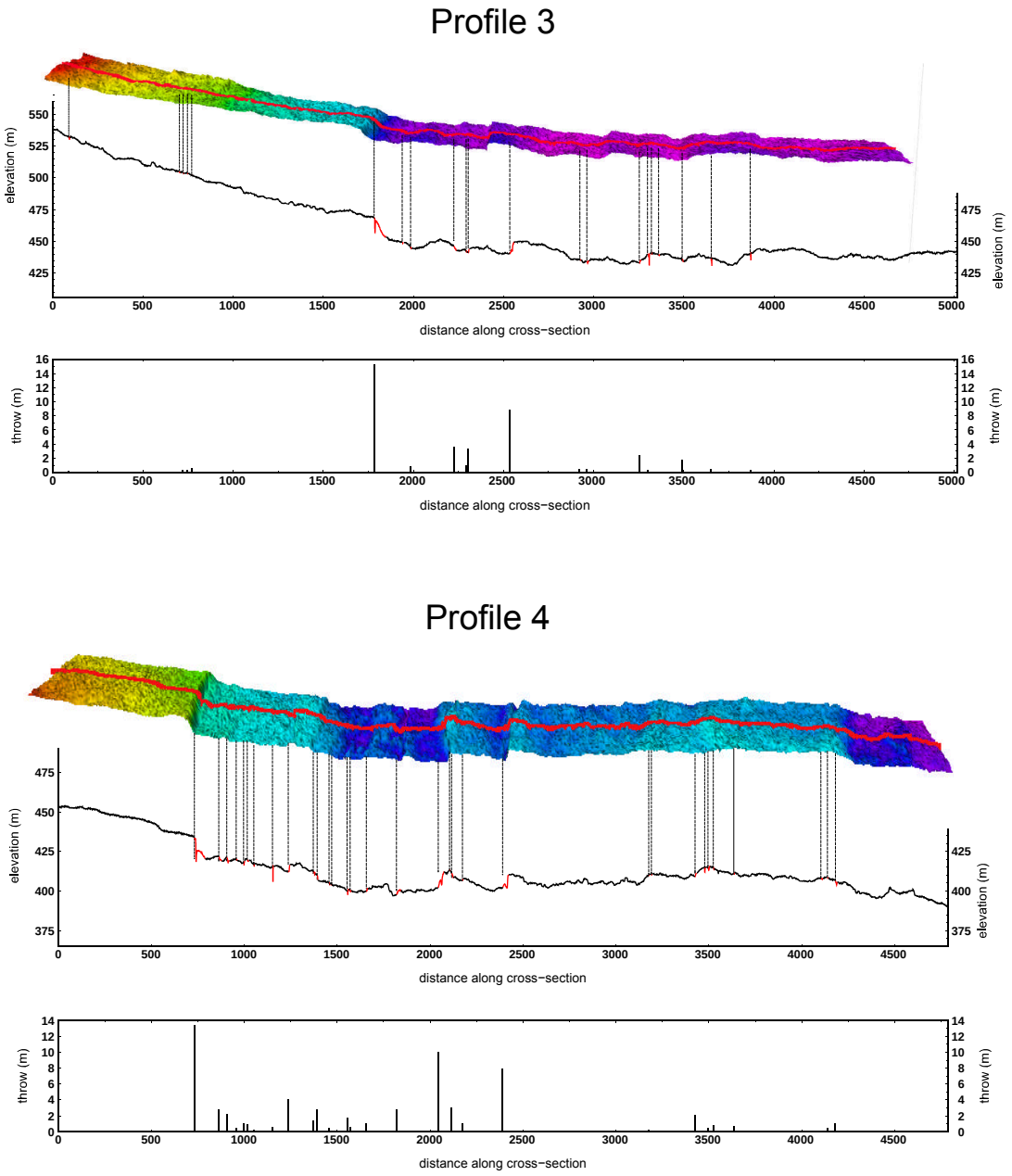

Figure 7.16: Cross-section 3 and 4 used to calculate throw and horizontal opening. Each profile consists of a DEM plot of the surface with the red line showing the profile, below this is a plot of the elevation across the profile, with the red sections showing the areas of vertical displacement by faulting - the throw was extracted for these sections and is plotted in the bottom plot.

Table 7.2

profile number	dip angle	total throw (m)	opening from throw (m)	number of fissures	opening from fissures (m)	total opening (m)
1	70	36.64	13.3	22	135.1	148.4
	45	36.64	36.64	22	135.1	171.74
2	70	57.87	21.06	14	68.3	89.36
	45	57.87	57.87	14	68.3	126.17
3	70	40.78	14.84	11	59.8	74.64
	45	40.78	40.78	11	59.8	100.58
4	70	64.34	23.41	14	84.2	107.61
	45	64.34	64.34	14	84.2	148.54

Chapter 8

Discussion and Conclusions

8.1 Discussion and conclusions

8.1.1 Fault Growth

Using a high resolution DEM I was able to identify and measure over 700 individual fractures and established a categorisation of faults into phases of growth based on the amount of fault that had zero vertical displacement. Using the fault categorisation I was able to identify a pattern of fault growth in the D_{max}/L relationship and propose a model of growth from fissure to fault. In addition I was able to identify that linked faults were mainly composed of fully displaced faults. I suggest that stress is more easily accommodated by slip of a single fault that is not fully displaced (category 1-4) than by breaching the relay zones between two faults and that breaching will only occur once stress has been fully accommodated by growth to fully formed fault on both sides of the relay.

8.1.2 Resolution

By using three different resolution surfaces I was able to establish that, for the structures in the Krafla fissure swarm, the distribution of the spread in the published D_{max}/L data could be explained by measuring fault structures at different resolutions. If the fault data are collected at a resolution that is sufficiently high to able to identify all the segmented structures within a fault system then the resulting D_{max}/L should lie at the top end of the published distribution. If the data resolution is not high enough to identify individual segments, then the structure measured actually has the length of all its segments and the maximum displacement of its largest segment. This results

in a fault appearing to have a low displacement for its length and the D_{max}/L would lie towards the bottom end of the distribution. I suggest that it could be possible to identify the structure of a measured fault based on the location of its D_{max}/L within the published distribution. A fault that lies at the high end of the distribution is likely to be a single fault and a fault at the low end of the distribution is likely to be a segmented fault system, with increasing segmentation going across the distribution. This is illustrated in figure 8.1 and could be used as a way to identify the structure of a fault measured at lower resolutions e.g. sub-surface seismic mapping and exploration. The D_{max}/L of the measured range of category 1-4 faults also fit within the published distribution and showed to have limit to the maximum length within the measured faults of ~500 m, with only fully-displaced faults achieving lengths greater than this. The category 1-4 faults range across the entire published distribution for the lengths involved. This implies that for Krafla the lower end of the distribution is a region of fissure to fault growth (shown by the red arrow in 8.1).

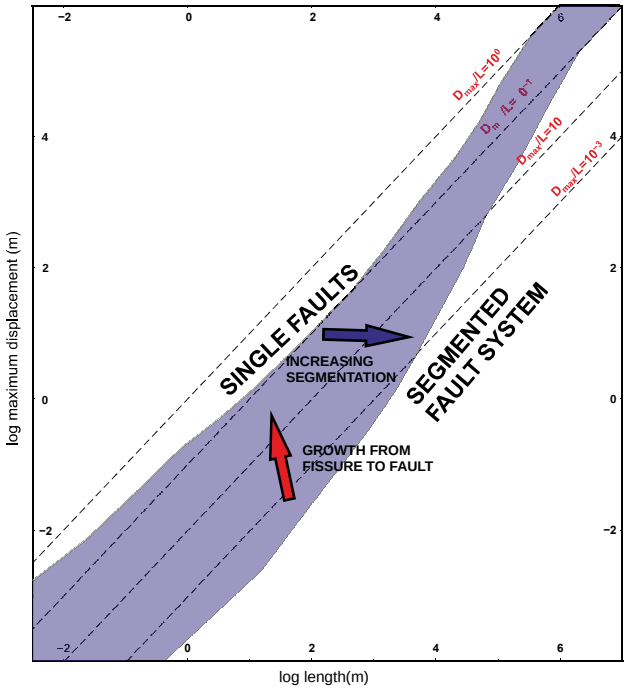

Figure 8.1: Schematic showing the trend of growth from fissure to fault in the published distribution for D_{max}/L (shown by red arrow) and also the location of single faults at the upper boundary of the distribution tending to multi-segmented fault systems at the lower boundary (shown by blue arrow).

8.1.3 16 years of surface displacement

Using InSAR I was able to build a time series over Krafla and Askja that consisted of 24 epochs over 16 years (1992-2008). From this I was able to identify trends in the time series that represented changes in the rates of displacement over both Krafla and Askja. With increased resolution in the time series I was able to establish that the Askja caldera, rather than undergoing a gradual decrease in inflation rate through time, had an increase in rate of inflation between 1996-2004 followed by a sharp decline in 2004. Additionally I identified 3 main periods of rate change in Krafla: 1) a period of post-rifting deflation at the caldera that decayed with time accompanied by a long-wavelength inflation focused north of the caldera between the Krafla and Fremrinamar fissure swarm, 2) a period of quiescence across the region, and finally 3) a resurgence of the long-wavelength surface inflation, this time focused in the Theistareykir volcanic centre. This implies that there are three possible sub-surface sources: 1) the shallow magma chamber underneath the Krafla caldera causing the relatively short wavelength surface displacement with most of the displacement confined to the caldera itself, with 2) and 3) representing deeper sources beneath the region between Krafla and Fremrinamar and underneath the Theistareykir volcanic centre.

Using whole profile time series, based on the trends established using the single point time series, I was able to able to identify the surface displacement behaviour along both the major and minor axes of both the Krafla and Askja volcanic systems.

Furthermore I identified that the deflation signature to the north of the Krafla caldera is most likely caused by either a cooling or settling (or a combination of both) of the 1984 lava flow. The possible combination of a large fault underneath the lava flow and the creation of a region of deeper lava that would give a longer-term signature of deflation has caused the presence of a deflation signature in the region north of the caldera for the entire 16 years.

8.2 Further Work

The Krafla rifting environment is driven by fissuring and slip through dyking and the large proportion of surface fractures with no displacement may not be representative of all faulted environments, particularly non-magmatically driven ones. In order to establish whether the observations in this work represent fault behaviour for the given

lithological and rehological conditions at Krafla alone, or if they can be more generically applied, it will be necessary to perform similar studies on other rifting environments, both oceanic and continental rifting. A similarly high resolution LiDAR DEM was acquired by NERC's ARSF aircraft over the Afar region. Measuring the length and displacement of faults and establishing the D_{max}/L relationship of the fissure swarm in Afar would give a good comparison to Krafla and would establish if the fissure to fault model is valid for other magmatically driven tectonic environments.

A better understanding of where in a fault system future failure is most likely to occur lies in understanding where the stress is most likely to be accommodated: surface opening, vertical displacement of a fissure, growth of a single fault or in linkage of two fully developed faults. Identification of locations of fissuring and slip within fault systems during previous rifting episodes could help identify the relationship between faults in a fault system and be applied to understanding the future mechanics of fissure swarms.

The Afar DEM provides the opportunity to examine the locations of surface opening and slip events during the Afar rifting episodes of 2005-2010 (e.g. Hamling et al., 2009, Ebinger et al., 2010). It can be used to identify what structures within a fault system failed and where new surface openings occurred in relation to already established fault systems. As the rifting events of both Afar and Krafla had noticeable similarities in the locations of the sequence of rifting events within the rifting episode, (see figure 8.2 and Einarsson (1991b), Buck et al. (2006), Hamling et al. (2009), Wright et al. (2012)) it should be possible to use a detailed examination of the location of fault failure in Afar and the observed stress release and consequent stress transfer observed by Hamling et al. (2009) to make inferences about possible locations for future failure in the fissure swarm in Krafla.

One of the issues with identifying smaller scale surface displacement trends using InSAR time series is that of noise in the final LOS displacement map. In using both the two separate time series (ERS and Envisat) for the 2004-2008 time period I was able compare the trends of both and make an educated decision about which time series contained incorrect displacement values due to noise. There are 3 additional satellite tracks for ERS and Envisat over the Krafla region and processing of these to provide independent time series would allow the comparison of 8 different time series. This would provide much tighter constraints on rate changes and possibly aid in identifying

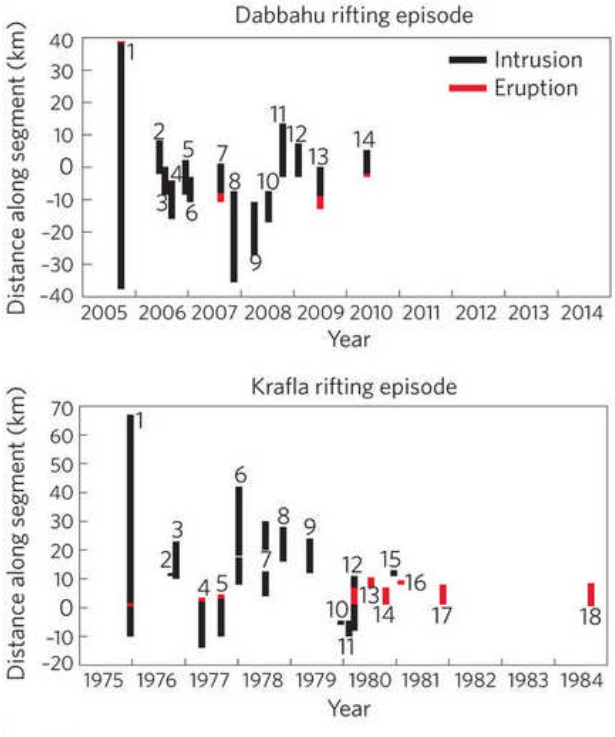

Figure 8.2: The distance of surface fissuring (black) and lava extrusion (red) from the central point of inflation in the caldera. Figure from Wright et al. (2012) (redrawn from Einarsson (1991b) Hamling et al. (2009)). Reprinted by permission from Macmillan Publishers Ltd: Nature Geoscience, Wright et al. (2012)

smaller scale displacement trends.

Identifying the total surface opening across the Krafla fissure swarm showed that only a portion of the total plate spreading rate is accommodated. The region of Krafla used for extracting throw and horizontal opening measurements is located in a region where there is much overlap between fissure swarms in the en echelon formation of the NVZ and a line perpendicular to the spreading centre would pass through the Theistareykir, Krafla, Fremrinamar and the far north of the Askja fissure swarms. Plate spreading would be accommodated across this entire region and the total opening should not necessarily represent the total plate spreading. A measure of the opening across the Theistareykir, Fremrinamar and Askja fissure swarms, along the same line perpendicular to the main spreading axis, would answer the question of whether plate spreading is fully accommodated by surface opening and slip during rifting events or if there is an additional inter-rifting surface displacement needed.

References

Ágústsson, S. (2001), Landhæðarbreytingar á Kröflusvæðinu, *Háskóli íslands, Reykjavik*. 6.1, 6.1.2, 6.8.1, 6.26

Aitkenhead, N., J. Chisholm, I. Stevenson, and B. G. Survey (1985), *Geology of the country around Buxton, Leek, and Bakewell*, Natural Environment Research Council. 4.19, 5.1

Allen, R., G. Nolet, W. Morgan, K. Vogfjord, B. Bergsson, P. Erlendsson, G. Foulger, S. Jakobsdóttir, B. Julian, M. Pritchard, et al. (2002), Imaging the mantle beneath Iceland using integrated seismological techniques, *J. geophys. Res*, *107*(10.1029). 2.1

Angelier, J., F. Bergerat, O. Dauteuil, and T. Villemin (1997), Effective tension-shear relationships in extensional fissure swarms, axial rift zone of northeastern Iceland, *Journal of Structural Geology*, *19*(5), 673–685. 4.1.2

Ármannsson, H., G. Gíslason, and H. Torfason (1986), Surface exploration of the Theistareykir high-temperature geothermal area, Iceland, with special reference to the application of geochemical methods, *Applied geochemistry*, *1*(1), 47–64. 6.8.1

Árnadóttir, T., F. Sigmundsson, and P. T. Delaney (1998), Sources of crustal deformation associated with the krafla, iceland, eruption of september 1984, *Geophysical research letters*, *25*(7), 1043–1046. 2.4.2

Árnadóttir, T., S. Jónsson, F. F. Pollitz, W. Jiang, and K. L. Feigl (2005), Postseismic deformation following the June 2000 earthquake sequence in the south Iceland seismic zone, *Journal of geophysical research*, *110*(B12), B12,308. 6.1.1

Árnadóttir, T., B. Lund, W. Jiang, H. Geirsson, H. Björnsson, P. Einarsson, and T. Sigurdsson (2009), Glacial rebound and plate spreading: results from the first countrywide GPS observations in Iceland, *Geophysical Journal International*, *177*(2), 691–716. 2.4, 7.1, 7.2, 7.2.1, 7.3

Bailey, W., J. Walsh, and T. Manzocchi (2005), Fault populations, strain distribution and basement fault reactivation in the East Pennines Coalfield, UK, *Journal of structural geology*, *27*(5), 913–928. 4.1.1, 4.1.1, 4.4, 4.19, 4.5, 5.1, 5.1

Bater, C. W., and N. C. Coops (2009), Evaluating error associated with lidar-derived DEM interpolation, *Computers & Geosciences*, *35*(2), 289–300. 3.3.2

Berardino, P., G. Fornaro, R. Lanari, and E. Sansosti (2002), A new algorithm for surface deformation monitoring based on small baseline differential SAR interferograms, *Geoscience and Remote Sensing, IEEE Transactions on*, *40*(11), 2375–2383. 6.7.5

Biggs, J., T. Wright, Z. Lu, and B. Parsons (2007), Multi-interferogram method for measuring interseismic deformation: Denali fault, Alaska, *Geophysical Journal International*, *170*(3), 1165–1179. 6.1.1, 6.6.8, 6.7, 6.7.3

Biggs, J., F. Amelung, N. Gourmelen, T. H. Dixon, and S.-W. Kim (2009), InSAR observations of 2007 Tanzania rifting episode reveal mixed fault and dyke extension in an immature continental rift, *Geophysical Journal International*, *179*(1), 549–558. 6.1.1, 6.2

Björnsson, A. (1985), Dynamics of crustal rifting in NE Iceland, *Journal of geophysical research*, *90*(B12), 10,151–10. 2.4.2, 4.1

Björnsson, A., and H. Eysteinsson (1998), *Breytingar á landhæð við Kröflu 1974-1995: samantekt á landhæðarmælingum: samvinnuverk Orkustofnunar, Norrænu eldfjallastöðvarinnar og landsvirkjunar*, Orkustofnun. 6.1, 6.1.2, 6.8.1, 6.26

Björnsson, A., and K. Saemundsson (1977), Current rifting episode in north Iceland, *Nature*, *266*, 318–323. 2.3, 2.3.2, 2.3.2, 4.1.2

Björnsson, A., G. Johnsen, S. Sigurdsson, G. Thorbergsson, and E. Tryggvason (1979), Rifting of the plate boundary in North Iceland 1975-1978, *Journal of Geophysical Research: Solid Earth*, *84*(B6), 3029–3038. 2.3.2, 4.1, 4.1.2

Boissonnat, J.-D., and F. Cazals (2000), Smooth surface reconstruction via natural neighbour interpolation of distance functions, in *Proceedings of the sixteenth annual symposium on Computational geometry*, pp. 223–232, ACM. 3.3.2

Brandsdottir, B., and P. Einarsson (1979), Seismic activity associated with the September 1977 deflation of the Krafla central volcano in northeastern Iceland, *Journal of Volcanology and Geothermal Research*, *6*(3-4), 197–212. 2.3.2, 2.3.2, 2.11, 2.4.2, 4.1.2, 6.1.1

Brandsdóttir, B., W. Menke, P. Einarsson, R. White, and R. Staples (1997), Færoe-Iceland ridge experiment 2. Crustal structure of the Krafla central volcano, *Journal of geophysical research*, *102*(B4), 7867–7886. 2.3, 4.1.2

Briggs, I. C. (1974), Machine contouring using minimum curvature, *Geophysics*, *39*(1), 39–48. 3.4, 3.3.1

Briole, P., D. Massonnet, and C. Delacourt (1997), Post-eruptive deformation associated with the 1986–87 and 1989 lava flows of etna detected by radar interferometry, *Geophysical Research Letters*, *24*(1), 37–40. 7.3

Buck, W., P. Einarsson, and B. Brandsdóttir (2006), Tectonic stress and magma chamber size as controls on dike propagation: constraints from the 1975–1984 Krafla rifting episode, *J. geophys. Res*, *111*, B12,404. 2.3.2, 4.1, 4.1.2, 8.2

Bürgmann, R., P. A. Rosen, and E. J. Fielding (2000), Synthetic aperture radar interferometry to measure Earth's surface topography and its deformation, *Annual Review of Earth and Planetary Sciences*, *28*(1), 169–209. 6.5, 6.2, 6.3.1, 6.6

Calais, E., A. Freed, G. Mattioli, F. Amelung, S. Jónsson, P. Jansma, S.-H. Hong, T. Dixon, C. Prépetit, and R. Momplaisir (2010), Transpressional rupture of an unmapped fault during the 2010 Haiti earthquake, *Nature Geoscience*, *3*(11), 794–799. 6.1.1

Cartwright, J., B. Trudgill, and C. Mansfield (1995), Fault growth by segment linkage: an explanation for scatter in maximum displacement and trace length data from the Canyonlands Grabens of SE Utah, *Journal of Structural Geology*, *17*(9), 1319–1326. 4.1, 4.19, 5.1, 5.1, 5.4

Catalão, J., G. Nico, R. Hanssen, and C. Catita (2011), Merging GPS and atmospherically corrected InSAR data to map 3-D terrain displacement velocity, *Geoscience and Remote Sensing, IEEE Transactions on*, *49*(6), 2354–2360. 7.1

Cowie, P., and C. Scholz (1992a), Displacement-length scaling relationship for faults: data synthesis and discussion, *Journal of Structural Geology*, *14*(10), 1149–1156. 4.1, 4.1.1

Cowie, P. A., and C. H. Scholz (1992b), Physical explanation for the displacement-length relationship of faults using a post-yield fracture mechanics model, *Journal of Structural Geology*, *14*(10), 1133–1148. 4.1.1

Davison, I. (1994), Linked fault systems; extensional, strike-slip and contractional, *Continental deformation*, *14*, 121–142. 4.19, 5.1

Dawers, N., and M. Anders (1995), Displacement-length scaling and fault linkage, *Journal of Structural Geology*, *17*(5), 607–614. 4.19, 5.1

Dawers, N., M. Anders, and C. Scholz (1993), Growth of normal faults: Displacement-length scaling, *Geology*, *21*(12), 1107–1110. 4.1.1, 4.19, 5.1, 5.4

de Zeeuw-van Dalfsen, E., R. Pedersen, F. Sigmundsson, and C. Pagli (2004), Satellite radar interferometry 1993–1999 suggests deep accumulation of magma near the crust-mantle boundary at the Krafla volcanic system, Iceland, *Geophysical research letters*, *31*(13), L13,611. (document), 6.1.2, 6.2, 6.9

de Zeeuw-van Dalfsen, E., H. Rymer, G. Williams-Jones, E. Sturkell, and F. Sigmundsson (2006), Integration of micro-gravity and geodetic data to constrain shallow system mass changes at Krafla Volcano, N Iceland, *Bulletin of volcanology*, *68*(5), 420–431. 6.1, 6.1.2, 6.8.1, 6.26

de Zeeuw-van Dalfsen, E., R. Pedersen, A. Hooper, and F. Sigmundsson (2012), Subsidence of Askja caldera 2000â..2009: Modelling of deformation processes at an extensional plate boundary, constrained by time series InSAR analysis , *Journal of Volcanology and Geothermal Research*, *213-214*(0), 72–82. 6.9

de Zeeuw-van Dalfsen, E., H. Rymer, E. Sturkell, R. Pedersen, A. Hooper, F. Sigmundsson, and B. Ófeigsson (2013), Geodetic data shed light on ongoing caldera subsidence at Askja, Iceland, *Bulletin of Volcanology*, *75*(5), 1–13. 6.1.3, 6.4, 6.8.2, 6.9

DeMets, C., R. G. Gordon, D. F. Argus, and S. Stein (1994), Effect of recent revisions to the geomagnetic reversal time scale on estimates of current plate motions, *Geophysical research letters*, *21*(20), 2191–2194. 2.1

Doubre, C., I. Manighetti, L. Dorbath, C. Dorbath, D. Bertil, and J. C. Delmond (2007), Crustal structure and magmato-tectonic processes in an active rift (Asal-Ghoubbet, Afar, East Africa): 2. Insights from the 23-year recording of seismicity since the last rifting event, *Journal of Geophysical Research: Solid Earth*, *112*(B5). 2.4.2

Ebinger, C., A. Ayele, D. Keir, J. Rowland, G. Yirgu, T. Wright, M. Belachew, and I. Hamling (2010), Length and timescales of rift faulting and magma intrusion: The Afar rifting cycle from 2005 to present, *Annual Review of Earth and Planetary Sciences*, *38*, 439–466. 2.14, 2.4, 8.2

Einarsson, P. (1991a), Earthquakes and present-day tectonism in Iceland, *Tectonophysics*, *189*(1-4), 261–279. 2.1, 2.3.2, 2.10, 2.4.2, 4.1.2

Einarsson, P. (1991b), The Krafla rifting episode 1975–1989, *Náttúra Myvatns,(The Nature of lake Myvatn)*, pp. 97–139. 8.2, 8.2

Einarsson, P. (2008), Plate boundaries, rifts and transforms in Iceland, *Jökull, The Icelandic Journal of Earth Sciences*, *58*, 35–58. 2.1, 2.2

Einarsson, P., and B. Brandsdottir (1978), Seismological evidence for lateral magma intrusion during the July 1978 deflation of the Krafla volcano in NE-Iceland, *Tech. rep.*, University of Iceland, Reykjavik, IS. 2.3, 2.3.2, 2.11, 4.1, 4.1.2

Elliott, J., J. Biggs, B. Parsons, and T. Wright (2008), InSAR slip rate determination on the Altyn Tagh Fault, northern Tibet, in the presence of topographically correlated atmospheric delays, *Geophysical Research Letters*, *35*(12), L12,309. 6.1.1, 6.7

Elliott, J., E. Nissen, P. England, J. A. Jackson, S. Lamb, Z. Li, M. Oehlers, and B. Parsons (2012), Slip in the 2010–2011 Canterbury earthquakes, New Zealand, *Journal of Geophysical Research: Solid Earth (1978–2012)*, *117*(B3). 6.1.1

England, P., and P. Molnar (1997), Active deformation of Asia: From kinematics to dynamics, *Science*, *278*(5338), 647–650. 7.2.1

England, P., and P. Molnar (2005), Late Quaternary to decadal velocity fields in Asia, *Journal of Geophysical Research: Solid Earth (1978–2012)*, *110*(B12). 7.2.1

Ferguson, D. J., T. D. Barnie, D. M. Pyle, C. Oppenheimer, G. Yirgu, E. Lewi, T. Kidane, S. Carn, and I. Hamling (2010), Recent rift-related volcanism in Afar, Ethiopia, *Earth and Planetary Science Letters*, *292*(3), 409–418. 2.4.2

Fialko, Y. (2004), Evidence of fluid-filled upper crust from observations of postseismic deformation due to the 1992 Mw7. 3 Landers earthquake, *Journal of Geophysical Research: Solid Earth (1978–2012)*, *109*(B8). 6.1.1

Fialko, Y. (2006), Interseismic strain accumulation and the earthquake potential on the southern San Andreas fault system, *Nature*, *441*(7096), 968–971. 6.1.1

Fossen, H. (2010), *Structural geology*, Cambridge University Press. 4.1, 4.1, 4.2

Fossen, H., and J. Hesthammer (1998), Deformation bands and their significance in porous sandstone reservoirs, *First Break*, *16*(1), 21–25. 4.19, 5.1

Foulger, G., R. Bilham, W. J. Morgan, and P. Einarsson (1987), The Iceland GPS Geodetic Field Campain 1986, *Eos, Transactions American Geophysical Union*, *68*(52), 1809–1818. 6.1.2

Foulger, G., C. Jahn, G. Seeber, P. Einarsson, B. Julian, and K. Heki (1992), Post-rifting stress relaxation at the divergent plate boundary in northeast Iceland, *Nature*, *358*(6386), 488–490. 6.1.2

Freeman, A., and S. S. Saatchi (2004), On the detection of Faraday rotation in linearly polarized L-band SAR backscatter signatures, *Geoscience and Remote Sensing, IEEE Transactions on*, *42*(8), 1607–1616. 6.3.3

Gabriel, A. K., and R. M. Goldstein (1988), Crossed orbit interferometry: theory and experimental results from SIR-B, *International Journal of Remote Sensing*, *9*(5), 857–872. 6.6.3

Garthwaite, M. C. (2011), *Deformation of Tibet: InSAR analysis and viscous flow models*, University of Leeds. 6.5, 6.7

Gillespie, P. (1991), Structural analysis of faults and folds with examples from the South Wales Coalfield and the Ruhr Coalfield, *Unpublished PhD thesis, University of Wales*. 4.19

Gillespie, P., J. Walsh, and J. Watterson (1992), Limitations of dimension and displacement data from single faults and the consequences for data analysis and interpretation, *Journal of Structural Geology*, *14*(10), 1157–1172. 4.1.1, 4.1.1, 4.19, 5.1, 5.1

Gillespie, P., C. Howard, J. Walsh, and J. Watterson (1993), Measurement and characterisation of spatial distributions of fractures, *Tectonophysics*, *226*(1-4), 113–141. 4.19, 5.1

Goldstein, R. M., and C. L. Werner (1998), Radar interferogram filtering for geophysical applications, *Geophysical Research Letters*, *25*(21), 4035–4038. 6.3.4, 6.6.7

Goldstein, R. M., H. A. Zebker, and C. L. Werner (1988), Satellite radar interferometry: Two-dimensional phase unwrapping, *Radio Science*, *23*(4), 713–720. 6.6.8

Goldstein, R. M., H. Engelhardt, B. Kamb, and R. M. Frolich (1993), Satellite radar interferometry for monitoring ice-sheet motion: Application to an Antarctic ice stream. 6.2

Goodwin, N. R., N. C. Coops, and D. S. Culvenor (2006), Assessment of forest structure with airborne lidar and the effects of platform altitude, *Remote Sensing of Environment*, *103*(2), 140–152. 3.3.2

Gourmelen, N., S. Kim, A. Shepherd, J. Park, A. Sundal, H. Björnsson, and F. Palsson (2011), Ice velocity determined using conventional and multiple-aperture InSAR, *Earth and Planetary Science Letters*, *307*(1), 156–160. 6.2

Grandin, R., A. Socquet, R. Binet, Y. Klinger, E. Jacques, J.-B. de Chabalier, G. King, C. Lasserre, S. Tait, P. Tapponnier, et al. (2009), September 2005 Manda Hararo-Dabbahu rifting event, Afar (Ethiopia): Constraints provided by geodetic data, *Journal of Geophysical Research: Solid Earth (1978–2012)*, *114*(B8). 2.4.2, 2.4.2, 6.1.1

Gudmundsson, A. (1984), Tectonic aspects of dykes in northwestern Iceland, *Jökull*, *34*, 81–96. 4.1.2

Gudmundsson, A. (1992), Formation and growth of normal faults at the divergent plate boundary in Iceland, *Terra nova*, *4*(4), 464–471. 4.1.1

Gudmundsson, A. (1995), Infrastructure and mechanics of volcanic systems in Iceland, *Journal of Volcanology and Geothermal Research*, *64*(1), 1–22. 2.4.2

Gudmundsson, A. (2000), Dynamics of volcanic systems in Iceland: example of tectonism and volcanism at juxtaposed hot spot and mid-ocean ridge systems, *Annual Review of Earth and Planetary Sciences*, *28*(1), 107–140. 2.4.2

Haecker, M. (1992), Convergent gridding: a new approach to surface reconstruction, *Geobyte*, *7*(3), 48–53. 3.3.1

Hamling, I. J., A. Ayele, L. Bennati, E. Calais, C. J. Ebinger, D. Keir, E. Lewi, T. J. Wright, and G. Yirgu (2009), Geodetic observations of the ongoing Dabbahu rifting episode: new dyke intrusions in 2006 and 2007, *Geophysical Journal International*, *178*(2), 989–1003. 2.3.2, 8.2, 8.2

Hamling, I. J., T. J. Wright, E. Calais, L. Bennati, and E. Lewi (2010), Stress transfer between thirteen successive dyke intrusions in Ethiopia, *Nature Geoscience*, *3*(10), 713–717. 2.3.2, 6.1.1, 6.2

Hanssen, R. F. (2001), *Radar interferometry: data interpretation and error analysis*, vol. 2, Springer. 6.3.2

Heki, K., G. Foulger, B. Julian, and C.-H. Jahn (1993), Plate dynamics near divergent boundaries: Geophysical implications of postrifting crustal deformation in NE Iceland, *Journal of Geophysical Research: Solid Earth (1978–2012)*, *98*(B8), 14,279–14,297. 6.1.2

Henriot, O., and T. Villemin (2005), Deformation at the northern end of the Icelandic rift mapped by InSAR (1992-2000), a decade after the Krafla Rifting Episode, *Geodinamica Acta*, *18*(1), 43–57. 6.1.2

Henriot, O., T. Villemin, and F. Jouanne (2001), Long period interferograms reveal 1992–1998 steady rate of deformation at Krafla Volcano (North Iceland)., *Geophysical research letters*, *28*(6), 1067–1070. 6.1, 6.1.2, 6.1.2, 6.8.1, 6.26

Hjartardóttir, Á. (2008), The fissure swarm of the Askja central volcano, *MSc Thesis, University of Iceland*. 2.2

Hjartardóttir, Á., P. Einarsson, E. Bramham, and T. Wright (2012), The Krafla fissure swarm, Iceland, and its formation by rifting events, *Bulletin of Volcanology*, *74*(9), 2139–2153. 2.5, 2.1, 4.1.2

Hofton, M., and G. Foulger (1996), Postrifting anelastic deformation around the spreading plate boundary, north Iceland 1. Modeling of the 1987–1992 deformation field using a viscoelastic Earth structure, *Journal of geophysical research*, *101*(B11), 25,403–25. 6.1.2

Hollingsworth, J., S. Leprince, F. Ayoub, and J.-P. Avouac (2012), Deformation during the 1975–1984 krafla rifting crisis, ne iceland, measured from historical optical imagery, *Journal of Geophysical Research: Solid Earth (1978–2012)*, *117*(B11). 2.3.2

Hooper, A., R. Pedersen, and F. Sigmundsson (2009), Constraints on magma intrusion at Eyjafjallajökull and Katla volcanoes in Iceland, from time series SAR interferometry, *The VOLUME Project–Volcanoes: Understanding Subsurface Mass Movement. Dublin: University College*, pp. 13–24. 6.1.1

Höskuldsson, A., C. Dyhr, and T. Dolvik (2010), Grænavatnsbruni og Laxárhraun yngra, in *Autumn conference of the Iceland Geoscience Society. Reykjavík*, pp. 41–42. 2.3, 2.1

Jackson, J., R. Norris, and J. Youngson (1996), The structural evolution of active fault and fold systems in central Otago, New Zealand: evidence revealed by drainage patterns, *Journal of Structural Geology*, *18*(2), 217–234. 4.19, 5.1

Jahn, C. (1990), A highly precise GPS-epoch measurement in the northeast volcanic zone of Iceland, *Cahiers du Centre Européen de Géodynamique et de Séismologie P. Paquet, J. Flick, B. Ducarme*, pp. 292–304. 6.1.2

Jóhannesson, H., and K. Sæmundsson (1998), Geological map of Iceland. 1: 500 000, *Tectonics. Icelandic Institute of Natural History, Reykjavik*. 2.2

Jónsson, S. (2008), Importance of post-seismic viscous relaxation in southern Iceland, *Nature Geoscience*, *1*(2), 136–139. 6.1.1

Jouanne, F., T. Villemin, A. Berger, and O. Henriot (2006), Rift-transform junction in North Iceland: rigid blocks and narrow accommodation zones revealed by GPS 1997–1999–2002, *Geophysical Journal International*, *167*(3), 1439–1446. 7.1, 7.3

Kim, Y.-S., and D. J. Sanderson (2005), The relationship between displacement and length of faults: a review, *Earth-Science Reviews*, *68*(3), 317–334. 4.1, 5.2

Kim, Y.-S., J. R. Andrews, and D. J. Sanderson (2000), Damage zones around strike-slip fault systems and strike-slip fault evolution, Crackington Haven, southwest England, *Geosciences Journal*, *4*(2), 53–72. 4.1

Krantz, R. W. (1988), Multiple fault sets and three-dimensional strain: theory and application, *Journal of Structural Geology*, *10*(3), 225–237. 5.1

Kruskal, J. B. (1956), On the shortest spanning subtree of a graph and the traveling salesman problem, *Proceedings of the American Mathematical society*, *7*(1), 48–50. 6.7.1

Le Breton, E., O. Dauteuil, and G. Biessy (2010), Post-glacial rebound of Iceland during the Holocene, *Journal of the Geological Society*, *167*(2), 417–432. 2.2

Li, Z., X.-L. Ding, and G. Liu (2004), Modeling atmospheric effects on InSAR with meteorological and continuous GPS observations: algorithms and some test results, *Journal of Atmospheric and Solar-Terrestrial Physics*, *66*(11), 907–917. 6.3.3

Maclennan, J., D. McKenzie, and K. Gronvöld (2001), Plume-driven upwelling under central iceland, *Earth and Planetary Science Letters*, *194*(1), 67–82. 2.1

Marrett, R., and R. Allmendinger (1991), Estimates of strain due to brittle faulting: sampling of fault populations, *Journal of Structural Geology*, *13*(6), 735–738. 4.1.1, 4.19

Massonnet, D., and K. L. Feigl (1998), Radar interferometry and its application to changes in the Earth's surface, *Reviews of geophysics*, *36*(4), 441–500. 6.6

Massonnet, D., M. Rossi, C. Carmona, F. Adragna, G. Peltzer, K. Feigl, and T. Rabaute (1993), The displacement field of the Landers earthquake mapped by radar interferometry, *Nature*, *364*(6433), 138–142. 6.2

Massonnet, D., P. Briole, and A. Arnaud (1995), Deflation of Mount Etna monitored by spaceborne radar interferometry, *Nature*, *375*(6532), 567–570. 6.2

Metzger, S., S. Jónsson, and H. Geirsson (2011), Locking depth and slip-rate of the Húsavík Flatey fault, North Iceland, derived from continuous GPS data 2006–2010, *Geophysical Journal International*, *187*(2), 564–576. 6.9

Meyer, F., R. Bamler, N. Jakowski, and T. Fritz (2006), The potential of low-frequency SAR systems for mapping ionospheric TEC distributions, *Geoscience and Remote Sensing Letters, IEEE*, *3*(4), 560–564. 6.3.3

Meyer, F. J., and B. Watkins (2011), A statistical model of ionospheric signals in low-frequency SAR data, in *Geoscience and Remote Sensing Symposium (IGARSS), 2011 IEEE International*, pp. 1493–1496, IEEE. 6.3.3

Morgan, W. J. (1971), Convection plumes in the lower mantle. 2.1

Muraoka, H., and H. Kamata (1983), Displacement distribution along minor fault traces, *Journal of Structural Geology*, *5*(5), 483–495. 5.1

Nicol, A., J. Watterson, J. Walsh, and C. Childs (1996), The shapes, major axis orientations and displacement patterns of fault surfaces, *Journal of Structural Geology*, *18*(2), 235–248. 4.19, 5.1

Nooner, S. L., L. Bennati, E. Calais, W. R. Buck, I. J. Hamling, T. J. Wright, and E. Lewi (2009), Post-rifting relaxation in the Afar region, Ethiopia, *Geophysical Research Letters*, *36*(21), L21,308. 6.1.1

Ofeigsson, B. G., A. Hooper, F. Sigmundsson, E. Sturkell, and R. Grapenthin (2011), Deep magma storage at Hekla volcano, Iceland, revealed by InSAR time series analysis, *Journal of Geophysical Research: Solid Earth (1978–2012)*, *116*(B5). 6.1.1

Opheim, J., and A. Gudmundsson (1989), Formation and geometry of fractures, and related volcanism, of the Krafla fissure swarm, northeast Iceland, *Geological Society of America Bulletin*, *101*(12), 1608–1622. 2.1, 4.1.2, 4.3, 4.4, 4.19, 4.5, 5.1, 7.6

Pagli, C., F. Sigmundsson, T. Arnadóttir, P. Einarsson, and E. Sturkell (2006), Deflation of the Askja volcanic system: constraints on the deformation source from combined inversion of satellite radar interferograms and GPS measurements, *Journal of volcanology and geothermal research*, *152*(1), 97–108. (document), 6.3, 6.1.3

Pagli, C., T. Wright, C. Ebinger, T. Barnie, and A. Ayele (2009), Inflate, Pause, Erupt, Recharge: the 2008 Alu eruption in the ErtaAle volcanic system (Ethiopia), in *AGU Fall Meeting Abstracts*, vol. 1, p. 1813. 2.14

Pagli, C., T. J. Wright, C. J. Ebinger, S.-H. Yun, J. R. Cann, T. Barnie, and A. Ayele (2012), Shallow axial magma chamber at the slow-spreading Erta Ale Ridge, *Nature Geoscience*, *5*(4), 284–288. 6.2

Pálmason, G. (1973), Kinematics and heat flow in a volcanic rift zone, with application to Iceland, *Geophysical Journal of the Royal Astronomical Society*, *33*(4), 451–481. 2.2

Parsons, B., T. Wright, P. Rowe, J. Andrews, J. Jackson, R. Walker, M. Khatib, M. Talebian, E. Bergman, and E. Engdahl (2006), The 1994 Sefidabeh (eastern Iran) earthquakes revisited: new evidence from satellite radar interferometry and carbonate dating about the growth of an active fold above a blind thrust fault, *Geophysical Journal International*, *164* (1), 202–217. 6.7.5

Peacock, D. (1991), Displacements and segment linkage in strike-slip fault zones, *Journal of Structural Geology*, *13* (9), 1025–1035. 4.1, 4.19, 5.1

Peacock, D., and D. Sanderson (1991), Displacements, segment linkage and relay ramps in normal fault zones, *Journal of Structural Geology*, *13* (6), 721–733. 4.1

Pedersen, R., F. Sigmundsson, and T. Masterlark (2009), Rheologic controls on interrifting deformation of the Northern Volcanic Zone, Iceland, *Earth and Planetary Science Letters*, *281* (1), 14–26. 2.4, 2.4, 7.3

Peltzer, G., and P. Rosen (1995), Surface displacement of the 17 May 1993 Eureka Valley, California, earthquake observed by SAR interferometry, *Science*, *268* (5215), 1333–1336. 6.2

Peyret, M., S. Dominguez, R. Cattin, J. Champenois, M. Leroy, and A. Zajac (2011), Present-day interseismic surface deformation along the Longitudinal Valley, eastern Taiwan, from a PS-InSAR analysis of the ERS satellite archives, *Journal of Geophysical Research: Solid Earth (1978–2012)*, *116* (B3). 6.5

Pollitz, F. F., and I. S. Sacks (1996), Viscosity structure beneath northeast Iceland, *Journal of geophysical research*, *101* (B8), 17,771–17. 6.1.2

Rodriguez, E., and J. Martin (1992), Theory and design of interferometric synthetic aperture radars, in *Radar and Signal Processing, IEE Proceedings F*, vol. 139, pp. 147–159, IET. 6.3.4

Rosen, P., S. Hensley, H. Zebker, F. Webb, and E. Fielding (1996), Surface deformation and coherence measurements of Kilauea Volcano, Hawaii, from SIR-C radar interferometry, *Journal of Geophysical Research: Planets (1991–2012)*, *101* (E10), 23,109–23,125. 6.2

Rosen, P. A., S. Hensley, I. R. Joughin, F. K. Li, S. N. Madsen, E. Rodriguez, and R. M. Goldstein (2000), Synthetic aperture radar interferometry, *Proceedings of the IEEE*, *88* (3), 333–382. 6.3.3, 6.5.3, 6.6

Rosen, P. A., S. Hensley, G. Peltzer, and M. Simons (2004), Updated repeat orbit interferometry package released, *Eos, Transactions American Geophysical Union*, *85* (5), 47–47. 6.6

Rowan, M. (1997), Three-dimensional geometry and evolution of a segmented detachment fold, Mississippi Fan foldbelt, Gulf of Mexico, *Journal of Structural Geology*, *19* (3), 463–480. 4.19, 5.1

Ryder, I., B. Parsons, T. J. Wright, and G. J. Funning (2007), Post-seismic motion following the 1997 Manyi (Tibet) earthquake: InSAR observations and modelling, *Geophysical Journal International*, *169* (3), 1009–1027. 6.1.1

Saemundsson, K. (1978), Fissure swarms and central volcanoes of the neovolcanic zones of Iceland, in *Crustal evolution in northwestern Britain and adjacent regions*, pp. 415–432, Seel House Press, Liverpool. 2.1

Saemundsson, K. (1979), *Outline of the geology of Iceland*. 2.1, 2.2

Saemundsson, K. (1991), Geology of the Krafla system, *Nattura Myvatns, Hid Islenska Natturufraedifelag, Reykjavik*, pp. 25–95. 2.3, 2.1, 2.3, 2.3.1, 2.9, 2.12, 4.1.2

Saunders, A., J. Fitton, A. Kerr, M. Norry, and R. Kent (1997), The north Atlantic igneous province, *Large igneous provinces: Continental, oceanic, and planetary flood volcanism*, pp. 45–93. 2.1

Scharroo, R., and P. Visser (1998), Precise orbit determination and gravity field improvement for the ERS satellites, *Journal of Geophysical Research: Oceans (1978–2012)*, *103*(C4), 8113–8127. 6.3.1, 6.7.3

Schlische, R., S. Young, R. Ackermann, and A. Gupta (1996), Geometry and scaling relations of a population of very small rift-related normal faults, *Geology*, *24*(8), 683. 4.19, 5.1

Schmidt, D. A., and R. Bürgmann (2003), Time-dependent land uplift and subsidence in the Santa Clara valley, California, from a large interferometric synthetic aperture radar data set, *Journal of Geophysical Research*, *108*(B9), 2416. 6.7.5

Scholz, C., and P. A. Cowie (1990), Determination of total strain from faulting using slip measurements, *Nature*, *346*(6287), 837–839. 5.1

Shen, Y., S. C. Solomon, I. T. Bjarnason, and G. Purdy (1996), Hot mantle transition zone beneath iceland and the adjacent mid-atlantic ridge inferred from p-to-s conversions at the 410-and 660-km discontinuities, *Geophysical research letters*, *23*(24), 3527–3530. 2.1

Shen, Y., S. C. Solomon, I. T. Bjarnason, and C. J. Wolfe (1998), Seismic evidence for a lower-mantle origin of the iceland plume, *Nature*, *395*(6697), 62–65. 2.1

Shipton, Z., and P. Cowie (2001), Damage zone and slip-surface evolution over μm to km scales in high-porosity Navajo sandstone, Utah, *Journal of Structural Geology*, *23*(12), 1825–1844. 4.1, 4.4

Sibson, R. (1981), A brief description of natural neighbour interpolation, *Interpreting multivariate data*, pp. 21–36. 3.3.2

Sigmundsson, F. (2006a), *Iceland geodynamics - crustal deformation and divergent plate tectonics*, Springer Verlag. 2.4.1, 2.4.2, 2.4.3, 6.1.1

Sigmundsson, F. (2006b), Plate tectonics: Magma does the splits, *Nature*, *442*(7100), 251–252. 2.4.2, 2.16

Sigmundsson, F., H. Vadon, and D. Massonnet (1997), Readjustment of the Krafla spreading segment to crustal rifting measured by satellite radar interferometry, *Geophysical Research Letters*, *24*(15), 1843–1846. 6.1, 6.1.2, 6.1.2, 6.8.1, 6.26

Sigurdsson, H., and R. Sparks (1978), Rifting episode in north Iceland in 1874–1875 and the eruptions of Askja and Sveinagja, *Bulletin Volcanologique*, *41*(3), 149–167. 2.4.3, 6.1.3

Sigvaldason, G. (1979), Rifting, magmatic activity and interaction between acid and basic liquids. The 1875 Askja Eruption in Iceland. Rep. 7903, *Nord. Volcanol. Inst., Univ. of Iceland, Reykjavik, Iceland*. 6.1.3

Stevens, N., G. Wadge, C. Williams, J. Morley, J.-P. Muller, J. Murray, and M. Upton (2001), Surface movements of emplaced lava flows measured by synthetic aperture radar interferometry, *Journal of geophysical research*, *106*(B6), 11,293–11. 7.3

Sturkell, E., and F. Sigmundsson (2000), Continuous deflation of the Askja caldera, Iceland, during the 1983–1998 noneruptive period, *Journal of Geophysical Research: Solid Earth (1978–2012)*, *105*(B11), 25,671–25,684. 6.1.3, 6.1.3

Sturkell, E., F. Sigmundsson, and R. Slunga (2006), 1983–2003 decaying rate of deflation at Askja caldera: Pressure decrease in an extensive magma plumbing system at a spreading plate boundary, *Bulletin of volcanology*, *68*(7-8), 727–735. (document), 6.1.3, 6.4

Sturkell, E., F. Sigmundsson, H. Geirsson, H. Ólafsson, and T. Theodórsson (2008), Multiple volcano deformation sources in a post-rifting period: 1989–2005 behaviour of Krafla, Iceland constrained by levelling, tilt and GPS observations, *Journal of Volcanology and Geothermal Research*, *177*(2), 405–417. 6.1, 6.1.2, 6.8.1, 6.8.1, 6.26, 6.8.1

Sunda, M., R. Crapolicchio, and P. Lecomte (2002), Impact of satellite degraded attitude on ERS-2 scatterometer data, in *Proceedings of SPIE: Remote Sensing of the Ocean and Sea Ice 2002*. 6.5.4

Thorarinsson, S. (1952), Hverfjall I, *Náttúrufrædingurinn*, *22*, 113–129. 2.3

Thorarinsson, S. (1979), The postglacial history of the Mỳvatn area, *Oikos*, pp. 17–28. 2.3, 2.1

Thorarinsson, S., and G. E. Sigvaldason (1962), The eruption in Askja, 1961; a preliminary report, *American Journal of Science*, *260*(9), 641–651. 6.1.3

Thordarson, T., and G. Larsen (2007), Volcanism in Iceland in historical time: Volcano types, eruption styles and eruptive history, *Journal of Geodynamics*, *43*(1), 118–152. 2.1, 2.12, 2.15

Toombs, A., and G. Wadge (2012), Co-eruptive and inter-eruptive surface deformation measured by satellite radar interferometry at Nyamuragira volcano, DR Congo, 1996 to 2010, *Journal of Volcanology and Geothermal Research*. 7.3

Tryggvason, E. (1980), Subsidence events in the Krafla area, North Iceland, 1975–1979, *J. Geophys*, *47*(1-3), 141–153. 2.3, 2.3.2, 4.1, 4.1.2

Tryggvason, E. (1984), Widening of the Krafla fissure swarm during the 1975–1981 volcano-tectonic episode, *Bulletin of Volcanology*, *47*(1), 47–69. 2.3.2, 2.3.2, 2.10, 4.1, 4.1.2

Tryggvason, E. (1986), Multiple magma reservoirs in a rift zone volcano: ground deformation and magma transport during the September 1984 eruption of Krafla, Iceland, *Journal of volcanology and geothermal research*, *28*(1-2), 1–44. 2.3.2, 2.4.2, 7.3

Tryggvason, E. (1989), Ground deformation in Askja, Iceland: its source and possible relation to flow of the mantle plume, *Journal of volcanology and geothermal research*, *39*(1), 61–71. 6.1.3

Tryggvason, E. (1994), Surface deformation at the Krafla volcano, North Iceland, 1982–1992, *Bulletin of volcanology*, *56*(2), 98–107. 2.3.2, 6.1, 6.1.2, 6.8.1, 6.26

Tryggvason, K., E. Husebye, and R. Stefánsson (1983), Seismic image of the hypothesized Icelandic hot spot, *Tectonophysics*, *100*(1-3), 97–118. 2.1

Villemin, T., and C. SUNWOO (1987), Distribution logarithmique self-similaire des rejets et longueurs de failles: exemple du Bassin Houiller Lorrain, *Comptes rendus de l'Académie des sciences. Série 2, Mécanique, Physique, Chimie, Sciences de l'univers, Sciences de la Terre*, *305*(16), 1309–1312. 4.19

Villemin, T., J. Angelier, and C. Sunwoo (1995), Fractal distribution of fault length and offsets: Implications of brittle deformation evaluation.Lorraine Coal Basin, *Fractals in the Earth Sciences, Plenum Press, New York*, pp. 205–226. 5.1

Walsh, J., and J. Watterson (1987), Distributions of cumulative displacement and seismic slip on a single normal fault surface, *Journal of Structural Geology*, *9*(8), 1039–1046. 4.1, 5.1

Walsh, J., and J. Watterson (1988), Analysis of the relationship between displacements and dimensions of faults, *Journal of Structural Geology*, *10*(3), 239–247. 4.1.1, 4.19, 5.1

Walsh, J., A. Nicol, and C. Childs (2002), An alternative model for the growth of faults, *Journal of Structural Geology*, *24*(11), 1669–1675. 4.1, 5.1

Walsh, J., W. Bailey, C. Childs, A. Nicol, and C. Bonson (2003), Formation of segmented normal faults: a 3-D perspective, *Journal of Structural Geology*, *25*(8), 1251–1262. 4.3

Walters, R., J. Elliott, N. D'Agostino, P. England, I. Hunstad, J. Jackson, B. Parsons, R. Phillips, and G. Roberts (2009), The 2009 L'Aquila earthquake (central Italy): A source mechanism and implications for seismic hazard, *Geophysical Research Letters*, *36*(17). 6.1.1

Wang, H., and T. Wright (2012), Satellite geodetic imaging reveals internal deformation of western Tibet, *Geophysical Research Letters*, *39*(7). 6.7.5, 7.2.1

Wang, H., T. Wright, and J. Biggs (2009), Interseismic slip rate of the northwestern Xianshuihe fault from InSAR data, *Geophysical Research Letters*, *36*(3), L03,302. 6.1.1, 6.7

Wang, H., T. J. Wright, Y. Yu, H. Lin, L. Jiang, C. Li, and G. Qiu (2012), Insar reveals coastal subsidence in the pearl river delta, china, *Geophysical Journal International*, *191*(3), 1119–1128. 6.7

Watterson, J. (1986), Fault dimensions, displacements and growth, *Pure and Applied Geophysics*, *124*(1), 365–373. 4.1.1, 4.1.1

Wilkins, S. J., and M. R. Gross (2002), Normal fault growth in layered rocks at Split Mountain, Utah: influence of mechanical stratigraphy on dip linkage, fault restriction and fault scaling, *Journal of Structural Geology*, *24*(9), 1413–1429. 5.1

Wolfe, C., I. Bjarnason, J. VanDecar, and S. Solomon (1997), Seismic structure of the Iceland mantle plume, *Nature*, *385*(6613), 245–247. 2.1

Wright, T., F. Sigmundsson, C. Pagli, M. Belachew, I. Hamling, B. Brandsdóttir, D. Keir, R. Pedersen, A. Ayele, C. Ebinger, et al. (2012), Geophysical constraints on the dynamics of spreading centres from rifting episodes on land, *Nature Geoscience*, *5*(4), 242–250. 2.3, 2.10, 2.11, 4.1.2, 6.1.1, 8.2, 8.2

Wright, T. J., B. Parsons, P. C. England, and E. J. Fielding (2004), InSAR observations of low slip rates on the major faults of western Tibet, *Science*, *305*(5681), 236–239. 6.1.1

Wright, T. J., C. Ebinger, J. Biggs, A. Ayele, G. Yirgu, D. Keir, and A. Stork (2006), Magma-maintained rift segmentation at continental rupture in the 2005 Afar dyking episode, *Nature*, *442*(7100), 291–294. 2.14, 2.4.2, 2.4.2, 2.16, 6.1.1, 6.2

Wright, T. J., J. R. Elliott, H. Wang, and I. Ryder (2013), Earthquake cycle deformation and the Moho: Implications for the rheology of continental lithosphere, *Tectonophysics*, *609*, 504–523. 6.1.1

Zebker, H., and R. Goldstein (1986), Topographic mapping from interferometric synthetic radar observations, *J. Geophys. Res.*, *91*(B5), 4993–4999. 6.2, 6.6

Zebker, H. A., S. N. Madsen, J. Martin, K. B. Wheeler, T. Miller, Y. Lou, G. Alberti, S. Vetrella, and A. Cucci (1992), The TOPSAR interferometric radar topographic mapping instrument, *Geoscience and Remote Sensing, IEEE Transactions on*, *30*(5), 933–940. 6.2

Zebker, H. A., P. A. Rosen, R. M. Goldstein, A. Gabriel, and C. L. Werner (1994), On the derivation of coseismic displacement fields using differential radar interferometry: The Landers earthquake, *Journal of Geophysical Research: Solid Earth (1978–2012)*, *99*(B10), 19,617–19,634. 6.2, 6.3.1

Appendix A

Fault $D_{max}L$ measurements for Krafla, 0.5 m resolution

Table A.1: Table shows the category 1 fault length and corresponding fault maximum displacement data for faults picked using 0.5 m resolution DEM. Values are the log of measurements made in metres.

Category	Log length	Log Displ.	Category	Log length	Log Displ.
1	1.84	0.19	1	1.93	-0.31
1	1.811	0.025	1	2.131	-0.398
1	1.67	-0.337	1	2.083	0.041
1	2.373	0.149	1	2.786	0.433
1	1.817	0.079	1	2.146	-0.229
1	1.872	0.14	1	1.62	-0.036
1	1.953	-0.161	1	2.143	-0.097
1	2.131	-0.301	1	2.214	-0.097
1	2.122	-0.167	1	1.922	0.025
1	1.85	-0.292	1	1.976	-0.276
1	1.399	0.083	1	2.093	0
1	2.389	0.201	1	2.052	0.25
1	1.656	-0.06	1	1.932	-0.284
1	1.661	-0.155	1	2.92	0.307
1	1.94	-0.137	1	2.43	0.072
1	2.077	-0.469	1	2.066	0.093
1	2.308	0.1	1	1.82	-0.013
1	2.438	0.143	1	1.925	0.061
1	1.323	0.009	1	2.141	0.045
1	1.879	0.13	1	2.062	-0.276

Continued on next page

Table A.1 – *Continued from previous page*

Category	Log length	Log Displ.	Category	Log length	Log Displ.
1	2.266	0.107	1	2.2	-0.143
1	1.798	-0.125	1	2.507	-0.284
1	2.014	-0.004	1	2.258	-0.056
1	1.697	-0.31	1	2.299	0.013
1	1.847	-0.854	1	1.932	-0.387
1	1.325	-0.167	1	2.248	0.294
1	2.224	-0.337	1	2.304	0.111
1	2.389	-0.051	1	2.363	0.093
1	2.316	-0.06	1	1.752	-0.143
1	2.147	-0.174	1	1.576	-0.125
1	2.375	-0.174	1	2.111	0.083
1	1.872	-0.194	1	2.146	0.164
1	1.984	-0.081	1	2.073	-0.538
1	1.958	-0.114	1	1.511	-0.276
1	1.753	-0.292	1	1.897	0.312
1	2.078	-0.31	1	1.586	0.083
1	1.944	-0.538	1	1.491	-0.125
1	1.972	-0.538	1	1.517	-1.523
1	1.922	-0.208	1	1.865	-0.155
1	1.853	0.061	1	2.462	-0.125
1	1.368	-0.301	1	1.659	-0.032
1	1.894	-0.367	1	1.577	-0.357
1	1.48	-0.194	1	1.592	-0.444
1	1.504	-0.824	1	1.39	-0.229
1	1.628	0.053	1	1.878	-0.027
1	1.626	0.004	1	2.099	0.117
1	1.765	-0.432	1	2.09	-0.076
1	1.728	-0.009	1	1.535	0.143
1	1.742	0.004	1	2.304	0.017
1	1.914	-0.602	1	1.782	0
1	1.429	-0.357	1	1.502	-0.081
1	1.831	-0.444	1	2.303	-0.18
1	2.144	0	1	2.197	-0.337
1	1.811	0.09	1	1.837	-0.222
1	1.481	-0.444	1	1.887	-0.959
1	1.545	-0.481	1	1.693	-0.022
1	1.923	-0.222	1	1.627	-0.921

Continued on next page

Table A.1 – *Continued from previous page*

Category	Log length	Log Displ.	Category	Log length	Log Displ.
1	1.636	-0.149	1	1.592	-0.252
1	1.678	-0.284	1	1.706	-0.301
1	2.12	-0.174	1	1.976	-0.301
1	2.164	-0.125	1	2.033	-0.06
1	1.673	0.029	1	2.059	-0.143
1	1.594	0.158	1	2.109	-0.658
1	1.615	-0.276	1	1.984	0
1	2.216	-0.268	1	1.562	-0.678
1	1.783	-0.398	1	1.902	-0.06
1	1.439	-0.602	1	2.117	0.053
1	1.804	0.061	1	2.046	0.167
1	1.831	-0.027	1	1.99	-0.319
1	1.611	-0.119	1	1.499	0.025
1	1.72	-0.456	1	1.844	-0.658
1	2.339	-0.06	1	2.098	-0.131
1	1.652	-0.215	1	1.733	-0.26
1	1.821	0.076	1	2.499	0.009
1	1.798	-0.222	1	2.128	0.049
1	1.999	-0.076	1	2.059	-0.102
1	1.972	0.107	1	1.927	-0.292
1	2.091	0.104	1	1.858	-0.167
1	2.171	0.09	1	1.732	0.09
1	1.775	0.117	1	1.851	-0.208
1	1.759	0.057	1	2.189	-0.409
1	1.232	-0.149	1	1.56	0.114
1	1.266	-0.102	1	1.91	-0.161
1	2.072	-0.237	1	1.814	-0.174
1	1.543	-0.076	1	2.103	-0.056
1	1.504	-0.276	1	2.065	0.057
1	2.149	-0.42	1	1.832	0
1	1.977	0.049	1	2.101	0.083
1	1.48	-0.638	1	2.181	-0.215
1	1.681	-0.292	1	2.269	0.064
1	1.61	-0.347	1	2.01	-0.301
1	1.8	0.009	1	1.788	-0.056
1	1.375	-0.495	1	1.937	0.025
1	1.871	0.124	1	1.494	0.1

Continued on next page

Table A.1 – *Continued from previous page*

Category	Log length	Log Displ.	Category	Log length	Log Displ.
1	2.026	-0.143	1	2.002	-0.347
1	1.625	-0.319	1	1.894	-0.102
1	1.799	-0.081	1	1.688	-0.301
1	2.094	0.029	1	2.086	-0.31
1	1.888	-0.066	1	1.969	0.093
1	1.969	0.017	1	2.115	-0.26
1	1.743	0.009	1	2.173	-0.167
1	2.546	-0.081	1	1.545	-0.149
1	2.225	0.127	1	2.278	-0.721
1	1.524	0.061	1	1.84	0.068
1	1.72	-0.244	1	1.999	-0.086
1	1.409	-0.721	1	1.874	-0.009
1	2.001	-0.194	1	1.836	-0.523
1	1.516	-0.469	1	2.298	0.068
1	2.235	0.152	1	1.837	-0.292
1	1.563	-0.004	1	1.631	-0.456
1	1.763	-0.161	1	2.156	0.212
1	1.66	-0.131	1	1.446	-0.456
1	1.982	-0.056	1	2.067	0.336
1	1.792	-0.268	1	1.629	-0.268
1	2.181	-0.114	1	1.85	-0.602
1	2.177	0.083	1	2.064	0.017
1	2.254	0.004	1	1.655	0.045
1	2.331	-0.114	1	2.206	0.152
1	2.302	-0.086	1	2.116	-0.18
1	1.553	-1.523	1	1.365	-0.824
1	1.799	-0.137	1	1.463	-0.678
1	1.8	-0.26	1	1.374	-0.292
1	1.841	-0.26	1	1.715	-0.086
1	1.659	-0.721	1	1.661	-0.284
1	2.237	-0.237	1	1.868	-0.18
1	2.247	-0.42	1	1.225	-0.237
1	1.781	-0.602	1	1.519	0.009
1	2.072	-0.137	1	2.131	0.301
1	1.46	-0.824	1	1.611	0.021
1	1.841	-0.377	1	1.679	-0.347
1	2.197	-0.569	1	1.664	-0.027

Continued on next page

Table A.1 – *Continued from previous page*

Category	Log length	Log Displ.	Category	Log length	Log Displ.
1	2.04	-0.009	1	1.706	-0.081
1	1.782	-0.252	1	2.113	0.013
1	1.867	-0.097	1	1.95	-0.509
1	1.861	-0.208	1	1.644	-0.161
1	1.987	-0.509	1	1.972	0.076
1	1.748	-0.229	1	1.648	-0.167
1	1.847	-0.387	1	1.766	-0.041
1	2.024	-0.347	1	1.381	-0.036
1	1.936	-0.301	1	1.733	-0.18
1	2.091	-0.523	1	1.339	-0.387
1	1.856	-0.046	1	2.174	-0.229
1	1.636	-0.638	1	1.403	-0.174
1	1.665	0.076	1	2.003	-0.201
1	1.771	-0.187	1	1.831	-0.409
1	1.756	-0.337	1	1.86	-0.276
1	2.329	-0.222	1	1.817	-0.18
1	1.559	-0.42	1	597	-0.585
1	2.335	0.033	1	1.936	-0.161
1	1.993	-0.357	1	2.125	-0.046
1	2.042	-0.201	1	2.228	-0.032
1	2.383	-0.076	1	2.015	-0.032
1	1.808	-0.367	1	1.678	-0.509
1	1.88	-0.42	1	2.014	-0.387
1	1.948	-0.42	1	2.183	-0.009
1	1.621	-0.097	1	942	-0.066
1	1.684	-0.066	1	2.086	-0.602
1	2.08	0.068	1	1.977	-0.125
1	1.75	0.017	1	1.861	-0.131
1	2.243	-0.036	1	1.93	-0.319
1	1.526	-0.229	1	2.257	-0.108
1	1.81	-0.086	1	1.582	-0.854
1	2.257	-0.215	1	2.031	-0.018
1	2.039	0.104	1	2.064	-0.276
1	1.44	-0.538	1	1.68	-0.066
1	1.942	-0.244	1	1.549	-0.481
1	1.638	-0.155	1	1.532	-0.509
1	1.973	-0.167	1	2.023	-0.071

Continued on next page

Table A.1 – *Continued from previous page*

Category	Log length	Log Displ.	Category	Log length	Log Displ.
1	2.296	-0.013	1	2.157	0.143
1	1.791	0.045	1	2.191	-0.208
1	1.833	-0.252	1	2.313	-0.337
1	2.217	-0.337	1	2.23	0.117
1	2.185	0.079	1	1.731	-0.143
1	1.75	-0.276	1	1.877	-0.143
1	1.79	0.013	1	1.948	0.013
1	1.906	-0.26	1	1.794	-0.252
1	1.878	-0.387	1	1.924	-0.319

Table A.2: Table shows the category 2 fault length and corresponding fault maximum displacement data for faults picked using 0.5 m resolution DEM. Values are the log of measurements made in metres.

Category	Log length	Log Displ.	Category	Log length	Log Displ.
2	2.702	0.74	2	1.9	0.32
2	1.815	0.326	2	2.562	0.441
2	1.894	0.42	2	1.825	0.286
2	2.202	0.389	2	2.125	0.199
2	2.203	0.179	2	2.075	0.436
2	1.876	0.29	2	1.631	0.107
2	2.258	0.292	2	1.96	0.348
2	1.499	-0.046	2	1.792	-0.328
2	1.963	0.225	2	2.587	0.498
2	2.044	0.67	2	2.04	0.382
2	2.303	0.584	2	1.972	0.111
2	2.377	0.334	2	2.317	0.283
2	2.165	0.164	2	2.366	0.594
2	2.263	0.657	2	2.388	0.299
2	2.456	0.204	2	2.168	0.124
2	2.394	0.52	2	2.163	0.358
2	2.197	0.621	2	1.962	0.292
2	2.124	0.265	2	1.832	0.238
2	2.418	0.328	2	1.953	0.124
2	2.165	0.438	2	1.965	0.34
2	2.062	0.318	2	2.594	0.223

Continued on next page

Table A.2 – *Continued from previous page*

Category	Log length	Log Displ.	Category	Log length	Log Displ.
2	2.356	0.422	2	2.101	0.217
2	2.119	0.25	2	2.246	0.303
2	1.748	0.013	2	2.005	0.164
2	2.389	0.701	2	1.911	0.29
2	2.772	0.425	2	2.309	0.307
2	2.4	0.524	2	1.797	0.143
2	2.359	0.356	2	2.336	0.279
2	1.835	0.649	2	1.79	0.137
2	2.112	0.378	2	1.748	0.307
2	2.345	0.31	2	1.44	0.176
2	1.785	0.173	2	1.481	0.207
2	1.697	0.121	2	1.591	0.238
2	2.533	0.303	2	1.364	0.134
2	1.984	0.352	2	1.496	0.217
2	1.893	0.137	2	1.71	0.583
2	2.018	0.149	2	1.985	0.107
2	2.09	0.167	2	1.613	0.124
2	2.157	0.248	2	1.664	0.13
2	2.284	0.25	2	1.193	-0.027
2	2.307	0.305	2	1.947	0.225
2	2.283	0.276	2	1.819	0.253
2	2.117	0.393	2	2.354	0.207
2	1.888	0.25	2	2.315	0.164
2	2.058	0.358	2	2.257	0.188
2	2.11	0.512	2	2.252	0.158
2	1.674	0.228	2	2.293	0.23
2	1.674	0.137	2	1.83	0.107
2	1.501	0.09	2	1.712	0.072
2	1.868	0.491	2	2.472	0.146
2	2.017	0.386	2	1.998	0.09
2	1.705	-0.538	2	1.905	0.021
2	1.587	0.215	2	1.789	0.072
2	1.669	0.045			

Table A.3: Table shows the category 3 fault length and corresponding fault maximum displacement data for faults picked using 0.5 m resolution DEM. Values are the log of measurements made in metres.

Category	Log length	Log Displ.	Category	Log length	Log Displ.
3	2.611	0.845	3	2.264	0.678
3	2.729	0.707	3	2.097	0.43
3	2.158	0.675	3	1.818	0.442
3	1.938	0.281	3	2.23	0.68
3	2.578	0.758	3	2.267	0.599
3	2.34	0.689	3	1.853	0.352
3	2.497	0.589	3	2.174	0.423
3	1.871	0.173	3	1.999	0.324
3	1.88	0.152	3	2.051	0.439
3	2.08	0.097	3	2.517	0.705
3	1.738	0.207	3	1.917	0.496
3	1.684	0.274	3	2.071	0.449
3	1.993	0.182	3	2.205	0.793
3	2.276	0.377	3	1.792	0.243
3	2.353	0.453	3	1.697	0.342
3	2.425	0.671	3	1.969	0.262
3	2.119	0.431	3	1.871	0.344
3	2.021	0.688	3	2.592	0.6998
3	1.927	0.484	3	2.175	0.292
3	2.184	0.537	3	1.706	0.262
3	2.556	0.646	3	2.36	0.539
3	2.179	0.491	3	2.16	0.577
3	2.213	0.766	3	1.961	0.729
3	2.453	0.668	3	1.692	0.238
3	2.029	0.728	3	2.437	0.617
3	2.333	0.835	3	2.335	0.618
3	2.476	0.9	3	1.983	0.31
3	1.945	0.236	3	1.668	0.467
3	2.354	0.567	3	1.743	0.446
3	2.566	0.782	3	2.016	0.442
3	2.075	0.396	3	1.667	0.348
3	2.422	0.697	3	1.956	0.422
3	2.142	0.559	3	1.607	0.196

Table A.4: Table shows the category 4 fault length and corresponding fault maximum displacement data for faults picked using 0.5 m resolution DEM. Values are the log of measurements made in metres.

Category	Log length	Log Displ.	Category	Log length	Log Displ.
4	1.784	0.597	4	2.218	0.678
4	1.993	0.829	4	2.494	1.078
4	2.262	0.656	4	2.491	0.905
4	2.051	0.627	4	2.297	0.605
4	2.438	0.615	4	1.972	0.452
4	2.619	0.594	4	2.324	0.497
4	2.379	0.413	4	2.176	0.611
4	2.21	0.768	4	2.745	1.122
4	2.11	0.772	4	2.434	0.87
4	1.505	0.582	4	2.476	0.822
4	2.464	0.826	4	2.512	0.679
4	2.506	0.76	4	2.153	0.484
4	3.059	1.272	4	1.964	0.516
4	2.216	0.458	4	2.315	0.716
4	2.174	0.822	4	2.049	0.626
4	2.201	0.656	4	2.016	0.516
4	2.494	0.859	4	2.591	0.651
4	2.217	0.893	4	2.445	0.749
4	1.63	0.865	4	2.387	0.507
4	2.267	0.225	4	2.279	0.704
4	2.425	0.636	4	2.369	0.407
4	2.203	0.553	4	2.716	1.164
4	2.073	0.238	4	2.175	0.611
4	2.571	0.444	4	2.236	0.516
4	2.292	0.49	4	1.641	0.893
4	2.85	1.189	4	1.872	0.703
4	2.43	0.413	4	2.16	0.879
4	2.369	0.575	4	1.669	0.602
4	2.025	0.316	4	2.413	0.887
4	2.405	1	4	2.152	0.49
4	2.281	0.88	4	2.755	1.002
4	1.737	0.378	4	2.144	0.679
4	2.706	1.134	4	2.588	0.793
4	2.548	0.721	4	2.08	0.588

Continued on next page

Table A.4 – *Continued from previous page*

Category	Log length	Log Displ.	Category	Log length	Log Displ.
4	2.38	0.816	4	2.344	1.085
4	1.934	0.58	4	2.625	1.194
4	2.241	0.67	4	2.171	0.569
4	2.221	0.943	4	2.204	0.453
4	2.291	0.433	4	1.504	0.093
4	2.316	0.992	4	2.101	0.479
4	2.487	0.901	4	2.179	0.356
4	1.814	0.55	4	1.345	0.294
4	1.933	0.253	4	2.011	0.891
4	2.84	1.16	4	2.216	0.631
4	2.606	0.576	4	2.185	0.396
4	2.443	0.867	4	2.087	0.474
4	2.352	0.693	4	1.684	0.1553
4	2.294	0.695	4	1.441	0.253
4	2.896	1.43	4	1.803	0.398
4	2.323	0.579			

Table A.5: Table shows the category 5A fault length and corresponding fault maximum displacement data for faults picked using 0.5 m resolution DEM. Values are the log of measurements made in metres.

Category	Log length	Log Displ.	Category	Log length	Log Displ.
5A	2.494	0.922	5A	1.225	0.775
5A	2.346	1.093	5A	2.737	1.104
5A	2.196	0.734	5A	2.405	0.971
5A	2.309	0.897	5A	3.232	1.524
5A	2.734	0.652	5A	2.356	0.902
5A	2.786	0.928	5A	2.919	1.317
5A	2.452	0.64	5A	2.004	0.539
5A	2.396	0.566	5A	1.966	0.377
5A	2.235	0.531	5A	1.822	0.563
5A	2.458	1.042	5A	1.718	0.62
5A	2.267	1.028	5A	2.631	0.822
5A	2.16	0.819	5A	3.022	1.568
5A	2.57	1.161	5A	1.713	0.589
5A	2.038	0.843	5A	3.099	1.328

Continued on next page

Table A.5 – *Continued from previous page*

Category	Log length	Log Displ.	Category	Log length	Log Displ.
5A	1.876	0.62	5A	2.556	0.968
5A	2.643	1.1	5A	2.208	0.594
5A	2.606	1.074	5A	2.559	0.923
5A	2.651	1.202	5A	3.033	1.33
5A	2.399	0.777	5A	2.545	0.927
5A	1.8	0.695	5A	2.511	0.88
5A	2.631	0.822	5A	2.44	0.858
5A	3.022	1.568	5A	1.715	0.695
5A	1.713	0.589	5A	3.279	1.364
5A	3.099	1.328	5A	2.177	0.65
5A	2.556	0.968	5A	3.097	1.388
5A	2.208	0.594	5A	2.301	0.484
5A	2.559	0.923	5A	2.279	0.802
5A	3.033	1.33	5A	2.436	0.691
5A	2.545	0.927	5A	2.755	0.927
5A	2.511	0.88	5A	2.276	0.566
5A	2.44	0.858	5A	2.636	0.66
5A	1.715	0.695	5A	2.122	0.35
5A	3.279	1.364	5A	2.984	1.048
5A	2.177	0.65	5A	2.164	0.666
5A	3.097	1.388	5A	2.255	0.544
5A	2.301	0.484	5A	2.775	1.09
5A	2.279	0.802	5A	2.459	0.795
5A	2.436	0.691	5A	2.893	1.496
5A	2.755	0.927	5A	2.416	0.676
5A	2.276	0.566	5A	2.498	1.088
5A	2.636	0.66	5A	2.826	1.409
5A	2.122	0.35	5A	2.408	0.869
5A	2.984	1.048	5A	1.999	0.34
5A	2.164	0.666	5A	2.72	1.235
5A	2.255	0.544	5A	2.042	0.898
5A	2.775	1.09	5A	2.06	0.615
5A	2.459	0.795	5A	2.022	0.744
5A	2.893	1.496	5A	2.415	0.851
5A	2.416	0.676	5A	1.938	0.511
5A	2.498	1.088	5A	1.803	0.559
5A	2.826	1.409	5A	1.92	0.563

Continued on next page

Table A.5 – *Continued from previous page*

Category	Log length	Log Displ.	Category	Log length	Log Displ.
5A	2.408	0.869	5A	2.339	0.673
5A	1.999	0.34	5A	2.084	0.835
5A	2.72	1.235	5A	2.568	1.132
5A	2.042	0.898	5A	2.396	0.876
5A	2.06	0.615	5A	2.977	1.284
5A	2.022	0.744	5A	1.911	0.731
5A	2.415	0.851	5A	2.625	1.131
5A	1.938	0.511	5A	2.496	0.679
5A	1.803	0.559	5A	1.498	0.377
5A	1.92	0.563	5A	1.935	0.49
5A	2.339	0.673	5A	2.609	1.026
5A	2.084	0.835	5A	2.149	0.526
5A	2.568	1.132	5A	2.41	1.112
5A	2.396	0.876	5A	2.246	0.714
5A	2.977	1.284	5A	2.206	0.691
5A	1.911	0.731	5A	2.51	1.037
5A	2.625	1.131	5A	2.44	0.901
5A	2.496	0.679	5A	2.152	0.842
5A	1.498	0.377	5A	2.279	0.836
5A	1.935	0.49	5A	2.363	0.857
5A	2.609	1.026	5A	2.374	0.61
5A	2.149	0.526	5A	2.322	0.757
5A	2.41	1.112	5A	2.155	0.725
5A	2.246	0.714	5A	2.013	0.496
5A	2.206	0.691	5A	1.857	0.501
5A	2.51	1.037	5A	2.06	0.757
5A	2.44	0.901	5A	2.287	0.674
5A	2.152	0.842	5A	2.811	1.235
5A	2.279	0.836	5A	2.844	1.223
5A	2.363	0.857	5A	2.105	0.601
5A	2.374	0.61	5A	2.494	0.952
5A	2.322	0.757	5A	1.635	0.713
5A	2.155	0.725	5A	1.443	0.547
5A	2.013	0.496	5A	1.225	0.775
5A	1.857	0.501	5A	2.737	1.104
5A	2.06	0.757	5A	2.405	0.971
5A	2.287	0.674	5A	3.232	1.524

Continued on next page

Table A.5 – *Continued from previous page*

Category	Log length	Log Displ.	Category	Log length	Log Displ.
5A	2.811	1.235	5A	2.356	0.902
5A	2.844	1.223	5A	2.919	1.317
5A	2.105	0.601	5A	2.004	0.539
5A	2.494	0.952	5A	1.966	0.377
5A	1.635	0.713	5A	1.822	0.563
5A	1.443	0.547	5A	1.718	0.62

Table A.6: Table shows the category 5B fault length and corresponding fault maximum displacement data for faults picked using 0.5 m resolution DEM. Values are the log of measurements made in metres.

Category	Log length	Log Displ.	Category	Log length	Log Displ.
5B	2.311	0.865	5B	2.967	1.072
5B	2.692	0.968	5B	3.008	1.233
5B	2.133	0.526	5B	2.408	0.939
5B	3.003	1.247	5B	2.627	1.098
5B	2.774	0.973	5B	2.659	0.699
5B	2.439	0.788	5B	2.908	0.905
5B	3.111	1.125	5B	2.765	1.392
5B	3.202	1.287	5B	2.37	0.755
5B	3.15	1.319	5B	2.557	0.925
5B	2.845	0.915	5B	1.975	0.521
5B	3.165	1.331	5B	3.303	1.324
5B	2.8	0.943	5B	2.024	0.505

Table A.7: Table shows the category 5C fault length and corresponding fault maximum displacement data for faults picked using 0.5 m resolution DEM. Values are the log of measurements made in metres.

Category	Log length	Log Displ.	Category	Log length	Log Displ.
5C	2.587	0.8	5C	2.533	0.699
5C	2.837	0.915	5C	2.416	0.658
5C	2.538	0.811	5C	2.34	0.58
5C	2.703	0.77	5C	2.035	0.407
5C	2.571	0.881	5C	2.25	0.577

Continued on next page

Table A.7 – *Continued from previous page*

Category	**Log length**	**Log Displ.**	**Category**	**Log length**	**Log Displ.**
5C	2.935	1.084	5C	2.557	0.744
5C	2.344	0.369	5C	2.193	0.593
5C	3.138	1.088	5C	2.329	0.862
5C	2.293	0.585	5C	2.34	0.603
5C	2.354	0.676			

Appendix B

Fault $D_{max}L$ measurements for Krafla, 10 m resolution

Table B.1: Table shows the fault length and corresponding fault maximum displacement data for faults picked using 10 m resolution DEM. Values are the log of measurements made in metres.

Log length	Log Displ.	Log length	Log Displ.	Log length	Log Displ.
2.808	0.62	3.48	1.107	2.544	1.33
2.697	0.628	2.968	1.113	3.407	1.334
2.618	0.667	2.935	1.115	3.016	1.337
2.987	0.721	3.304	1.134	3.569	1.357
2.471	0.742	3.053	1.137	3.433	1.361
2.66	0.753	3.037	1.144	2.752	1.367
2.605	0.827	2.796	1.153	3.024	1.379
2.714	0.831	3.341	1.164	3.185	1.394
3.112	0.854	3.563	1.182	3.175	1.395
2.612	0.881	3.141	1.205	3.556	1.406
3.421	0.916	2.938	1.214	3.2	1.425
3.146	0.929	2.917	1.228	3.32	1.44
2.876	0.937	3.222	1.235	2.916	1.447
2.899	0.973	3.222	1.235	3.062	1.472
2.964	0.985	3.425	1.239	3.592	1.518
3.159	0.993	3.188	1.257	3.223	1.521
2.713	0.999	3.035	1.266	3.199	1.554
2.645	0.999	3.868	1.272	3.068	1.556
2.695	1.032	3.059	1.285	3.061	1.562
2.83	1.036	3.267	1.287	3.37	1.571

Continued on next page

Table B.1 – *Continued from previous page*

Log length	**Log Displ.**	**Log length**	**Log Displ.**	**Log length**	**Log Displ.**
3.343	1.043	3.15	1.296	3.301	1.572
2.953	1.05	3.193	1.313	3.289	1.591
2.884	1.062	2.93	1.317	3.085	1.596
2.969	1.078	2.837	1.324	3.205	1.631
2.839	1.083	3.065	1.325	3.278	1.768
2.839	1.09	2.944	1.326	3.284	1.831

Appendix C

Fault $D_{max}L$ measurements for Krafla, 30 m resolution

Table C.1: Table shows the fault length and corresponding fault maximum displacement data for faults picked using 30 m resolution DEM. Values are the log of measurements made in metres.

Log length	Log Displ.	Log length	Log Displ.	Log length	Log Displ.
3.304	0.751	2.895	1.201	3.292	1.385
3.349	0.806	3.356	1.207	3.558	1.414
3.313	0.872	3.418	1.214	3.143	1.424
3.471	0.901	3.738	1.24	3.481	1.467
3.564	0.904	3.329	1.264	3.567	1.487
2.929	0.922	3.683	1.264	3.505	1.494
2.813	0.961	3.551	1.286	3.385	1.518
3.189	0.973	3.407	1.292	3.312	1.557
3.228	0.974	3.261	1.308	3.308	1.585
3.129	0.979	3.862	1.321	3.418	1.586
3.745	1.03	3.37	1.322	3.418	1.586
3.156	1.05	3.287	1.363	3.285	1.588
3.346	1.078	3.351	1.364	3.495	1.62
3.053	1.139	3.696	1.375	3.178	1.658
3.297	1.195	3.272	1.376	3.485	1.789

Appendix D

Interferograms

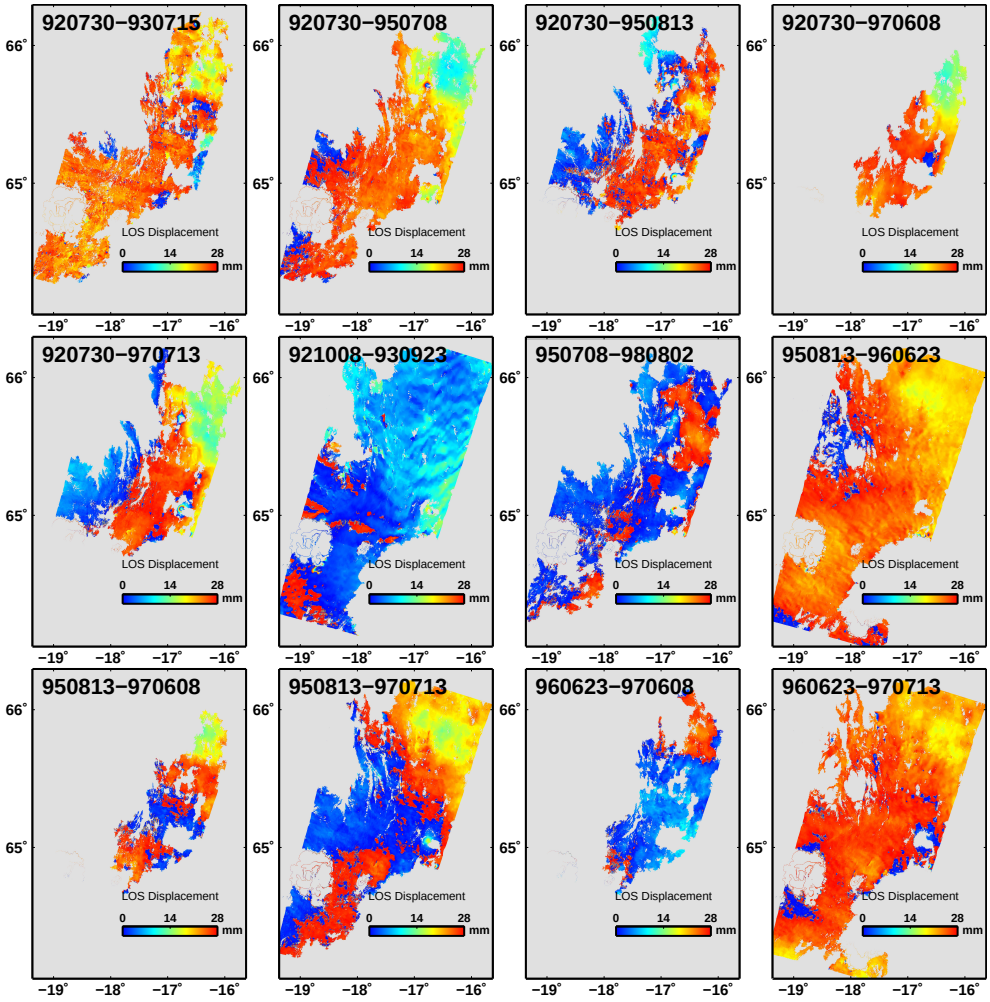

Figure D.1: Plot of the geocoded interferograms as processed through ROI_pac, interferograms 1-12.

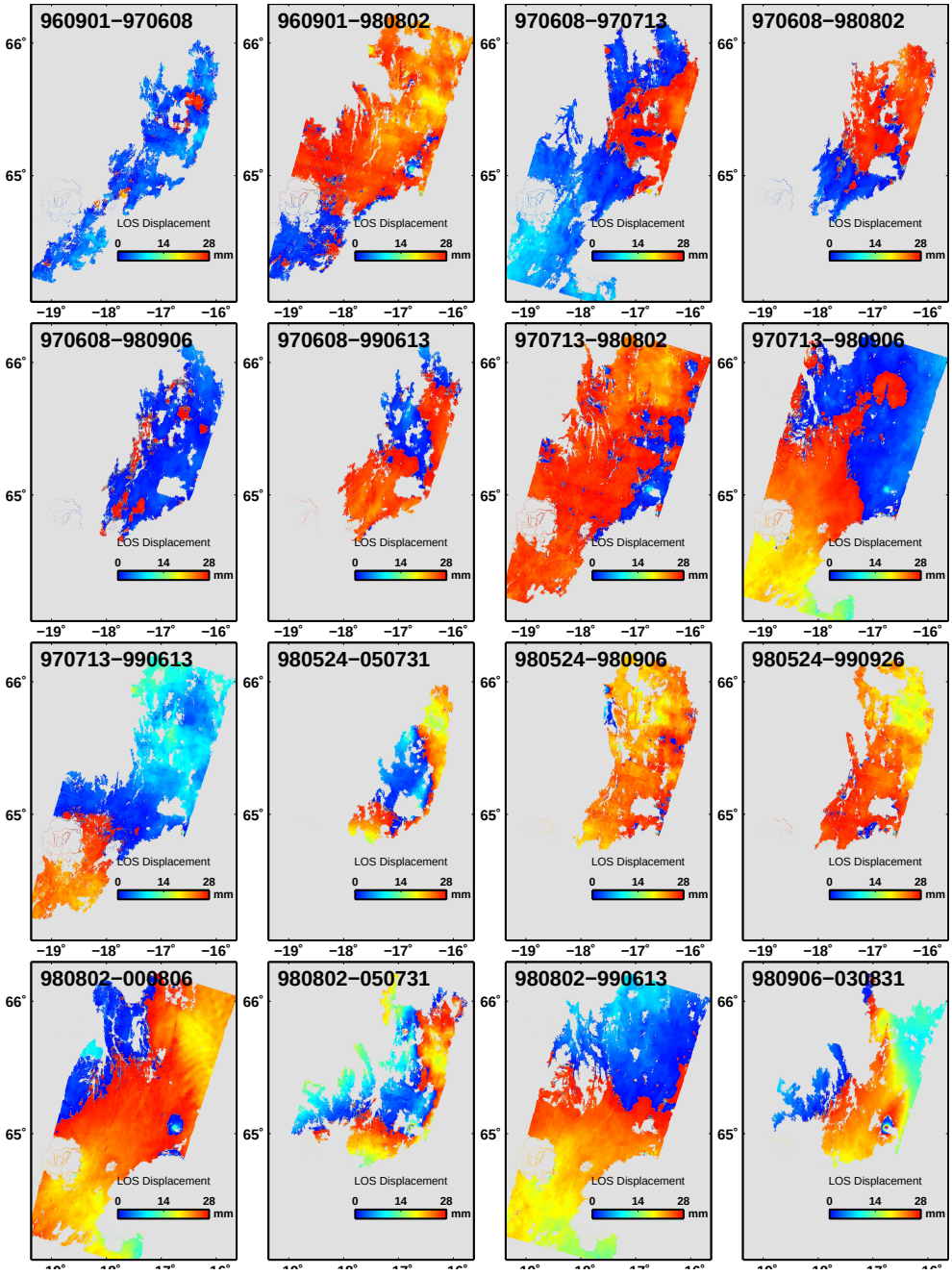

Figure D.2: Plot of the geocoded interferograms as processed through ROI_pac, interferograms 13-28.

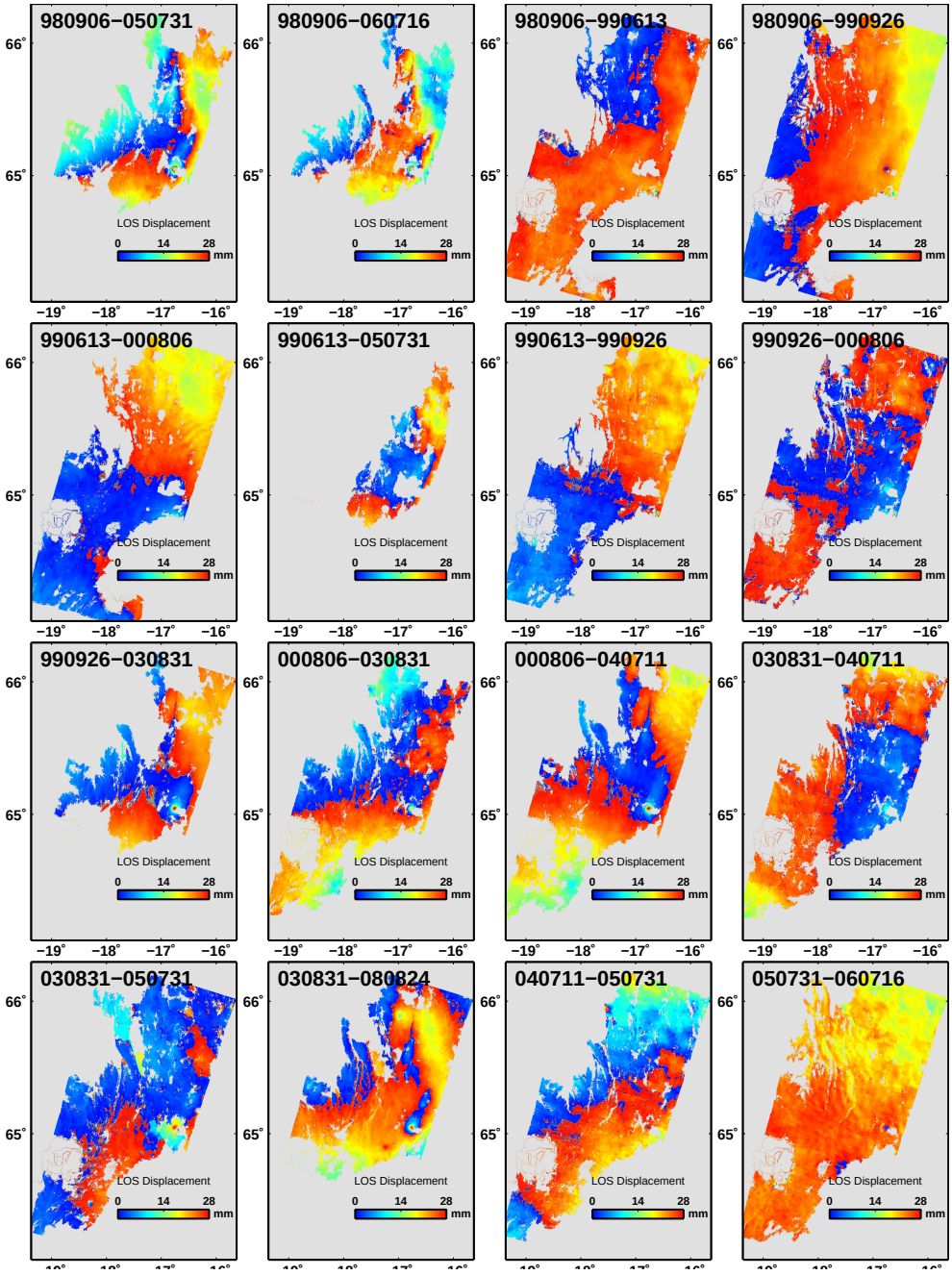

Figure D.3: Plot of the geocoded interferograms as processed through ROI_pac, interferograms 29-44.

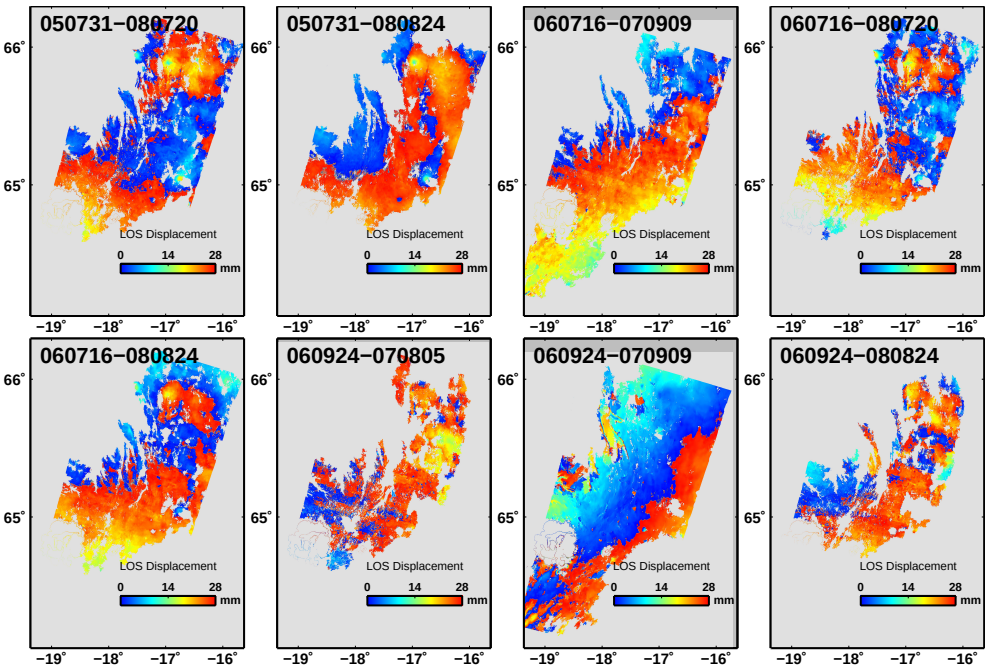

Figure D.4: Plot of the geocoded interferograms as processed through ROI_pac, interferograms 45-52.

Appendix E

$\pi - rate$ interferogram groups

Table E.1: Table shows the groups (A, B and C) of interferograms that were selected and processed through Pi-RATE for time-series.analysis

ifg pair	A	B	C	ifg pair	A	B	C	ifg pair	A	B	C
920730-930715			√	970713-980802	√	√	√	990926-030831		√	√
920730-950708	√	√	√	970713-980906		√	√	000806-020915			√
920730-950813			√	970713-990613	√	√	√	000806-030831	√	√	√
920730-970608			√	980524-050731		√	√	000806-040711	√	√	√
920730-970713	√	√	√	980524-980906			√	030831-040711	√	√	√
921008-930923		√	√	980524-990926			√	030831-050731	√	√	√
950708-980802		√	√	980802-000806		√	√	030831-080824	√	√	√
950813-960623	√	√	√	980802-050731		√	√	040711-050731		√	√
950813-970608			√	980802-990613	√	√	√	050731-060716		√	√
950813-970713	√	√	√	980906-030831		√	√	050731-080720		√	√
960623-970608			√	980906-050731		√	√	050731-080824	√	√	√
960623-970713	√	√	√	980906-060716		√	√	060716-070909		√	√
960901-970608			√	980906-990613		√	√	060716-080720			√
960901-980802		√	√	980906-990926		√	√	060716-080824		√	√
970608-970713		√	√	990613-000806	√	√	√	060924-070805			√
970608-980802			√	990613-050731			√	060924-070909		√	√
970608-980906			√	990613-990926	√	√	√	060924-080824			√
970608-990613			√	990926-000806	√	√	√				

Appendix F

Time Series from π-rate

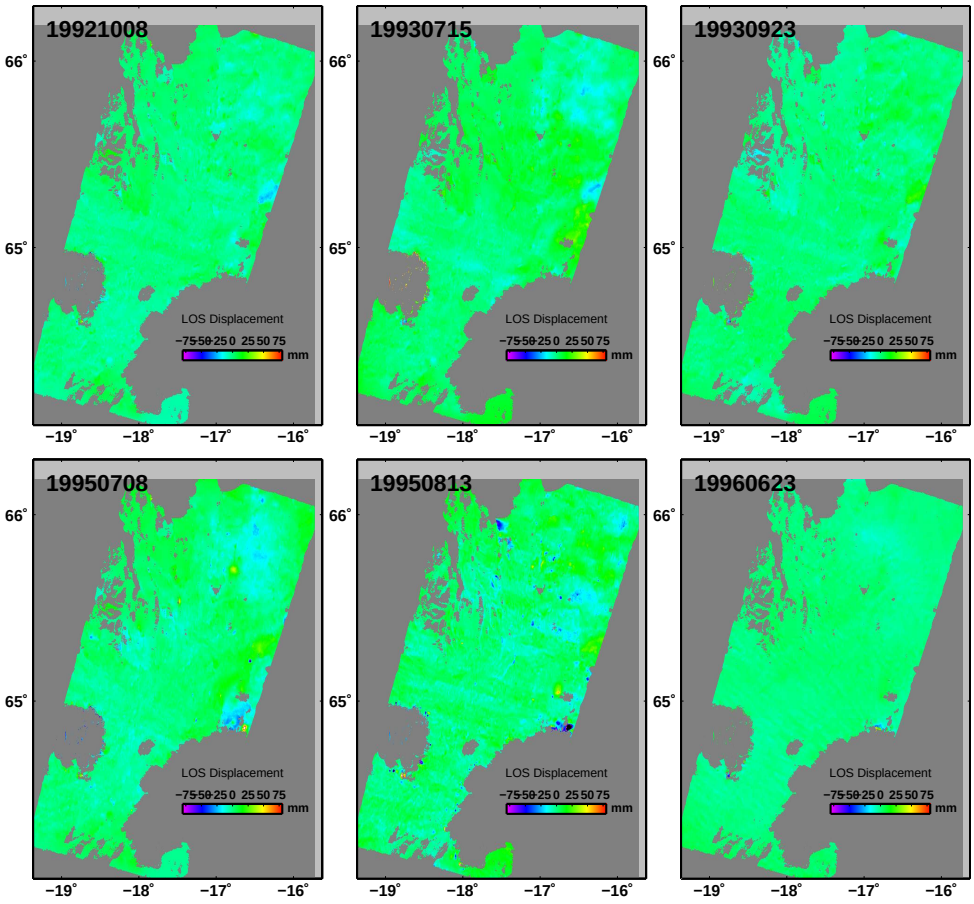

Figure F.1: Plots of the incremental timeseries produced by processing through π-rate,19921008 - 19960623.

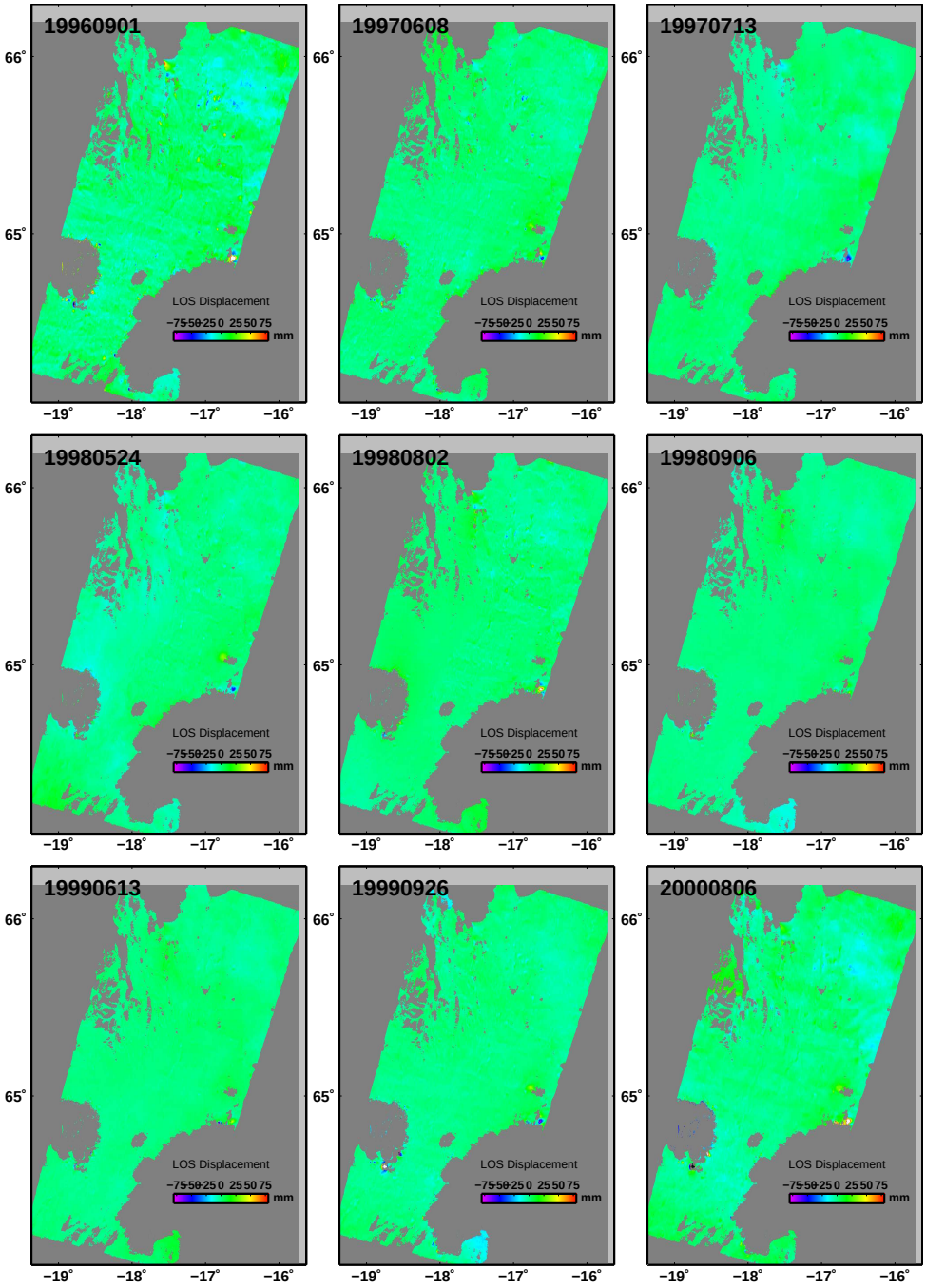

Figure F.2: Plots of the incremental timeseries produced by processing through π-rate,19960901 - 20000806.

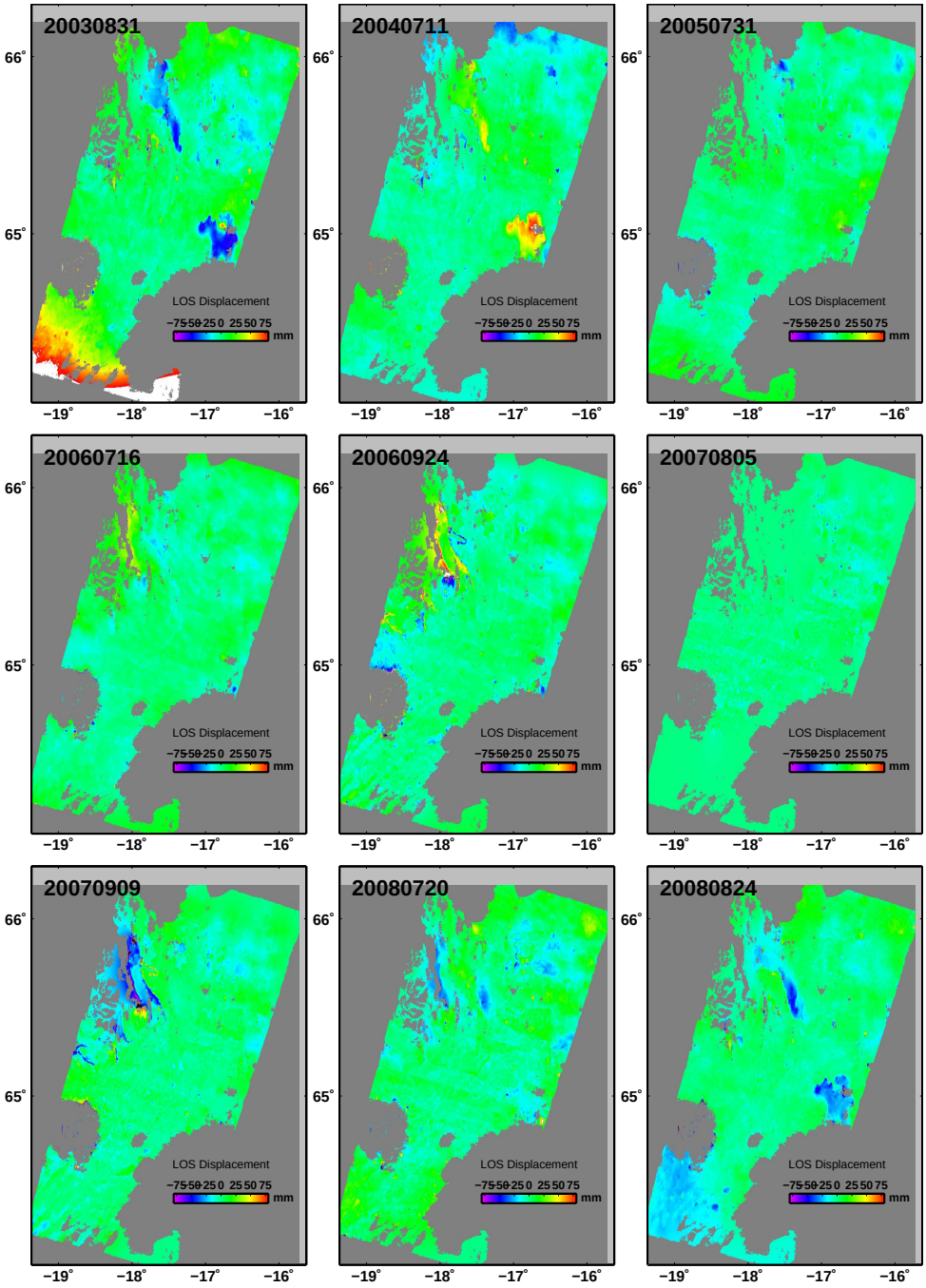

Figure F.3: Plots of the incremental timeseries produced by processing through π-rate,20030831 - 20080824.